

Electron-tunneling studies on $CeCoIn_5$ heavy-fermion thin films and microstructures

Dissertation zur Erlangung
des Doktorgrades der Naturwissenschaften

vorgelegt beim Fachbereich Physik
der Johann Wolfgang Goethe-Universität
in Frankfurt am Main

VON

Oleksandr Foyevtsov

aus Lviv, Ukraine

Frankfurt am Main (2012)

(D 30)

vom Fachbereich Physik der
Johann Wolfgang Goethe-Universität als Dissertation angenommen.

Dekan: Prof. Dr. Michael Huth

1. Gutachter: Prof. Dr. Michael Huth

2. Gutachter: Prof. Dr. Michael Lang

Datum der Disputation: 12 Juni 2012

Zusammenfassung

In vielen Fällen bieten qualitativ hochwertige dünne Schichten aus einem zu untersuchenden Material die Möglichkeit, wertvolle physikalische Informationen über seine Eigenschaften zu erhalten. Planare Tunnelspektroskopie und quantenmechanische Interferometrie zum Beispiel sind grundlegende Verfahren zur elektronischen Charakterisierung von Festkörpern. In dieser Arbeit berichten wir über die elektronischen Eigenschaften der Schweren-Fermionen-Verbindung $CeCoIn_5$. Bisherige Versuche, $CeCoIn_5$ -Dünnschichten mit der gewünschten Qualität herzustellen, waren nicht sehr erfolgreich. Diese Arbeit verfolgt daher die folgenden beiden Hauptziele:

- (1) Verbesserung der Qualität von $CeCoIn_5$ -Filmen mit Hilfe von molekularer Gasphasenabscheidung und
- (2) Untersuchung der Tieftemperatureigenschaften von $CeCoIn_5$ -Filmen mit direkten Messverfahren

Wachstum und Strukturuntersuchungen

Ein bekanntes Problem verbunden mit dem Wachstum von $CeCoIn_5$ -Dünnschichten ist die starke Variation der Oberflächenmorphologie bei unterschiedlichen Wachstumsversuchen, was aussagekräftige planare Tunnelexperimente unmöglich macht. Es wurde vermutet, dass dieses unregelmäßige Wachstum seine Ursache in den entnetzenden Eigenschaften von In und der großen Empfindlichkeit der Wachstumodynamik beim Abscheidungsbeginn hat. Um nun diese Schwierigkeiten zu umgehen, haben wir versucht, die Wachstumsparameter für dünne Schichten aus $CeIn_3$, einer mit $CeCoIn_5$ verwandten Verbindung mit ähnlich Eigenschaften, zu optimieren. Bei dieser Untersuchung stellten wir fest, dass die Morphologie von $CeIn_3$ -Dünnschichten ähnlich denen von $CeCoIn_5$ ist, da sie stark abhängig von verschiedenen Oxid-Substraten und Probenhaltermaterialien ist und bei sonst identischen Versuchsbedingungen stark variiert. Zudem wurden merkliche Unterschiede bei der elementaren Zusammensetzung von $CeIn_3$ -Filmen festgestellt. Bei einem Simultanversuch, wo verschiedene Serien von $CeIn_3$ -Filmen hergestellt wurden, änderten wir lediglich die Depositionstemperatur der Proben innerhalb einer Serie. Wir stellen nachvollziehbare Veränderungen der Oberflächenmorphologie, der kristallographischen und elementspezifischen Zusammensetzung und der elektronischen Transporteigenschaften bei tiefen Temperaturen innerhalb einer Probenserie fest. Dennoch gab es immer noch Abweichungen zwischen Schichten aus verschiedenen Serien.

Hochtemperatur-Knudsen Zellen für Ce und In und ein Elektronenstrahlverdampfer für Co wurden für die Deposition von $CeCoIn_5$ -Filmen verwendet. Die Filme waren morphologisch vergleichbar mit denen, die mit drei verschiedenen Effusionszellen hergestellt wurden. Elektronenbeugung unter streifendem Einfall und polarwinkelorientierte Röntgenbeugung bestätigten, dass $CeCoIn_5$ -Filme eine Tendenz zu epitaktischem Wachstum aufweisen, wenn der Co-Fluss mit einem Elektronenstrahlverdampfer gesteuert wird. Dieses Verhalten wurde mit keinem anderen bisherigen Verfahren gefunden. Rasterkraftmikroskopuntersuchungen, Röntgen-Linienprofilanalyse und einfache elektronische Transportmessungen deuten auf eine schlechte strukturelle Qualität der $CeCoIn_5$ Mikrokrystallite hin. Es wird von uns vermutet, dass dies an der hohen Konzentration von Versetzungen liegt.

Elektronische Transportmessungen

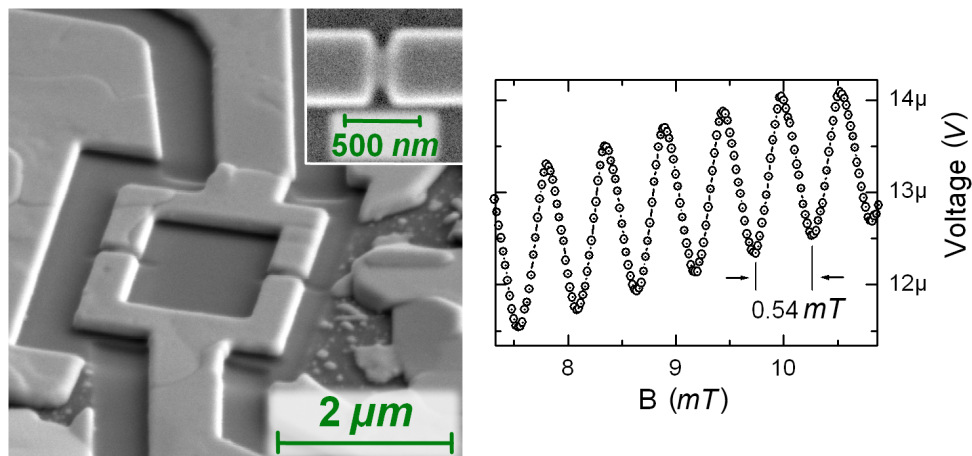
Bei der Durchführung elektronischer Transportmessungen bei tiefen Temperaturen beobachteten wir ein Verhalten, welches typisch ist für $CeIn_3$ Volumenproben und stellten zusätzliche Beiträge fest, die von einer segregierten In -Phase herrühren. Diese Phase war jedoch nicht anwesend bei den Transportmessungen an einem einzelnen Mikrokrystall eines $CeIn_3$ Films. Sowohl bei der Vermessung der gesamten Schicht als auch von einzelnen Mikrokrystallen fanden wir eine geringe Qualität der $CeIn_3$ kristallinen Phase. Dies läuft mit einem stark reduzierten Restwiderstandsverhältnis verglichen mit $CeIn_3$ -Kristallen einher.

Die temperaturabhängigen Transportmessungen von $CeCoIn_5$ -Dünnschichten und deren einzelner Mikrokrystalle ist äquivalent zu $CeCoIn_5$ -Volumenkrystallen und sind charakterisiert durch kleine Werte des Restwiderstandsverhältnisses. Die Restwiderstandsverhältniswerte der $CeCoIn_5$ -Mikrokrystalle sind etwas größer als die der gesamten Schicht, was erkennen lässt, dass der Beitrag zum Gesamtwiderstand durch Streuung von Ladungsträgern an Korngrenzen gering ist.

Nach der erfolgreichen Messung der Transporteigenschaften der $CeCoIn_5$ -Mikrokrystalle wurde planare Tunnelspektroskopie an diesen durchgeführt. Gegenelektroden für eine planare Tunneldiode können mit einem $W-C$ Nanokomposit (W -IBID) mit einem fokussiertem Ionenstrahl (FIBID) hergestellt werden. Um zu prüfen, ob W -IBID für diese Zwecke geeignet ist, wurden planare $Al - Al_2O_3 - W$ -IBID Tunneldioden hergestellt. Dynamische Leitfähigkeitsmessungen an diesen Dioden zeigten den erwarteten spektroskopischen Anteil der W -IBID Elektrode, welcher systematisch von der Tunnelbarriere abhängt.

Für Präparation die planarer Tunnelstruktur an $CeCoIn_5$ wurde ein $SiO-C$ Nanokomposit mit Hilfe von fokussierter Elektronenstrahldeposition als Tunnelbarriere auf die jeweiligen $CeCoIn_5$ -Schichten geschrieben. Als Precursor dienen Tetramethylsilan und Neopentasilan. Die erwähnten W -IBID Deponate bildeten die Gegenelektrode. Die Tunnelspektren, die an den Mikrostrukturen (geschrieben mit Tetramethylsilan) gemessen wurden, wiesen ein schwaches charakteristisches Verhalten der supraleitenden W -IBID Gegenelektrode und starke Nichtlinearitäten unterhalb der Supraleitungsübergangstemperatur von $CeCoIn_5$ auf. Dieses Verhalten war nicht reproduzierbar und konnte nicht hinreichend gut analysiert werden. Es ist wahrscheinlich auf die mangelnde Qualität und Durchlässigkeit der Tunnelbarriere zurückzuführen. Die Tunnelbarrieren, die mit dem Precursor Neopentasilan hergestellt wurden, hatten eine stark reduzierte Durchlässigkeit bei niedrigen Temperaturen, was spektroskopische Messungen schwierig machte.

In nächsten Schnitt präparieren wir mehrere $CeCoIn_5$ -Mikrokristall-Interferometer, wobei entweder die Breite oder die Dicke der supraleitenden Mikrobrücken variiert wurde. Für beide Fälle beobachteten wir das Auftreten eines kritischen Josephsonstromes durch die Mikrobrücken unterhalb der Supraleitungsübergangstemperatur für $CeCoIn_5$. Typisches SQUID-Verhalten, welches sich durch periodische Spannungsmodulation über ein magnetisches Feld auszeichnet, wurde bei den Interferometerstrukturen mit variabler Dicke nachgewiesen (siehe Abbildung), nicht jedoch bei denen mit variierender Breite. Dynamische Widerstandsmessungen, welche an dieser und an anderen Mikrobrücken un-



(links) $CeCoIn_5$ -Mikrokristall-Interferometer und (rechts) seine periodische Spannungsmodulation über dem magnetischen Feld.

terschiedlicher Dicke vorgenommen wurden, zeigten zusätzliche Besonderheiten, welche durch die periodische Bewegung von supraleitenden Abrikosov-Wirbeln entstehen, die von Aslamazov und Larkin in ihrer Theorie über supraleitende Mikrobrücken beschrieben wurden. Die Messungen an den Mikrostrukturen mit variable Dicke zeigten, dass die

Temperaturabhängigkeit des kritischen Josephsonstroms gut mit den theoretischen Voraussagen von Ambegaokar und Baratoff (AB) übereinstimmen. Es ist anzumerken, dass die Anwendung der AB-Gleichungen auf unsere Mikrobrücken kritisch zu betrachten ist: Jene Gleichungen wurden für Josephson-Tunnelstrukturen hergeleitet, während die Abmessungen unserer Mikrobrücken größer sind, als die Kohärenzlänge des Supraleiters $CeCoIn_5$. Andererseits sollte aber die Beschreibung der elektronischen Transporteigenschaften der supraleitenden Mikrobrücken anhand der charakteristischen supraleitenden Länge von $CeCoIn_5$, der Abmessungen der Mikrobrücken und der freien Weglänge der $CeCoIn_5$ Quasiteilchen erfolgen. Die ungewöhnlich große freie Weglänge der Quasiteilchen von $CeCoIn_5$ verhindert eine Klassifizierung der elektronischen Transporteigenschaften innerhalb der Mikrobrücken mit Hilfe von bekannten Modellen. Die unerwartete Übereinstimmung der Temperaturabhängigkeit des kritischen Josephsonstroms mit der AB Vorhersage mag damit zusammenhängen.

Beim Phasenübergang des $CeCoIn_5$ in den normalleitenden Zustand oberhalb der supraleitenden Übergangstemperatur ist zu erwarten, dass die dynamische Widerstandsmessung einen flachen Verlauf aufweist. Es wurde allerdings starkes nichtlineares Verhalten bis zu einer Temperatur von 10 K beobachtet, was eine fünfmal höhere Temperatur als die supraleitende Übergangstemperatur von $CeCoIn_5$ darstellt. Weiterhin wurden Magnetfeld-induzierte Anomalien festgestellt, welche ebenfalls im supraleitenden Zustand von $CeCoIn_5$ existierten. Aufgrund der Vielzahl der möglichen physikalischen Effekte bezüglich sowohl der elektronischen Niedertemperatureigenschaften von $CeCoIn_5$ als auch der Mikrobrücken-Geometrie ist es uns bisher nicht gelungen, eine gesamtheitliche Erklärung für das beobachtete Verhalten zu entwickeln. Repräsentative Ergebnisse von Transportmessungen der Mikrobrücken in normalleitender Phase werden hier allerdings vorgestellt.

Als weiteren Ausblick können Messungen an $CeCoIn_5$ Mikrobrücken mit variablen Breiten eine Möglichkeit bieten, den Anteil der intrinsischen Eigenschaften des normalleitenden Zustands von $CeCoIn_5$ vom Beitrag der Mikrobrückengeometrie zu trennen. Die große freie Weglänge der Quasiteilchen in $CeCoIn_5$ könnte eine Gelegenheit bieten, unserer Methoden der Mikrostrukturierung für einen Nachweis von Interferenzeffekten in der metallischen Phase von $CeCoIn_5$ zu verwenden. Dies würde einen direkten Zugang zur Untersuchung der Mechanismen bei der Relaxation von Elektronen in diesem Schwere-Fermionen-System darstellen.

Abstract

In many cases, the availability of high-quality thin films of a material under study allows to gain valuable physical insight into its properties. For example, when thin films are available, planar tunneling spectroscopy or quantum mechanical interferometry techniques can be used to probe the electronic properties in a very direct way. In this work, we study the rich but poorly understood electronic properties of the heavy-fermion compound $CeCoIn_5$. Numerous attempts to grow homogeneous $CeCoIn_5$ thin films of the desired quality have not been successful. Our work therefore pursues two goals:

- (1) to improve the $CeCoIn_5$ thin film quality using the molecular beam epitaxy and
- (2) to investigate the low-temperature electronic properties of the $CeCoIn_5$ thin films using direct probing methods.

Growth and structural studies

A common problem associated with $CeCoIn_5$ thin film growth is that the surface morphology of these films is coarse-grained with large variations from growth to growth, which makes reliable planar tunneling experiments on these films impossible. It was suggested that such a discontinuous growth might be due to the de-wetting properties of In and the large sensitivity of the growth dynamics at the initial stages of growth. In order to overcome these difficulties, we attempted to optimize the growth parameters for thin films of $CeIn_3$, which is the parent compound of $CeCoIn_5$ and demonstrates similar growth peculiarities. In that study we observed that the $CeIn_3$ thin film surface morphology is similar to that of $CeCoIn_5$, i.e., it strongly varies between growths performed using different oxide substrate materials and sample holder materials and even between growths performed under nominally identical conditions. Additionally, strong variations of the $CeIn_3$ thin film elemental composition were observed. In the “simultaneous growth” study, which we performed next, several sets of $CeIn_3$ thin films were grown such that only the substrate temperature varied from film to film within a single set. We found a logical variation of the surface morphology, crystallographic and elemental compositions, and low-temperature electronic transport properties of the $CeIn_3$ thin films grown within each set. However, strong variations between different sets were still observed.

The $CeCoIn_5$ thin films were grown using high-temperature Knudsen effusion cells for Ce and In and an electron beam evaporator for Co . The morphologies of these $CeCoIn_5$ films were found to be similar to those of the films grown using three effusion cells.

The grazing incidence diffraction and polar angle orientation x-ray analyses confirmed that $CeCoIn_5$ thin films have some tendencies to epitaxial growth when the Co flux is generated with an electron beam evaporator, which was neither observed before in films grown using three effusion cells nor reported for other growth methods. The results of the atomic force microscopy, line profile analysis, and simple electronic transport measurements all point to a rather poor structural quality of the $CeCoIn_5$ thin film microcrystals, which, as we argued, might be caused by a large concentration of threading type dislocations.

Electronic transport measurements

Performing low-temperature transport measurements on the $CeIn_3$ thin films, we systematically observed a behaviour typical to bulk $CeIn_3$ with additional features due to a segregated In phase. This In phase contribution, however, was absent in transport measurements performed on an individual microcrystal of a $CeIn_3$ thin film. In both, the whole film and the microcrystal transport measurements, we found a poor structural quality of the $CeIn_3$ crystal phase, which manifests itself through a strongly reduced residual resistance ratio (RRR) compared to $CeIn_3$ bulk crystals.

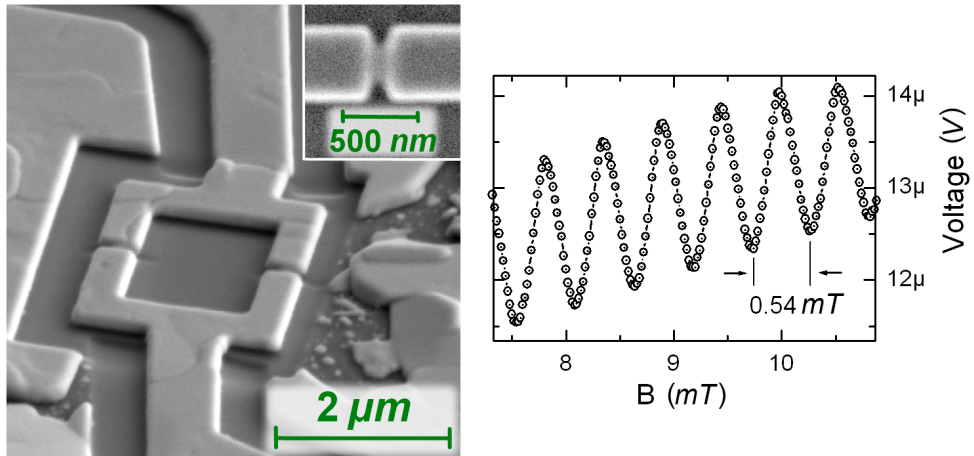
The temperature-dependent resistivity of the $CeCoIn_5$ thin films and of their individual microcrystals are similar to those of $CeCoIn_5$ bulk crystals and are characterized by small values of the RRR . The RRR values of the $CeCoIn_5$ microcrystals are slightly larger than those of the thin films, revealing that the scattering of charge carriers on grain boundaries contribution to the resistivity of the thin films is rather small.

Motivated by our successful measurements of $CeCoIn_5$ transport properties on microcrystals, we used these microcrystals for planar tunneling spectroscopy. Counter electrodes of such a planar tunneling diode can be made from $W-C$ nano-composites (W -IBID) by means of focused ion beam induced deposition (FIBID). In order to validate the usability of W -IBID for these purposes, we characterized them in $Al - Al_2O_3 - W$ -IBID planar tunneling diodes. The measured dynamic conductance curves on these diodes feature the expected spectroscopic response from the W -IBID electrode, which systematically depends on the tunneling barrier strength.

To prepare planar tunneling structures on individual $CeCoIn_5$ thin film microcrystals we used $SiO-C$ nano-composites as tunneling barriers deposited by means of focused electron beam induced deposition from tetramethylsilane and neopentasilane precursor gases. As mentioned, we used the previously characterized W -IBID nano-deposits as counter electrodes. The tunneling spectra measured on planar tunneling diodes, which

had been prepared using tetramethylsilane as precursor gas, demonstrated weak characteristic features assigned to the superconducting (SC) W -IBID counter electrode and strong non-linearities developing below the SC transition of $CeCoIn_5$. This behaviour, however, was poorly reproducible and could not be fully analyzed, which we related to the poor quality and large transparency of the tunneling barrier. The tunneling barriers prepared using neopentasilane as precursor gas had a strongly reduced transparency at low temperatures, which made spectroscopic measurements difficult.

In a next step, we prepared several $CeCoIn_5$ thin film microcrystal-based interferometers consisting of either variable width or variable thickness SC microbridges. For both geometries we observed an increase of the Josephson critical current through the microbridges below the SC transition in $CeCoIn_5$ with decreasing temperature. However, the expected SQUID voltage modulations were not found for interferometers with variable width microconstrictions. These modulations of high quality and predicted periodicity were observed for the SQUID with variable thickness microconstrictions (see figure). The dynamic resistance curves measured either on this SQUID or on a variable thickness



(left) $CeCoIn_5$ thin film microcrystal-based SQUID and (right) its voltage modulations by an external magnetic field.

single microbridge revealed additional peculiarities which we attributed to the periodic motion of SC Abrikosov vortices predicted in the Aslamazov and Larkin theory for SC microbridges. The temperature dependence of the Josephson critical current measured on the variable thickness microconstrictions agrees well with the theoretical predictions of Ambegaokar and Baratoff (AB). However, since the AB equations were derived for Josephson tunneling structures, one would not expect them to be applicable to our microbridges whose dimensions are larger than the SC coherence length of $CeCoIn_5$. On the other hand, the electronic transport regimes within the SC microbridges should be classified by the $CeCoIn_5$ characteristic SC lengths, the microbridge dimensions, and

the $CeCoIn_5$ quasiparticle mean free path. The anomalously large $CeCoIn_5$ quasiparticle mean free path does not allow for a strict classification of the electronic transport regimes within our microbridges in terms of existing models, which might be related to the unexpected agreement between the observed temperature dependence of the Josephson critical current and the AB predictions.

When $CeCoIn_5$ in the patterned microbridges becomes normal, i.e., above the SC transition temperature of $CeCoIn_5$, their dynamic conductance response is expected to be essentially flat. However, we observed strong non-linearities up to about 10 K, which is of the order of five times larger than the SC transition temperature of $CeCoIn_5$. Moreover, we also observed anomalies induced by an external magnetic field. These field-induced features are found to survive in the $CeCoIn_5$ SC state. Due to a large diversity of physical effects related to both, the peculiar low-temperature electronic properties of $CeCoIn_5$ and the microbridges geometry, we were not able to suggest a unified explanation of the observed behaviour. Nevertheless, some representative results of the transport measurements in the normal state of $CeCoIn_5$ microbridges are presented.

As an outlook, measurements on $CeCoIn_5$ microbridges of different widths could allow to separate the intrinsic $CeCoIn_5$ normal state properties and the microbridge induced behaviour. We can also take advantage of the anomalously large quasiparticle mean free path in $CeCoIn_5$ and apply our microstructuring methods for observation of interference effects in the $CeCoIn_5$ metallic state, which would give a unique and very direct access to the electron relaxation dynamics in this heavy-fermion compound.

There are neither complicated nor simple descriptions in physics, there are only those that one does understand or does not.

Contents

List of Figures	xvii
List of Tables	xxi
Abbreviations	xxiii
Physical Constants	xxv
Symbols	xxvii
Introduction	1
1 Theoretical background	5
1.1 Introduction	5
1.2 Thin film growth techniques	6
1.3 Physics at surfaces	8
1.3.1 Thermodynamics	9
1.3.2 Adsorption on surfaces and growth	14
1.4 Localization and Heavy-fermion systems	22
1.4.1 Single impurity Kondo effect	22
1.4.2 Multi-valence systems	27
1.4.3 Periodic Kondo lattices	31
1.4.4 Magnetism in rare earths	35
1.4.5 Heavy fermions and non-Fermi liquids	36
1.4.6 Superconductivity in heavy fermions	41
1.5 Quantum mechanical tunneling	44
1.5.1 The tunneling phenomenon	44
1.5.2 Tunneling in the solid state	45
1.5.3 Josephson effect	49
1.6 Quantum interference	51
1.6.1 Cooper pair interference	51
1.6.2 Weak localization and single electron interference	54
2 Methods and techniques	65
2.1 Introduction	65
2.2 Preparation for thin film growth	66
2.2.1 Molecular beam epitaxy system	66

2.2.2	Substrate preparation	69
2.2.3	Transfer into the growth chamber	71
2.3	Thin film growth	72
2.3.1	Vacuum concept	72
2.3.2	Gas kinetics	73
2.3.3	Vacuum calculations	75
2.3.4	Tube conductance	77
2.3.5	Growth procedure	77
2.4	Characterization	78
2.4.1	X-ray diffractometry	80
	Individual scatterers	80
	Scattering on a periodic lattice	81
	Diffractometry	86
	Intensity of Bragg reflections	87
	Diffractometer used in this work	91
	Scanning regimes and alignments	93
2.4.2	Line profile analysis	95
	Model functions	95
	Instrumental line profile	97
	Scherrer equation and crystallite shapes	99
	Size and strain broadening, Williamson-Hall plots	99
2.5	Low-temperature measurements	101
2.5.1	Low-level electrical measurements	104
	Lock-in measurements	106
3	Overview of experimental results	111
3.1	Introduction	111
3.2	$CeIn_3$ growth study	112
3.2.1	Surface morphology	112
3.2.2	Simultaneous growth	117
3.2.3	Microcrystal measurements	122
3.3	$CeCoIn_5$ growth study	126
3.3.1	Variations and lack of repeatability	126
3.3.2	Polar angle orientation of microcrystals	132
3.3.3	Microstrain study with LPA	135
3.4	$CeCoIn_5$ microcrystal studies	140
3.4.1	Transport properties of a single $CeCoIn_5$ microcrystal	140
3.4.2	Planar tunneling in $Al - Al_2O_3 - W$ -IBID	142
3.4.3	Planar tunneling on $CeCoIn_5$ microcrystals	146
3.4.4	Quantum interferometers on $CeCoIn_5$ microcrystals	153
	Summary and outlook	173
	Appendices	177
A	Tunneling measurement calculations	177
B	Vapour pressure charts for 4He and 3He	178

C	Random walk	179
D	Crystallographic data	180
E	Equipment settings	182
F	<i>CeCoIn₅</i> normal state properties	186
 Bibliography		191
 Acknowledgements		203
 Curriculum Vitae		205

List of Figures

1.1	Vacuum evaporation system	8
1.2	Surface tension of metals	10
1.3	Stepped atomic surface	11
1.4	Polar plot of the surface free energy	11
1.5	Surface ions relaxation	13
1.6	Equilibrium vapour pressure chart	16
1.7	Van der Waals force illustration	17
1.8	Lennard-Jones potential	18
1.9	Langmuir isotherm	19
1.10	Thin film growth regimes	21
1.11	Temperature dependence of resistivity in metals	23
1.12	Resistance minimum in <i>Mo-Nb</i> alloy	23
1.13	Single-impurity virtual transitions	25
1.14	Chemical potential of a two-band Hubbard-like system	29
1.15	$Ce_xLa_{1-x}Cu_6$ Kondo lattice system	31
1.16	Indirect exchange interaction	32
1.17	Doniach phase diagram	34
1.18	Fermi distribution function of interacting electrons	37
1.19	Brinkman-Rice transition	37
1.20	Several temperature dependencies in the BCS theory	42
1.21	Function $\sin^2(tx/2\hbar)/x^2$	47
1.22	Quantum mechanical tunneling through a potential barrier	48
1.23	Schematic view of a SQUID	52
1.24	Self-crossing interfering paths	56
1.25	Interference between single-electron wave functions	61
1.26	Characteristic electron interference times	62
2.1	MBE system	67
2.2	Effusion cell	68
2.3	Substrate holders	71
2.4	Electron elastic scattering	81
2.5	X-ray diffraction on 1D and 2D chains	82
2.6	Scattering vector \mathbf{Q}	83
2.7	Bragg law representation	84
2.8	Reciprocal space representation	85
2.9	Bragg-Brentano or self-focusing geometry	87
2.10	Atomic form factor	88
2.11	Bruker D8 Discover diffractometer	92

2.12	Alignment procedure for x-ray measurements	94
2.13	Gauss and Cauchy shape functions	96
2.14	Schematic Williamson-Hall plot	101
2.15	^3He cryostat scheme	103
2.16	Lock-in measurement setup	107
2.17	Lock-in operational principle	108
3.1	Spiral holder for thin films growth	118
3.2	Surface morphologies of CeIn_3 thin films	119
3.3	X-ray diffractograms of CeIn_3 thin films	120
3.4	Temperature-dependent resistance of CeIn_3 thin films	121
3.5	Pre-patterning of a CeIn_3 film	124
3.6	CeIn_3 microcrystal patterning	124
3.7	Temperature-dependent resistance of a CeIn_3 crystallite	125
3.8	X-ray diffractograms of CeCoIn_5 thin films	129
3.9	X-ray φ -scans on oriented CeCoIn_5 thin films	130
3.10	Indium segregation on a CeCoIn_5 thin film	131
3.11	Implications of the substrate miscut for x-ray measurements	132
3.12	Nucleation processes at a vicinal substrate surface	133
3.13	X-ray polar scan maps for an Al_2O_3 substrate and a CeCoIn_5 thin film	135
3.14	Williamson-Hall plots for CeCoIn_5 thin films	137
3.15	Surface morphology of a CeCoIn_5 thin film seen via AFM	138
3.16	Williamson-Hall plot for an Al_2O_3 substrate	139
3.17	Temperature-dependent resistance of a CeCoIn_5 microcrystal	141
3.18	Surface morphology of as-sputtered aluminium thin film	142
3.19	SEM micrograph of planar tunneling diodes	143
3.20	Temperature-dependent resistance of a planar tunneling diode	144
3.21	Dynamic conductance curves of $\text{Al} - \text{Al}_2\text{O}_3 - \text{W}$ -IBID planar tunnel diodes	145
3.22	Photo-mask for positive photolithography process	147
3.23	Preparation of a planar tunneling diode on a CeCoIn_5 microcrystal	149
3.24	Temperature-dependent tunnel resistance of a CeCoIn_5 planar tunnel diode	150
3.25	Set of dI/dV curves of a CeCoIn_5 planar tunneling diode	152
3.26	Temperature-dependent tunneling resistance of a CeCoIn_5 crystallite planar tunneling diode	153
3.27	Micropatterning of an interferometer on a CeCoIn_5 crystallite	154
3.28	Interferometer on a CeCoIn_5 crystallite	155
3.29	$V-I$ curves of a CeCoIn_5 interferometer for selected temperatures	156
3.30	Critical current of $W-C$ nanowires as a function of temperature	157
3.31	Josephson critical current modulation for a CeCoIn_5 interferometer	158
3.32	Micropatterning of an interferometer on a CeCoIn_5 crystallite	159
3.33	SEM micrograph of the SQUID and its equivalent electrical scheme	159
3.34	CeCoIn_5 SQUID's temperature-dependent resistivity	160
3.35	CeCoIn_5 SQUID's dynamic resistance curves	162
3.36	CeCoIn_5 SQUID's field-induced voltage modulations	163
3.37	CeCoIn_5 SQUID's Josephson critical current modulations	164
3.38	Abrikosov vortices penetrating a microbridge	165

3.39	Temperature-dependent Josephson critical current of the SQUID microbridges	166
3.40	Temperature-dependent resistivity of a $CeCoIn_5$ microbridge	168
3.41	$CeCoIn_5$ weak link voltage modulations by an external magnetic field at $T = 0.3 K$	169
3.42	Temperature-dependent Josephson critical current for a single $CeCoIn_5$ microbridge	170
3.43	Comparison between the dynamic resistance/conductance curves of the $CeCoIn_5$ SQUID and the $CeCoIn_5$ microbridge	171
B.1	Vapour pressure charts for 4He and 3He	178
C.1	Diffusion of a particle	179
D.1	$CeIn_3$ and $CeCoIn_5$ crystal structures	180
F.1	$CeCoIn_5$ SQUID dynamic conductance curves at zero magnetic field and several temperatures	186
F.2	$CeCoIn_5$ SQUID dynamic conductance curves for several temperatures and variable magnetic field	187
F.3	$CeCoIn_5$ SQUID dynamic conductance curves at $2.5 K$ and variable magnetic field	188
F.4	Field-temperature phase diagram based on $CeCoIn_5$ SQUID magnetoresistance measurements	188
F.5	Splitting of the broad maximum on the dynamic conductance curves in magnetic field at several temperatures measured on both the $CeCoIn_5$ SQUID and single microbridge geometries	189

List of Tables

1.1	Thin film growth regimes in terms of free energy slopes	22
2.1	Parameters of the characteristic $Cu-K^\alpha$ lines.	98
3.1	Surface morphology of $CeIn_3$ thin films grown at substrate temperature $T_s = 500^\circ C$	113
3.2	Surface morphology of $CeIn_3$ thin films grown at substrate temperature $T_s = 600^\circ C$	114
3.3	X-ray diffractograms of $CeIn_3$ thin films grown at substrate temperature $T_s = 500^\circ C$	115
3.4	X-ray diffractograms of $CeIn_3$ thin films grown at substrate temperature $T_s = 600^\circ C$	116
3.5	Typical surface morphologies of $CeCoIn_5$ thin films as seen by SEM and optical microscopy	128

Abbreviations

AC	A lternating C urrent
AL	A slamazov and L arkin
BCC	B ase C entered C ubic
BCS	B ardeen C ooper S chrieffer
ccm	cubic centimeters per minute
CVD	C hemical V apour D eposition
DC	D irect C urrent
DOS	D ensity O f S tates
EDXS	E nergy D ispersive X -ray S pectroscopy
ESD	E lectro S tatic D ischarge
FCC	F ace C entered C ubic
FEBID	F ocused E lectron B eam I nduced D eposition
FFLO	F ulde F errel L arkin O vchinnikov
FIBID	F ocused I on B eam I nduced D eposition
FIBM	F ocused I on B eam M illing
FL	F ermi L iquid
FPPF	F undamental P arameters P rofile F itting
FWHM	F ull W idth on H alf M aximum
HCP	H exagonal C lose P acked
HF	H eavy F ermion
KLM	K ondo L attice M odel
LPA	L ine P rofile A nalysis
MBE	M olecular B eam E pitaxy
NFL	N on- F ermi L iquid
PAM	P eriodic A nderson M odel

PCB	Printed Circuit Board
ppb	part per billion
ppm	part per million
psi	Pounds per Square Inch
PVD	Physical Vapour Deposition
QCP	Quantum Critical Point
RCSJ	Resistively and Capacitively Shunted Junction
RKKY	Rudeman Kittel Kasuya Yosida
RRR	Residual Resistance Ratio
SC	SuperConducting
sccm	standard cubic centimeters per minute
SEM	Scanning Electron Microscope
S-I-N	Superconductor-Insulator-Normal metal
S-I-S	Superconductor-Insulator-Superconductor
SQUID	Superconducting Quantum Interference Device
TLP	Top-Loading Probe
UHV	Ultra High Vacuum
VTI	Variable Temperature Insert

Physical Constants

Boltzmann constant	k_B	$=$	$1.3806488 \times 10^{-23} \text{ J/K}$
		$=$	$86.173324 \text{ } \mu\text{eV/K}$
Magnetic flux quantum	Φ_0	$=$	$2.067833758 \times 10^{-15} \text{ T} \cdot \text{m}^2$
Bohr magneton	μ_B	$=$	$9.274 \times 10^{-24} \text{ J/T}$
		$=$	$57.8838 \text{ } \mu\text{eV/T}$
Elementary charge	e	$=$	$1.6021756 \times 10^{-19} \text{ C}$
Plank constant	h	$=$	$6.6260696 \times 10^{-34} \text{ J} \cdot \text{s}$
		$=$	$4.1356675 \times 10^{-15} \text{ eV} \cdot \text{s}$
	\hbar	$=$	$1.0545717 \times 10^{-34} \text{ eV} \cdot \text{s}$
		$=$	$6.5821193 \times 10^{-16} \text{ eV} \cdot \text{s}$

Symbols

T_D	Debye temperature	K
T_F	Fermi temperature	K
ϵ_F	Fermi energy	units of energy
I_c^J	Josephson critical current	A
T_J	Josephson coupling temperature	K
τ_r	monoatomic layer arrival time	s
τ_{el}	time between two subsequent electron collisions	s
τ_{ph}	electron-phonon relaxation time	s
τ_B	magnetic relaxation time	s
τ_{ee}	electron-electron relaxation time	s
τ_m	electron relaxation time due to localized moments	s
τ_ϕ	electron dephasing time	s
ρ	electrical resistivity	Ωm

To my parents...

Introduction

Understanding collective phenomena is undoubtedly one of the central goals of modern solid state physics and superconductivity is one of the most exciting collective phenomena. Having been discovered more than a hundred years ago and relatively well understood only in simple solids, nowadays superconductivity is associated with materials that are much more complex, not only from the structural point of view but also in terms of the microscopical mechanisms responsible for its occurrence.

The superconducting (SC) state in materials like *Al* or *Nb* can be well understood in the framework of the Bardeen-Cooper-Schrieffer (BCS) theory and its strong coupling extension, where the SC electrons are bound in pairs via a specific coupling to phononic degrees of freedom and occupy a single bosonic state. In such materials, the SC coupling between electrons is strongly suppressed by magnetic impurities and weakly affected by structural defects. However, in 1979 superconductivity was first observed below 0.5 *K* in *CeCu₂Si₂* (Steglich, Aarts *et al.* 1979), a material whose properties are incompatible with superconductivity at a first glance. A number of similar compounds with rare earth constituent elements demonstrating low-temperature superconductivity were discovered in the following years, such as *UBe₁₃* (Ott, Rudigier *et al.* 1983) and several *Yb*, *La*, and *Th* based compounds. The SC state in these materials emerges from a so-called heavy-fermion state and coexists with regularly arranged localized magnetic moments (rare-earth ions). Surprisingly enough, the SC state in these heavy-fermion compounds was found to be strongly suppressed by the substitution of magnetic ions with non-magnetic ones. It has to be mentioned that superconductivity has also been found in ceramics, fullerenes, organic materials, borocarbides, ruthenates *etc.* (Narlikar 2005) and in many cases cannot be explained within the BCS theory.

Heavy fermions are essentially Kondo lattices whose localized magnetic moments interact via the so-called Rudeman-Kittel-Kasuya-Yosida (RKKY) superexchange interaction. Although there is still no coherent view on their low-temperature electronic properties, the behaviour of heavy fermions can be generally understood in terms of a competition between the Kondo screening and the RKKY interaction. As a result of this competition

and fairly unique properties of every compound, their phase diagrams can be extremely rich demonstrating a variety of magnetic phases, superconductivity, a Kondo insulating regime, the Fulde-Ferrell-Larkin-Ovchinnikov (FFLO) state *etc.* The SC state is known to even coexist with a magnetically ordered phase (e.g., $CeCu_2(Se_{1-x}Ge_x)_2$ (Kitaoka, Ishida *et al.* 2001), $U(Pt_{1-x}Pd_x)_3$ (Stewart 2001), UPd_2Al_3 (Sato, Sakon *et al.* 1993)). There is also a special kind of such a coexistence, like the FFLO state in $CeCoIn_5$ (Bianchi, Movshovich *et al.* 2002), where superconductivity is spatially inhomogeneous. A common property of heavy fermions is the strong quasiparticle mass renormalization observed at low temperatures which stems from the hybridization between localized moments and conduction electrons. The mass renormalization is manifested in many physical properties such as the low-temperature electronic specific heat, the Fermi temperature, the Pauli spin susceptibility, the quadratic term in the low-temperature resistivity, the electron relaxation times *etc.* While some heavy fermions at low temperatures behave like Fermi liquids, i.e., like renormalized metals (e.g., $CeAl_3$), others demonstrate strong deviations from such a behavior (e.g., $CeCoIn_5$, UBe_{13} *etc.*)

The large complexity of the low-temperature electronic properties of heavy fermions stimulates the application of new investigation methods. Several such conceptually simple but powerful methods, like planar tunneling spectroscopy or quantum interferometry, allow for a direct access to the density of single electron energy levels, pairing symmetry in the SC state, and some of the quasiparticle relaxation times. Their reliable application is thought to be only possible utilizing high-quality thin films, whose preparation is associated with certain difficulties in the case of $CeCoIn_5$.

In this work, we intended to improve the quality of $CeCoIn_5$ thin films in order to make them suitable for applications of the mentioned electronic transport investigation methods. Thus, our study consists of two parts, which are (1) the growth and structural study of $CeIn_3$ and $CeCoIn_5$ thin films and (2) the low-temperature transport investigations on thin films and microstructures of $CeIn_3$ and $CeCoIn_5$. This thesis aims to describe the progress in this research as well as the related theoretical and technical concepts. The discussion is divided into three chapters:

- **Chapter 1** discusses the basic surface physics, heavy-fermion physics, quantum mechanical tunneling, and quantum interference effects.
- **Chapter 2** describes methodological aspects of the vacuum system operation and thin film growth, characterization techniques and methods, and low-temperature electronic transport measurements.

- In **Chapter 3** we discuss the results of our studies, starting from the thin film growth and proceeding with the structural characterization and low-temperature measurements.

Chapter 1

Theoretical background

1.1 Introduction

In modern physics one understands transport and thermodynamic properties of solid bodies in terms of the collective behaviour of electrons and their coupling to the crystal lattice excitations. In many cases it is plausible to describe solid state properties by assuming independent or uncorrelated behaviour of its electrons, phonons *etc.* However, there are many examples when these assumptions do not lead to valid explanations of the experimentally observed properties and correlations must be accounted for. Superconductivity, on the one hand, is one important example of a collective phenomenon, which in simple superconducting metals may be explained with little or no account for correlations between the electrons. On the other hand, there are many novel superconductors in which the uncorrelated frameworks do not work. Hence, one goal of solid state physics is to learn how to appropriately combine in the right way the knowledge of electronic correlations and the mechanisms that may lead to superconductivity.

Up to now, a unified view on the problem of electronic correlations and superconductivity does not exist and one has to look more carefully into the specific material properties at hand. This requires the synthesis of new materials, the development/improvement of investigation techniques, and the generalization of the experimental results. In this work, the transport properties of the heavy fermion compound $CeCoIn_5$, which demonstrates strong correlations and superconductivity at the same time, have been investigated. The work consisted of three steps: synthesis, characterization, and measurements. Of course, each of these steps contains its own exciting physics and specific difficulties, which often slows the overall progress.

In this chapter we will briefly consider the basic physics related to the surfaces of solids and problems which one faces during thin film growth. Then, we will focus on the electronic properties of heavy fermions and their magnetism. Since these materials feature Kondo physics, we will consider the single impurity Kondo model first and the Kondo lattice next. Next, the superconducting properties of heavy fermions are briefly reviewed. The physics of the quantum mechanical tunneling phenomenon is fundamental for the main experimental method that we used for investigations in our work, tunneling spectroscopy, which will be covered next. The last topic of this chapter is the quantum mechanical interference phenomenon for superconducting and normal states. It should be emphasized that both interference effects can give a deeper insight into the superconducting properties of $CeCoIn_5$ and its normal state properties out of which the superconducting state emerges.

1.2 Thin film growth techniques

The field of growing and studying the properties of thin films has been demonstrating an extremely fast development for the last half century. By now it has entered many areas of engineering, applied and fundamental science.

By thin films we mean a thin layer of material which is grown on a thick solid substrate. The morphology of this thin layer can be classified as:

- Crystalline continuous film which covers the complete substrate area
- Amorphous film with full coverage, and
- Discontinuous film which consists of individual (interconnected) islands

The corresponding growth regimes will be discussed in Sec. 1.3.2. There are many techniques for growing thin films (see also (Vossen & Kern 1991)). A classification of those methods can be made as following:

- Evaporative methods
- Glow-discharge processes
- Gas phase techniques
- Liquid phase techniques

The first two methods from the list above involve a solid-(liquid)-gas phase transition. During such a transition some molecules leave the source in the direction of a substrate with subsequent condensation on it. For the phase transition to occur, the energy is transferred to the source by means of either heat transfer (evaporation or sublimation processes) or momentum transfer (glow-discharge or sputtering). In the gas phase method a substrate is located within a continuous gas flow, which dissociates into the constituent elements in the vicinity of the substrate with subsequent condensation on it. In the last method the substrate is completely dipped into a liquid containing a dissolved material being adsorbed on the substrate surface.

The physical vapour deposition (PVD) is a versatile technique for depositing thin films of many materials. The simplicity and wide control possibilities are its main advantages. This technique is conceptually simpler than sputtering but requires better vacuum conditions which today are easily available. In principle, evaporation of a material and its consequent deposition on a substrate is possible at higher pressures as well. However, firstly, lowering the process chamber pressure of residual gases reduces the temperature needed for creating the desired vapour pressure of the material to be deposited. Secondly, lowering the pressure enough one enters into a different gas kinetics regime, which will also be addressed in Sec. 2.3.3. And finally, the lower the pressure of residual gases in the processing chamber the better the quality of the films that may be obtained.

A typical evaporation system consists of five elements: (i) processing chamber, (ii) pumping system, (iii) vapour source, (iv) substrate, and (v) transfer system, which is illustrated in Fig. 1.1. One of the most common methods of bringing the temperature of the source material up is thermal heating using a heating coil. A second method is to use an electron beam to heat up the source. A crucible or boat is used to hold the source material. The crucible itself must be inert, exhibit low degassing and should have a much higher melting temperature than the source material. The selection of the specific crucible material also depends on the source material. Tungsten, alumina, boron nitride and tantalum are most commonly used in practice.

The PVD and chemical vapour deposition (CVD) methods may be referred to as evaporative methods. The major difference between these two is that chemical reactions are important for the film formation during CVD and are of small importance for PVD. There are also minor differences, like the evaporation temperatures, which are usually lower for CVD. In this work only PVD processes are considered.

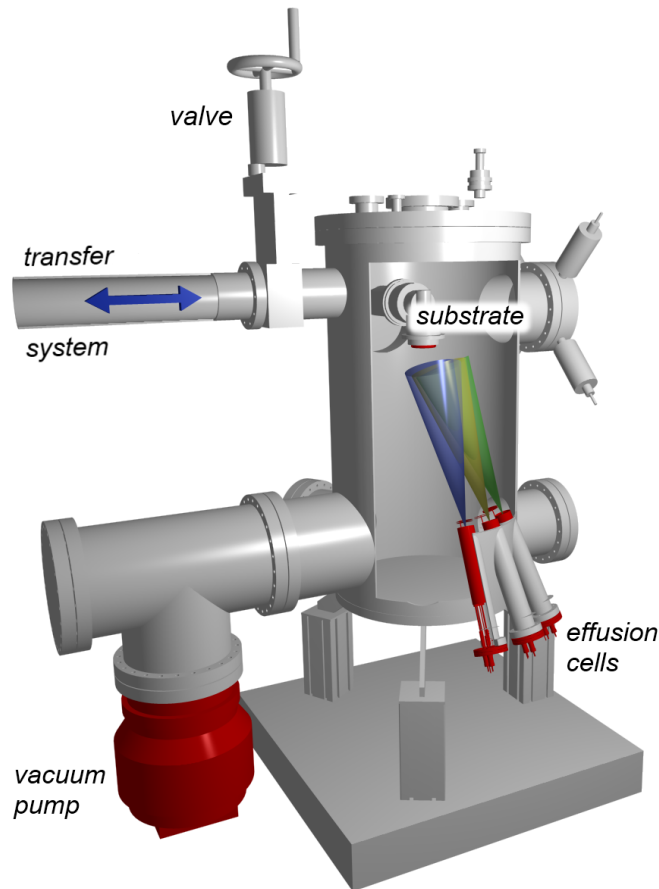


FIGURE 1.1: Schematic representation of a vacuum evaporation system.

1.3 Physics at surfaces

The study of unconventional superconductivity in this work substantially depends on controlling all thin film processes. Although the physics of solid surfaces, which is a central topic in thin film growth, was not the main subject of the investigations here, the understanding of its basics is essential for improving the quality of thin films. Surface physics has started its rapid development in conjunction with the continuous improvement of probing techniques, i.e., electron spectroscopy methods. The thermodynamic framework was applied to surfaces early on, but many results were appreciated only after suitable probing techniques became available. Additionally, the development of theories of the electronic properties in solids provided yet another “instrument” for understanding the properties of surfaces. In this section we give a general description of basic thermodynamical properties of the surfaces of solids. The physical adsorption processes, which occur during a crystal/thin film growth, are described next. Models of how thin films may form on the surface are briefly reviewed next. Eventually, we consider strains and defects, which cannot be neglected in real systems and define the growth dynamics itself.

1.3.1 Thermodynamics

Thermodynamics was applied to surfaces by Gibbs (Gibbs 1948) for studying equilibrium states and phase transitions on surfaces. It may be shown that an equilibrium state of a one-component system is characterized by its internal energy $U = U(S, V, N)$, which is a function of entropy, volume, and the number of particles in the system. When the first and the second laws of thermodynamics are combined¹, the change of the internal energy of the system can be described as:

$$dU = TdS - PdV + \mu dN \quad (1.1)$$

where μ is the chemical potential of the particles. Since all natural variables in (1.1) are extensive² quantities S , V , and N , it may be written using Euler's homogeneous function theorem as:

$$U = TS - PV + \mu N \quad (1.2)$$

which is referred to as the Euler equation. If the internal energy U from (1.2) is differentiated, then using (1.1) it can be written as

$$SdT - VdP + Nd\mu = 0 \quad (1.3)$$

which is called the Gibbs-Duhem equation and shows that the three intensive variables T , P , and μ are not independent, reducing the number of independent quantities. If we would attempt to create a surface with area A from the solid in thermodynamic limit described by (1.2), it will cost some work $W = \gamma A$, which would increase the internal energy of the system

$$U = TS - PV + \mu N + \gamma A \quad (1.4)$$

where γ is the proportionality constant called *surface tension* coefficient. Such a system then will consist of two phases: the solid and the vapour. We may assume that linear elasticity theory (Landau & Lifshitz 1970) correctly describes the energy change of the system under strain. Then we may write the Gibbs-Duhem equation for the entire system assuming that the vapour phase volume is zero (see pp. 9-10 in (Zangwill 1988))

$$Ad\gamma + S_s dT + A \sum_{ij} (\gamma \delta_{ij} - \sigma_{ij}) d\varepsilon_{ij} = 0 \quad (1.5)$$

which is called the Gibbs adsorption equation, which connects the surface area S_s , the surface tension γ , the surface stress tensor σ_{ij} , and the surface strain ε_{ij} . Here δ_{ij} is the

¹See also (Callen 1985).

²By *extensive* quantities in the thermodynamics one understands those which are proportional to the size of the system or the number of particles. The *intensive* quantities, in contrast, are those which do not depend on the system volume or the number of particles.

Kronecker delta symbol. Assuming $dT = 0$ in (1.5) we get

$$\sigma_{ij} = \gamma \delta_{ij} + \left. \frac{\partial \gamma}{\partial \varepsilon_{ij}} \right|_T \quad (1.6)$$

The second term in (1.6) defines the qualitative behaviour of the system. For example, if $\partial \gamma / \partial \varepsilon_{ij} \sim 0$, all strain added to the system is accommodated like in liquids. If, however, $\partial \gamma / \partial \varepsilon_{ij} < 0$, the surface may minimize its energy by buckling, like it was observed on *Au* (111) surfaces (Andreussi & Gurtin 1977, Marks, Heine *et al.* 1984).

The value of γ has units of energy/area according to (1.4) and may be measured experimentally³ (see Fig. 1.2). Its value may be estimated by using the cohesive energy for

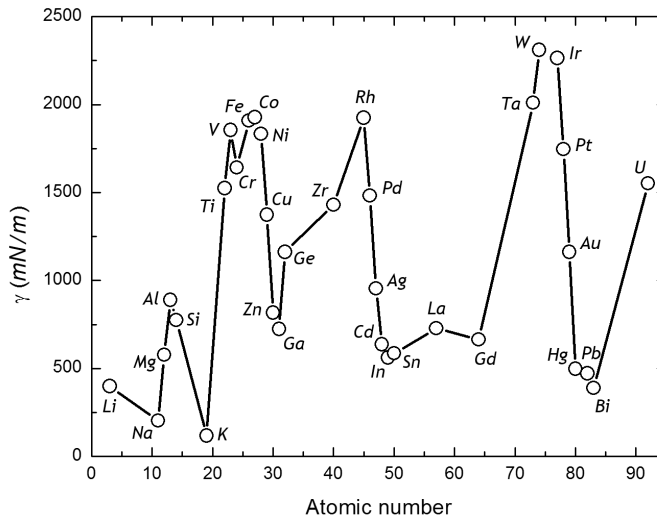


FIGURE 1.2: Surface tension of liquid pure metals. Data taken from (Keene 1993).

solids, a fraction of broken bonds per atom, and the surface density of atoms. Using average numbers for metals such an estimation gives approximately 1500 mN/m , which is in accordance with experiment (see Fig. 1.2).

In (1.4) the surface was created assuming implicitly a cleaving along a regular atomic plane, hence leaving no atomic steps. Let us now consider a two-dimensional situation as shown in sideview in Fig. 1.3. If one started with the flat surface (01), i.e., $\theta = 0$, and produced a number of steps to realize a new surface (1*n*), where *n* is large, tilted by an angle $\theta \neq 0$, it would cost an additional energy per each step. Eventually, creation of such a surface in this simple case will always cost more energy than creation of a flat one. More precisely, the surface tension will be anisotropic

$$\gamma(\theta) = \gamma(0) + (\beta/a)|\theta| \quad (1.7)$$

³For metals, commonly the value of the liquid surface tension is measured. These values are also usually tabulated for different temperatures, since the value of surface tension is a function of temperature (Keene 1993).

for small θ , where β is the energy per step, $\gamma(0)$ is the surface tension for a flat surface, and a is the atomic step height. For larger angles the number of steps will increase and

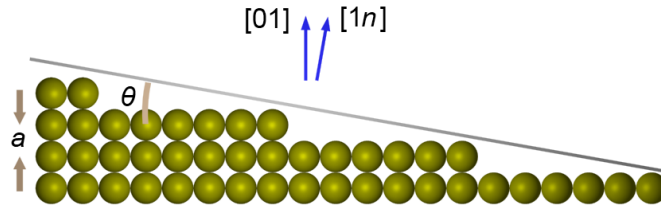


FIGURE 1.3: Stepped atomic surface with direction $[1n]$, which is tilted by an angle θ to a flat atomic surface with direction $[10]$. Here a is the unit cell length (assuming the square symmetry in the figure).

a proper analysis must include the interaction energy between steps. Such an analysis may be performed following (Landau & Ter-Haar 1965), and the results can be plotted as a polar plot $\beta = f(\theta)$. One may already guess that the different equilibrium shapes of crystals will be a result of minimizing its surface energy by increasing the area of the “low cost” planes and reducing otherwise the contribution of “high cost” planes. This was shown first by (Herring 1951) in his graphical analysis using polar plots as shown in Fig. 1.4.

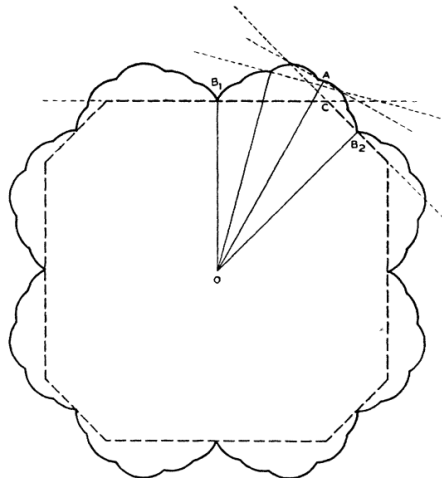


FIGURE 1.4: Polar plot of the surface free energy (solid line), equilibrium polyhedron (long dashed line) (Herring 1951)

Several decades later the theoretically expected crystallite shapes were observed on several metals’ crystallites using electron microscopy. The observed crystal shapes were found to be rather smooth. This was explained by the fact that the analytical derivation of crystal shapes was performed for zero absolute temperature and no entropy effects were included. At higher temperatures, however, not only one single state obtained theoretically as lowest energy state may be occupied by the system. The higher energy states become populated with a certain probability, given by the Boltzmann distribution

function. Qualitatively, the higher the temperature the easier it becomes for atoms to migrate on the crystal surface. Hence, the energy per step β introduced in (1.7) has less and less influence on the function $\gamma(\theta)$ and the latter becomes more and more isotropic. Expectedly, at some high enough temperature the crystal facets disappear and rounded crystal shapes appear. The temperature of this phase transition is called roughening temperature T_r .

Let us consider a flat surface with no atomic steps which is formed by a two-dimensional array of atomic columns of equal height. Let the energy of such a flat surface be zero, i.e., we assume the system to be initially in its ground state. According to (1.7), creating an excitation of one column of height a above the flat surface within this array will cost the energy $J \sim \beta$. The total energy of the system will be a function of all column height combinations, namely

$$U = J \sum_{i,j} |h_i - h_j| \quad (1.8)$$

where h_i are the relative heights of the columns with respect to the unperturbed surface and can be an integer multiple of a . The summation in (1.8) is performed over the nearest neighbors within the array. The higher the temperature of the system the more combinations in (1.8) will be accessible by the system. Nevertheless, at a non-zero temperature the system does not have to spread the column height randomly. In fact, it does not, but lowers its entropy by creating plateaux. Every new plateau has a perimeter L and the associated with it energy JL/a , since for all internal columns $|h_i - h_j| = 0$. Hence, the higher the temperature the larger L and the number of independent plateaux in the system will be. If we assume that the system contains only one such plateau, the number of combinations to complete such a perimeter (or microstates) may be written as $z^{L/a}$, where z is the number of nearest neighbors for every atomic column. Thus, the free energy of the system will be

$$F = U - TS = J \frac{L}{a} - T k_B \ln \left(z^{L/a} \right) = \frac{L}{a} (J - T k_B \ln z) \quad (1.9)$$

When the temperature is raised to above $T_r = J/(k_B \ln z)$ loops of non-zero length must occur, whereas they have zero length below the transition temperature. Such a roughening transition was observed first on a ${}^4\text{He}$ crystal surface above 0.8 K (Avron, Balfour *et al.* 1980). Other surface phase transitions were also predicted and systematically analyzed by (Kosterlitz & Thouless 1973).

It was noted above that the surfaces of solids are subject to phase changes at temperatures far below the melting temperature. But nothing was said about how the ions in the surface layers are rearranged when a clean surface is produced. Within the solid the ion cores are screened by symmetrically distributed electronic charge. But once the

surface has been created, this symmetrical electrostatic balance is perturbed. If this happens, the surface electronic charge becomes more strongly attracted by the ion cores from deeper layers (Fig. 1.5). This produces a compressive force on the surface ions, which are shifted towards the deeper layers relaxing the structure. The symmetry of the

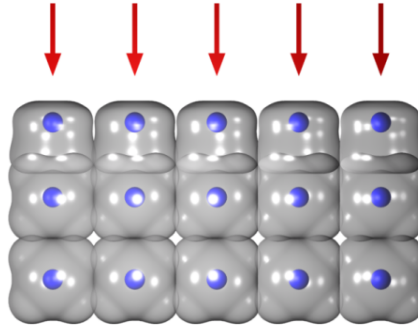


FIGURE 1.5: Schematic view of the surface ions relaxation. Red arrows denote an effective compressive force due to electronic charge density redistribution. Ion cores are shown in blue and the electronic charge is shown in transparent grey.

surface atoms arrangement may remain unchanged in some cases, which is called a 1×1 reconstruction⁴, as in the case of *Au* (110) 1×1 . However, more often the surface is more strongly reconstructed, as in the case of *Si* (111) 7×7 or *W* (100) $\sqrt{2} \times \sqrt{2} - 45^\circ$, *etc.* Such a reconstruction substantially influences the adhesion energies of the adsorbed ions on this surface, since now the rearranged surface is associated with a new value of γ .

From the brief thermodynamic analysis above follows that the surface structure may be changed as soon as the surface is created or if the temperature is changed. The minimization of its (surface) free energy $F = U - TS$ is the driving force of this change which is a phase transition, when the system changes its ordering between different surface types. Different ordering types, in turn, feature their own dependencies $U(T)$ and $S(T)$, which will define the temperature dependence of the system's free energy F . At some critical temperature T_c it may happen that the system lowers its energy by changing its ordering. In order to have a useful quantity for describing the system's state an *order parameter* is defined. This parameter is chosen such that it has a finite value in one state (usually the state at a lower temperature) and vanishes in the other state. It may be the loop perimeter, as in our analysis of surfaces, the volume for liquid-gas transitions, the magnetization for magnetic ordering transitions *etc.*

All phase transitions may be split in two classes. Some phase transitions may undergo a discontinuous change of the order parameter, the *first-order* phase transitions (e.g.,

⁴If two bulk unit vectors a and b , which lay in-plane of the surface, are used, then 1×1 denotes an unperturbed symmetry of the surface. The 2×2 reconstruction means stretched unit vectors on the surface with a stretching factor of 2. If a rotation of the surface unit vectors occurs, the rotation angle is appended, e.g., $2 \times 1 - 45^\circ$

nucleation and growth), while others are characterized by a smooth variation of the order parameter, the *second-order* phase transitions (e.g., magnetic ordering). For the second-order phase transitions the variation of the order parameter very close to T_c may be approximated by $(T - T_c)^\beta$, where β is called the *critical exponent*. β is related to the fundamental properties of the system, such as its dimensionality and symmetry and is of great importance in many theoretical models.

In surface physics, atomic order phase transitions were theoretically predicted and experimentally observed on semiconductors and metallic surfaces. We note here that melting, another example of phase transitions, is also modified on surfaces. It was shown by molecular dynamics simulations⁵ (Abraham, Rudge *et al.* 1984) that the melting of the surface ion lattice of a solid starts at lower temperatures than the bulk melting point. This surface initiated melting mechanism was also confirmed experimentally for the *Pb* (110) surface by using the scattered ion kinetic energy spectroscopy (Frenken & Veen 1985) and by experiments performed on Wigner crystals (Grimes & Adams 1979). Another example of surface-induced phase transitions is the magnetic phase transitions. Intensive studies of this topic for the last three decades revealed a peculiar nature of this type of magnetic order. As a result, unexpectedly, magnetism was observed in 30 nm *Au* thin films⁶ by (Reich, Leitus *et al.* 2006) as well as in 3 nm *Au* nano-particles with a large magnetic moment of about 20 Bohr magnetons particle (Hori, Teranishi *et al.* 1999, Li, Wu *et al.* 2011).

1.3.2 Adsorption on surfaces and growth

Typically, thin film growth consists of the molecule transfer to the substrate and subsequent formation of a film layer on its surface. This scheme will now be discussed in more detail for a specific growth method. Since the MBE growth is of main interest here, let us consider this specific case, i.e., the growth from the vapour phase in an ultra high vacuum (UHV) chamber. Here, the growth stages are classified as follows:

- Transfer of the molecules from the source to the vapour (evaporation/sublimation)
- Transfer of the molecules from the vapour to the substrate
- Adsorption/desorption processes in the vicinity of the substrate's surface
- Settling of the adsorbed molecules into their equilibrium positions

⁵Using the Lindemann criterion, which identifies melting of a crystal when the average atomic displacements from their mean positions become larger than $\sim 25\%$ of the unit cell dimensions.

⁶In that work authors excluded an influence of magnetic impurities such as *Fe*, *Ni*, *Co*, and *Mg*. Instead, anomalous polarization effects on the *Au*-substrate interface were suggested.

Evaporation

After the temperature of the source material has been brought up to a desired level and stabilized, an equilibrium establishes between the vapour and the liquid/solid. Under these stable conditions, infinitesimal changes of pressure and temperature are described as

$$\frac{dP}{dT} = \frac{H_e}{T\Delta V} \quad (1.10)$$

Here H_e is the enthalpy of vaporization of the source material, T is the equilibrium temperature. ΔV describes the change of material volume during the phase transition liquid/solid to gas as $V_{gas} - V_{solid/liquid}$. Making a small positive variation of temperature and pressure one evaporates a new small portion of material from the source and then the system reaches its next equilibrium state. Since V_{gas} is much bigger than V_{solid} and the vapour behaves essentially as an ideal gas we may write for one mole $\Delta V = V_{gas} = RT/P$, where R is the ideal gas constant. Equation (1.10) then rewrites as

$$\frac{dP}{dT} = \frac{H_e P}{RT^2} \quad (1.11)$$

The differential equation (1.11) relates the temperature of a substance with the pressure of its vapour under equilibrium conditions. If the enthalpy of vaporization of a substance is known, its $P(T)$ curve can be estimated. It is, however, known that the enthalpy of vaporization is also a function of temperature itself, which complicates the analysis. More often the dependence $P(T)$ is carefully measured and tabulated. These curves are typically very steep, which is shown for selected materials in Fig. 1.6. Hence, when the dependencies $P(T)$ for appropriate materials are known and the temperatures of the source materials within the MBE are precisely controlled, one may conveniently control the vapour pressures of these elements.

Transferring the molecules

When an equilibrium between the liquid/solid and its vapour for all individual material sources in the chamber is achieved, the following stage is the transfer of the vapour molecules to the substrate surface. While the physical arguments for this process are given in more details in Sec. 2.3.2, here we note that the UHV conditions ensure a ballistic motion regime of the gas molecules. If the chamber pressure under these conditions is taken to be homogeneous⁷, the molecules' arrival rate at the substrate surface can be

⁷Which is true when an equilibrium in the system liquid/solid-gas is reached.

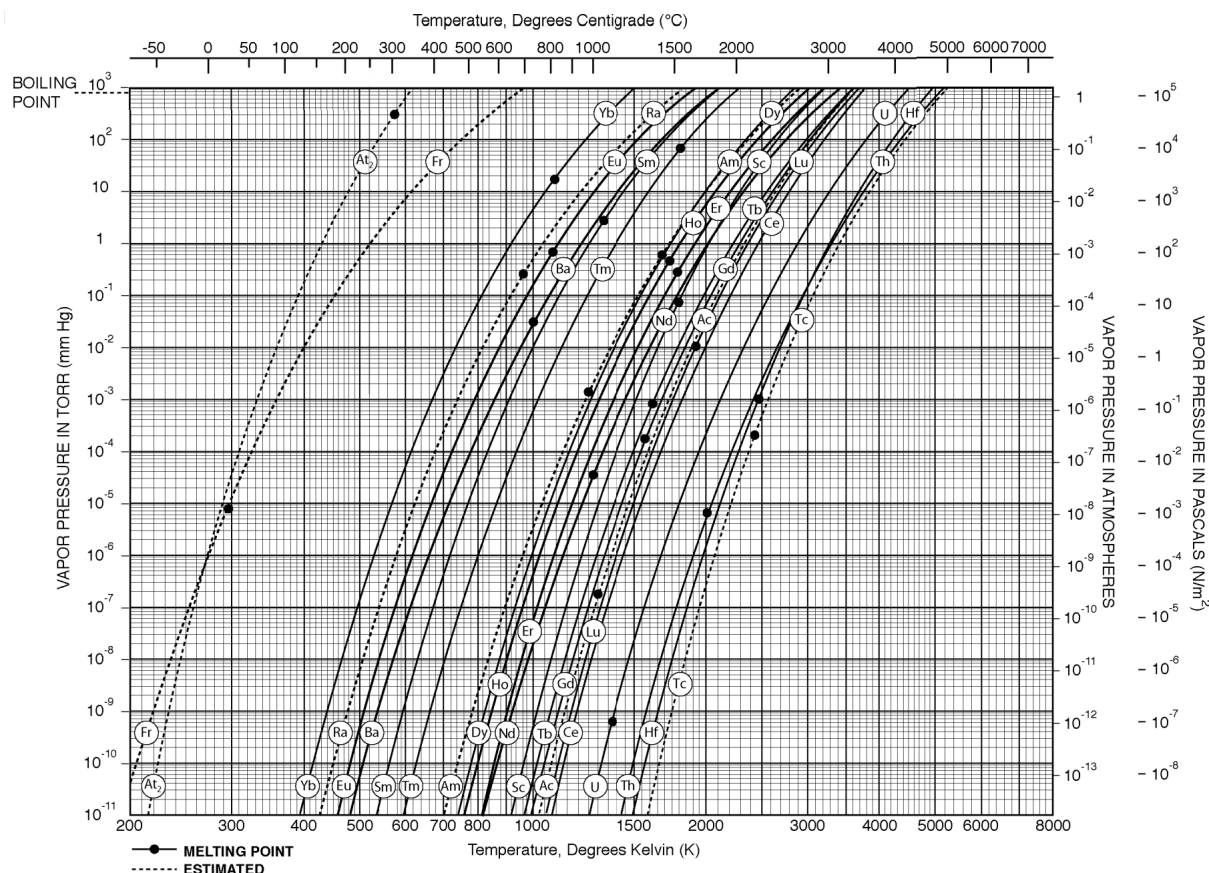


FIGURE 1.6: Equilibrium vapour pressure as a function of temperature for selected substances (Honig & Kramer 1969).

evaluated⁸. For this rate to be larger than the arrival rate of gas residues the chamber background pressure must be maintained as low as possible.

Adsorption on the surface

The process, in which molecules condense from the gas/liquid phase onto a solid surface and form a metastable state, is called adsorption. This process is usually classified as *physisorption* or *chemisorption*. In physisorption no chemical bonding, in its common sense, is formed between the adatoms⁹ and the substrate surface. However, an attractive force must exist to keep the adatoms on the surface, which is the van der Waals force. In chemisorption, the vapour molecules are attracted by the substrate surface via the physisorption mechanism first. Next, the molecules adsorb on the surface and form chemical bonds with the substrate surface. The energy of these bonds is rather large with

⁸The distribution of momenta of the arriving molecules on the substrate surface, however, will not be isotropic due to the mentioned ballistic motion regime. Hence, the momentum defined by the relative position of the evaporation source will dominate, which makes estimations of the arrival rate less straightforward.

⁹By adatoms we will understand atoms or molecules adsorbed on a substrate's surface.

typical strengths of about $1\text{-}10\text{ eV}/\text{atom}$. Chemisorption, in contrast to physisorption, is also characterized by a large heat release as a result of the chemical reaction. For physisorption, due to its weak nature, the surface sticking energies are much lower and are typically in the $50\text{-}500\text{ meV}/\text{atom}$ range. Hence the weakly bounded adatoms often desorb from the surface before being incorporated into the growing film.

Although a precise description of physisorption is a complex task, the essential physics may be caught by a simple model. In this model a closed-shell atom at a distance z from the solid surface (Fig. 1.7) and the surface atoms polarize each other¹⁰, causing a

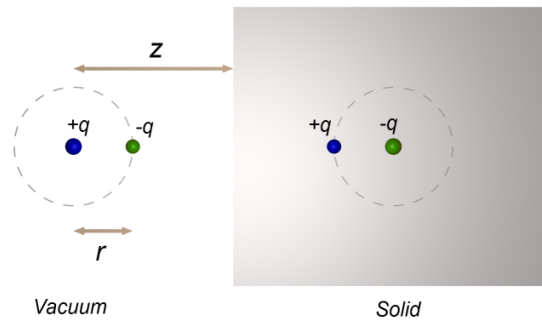


FIGURE 1.7: A free atom near the surface of a solid and its induced charge image.

weak attractive interaction, the van der Waals force. If the free atom and its image in the solid are considered, their total electrostatic energy is

$$U = \frac{1}{2} \left[-\frac{q^2}{2z} - \frac{q^2}{2(z-r)} + \frac{q^2}{2z-r} + \frac{q^2}{2z-r} \right] \quad (1.12)$$

By Taylor expansion in powers of r/z one obtains

$$U = -\frac{1}{8} \frac{q^2 r^2}{z^3} - \frac{3}{16} \frac{q^2 r^3}{z^4} - \mathcal{O}\left(\frac{1}{z^5}\right) \quad (1.13)$$

Usually the first term in (1.13) is written as $-C/z^3$, where C is the van der Waals constant. The value of this constant may be estimated analytically¹¹ and measured experimentally. By experiments with scattering of alkali atoms on a gold wire with closest approaching distances between 200 \AA and 800 \AA (1.13) was confirmed to fit well (Shih & Parsegian 1975). Nevertheless, the value of the van der Waals constant obtained from the fitting of the experimental data was $\sim 60\%$ smaller than the one obtained theoretically, which is quite reasonable for such a crude model. For other systems, however, even larger deviations were found.

¹⁰Such polarization of two closed-shell atoms is the result of their atomic charge density redistribution upon reducing the inter-atomic separation, which is generally treated by quantum mechanics.

¹¹For details see Sec. 8 in (Zangwill 1988).

When a free atom approaches a solid surface at a distance of the order of hundred angstroms, it is attracted by the surface due to polarization of both the surface and the atom. When the separation between the free atom and the surface is lowered further, at small distances the electronic wave functions of the free atom and the solid species start overlapping (Fig. 1.8). This causes a strong repulsion between them due to the Pauli exclusion principle.

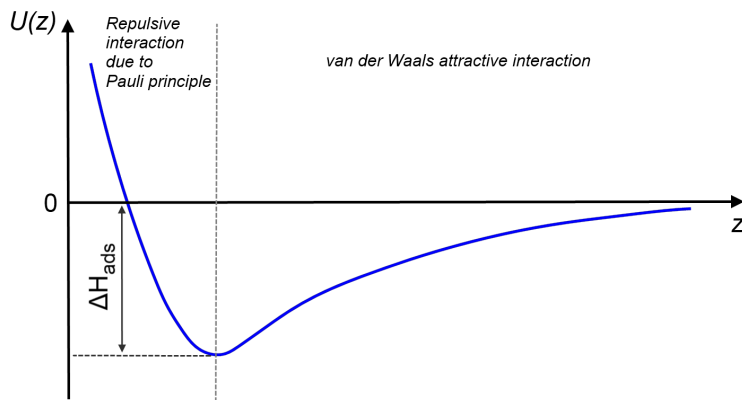


FIGURE 1.8: Lennard-Jones potential describing the interaction energy $U(z)$ between two neutral atoms as a function of their separation z . ΔH_{ads} is the energy gain due to adsorption process, which is usually less than 50 kJmol^{-1} (0.52 eV/atom).

Growth models and modes

It was pointed out that a surface created by cleavage may reconstruct. It also may undergo a phase transition if its temperature is varied, which is driven by the entropy of the system. Although we do not know the exact state of this surface, let it be already stabilized. The process of adsorption on this surface of the vapour molecules during the initial stages of the thin film growth is also associated with creation of a new surface. Hence, this new ensemble of adsorbed molecules may also reconstruct and undergo phase transitions. Let us first consider the case when the number of adatoms is small, i.e., the interactions between them can be neglected and the surface processes may be treated in terms of statistical physics. Within the Langmuir adsorption model (see, e.g., Ch. 4 in (Venables 2000)), the chemical potential of an adatom is $\mu_a = F/N_a$, where $F = -k_B T \ln(Z_a)$ is the Helmholtz free energy of the system, N_a is the number of adsorbed atoms on the surface, and k_B is the Boltzmann constant. The grand canonical partition function of the system is $Z_a = \sum_i \exp(-E_i/k_B T)$, where E_i are the energies of the system for all possible combinations of the adsorbed atoms. When the number of possible sites available for adsorption N_0 is considered, then μ_a may be expressed in terms of the surface coverage $\theta = N_a/N_0$ (see Ch. 7 in (Hill 1960) and Ch. 4 in

(Venables 2000))

$$\mu_a = k_B T \ln \left(\frac{\theta}{1 - \theta} \right) - E_a - k_B T \ln(q) \quad (1.14)$$

where E_a is the adsorption energy, and q is the vibrational degeneracy of the system. The analysis of the equilibrium between the adsorbate, the solid, and the vapour is rather complex and we may simplify it setting $\mu_a = \mu_s$, where μ_s is the chemical potential of the solid. The value of μ_s , in turn, may be obtained analytically for a given surface by the high-temperature Einstein model of solid bodies. If we now equalize the adatoms' chemical potential to that of the vapour, i.e., $\mu_a = \mu_v$, this would correspond to the equilibrium between adsorption and desorption processes. Hence, using (1.14) we may find the correspondence between θ and the vapour pressure¹², which is called the Langmuir adsorption isotherm (Fig. 1.9). The analysis based on the Langmuir adsorp-

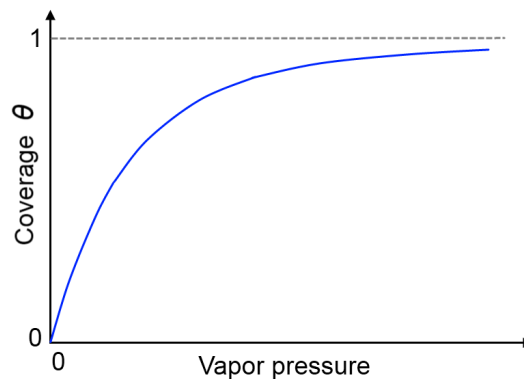


FIGURE 1.9: A schematic view of the Langmuir vapour pressure isotherm.

tion model catches only the basic behaviour of the adsorption process in real systems, while the details may vary substantially. For example, it gives fairly good results for, e.g., xenon on graphite, which is a test system for more complex models. In the case of a metal vapour, the Langmuir adsorption model fails due to strong interactions between the metallic adatoms even at low coverages.

No film growth or phase transition has occurred so far. If we keep increasing the density of adatoms¹³ on the substrate surface by increasing the vapour pressure, the adatom-adatom (or intralayer) interaction strength increases. At some coverage it becomes comparable with the substrate-adatom (interlayer) interaction strength and crystal growth may occur. The ratio of the intralayer to the interlayer interaction strengths will be referred to as λ . This growth may be viewed as a phase transition, which occurs out of the equilibrium state formed at the very first stages of deposition. The processes of thin

¹²The pressure variable enters the chemical potential μ_v defined through the equation of state of the vapour phase.

¹³We assume that they reside only in a single layer and do not form a second one.

film growth for which $\lambda \geq 1$ usually lead to *epitaxy*, i.e., formation of a coherent interface between the thin film and the substrate (see also p. 31 in (Freund & Suresh 2003), p. 421 in (Zangwill 1988)).

So far we dealt only with vapour-solid systems which consist only of atoms of the same kind. But what would happen if the vapour and the substrate atoms were of a different kind? This corresponds to heteroepitaxy in contrast to homoepitaxy, when only atoms of the same kind are present in the vapour-film-substrate system. A number of experimental studies of heteroepitaxial growth since the 1950s showed that dissimilar crystal lattices select preferential relative orientations when they are brought in contact (see Seifert in (Smith & Gomer 1953)). Many experimental results of known orientation relationships between BCC/HCP and BCC/FCC lattices were analyzed by (Dahmen 1982). Using pure geometrical considerations (Dahmen 1982) showed that an FCC(111)-oriented film (unit cell period a) grown on a BCC(110) substrate (unit cell period b) may be matched for most close-packed rows to the substrate structure if it is stretched to obtain $r = a/b = 1.0887$ and if it is rotated by 5.26° . Practically identical results for this combination of crystal structures were obtained by (Ramirez, Rahman *et al.* 1984) by numerical simulations. In their simulations the authors used the Lennard-Jones potential and minimized the heteroepitaxial system energy for a set of combinations of stretching and rotation. They found that, indeed, the global minimum was obtained exactly for the specified angle and the specified value of r , although local energy minima are also possible. The effect of rotation in the heteroepitaxial growth is known as *rotational epitaxy*.

While the first several layers of the growing film may accommodate the dissimilar substrate structure with a short lateral coherence length¹⁴, the following layers will tend to relax towards the crystal structure of the film in its bulk single crystal symmetry. However, crystallographic defects, such as misfit and screw dislocations, grain boundaries, stacking faults *etc.* may be generated at this stage. The strain of the film, for example, is sometimes analyzed with a phase diagram in r and λ coordinates (Stoop & der Merwe 1982). Some of these defects, however, may be healed as the film thickness increases (e.g., stacking fault, misfit dislocations), while some of them have a tendency to replicate themselves over many atomic layers of the film, e.g., screw dislocations¹⁵. It is natural to expect from the analysis of the adatoms' dynamics on the surface that the films' morphology, as new material is added, will also demonstrate a great variety of morphology types. The film growth morphology may be categorized in three general cases, as was shown by (Bauer 1958). These growth modes are depicted in Fig. 1.10.

¹⁴Another example is the pseudomorphic epitaxial growth, when the film's first layers completely accommodate the substrate structure, hence, forming a structure with long lateral coherence. The following layers, however, will be relaxing to the film bulk structure.

¹⁵See also Sec. 3.3.3.

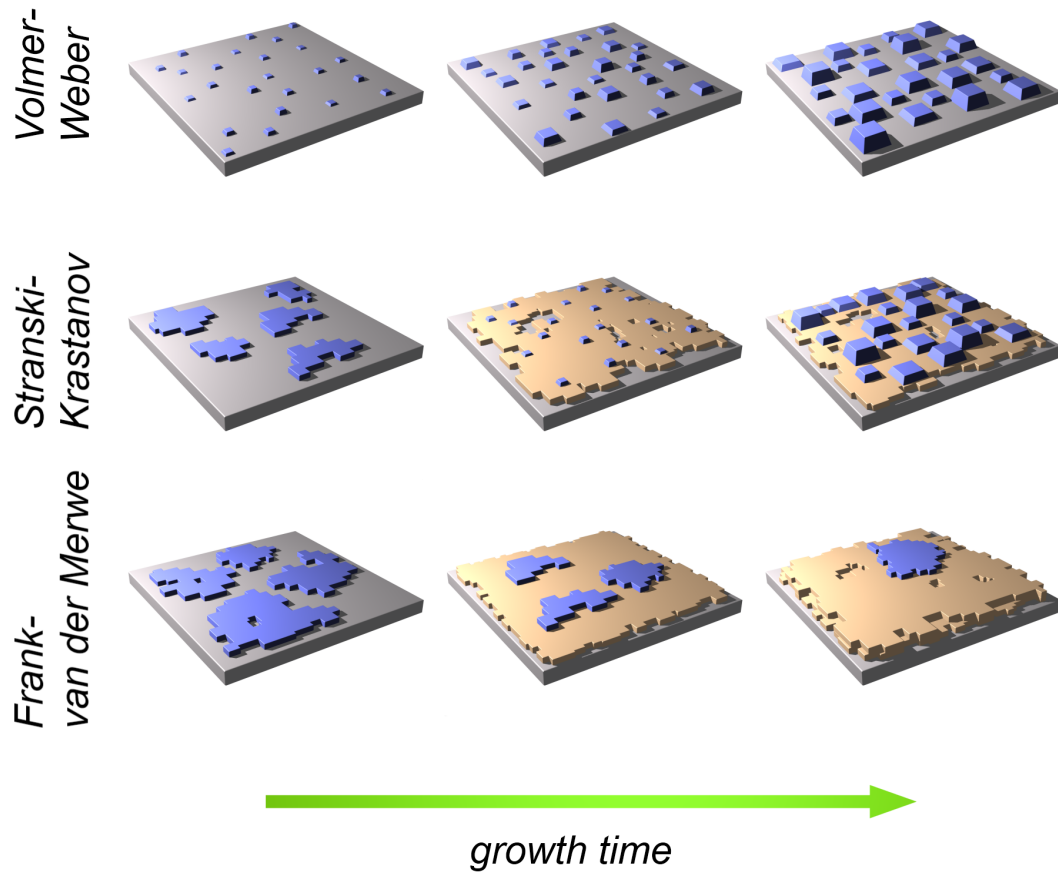


FIGURE 1.10: Classification of thin film growth regimes and a schematic representation of their evolution with growth time. The substrate is shown in grey colour, the forming islands are in blue, and the practically completed film layers are in beige.

The three growth regimes may be characterized by introducing the free energies per unit surface γ_{fv} , γ_{sf} , and γ_{vs} for the film-vacuum, the substrate-film, and the vacuum-substrate interface respectively. Let the area occupied by the film-vacuum interface be A_{fv} and the substrate-vacuum interface be A_{sv} , so that $A = A_{fv} + A_{sv}$ is the total substrate area. Then, the free energy of the system is

$$F = A_{fv}(\gamma_{sf} + \gamma_{fv}) + A_{sv}\gamma_{vs} = A_{fv}(\gamma_{sf} + \gamma_{fv}) + (A - A_{fv})\gamma_{vs} \quad (1.15)$$

By variation of the surface covered by the film A_{fv} we get

$$\frac{dF}{dA_{fv}} = \gamma_{sf} + \gamma_{fv} - \gamma_{vs} \quad (1.16)$$

Equation (1.16) directly motivates the three different growth regimes with explanations in the table below. Each of the three regimes is characterized by an individual adsorption isotherm similar to the one shown in Fig. 1.9, but drawn as a function of chemical potential of the deposit relative to the bulk substrate. In the Volmer-Weber regime at the equilibrium vapour pressure the concentration of growth centers and the growth

TABLE 1.1: Free energy slopes dF/dA_{fv} and the explanation of the three thin film growth regimes.

Volmer-Weber	Stranski-Krastanov	Frank-van der Merwe
$\frac{dF}{dA_{fv}} > 0$ $\gamma_{vs} < \gamma_{sf} + \gamma_{fv}$	$\frac{dF}{dA_{fv}} \simeq 0$ $\gamma_{vs} \simeq \gamma_{sf} + \gamma_{fv}$	$\frac{dF}{dA_{fv}} < 0$ $\gamma_{vs} > \gamma_{sf} + \gamma_{fv}$
The system wins energy by increasing the area of the substrate-vacuum interface, which results in a strong island growth mode	The degeneracy of the system's states is large, which may result in the formation of a close-packed layer first and the initiation of an island growth regime next	The system wins energy by reducing the area occupied by the substrate-vacuum interface, hence increasing the film-vacuum area, which results in the so-called layer-by-layer growth mode

rate is small and a supersaturation is needed for steady growth. In the Frank-van der Merwe regime the growth of layers is initiated already in an undersaturated regime. In the Stranski-Krastanov mode the formation of several layers is possible already in an undersaturated regime, but soon a nucleation barrier emerges, which requires a supersaturation for further growth in the island mode, as in the Volmer-Weber regime.

1.4 Localization and Heavy-fermion systems

1.4.1 Single impurity Kondo effect

Till the early 1930s it had been established experimentally and supported theoretically that the temperature dependence of the resistivity of metals may only decrease with decreasing temperature (see, e.g., (Sondheimer 1950)), which is the result of the decrease of electron scattering due to phonon freeze-out. The temperature dependence of the resistivity was described well by the Bloch-Grüneisen resistivity function. The only unexplained phenomenon at that time remained superconductivity, which led to a sudden decrease of resistivity at low temperatures. However, in 1934 low-temperature measurements of the electrical resistivity of pure¹⁶ gold, copper, lead (De Haas, De Boer *et al.* 1934) and platinum (De Haas & De Boer 1934), performed in the Kammerling Onnes laboratory, revealed a new qualitative behaviour in these materials: something was giving rise to resistivity even as the temperature was lowered towards absolute zero

¹⁶Actually, it is the uncontrolled minute admixture of foreign ions that is responsible for such a behaviour.

(see Fig. 1.11). Soon, it became apparent that a new mechanism is involved. In the

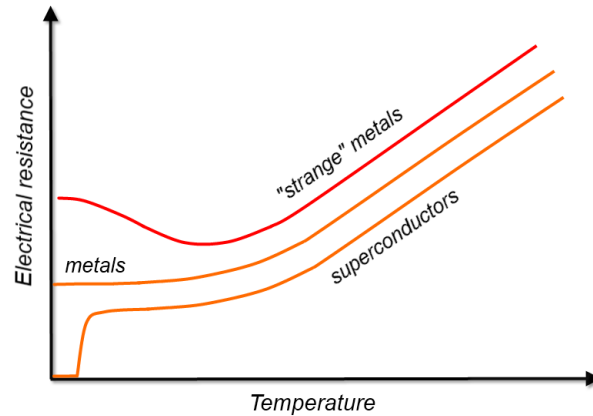


FIGURE 1.11: Schematic view of the possible temperature dependencies of the electrical resistance in metals. The orange curves correspond to the superconducting and normal metals, while the red curve is one typically measured by de Haas and collaborators for metals which demonstrated a minimum at low temperatures. At the lowest temperatures all the curves tend to be saturated.

early 1960s it was proposed by (Anderson 1961) in his single impurity model that the phenomenon may be caused by magnetic impurities even with tiny concentrations. In his calculations, however, the electrical resistance did not show such a strong temperature dependence. The question remained whether the phenomenon emerges at all due to the presence of magnetic impurities and if so whether it is a single- or a many impurity effect. A hint was given a few years later in an experiment measuring the low-temperature resistivity of *Mo-Nb* alloys with 1% of iron impurities. It was already known that by tuning the ratio *Mo/Nb* the magnetic moment of iron in such alloys may be continuously tuned from zero to two Bohr magnetons, hence giving way to investigating the localized magnetic moments in a controllable fashion. The observations revealed that it is possible

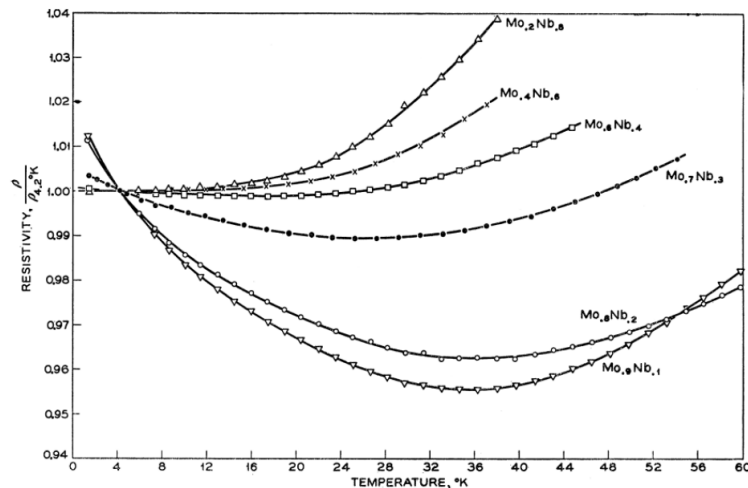


FIGURE 1.12: Electrical resistance minimum in *Mo-Nb* alloy containing 1% of iron impurities (Sarachik *et al.* 1964).

to change the qualitative behaviour of the resistivity for such a system from a normal metal to a metal demonstrating a resistance minimum by tuning the size of the impurity magnetic moment (Fig. 1.12). Hence, the importance of localized magnetic moments was out of doubt.

The single impurity Anderson model, as mentioned above, failed at first to explain the phenomenon although it was conceptually correct. Later, (Kondo 1964) solved the problem of the resistance minimum utilizing this model, but using higher order terms in perturbation theory, which were neglected by Anderson. Briefly, Kondo's derivation was as follows. A scattering event of an electron between states \mathbf{k} and \mathbf{k}' at the impurity potential $V(\mathbf{r})$ is proportional to the matrix element

$$V_{\mathbf{k}\rightarrow\mathbf{k}'} = \int \psi_{\mathbf{k}'}^*(\mathbf{r})V(\mathbf{r})\psi_{\mathbf{k}}(\mathbf{r})d\mathbf{r} \quad (1.17)$$

The rate of such a transition is $W_{\mathbf{k}\rightarrow\mathbf{k}'} \propto |V_{\mathbf{k}\rightarrow\mathbf{k}'}|^2$, which is not zero only for states of equal energy $\epsilon_{\mathbf{k}} = \epsilon_{\mathbf{k}'}$ due to the energy conservation law¹⁷. The electrical resistivity is then given by

$$\rho = m\langle\gamma_{\mathbf{k}}\rangle/ne^2 \quad (1.18)$$

where $\gamma_{\mathbf{k}} = \sum_{\mathbf{k}'} W_{\mathbf{k}\rightarrow\mathbf{k}'}$ is the probability for the electron \mathbf{k} to be scattered¹⁸ and $\langle\gamma_{\mathbf{k}}\rangle$ is its thermal average, n is the electron density, and m is the electron mass. Since $\gamma_{\mathbf{k}}$ weakly depends on temperature, the resistivity at small $k_B T$ is expected to saturate. The situation, however, becomes different if a small concentration¹⁹ of magnetic impurities is present. In Anderson's model, an electron may scatter into a state \mathbf{k}' by virtue of a state \mathbf{k}'' involving a localized f -state even if²⁰ $\epsilon_{\mathbf{k}} = \epsilon_{\mathbf{k}'} \neq \epsilon_{\mathbf{k}''}$. Let us assume that initially \mathbf{k} state is occupied by a spin down electron and the localized f state by a spin up electron (see Fig. 1.13). The matrix element for this transition is denoted as $J(\mathbf{k}\downarrow, f\uparrow \rightarrow \mathbf{k}'\downarrow, f\uparrow)$. If the scattering events $J(\mathbf{k}\downarrow, f\uparrow \rightarrow \mathbf{k}''\downarrow, f\uparrow) \cdot J(\mathbf{k}''\downarrow, f\uparrow \rightarrow \mathbf{k}'\downarrow, f\uparrow)$ and $J(\mathbf{k}''\downarrow, f\uparrow \rightarrow \mathbf{k}'\downarrow, f\uparrow) \cdot J(\mathbf{k}\downarrow, f\uparrow \rightarrow \mathbf{k}''\downarrow, f\uparrow)$ are considered (Fig. 1.13(a) and (b)), it can be shown that the matrix element of the scattering becomes $J^2 \rho_0 \log |\epsilon_{\mathbf{k}}/(\epsilon_{\mathbf{k}} - D)|$, which gives a weak temperature dependence of the resistivity. Here, ρ_0 is the density of states at the Fermi level and D is the upper limit of the integration energy, that is $D - \epsilon_F \gg k_B T$. While many theoreticians considered only these low order terms, Kondo considered a higher order process with a flipped spin in the intermediate state (Fig. 1.13(c) and (d)), like $J(\mathbf{k}\downarrow, f\uparrow \rightarrow \mathbf{k}''\uparrow, f\downarrow) \cdot J(\mathbf{k}''\uparrow, f\downarrow \rightarrow \mathbf{k}'\downarrow, f\uparrow)$, and showed that

¹⁷Assuming that no internal degrees of freedom can be excited.

¹⁸ $1/\langle\gamma_{\mathbf{k}}\rangle$ is the relaxation time.

¹⁹In fact, large concentrations of magnetic impurities may also produce a resistance minimum, which will be discussed in Sec. 1.4.3.

²⁰Although classically it is forbidden due to the energy conservation law, quantum mechanically it is possible with some probability if the two scattering processes occur in a short enough time. The states \mathbf{k} , \mathbf{k}' , and \mathbf{k}'' are the conduction band states, while f is a localized state.

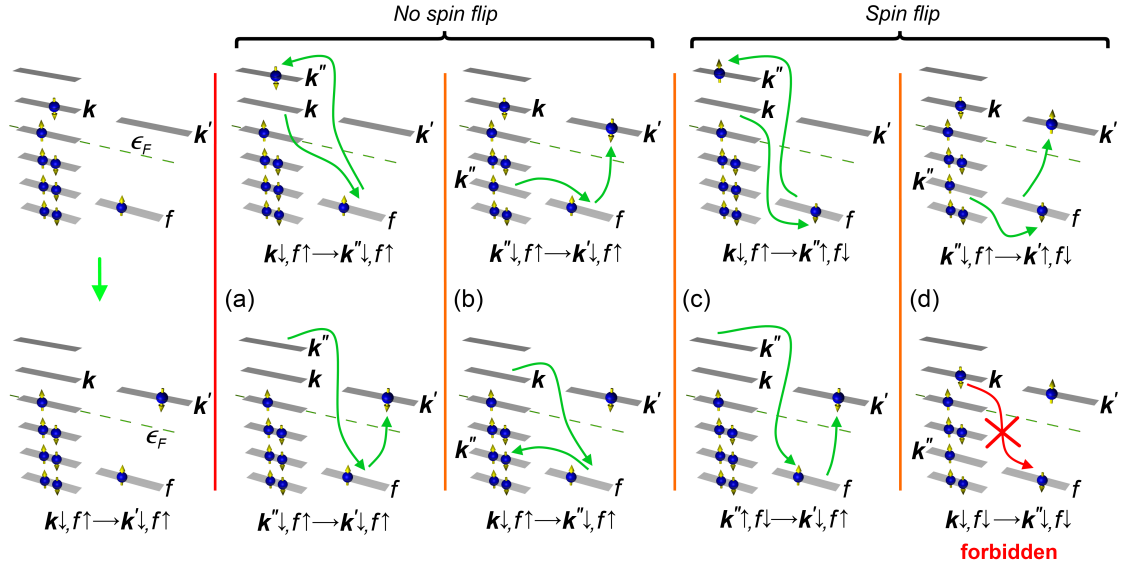


FIGURE 1.13: (left) Illustration of a transition $k_{\downarrow}, f_{\uparrow} \rightarrow k'_{\downarrow}, f_{\uparrow}$ involving virtual transition paths. The states k , k' , and k'' belong to the conduction band states (c -band) and f is a localized state. The transition is possible via sequences (a) and (b) without a spin flip of the localized f -electron during the transition in the intermediate k'' state, whereas transition (c) involves a spin flip. Transition (d), which one might expect to also take place due to symmetry considerations, is forbidden due to the Pauli principle leading to important consequences (see text). Transitions (a) and (c) involve c -band states k'' outside the Fermi sphere (energy larger than ϵ_F), while sequence (b) involves states inside the Fermi sphere.

due to the forbidden transition shown in Fig. 1.13(d) the matrix element of such a process becomes $J^2 \rho_0 \log |(\epsilon_k - \epsilon_F)/(\epsilon_k - D)|$, which diverges when $\epsilon_k \rightarrow \epsilon_F$ or, equivalently, as the temperature approaches zero. After some manipulations (see, e.g., (Kondo 2006)), the temperature dependence of the electrical resistance may be written using (1.18) as

$$R(T) = R_0 [1 + 2J\rho_0 \log |k_B T / (D - \epsilon_F)|] \quad (1.19)$$

where R_0 is the electrical resistance obtained considering the lowest order perturbation expansion term, i.e., direct scatterings $k \rightarrow k'$. Equation (1.19) successfully explained the feature of a minimum resistance found experimentally, for which J has to be negative. It has to be noted that the negative sign of J reflects the *antiferromagnetic* coupling between the localized f -states and the itinerant c -states.

In spite of the great success of (1.19), the applicability of Kondo's derivation was realized to be limited to temperatures higher than some temperature T_K , since the second term in (1.19) diverges, which was not confirmed experimentally, so further theoretical developments were needed. The temperature at which the second term approaches the

first one in (1.19) is called *Kondo temperature* T_K , and is given by²¹

$$k_B T_K \approx (D - \epsilon_F) e^{-1/J\rho_0} \quad (1.20)$$

It follows from (1.20) that T_K is sensitive to $J\rho_0$, which may lead to characteristic temperatures T_K from the sub-Kelvin range to several hundred Kelvin.

Not only the electrical resistivity is influenced by the local moments of the impurities, but also other electronic properties as well, such as the electronic specific heat C and the magnetic susceptibility χ . Logarithmic corrections to these quantities also scale with T_K and may be derived similarly to the resistivity function. It should also be noted that the correction terms for these three quantities are expected to scale linearly with the relative impurity concentration c_{imp} , which is assumed to be much less than unity. The specific heat and the magnetic susceptibility corrections from the impurities are

$$\begin{aligned} \Delta C &= c_{imp} \gamma_{imp} T \\ \Delta \chi &= c_{imp} \chi_{imp}(T) \end{aligned} \quad (1.21)$$

where γ_{imp} and $\chi_{imp}(T)$ are the single impurity linear specific heat coefficient and the magnetic susceptibility respectively (see also Ch.11 in (Fazekas 1999)). The χ_{imp} in (1.21) is a negative sign correction to the Curie behaviour of localized moments, which reflects the antiparallel coupling of the c -electrons to the f -electrons as the temperature decreases towards T_K .

At temperatures $T < T_K$ the f -electrons become a part of the Fermi sea²², as it was proposed by Anderson in the weak localization hypothesis. As the f -electrons hybridize with the Fermi sea, the density of states around $\rho(\epsilon_F)$ is enhanced by the number of f -levels accessible to the c -electrons. This density of states enhancement is called *Kondo resonance*. Within this hypothesis the scattering events of c -electrons approaching an impurity ion from far become proportional to a large, but still finite, usual potential scattering matrix element, since the impurity's moment has been locally screened and the spin-flip scattering of those c -electrons becomes less probable. This results in a saturation of the electrical resistivity and other sensitive quantities towards zero temperature, which was observed experimentally.

The anomalies in the temperature dependencies of the electrical resistivity, specific heat, and magnetic susceptibility in reasonably simple cases of dilute magnetic alloys were understood quite well in terms of the single impurity Kondo temperature scale. Although

²¹ $D - \epsilon_F$ is of the order of the bandwidth W of the conduction band.

²²This, however, does not imply that the f -electrons become fully itinerant. The f -states still remain half-occupied and localized, but the Fermi sea is extended with an extra f -level, which is participating in formation of the local singlet state by the c - and f -electrons.

the theoretical derivations were obtained perturbatively, an exact solution by the renormalization group theory (Wilson 1975) also became available later²³. The observed low-temperature saturation of the electrical resistivity was initially absent in the theoretical models, but was explained later by formation of the Kondo cloud of c -electrons, which screens the localized f -moments.

1.4.2 Multi-valence systems

The localized moments discussed above were postulated without considering the mechanisms of their formation in solids. Let us, however, consider the nature of these localized moments, their formation and influence on the electronic properties of solids.

The valence of an ion in solids by definition is the number of electrons it provides to the hybridized levels or conduction band. In intermetallic compounds with rare earth ions the latter usually demonstrate trivalent states with several exceptions. The classification, however, is very often put differently for the rare earth elements. Their f -shells tend to be strongly confined close to the heavily charged ion cores lying well below the hybridized $5d - 6s$ or $5s - 5p$ shells. This poses an interesting feature of strong intrasite interactions of f -electrons, which remain essentially screened from the crystal fields, but still may define many properties of the solid state. Due to this, one may conveniently represent a state of such a heavy ion by the number of remaining electrons in its outer f -shell, e.g., the electron configuration of a free Ce atom is $[Xe] 4f^1 5d^1 6s^2$. When such an atom forms chemical bonding its $5d - 6s$ shells hybridize contributing electrons to the crystal band. The resulting configuration of the Ce ion core becomes $Ce^{3+} = [Xe] 4f^1$, or $Ce^{4+} = [Xe] 4f^0$, when it is oxidized even stronger. Hence, in chemical compounds the outer partially occupied shell of the Ce ions is the f -shell.

For example, in simple metals, like alkali or transition metals, their partially filled bands are s or d bands. Their bandwidth W is typically large due to the strong overlap of the respective atomic orbitals between neighboring ions, e.g., the $3s$ -band becomes wider than the $2p$ band. The f -band metals, due to small hybridizations of their f -shells, feature a very narrow valence band. On the other hand, the characteristic lifetime of the electronic fluctuations between the allowed degenerate shell levels is $\tau_{band} \propto \hbar/W$. Hence, in simple metals τ_{band} is short enough to prohibit an electron to be found in any

²³Wilson also showed that the low-temperature electronic properties of diluted Kondo alloys may be derived from Landau Fermi liquid theory, i.e., explaining them by renormalized normal metal properties.

preferential state. As a result, the valence of such metals always appears as integer²⁴. For rare earths or the f -electron compounds, in contrast, not all valence states are easily accessible, so their averaged valence may become non-integer. It is the strong Coulomb on-site repulsion that limits the accessibility of the available states, which naturally occurs due to the small spatial extension of the f -shells. The compactness and the negligible overlap between the neighboring f -shells allow to model such a system by a degenerate set of Hubbard sites within the Fermi sea

$$H^{(0)} = H_{band} + H_f = \sum_{\mathbf{k}\sigma} \epsilon_{\mathbf{k}} c_{\mathbf{k}\sigma}^\dagger c_{\mathbf{k}\sigma} + U \sum_j \sum_{\alpha < \beta}^N f_{j\alpha}^\dagger f_{j\alpha} f_{j\beta}^\dagger f_{j\beta} \quad (1.22)$$

where α, β count over N orbital and spin degeneracies, j counts over the f -sites, and U is the on-site Coulomb interaction. Here, the c -electron levels form a continuous band and the f -electrons occupy a discrete energy spectrum of levels separated by U , i.e., $\epsilon_f, \epsilon_f + U, \epsilon_f + 2U$ etc. How would the energy spectrum of this two-band system look like? Let us assume that the concentration of electrons per unit cell is $n = n_c + n_f$, where n_c is the concentration of conduction electrons and n_f is the concentration of f -electrons. If we start from $n = 0$, i.e., an empty band and f -levels, the chemical potential of the system would be essentially zero (Fig. 1.14). Additional electrons will enter the c -band first, so the chemical potential μ increases continuously (solid line in Fig. 1.14). None of the f -sites is populated so far, which is characterized as the f^0 or an integer valence state. At a concentration n_{c1} some of the f -sites will start being populated, so that within the range $n_{c1} < n < n_{c1} + a$ the f^1 -states of the system will be partially filled fixing $\mu = \epsilon_f$. In this regime the system will exhibit $f^0 - f^1$ valence mixing, with the overall valence having a non-integer value. At higher concentrations n , when all f^1 -states are filled (i.e., all f -sites are singly occupied), μ again starts increasing monotonically and the system is in the next integer valence state f^1 . Later, when $n > n_{c2}$, the system mixes its valence again between f^1 and f^2 , since some of the f -sites become doubly occupied while some remain singly occupied. Within this region, the rise of n does not lead to a rise of μ until all f -states are doubly occupied. The population of the two-band system levels may continue until the last level is filled completely (f^{14}), alternating between the integer and the non-integer valence states. As a result, one obtains sharply defined steps of the valence mixing regimes. The model (1.22) we started with assumes contact of the f and c bands to a common fermionic bath, but does not include hybridization between them, which, as we know from the previous section, should be included. If

²⁴From the energy-time uncertainty principle $\Delta E \Delta t \geq \hbar$, $\tau = \Delta t$ is referred to as the lifetime of an energy state whose energy is measured as precisely as ΔE . If different valence states are determined to be somewhere within the bandwidth energy W (very large, say ~ 3 eV), then the lifetime of such states on average will be τ (very small, say $\sim 1 \times 10^{-17}$ s). If we measure much longer than this time, the system's valence state will appear to be averaged. It happens that such a relaxation time is very short compared to many other characteristic times.

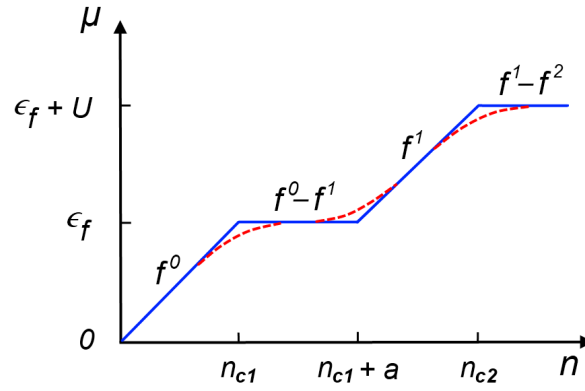


FIGURE 1.14: Chemical potential as a function of the electron density for a two-band Hubbard-like system with a large U within one band. The blue curve corresponds to the case of non-hybridized bands, while the red dashed curve demonstrates smoothening of the steps when such a hybridization is included.

(1.22) is extended by a weak hybridization between the f and c bands, the sharp steps of the $\mu - n$ spectrum become smeared (red dashed curve in Fig. 1.14). In this case, the system having any of the critical concentrations of electrons $n_{ci} + ja$ (here i and j are integer numbers) is said to be in the *nearly integral valence* regime²⁵.

It follows from the arguments above, that the ground state of $H^{(0)}$ of a system in the mixed valence regime (1.22) is degenerate due to a large number of possible filling combinations of all f -sites plus additional degeneracy of the ionic f -states. If the hybridization is included as

$$H = H^{(0)} + H_{hyb} = H^{(0)} + \sum_{\mathbf{k}\sigma} \sum_{j\alpha} [V_{\mathbf{k}\sigma j\alpha} c_{\mathbf{k}\sigma}^\dagger f_{j\alpha} + h.c.] \quad (1.23)$$

the entropy is further increased by redistribution of hole-like excitations in the vicinity of the chemical potential μ . The degeneracy, in turn, makes the population of f -sites a dynamical process referred to as *fluctuating valence*, which is often used interchangeably with the mixed or intermediate valence notion.

The introduced hybridization term H_{hyb} in (1.23) would cause broadening of the f -levels into an effective f -band. Since it is accessible only by c -electrons within $k_B T$ around ϵ_F , the f -band will be centered around the Fermi level. The hybridization strength defines also its width, which is proportional to $V^2 \rho(\epsilon_f)$, where $V^2 = \langle |V_{\mathbf{k}\sigma j\alpha}|^2 \rangle$, and $\rho(\epsilon_f) \equiv \rho$ is the density of states at the Fermi level of $H^{(0)}$. Similarly to the arguments above, if the temperature of the system is $k_B T > V^2 \rho$, valence fluctuations $\tau_{fluct} \sim \hbar / V^2 \rho$ are driven by thermal energy. If $k_B T < V^2 \rho$, quantum fluctuations become more relevant.

²⁵An interesting effect may happen if the effective U is assumed to be negative. By reaching $\mu = \epsilon_f - |U|/2$ we already start filling the f^2 states, hence creating $f^0 - f^2$ valence mixing. The effect is known as *valence skipping*.

In other words, measuring f -levels filling for a longer time than τ_{fluc} would result in an average nearly integer valence, while measuring it “faster” than τ_{fluc} gives a snapshot of the frozen states²⁶.

By using the orbitally non-degenerate periodic Anderson model (PAM) of a form similar to (1.23) it may be shown that switching the on-site interaction U from zero to infinity forces the f -electrons to redistribute their density far in real space. This also redistributes their states in \mathbf{k} -space. This has consequences for the Fermi-step of the occupation number distribution such that the f -electrons gain a non-vanishing probability of being found in the entire Brillouin zone: confining Δx we increase Δp . The height of the step around \mathbf{k}_F is also lowered, similarly to the well-known Fermi-liquid case. It is also known from Fermi-liquid theory that for simple metals such changes are related to the enhancement of the effective mass m^* of the charge carriers, which, however, is known to be a small effect. Similarly, for a system with localized f -levels it may be derived by a variational approach to the PAM (Shiba 1986):

$$\frac{m^*}{m} = \frac{1 - \Delta n_c - \Delta n_f}{\Delta n_f} \propto \frac{n_f}{2(1 - n_f)} \quad (1.24)$$

where Δn_c and Δn_f are the U -induced changes of the respective charge carrier concentrations, and n_f is the concentration of f -electrons in the system. Different consequences of (1.24) have to be discriminated for the mixed and the nearly integral valence cases. For an intermediate value of $f^0 - f^1$, i.e., for a mixed valence system, the mass enhancement is rather weak, but for a f^1 system with small fluctuations towards the f^0 state the mass enhancement may reach 1000 or even more. The latter systems are referred to as *heavy fermion* systems and will be discussed in Sec. 1.4.5.

Generally, the mixed valence phenomena are strongly affected by the stability of chemical phases, which may put some restrictions on the valence of rare earth ions within those structures. So, not all compounds demonstrate the nearly integral phenomena, which is an experimental fact. Though the nearly integral valence regime is less common than the integral valence or the mixed valence regimes, many compounds which demonstrate the nearly integral valence phenomena feature dramatic variations of their low-temperature electronic properties involving strong correlation effects in different ways.

²⁶This does not violate the uncertainty principle, since we are not able to say when this exact caught state will relax. For rare earth elements $\tau_{fluc} \sim 10^{-12}$ s and one would expect to see a difference between the “slow” Mössbauer technique and the “fast” x-ray photoelectron spectroscopy technique.

1.4.3 Periodic Kondo lattices

In the single Kondo impurity case we assumed that the concentration of the foreign magnetic moments is large enough to be detectable by experiments, but still small enough so that an $f - f$ exchange energy and a superexchange via c -electrons are both negligibly small²⁷. But how small the concentration c_{imp} can be for our simple models above to remain valid? A crude estimation based on the energy gain by formation of the local Kondo singlet²⁸ ΔE for $T_K = 10$ K gives a Kondo “cloud” dimension of $1000a$, where a is the lattice constant (Fazekas 1999, Sørensen & Affleck 1996). It implies that in order to maintain a non-overlapping scenario the impurity concentration should be $c_{imp} < 10^{-9}$. This number is very small and one may assume that the model is not correct, in particular since many experimental results are in very good agreement with the single impurity Anderson model even at $c_{imp} \simeq 0.5$! E.g., $Ce_xLa_{1-x}Cu_6$ may be tuned between the Kondo minimum regime at “small” x and a new, coherent, regime at large x , which is shown in Fig. 1.15. $LaCu_6$ allows a continuous substitution

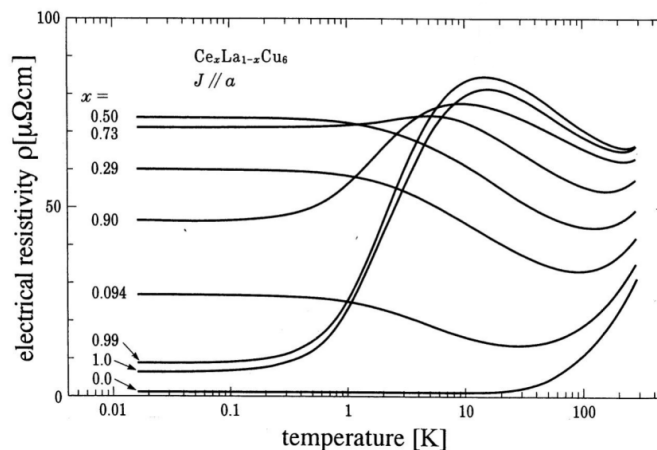


FIGURE 1.15: An example of an intermetallic compound, which can be tuned between the single impurity Kondo regime and the coherent scattering regime by varying the concentration of localized Ce ions (Sumiyama *et al.* 1986)

of the non-magnetic La ion by the magnetic Ce ion. The single impurity behaviour survives up to $x \simeq 0.5$. For larger values of x , including unity, a broad maximum of the resistivity²⁹ is observed, which is very common to many heavy fermion compounds. The resistivity below this maximum follows the Landau Fermi-liquid law³⁰ $\rho \simeq \rho_0 + AT^2$, eventually saturating towards zero temperature. Additionally, the large enhancement of the electronic specific heat coefficient γ at low temperatures demonstrated by this

²⁷It was suggested by (Zener 1951) as early as in 1951 that the localized f -moments could be coupled by indirect exchange interaction.

²⁸Derived for the weak coupling limit $J\rho(\epsilon_F) \ll 0$. See text later.

²⁹As well as on the temperature dependence of specific heat.

³⁰Commonly enough there are also materials which do not obey this dependence offering instead a linear or a non-integer power law dependence of the resistivity within this range, see also Sec. 1.4.5

compound may be explained by placing $c_{imp} \simeq 1$ in (1.21), which cannot be justified based on the theoretical derivations so far.

There are other examples which demonstrate the inability of the single impurity model to catch even the qualitative behaviour for large c_{imp} . It is even hard to tell with this model what the critical value of c_{imp} should be. This problem may be addressed by, probably, the simplest model used for study of Kondo lattices, namely the *Kondo lattice model* (KLM). Originally, it was derived from the orbitally non-degenerate periodic Anderson model (Schrieffer & Wolff 1966, Doniach 1977) in the form

$$H_{KLM} = \sum_{\mathbf{k}\sigma} \epsilon_{\mathbf{k}} c_{\mathbf{k}\sigma}^\dagger c_{\mathbf{k}\sigma} + \frac{J}{2} \sum_j \sum_{\sigma\sigma'} \mathbf{S}_j \cdot \left(c_{j\sigma}^\dagger \vec{\sigma}_{\sigma\sigma'} c_{j\sigma'} \right) \quad (1.25)$$

where $\vec{\sigma}$ is the vector of the Pauli matrices. The *Kondo coupling* here is

$$J = V^2 \sum_{\mathbf{k}} \left(\frac{\Theta(\epsilon_{\mathbf{k}} - \mu)}{\epsilon_{\mathbf{k}} - \epsilon_f} + \frac{\Theta(\mu - \epsilon_{\mathbf{k}})}{\epsilon_f + U - \epsilon_{\mathbf{k}}} \right) \quad (1.26)$$

where Θ is the step function and V is the hybridization strength as it was defined for (1.23). Hamiltonian (1.25) was systematically investigated by many researchers (for a review see, e.g., (Tsunetsugu, Sigrist *et al.* 1997)) and the main results are briefly compiled next.

What was realized first after a systematic investigation of dilute Kondo systems is that the effects stemming from the non-interacting magnetic moments may survive even at much higher values of c_{imp} . As it was already noted, resistivity and specific heat measurements require a model capable of dealing with $c_{imp} \simeq 1$, i.e., the model has to account for either direct or indirect $f-f$ coupling. As it was estimated above, one may

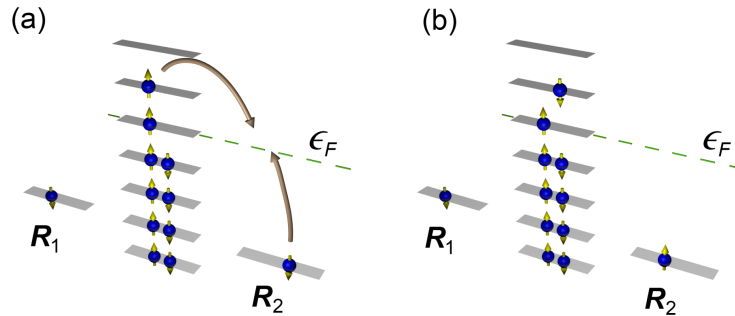


FIGURE 1.16: Schematic diagram of the indirect exchange interaction between localized moments at R_1 and R_2 via overlap with c -band states (shown between the two localized magnetic moments). (a) A c -electron virtually scatters on the R_2 ion which (b) may polarize the Fermi sea via a spin-flip process.

suggest large spatial extension of the Kondo cloud. This means that two neighboring

ions at \mathbf{R}_1 and \mathbf{R}_2 will share many c -electrons (Fig. 1.16) for all practical ranges of impurity concentrations. $c-f$ scattering events (Fig. 1.16(a)) can then polarize the Fermi sea, so that the ion at \mathbf{R}_1 will “feel” the effective potential created by the scattering on the ion at \mathbf{R}_2 (Fig. 1.16(b)). This type of indirect interaction is called Ruderman-Kittel-Kasuya-Yosida (RKKY) interaction. Its Hamiltonian may be derived from (1.25) in the form

$$H_{RKKY} = \sum_{\mathbf{k}\sigma} \epsilon_{\mathbf{k}} \hat{n}_{\mathbf{k}\sigma} + \frac{1}{2} \sum_{i \neq j} J(\mathbf{R}_i - \mathbf{R}_j) \mathbf{S}_i \cdot \mathbf{S}_j \quad (1.27)$$

where $J(\mathbf{R}_i - \mathbf{R}_j)$ is the indirect exchange coupling coefficient between the i -th and j -th magnetic moment. It is the form of the $J(\mathbf{R}_i - \mathbf{R}_j)$ coefficient that now contains the essential physics of systems with large c_{imp} within the KLM. $J(\mathbf{R}_i - \mathbf{R}_j)$ has been analyzed extensively within this model (see, e.g., (Yosida 1957, Kasuya 1956, Kittel & Fong 1987)) and for the free electron dispersion it was shown to be

$$J(R_{ij}) = -\frac{J^2}{\pi^3} \left(\frac{k_F a_0}{2} \right)^6 f(R_{ij}) \quad (1.28)$$

where $R_{ij} = |\mathbf{R}_i - \mathbf{R}_j|$, J is the Kondo coupling of the form (1.26), and $f(R_{ij})$ is a damped periodic function. The most important consequence of (1.28) is the decaying oscillating nature given by $f(R_{ij})$ with a period determined by the c -electrons concentration, the Fermi vector k_F and its symmetry. The RKKY coupling between the localized magnetic f -moments may be both antiferromagnetic and ferromagnetic, depending on the period length of the function $f(R_{ij})$ and the particular crystallographic structure³¹.

Taking into account both, the local Kondo singlet formation driven by J and the magnetic RKKY interaction driven by $J(R_{ij})$, the ground state of a Kondo lattice system is determined by these two counteracting processes. The first process tends to quench the local spins \mathbf{S}_i while the second one tends to align them either anti- or ferromagnetically. And because of the presence of the magic function $f(R_{ij})$ it is not easy to say which one will win under specific conditions. Both processes depend on the Kondo coupling J , but in different ways. This was noted by (Doniach 1977) who gave an estimation of this competition by providing a special phase diagram. The energy scales of the Kondo singlet formation (1.20) and the antiferromagnetic RKKY exchange interactions (1.28) are given by³²

$$\begin{aligned} T_K &\sim \frac{W}{k_B} e^{-1/J\rho(\epsilon_F)} \\ T_{RKKY} &\sim \frac{J^2}{Wk_B} \end{aligned} \quad (1.29)$$

³¹The understanding of the oscillating character of the RKKY interaction resulted in the synthesis of multilayered structures demonstrating the giant magnetoresistance effect by (Dieny, Speriou *et al.* 1991).

³²For derivation of T_{RKKY} see pp. 641-647 in (Fazekas 1999) and references therein.

where W is the bandwidth of the c -band. When both temperatures are plotted as a function of $J\rho(\epsilon_F)$ one obtains a Doniach phase diagram (Fig. 1.17). By applying

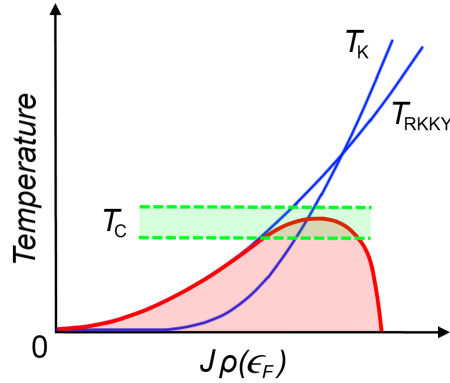


FIGURE 1.17: Doniach phase diagram. The shaded red region is the magnetically ordered (anti- or ferromagnetically) phase in contrast to paramagnetic phase outside this region. T_c corresponds to the highest magnetic ordering (Néel or Curie) temperature where the Kondo screening starts to win over the RKKY interaction with increasing $J\rho(\epsilon_F)$. The two curves cross at $J\rho(\epsilon_F) \sim 1$.

hydrostatic pressure one may tune $\rho(\epsilon_F)$, so it is possible to explore systematically the boundary phases of the Doniach diagram. The *CePdSb* systems is one of the compounds which obey the red line on the Doniach phase diagram (Cornelius, Gangopadhyay *et al.* 1997), showing a fast decrease of its Curie temperature³³ above 10 *GPa*. The zero-temperature right crossing point of the red line in the magnetic phase diagram (Fig. 1.17) is a special point called the *quantum critical point* (QCP).

The Doniach phase diagram has proven to be a valuable theoretical concept for the systematic analysis of Kondo lattices and heavy fermion systems. However, there are still unsolved issues which have to be mentioned. The regime when $T_K > T_{RKKY}$ suggests that the magnetic moments are screened first as the temperature is lowered, which does not allow for the formation of an ordered moment state at even lower temperatures. On the other hand, it was argued that the Kondo cloud compensates the local moment and spreads over many unit cells, thus including many other f -moments. In this view, the other f -moments may see the polarized cloud center with which they still may interact. However, the consequences of such superexchange interactions may differ dramatically from one compound to another, which still lacks an explanation. The Kondo and RKKY terms were derived perturbatively assuming that $J < W$. On the other hand, the downturn of the phase boundary was observed experimentally at unphysically large $J = \mathcal{O}(W)$, which is not justified within the model.

The large interest in the mixed valence and heavy fermion systems resulted in a large amount of data for hundreds of different compounds. The manifold of found ground

³³*CePdSb* orders ferromagnetically below 16 *K*.

states in these materials is large and it is still a challenge to unify the theoretical treatment for these two large material classes. Additionally, there is a subclass of compounds which do not demonstrate a low-temperature Landau Fermi liquid behaviour, the non-Fermi liquid subclass. In any case, using the two theoretical frameworks of the Kondo singlet formation and indirect exchange interaction between the f -moments, it is now clear that the possible ground states of these compounds are very diverse, although a universal treatment is not yet provided.

1.4.4 Magnetism in rare earths

The magnetism in rare earth materials and compounds is very often hard to explain due to the complexity of the effects mentioned above. Nevertheless, there are simple examples helping in the understanding of more sophisticated cases. Most of the rare earth elements have well localized f -moments except Yb and $\alpha-Ce$ ³⁴. The *standard model* used to explain magnetism in rare earths describes elements as integral valence systems, which predetermines its success for most rare earths.

Since the local moments in these metals are well localized, the crystal field splitting of the f -shell is very small, and sometimes negligible. It should also be noted that the strong spin-orbit coupling must be accounted for³⁵. Though the spin of f -electrons, used in (1.27), is not a good quantum number, we can express it via the total angular momentum J , which is conserved, (see p. 663 in (Fazekas 1999)) as

$$\mathbf{S} = (g - 1)\mathbf{J} \quad (1.30)$$

where g is the Lande factor. In the late 1930s Néel and Bommer showed that, within the mean-field theory, the magnetic ordering transition temperature for the rare earth metals should be proportional to

$$\xi = (g - 1)^2 J(J + 1) \quad (1.31)$$

which later became known as the *de Gennes factor*. The applicability of this formula for the magnetic transition temperatures of almost all rare earth metals was confirmed experimentally. In principle, equation (1.31) may be applied to inter-metallic compounds to test how complex their magnetic behaviour is.

³⁴As usually, there are exceptions. The γ - α phase transition in Ce may be initiated either by pressure or by reducing the temperature. The initial FCC crystal symmetry is not disturbed, but the unit cell contracts by 16.5% (Lawson & Tang 1949). This is associated with the rather complex hybridization of the localized f -electrons with the conduction band, which is not fully understood yet.

³⁵It is known that the effective magnetic moment of almost all trivalent rare earth ions calculated using Hund's rules demonstrate very good correspondence with experiments (see p.306 in (Kittel 2005)).

As an example, let us have a look at two compounds, $GdRh_3B_2$ and $CeRh_3B_2$. The $GdRh_3B_2$ compound is an RKKY magnet with localized Gd moments (Ohno, Kishimoto *et al.* 1989), which order ferromagnetically at $T_c = 93 K$. On the other hand $\xi_{Gd} = 15.75$ and $\xi_{Ce} = 0.18$, so for the $CeRh_3B_2$ compound one would expect, by simple scaling, to find $T_c \approx 1 K$ if the Ce -based system featured a similar qualitative behaviour. Instead, experiments show that $CeRh_3B_2$ orders ferromagnetically at the exceptionally high temperature $T_c = 117 K$ (Kitaoka, Kishimoto *et al.* 1985). This fact puts the Ce -based compound fairly far from a simple localized moment picture and strongly suggests an influence of the complex $c-f$ hybridization. Further investigations of this compound revealed a few times larger electronic specific heat coefficient, suggesting that this is a nearly integral valence system (see page 29), which is in accordance with qualitative expectations.

The behaviour of $4f$ electrons is the central point in the topic of magnetism in rare earth metals, which has been investigated in detail for a long time, and a unified understanding has been developed with several exceptions. Yet, even more complicated phenomena were found in many compounds with rare earth metals. Although the physical picture for the rare earth compounds is much less unified at the time of this writing, our knowledges on magnetism in rare earth metals build a good ground for a further understanding of this new physics.

1.4.5 Heavy fermions and non-Fermi liquids

Let us now switch from the magnetism to the electron-electron correlations, inevitably present in rare earth compounds, and see how they modify the electronic properties. It is known that the electronic properties of metals may be described better by allowing small interaction U between the electrons. Investigations of the metallic state by using the Hubbard model

$$H = H_{band} + H_U = \sum_{\mathbf{k}\sigma} \epsilon_{\mathbf{k}} \hat{n}_{\mathbf{k}\sigma} + U \sum_j \hat{n}_{j\uparrow} \hat{n}_{j\downarrow} \quad (1.32)$$

with variational methods (see Chapter 9 in (Fazekas 1999)) for values of U ranging from zero to infinity lead to important results, which should be briefly mentioned here. For the free, non-interacting electron gas (i.e., $U = 0$ in (1.32)) the occupation number $n_{\mathbf{k}}$, which is governed by Fermi-Dirac statistics, is a step function for $T = 0 K$ (blue dashed line in Fig. 1.18), where the step height is $q = 1$. For a non-zero $U > 0$ the height of the Fermi step is reduced to $q < 1$ (red solid line in Fig. 1.18). This may equivalently be described by an increased localization of electrons in real space, which leads to a reduced localization in \mathbf{k} -space. Hence, there is a finite probability for any state in the

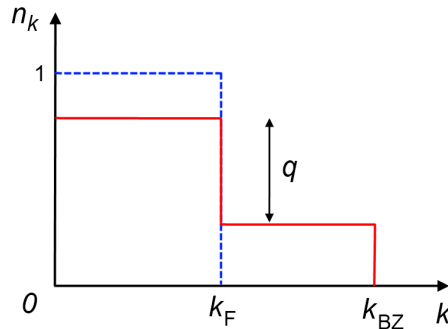


FIGURE 1.18: Fermi distribution function for the free non-interacting electron gas at $T = 0$ (dashed blue line) and for a gas of interacting electrons (red line). n_k is the band occupation number, k_F is the magnitude of the Fermi vector, k_{BZ} is the Brillouin zone boundary, and q is a renormalization factor.

entire Brillouin zone to be occupied even at $T = 0$. The parameter q may be found from (1.32) as

$$q = \begin{cases} 1 - \left(\frac{U}{U_{cr}}\right)^2 & \text{if } 0 \leq U \leq U_{cr} \\ 0 & \text{if } U > U_{cr} \end{cases} \quad (1.33)$$

Here, U_{cr} is some large value of U above which all electrons are localized in real space and delocalized in \mathbf{k} -space. Another important consequence of interactions is that the effective mass of the quasiparticles³⁶ is renormalized, with the renormalization factor q . It is instructive to depict the qualitative behaviour of a correlated metal in terms of q

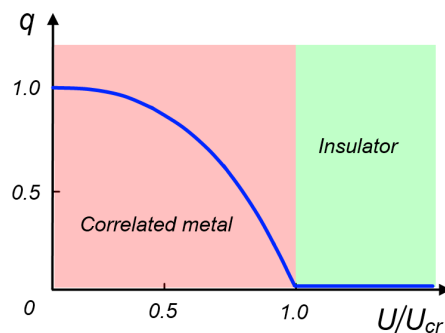


FIGURE 1.19: Renormalization factor q as a function of correlation strength U . Correlated metal behaviour is observed for $U/U_{cr} < 1$ and insulating behaviour is observed at $U/U_{cr} > 1$. The Brinkman-Rice transition from the metallic to the insulating state occurs at $U/U_{cr} = 1$.

and the correlation strength U/U_{cr} (Fig. 1.19). Simple metals like aluminium or sodium lie very close to zero along the U/U_{cr} axis, hence having $q \rightarrow 1$. As the correlations are added, the hopping probability of charge carriers from site to site decreases. This is known as the correlation enhancement of the quasiparticles *effective mass* m^* , which

³⁶From now on the charge carriers are electron excitations and, according to Landau's Fermi-liquid theory, should be treated as quasiparticles.

can be related to the mass of uncorrelated electrons (Mahan 1981) as

$$\frac{m^*}{m} = \frac{1}{q} = \frac{1}{1 - \left(\frac{U}{U_{cr}}\right)^2} \quad \text{for } U < U_{cr} \quad (1.34)$$

According to (1.34), the effective mass of, e.g., sodium, m^* is just by a factor of 1.27 larger than the bare electron mass (Pines & Nozières 1966), while the electron-electron correlations give even smaller enhancement if the electron-phonon correlations are subtracted.

The effective mass of this kind³⁷ can be experimentally determined from the value of the Sommerfeld coefficient γ of the electronic specific heat $C_{el} = \gamma T$, which is also renormalized for correlated, or Fermi-liquid, systems as

$$\frac{\gamma^*}{\gamma} = \frac{m^*}{m} = \frac{1}{q} \quad (1.35)$$

While γ^* requires a careful and precise measurement for simple metals due to its small value³⁸, for the strongly correlated materials, like heavy fermions, these requirements are much relaxed. Typically, the γ^* value for heavy fermions is a good part of or even larger than $1 \text{ J}/(\text{mol K}^2)$, like in the case of $CeAl_3$ for which $\gamma^* = 1.62 \text{ J}/(\text{mol K}^2)$ (Andres, Graebner *et al.* 1975).

The mentioned decrease of the site-to-site hopping probability also results in a band narrowing effect (Chao 1974), such that the band reduces to a single atomic level at $U = U_{cr}$

$$\frac{W^*}{W} \sim \frac{\rho(\epsilon_F)}{\rho^*(\epsilon_F)} \sim q \quad (1.36)$$

This also, in turn, has an effect of lowering the Fermi temperature T_F as

$$\frac{T_F^*}{T_F} \sim \frac{W^*}{W} \sim q \quad (1.37)$$

which, in heavy fermions, may be lower than room temperature. Nevertheless, the room temperature electronic properties of heavy fermions are those of simple metals, since their correlated state develops at much lower temperatures.

³⁷It is one of the possible effective masses in solid state physics and for correctness should be referred to as the *thermal effective mass* due to the source of its derivation.

³⁸The phonon specific heat dominates at high temperatures, but it dies off as βT^2 . Hence, there is a critical temperature T_{el} at which the electronic contribution starts to dominate over the phonon term. Since γ for weakly correlated materials like simple metals is small, e.g., $\gamma_{Cu} = 0.72 \text{ mJ}/(\text{mol K}^2)$, the temperature T_{el} is fairly small as well, which rises the demands on the measurement accuracy.

The Pauli susceptibility is yet another quantity which is renormalized due to a changed density of states $\rho^*(\epsilon_F)$ (Yamada 2004) as $\chi_P = \Delta M/H = \mu_B^2 \rho(\epsilon_F)$, so

$$\chi^* \sim \chi_P \frac{m^*}{m} \quad (1.38)$$

where χ_P is the uncorrelated Pauli susceptibility for $U = 0$.

Another remarkably affected physical quantity is the electrical resistivity. For metals at low temperatures it is usually described well by

$$\rho(T) = \rho_0 + AT^2 \quad (1.39)$$

where ρ_0 is the residual resistivity due to potential scattering and the AT^2 term in the Fermi liquid theory is ascribed to the electron-electron interaction (Abrikosov 1988). In fact, not only simple metals, but also many heavy-fermion systems obey (1.39) despite the strong effective mass renormalization. The effect of this renormalization on the electrical resistivity is quite dramatic due to the following ratio

$$\frac{A^*}{A} \sim \left(\frac{m^*}{m}\right)^2 \quad (1.40)$$

where A^* is the renormalized quantity in (1.39). Typical values of the quadratic term in (1.39) for metals are $\sim 10^{-12} - 10^{-13} \Omega \text{ cm}/K^2$, while for heavy fermions $\sim 10^{-9} \Omega \text{ cm}/K^2$, so that the visibility of the effect is extended up to tens of Kelvin for the latter. Speaking about heavy fermions, their Fermi liquid behaviour is usually testified by defining experimentally the ratios (1.35) and (1.40). The ratio between the resistivity quadratic term and the specific heat linear term $R_{KW} = A/\gamma^2$ is called the *Kadowaki-Woods ratio*. It was shown first by (Rice 1968) that this ratio must hold constant for transition metals ($\sim 0.4 \mu\Omega \text{ cm} (\text{mole } K/mJ)^2$) when electron-electron scattering is accounted for. In the late 1980s (Kadowaki & Woods 1986) showed that for heavy fermions this ratio also holds constant, although, due to the different nature of the correlation effects, it is two orders of magnitude larger ($\sim 10 \mu\Omega \text{ cm} (\text{mole } K/mJ)^2$). Interestingly, (Jacko, Fjærestad *et al.* 2009) also showed that accounting for the sample effective dimensionality, charge carrier concentration, and multi-band effects organic charge-transfer salts, transition-metal oxides, heavy fermions and transition metals can be treated in one universal diagram. Another commonly used empirical relationship for heavy fermions is the *Wilson ratio*, which relates the magnetic susceptibility $\chi^*(T = 0)$ and the enhanced linear specific heat coefficient γ^* . Without going into details, it should be noted that this ratio also holds approximately constant for a huge number of heavy fermion

compounds³⁹.

Many heavy fermion materials are well described by the Fermi liquid theory, which is reflected in the Kadowaki-Woods and the Wilson ratios. Such a behaviour is a result of strong electron-electron interactions in the vicinity of the Fermi surface. One may state that the f -electrons, at least partially, belong to the Fermi sea. Additionally, the strong effective mass renormalization of the charge carriers resonantly enhances the quasiparticle density of states at the Fermi level (Chao 1974).

There are also heavy fermion materials⁴⁰ which do not behave at low temperatures as it is predicted by Landau's Fermi liquid theory. Typically, such a behaviour is tested by measuring the low-temperature dependencies of several thermodynamic quantities. Non-Fermi liquid behaviour was found first in spin-liquid $AuCr$ dilute alloys with different concentrations of Cr (Ford, Babic *et al.* 1973) when their temperature dependence of resistivity unexpectedly followed $\rho - \rho_0 = AT^{3/2}$. The true interest in such systems, however, was generated later after the discovery of a similar behaviour in the heavy fermion compound $Y_{1-x}U_xPd_3$ by (Seaman, Maple *et al.* 1991) and also in the novel high-temperature superconductors. (Seaman *et al.* 1991) reported the temperature dependencies of the electrical resistivity and specific heat to be $\rho(T) \sim T$ and $C \sim \ln T$ below 20 K, in contrast to Fermi liquid theory expectations. Many other compounds with similar behaviour were discovered since then, many of which being Kondo lattice systems. Indeed, the discovery of non-Fermi liquid (NFL) behaviour at very low temperatures showed new essential physics, the detailed causes of which are still under debate (see, e.g., (Stewart 2001, Misra 2008)).

Qualitatively, NFL systems are usually reported to be close to a magnetically ordered state according to a diagram similar to Fig. 1.17 (see, e.g., (Stewart 2001)). For the FL systems, the electron-electron interactions remain temperature independent as well as short ranged in space and time as $T \rightarrow 0$. On the other hand, when a QCP is approached, the interaction coherence length ξ and the interaction time diverge, which is a quantum mechanical effect. Under these circumstances, it is evident that the FL mechanism may be violated (Varma, Nussinov *et al.* 2002, Coleman 1999). Phase boundaries which separate the FL and violated FL regimes were found for several HF materials in their phase diagrams of an order parameter as a function of some controlling parameter for $T = 0$, such as hydrostatic pressure, magnetic field, or doping. Of course, since

³⁹For a more detailed view on both universal relationships in heavy fermions see, e.g., (Continentino 2000).

⁴⁰Although here only strongly correlated f -electron compounds are considered, similar behaviour was found also for high- T_c cuprates, for charge and spin density wave materials, for organic superconductors like κ -BEDT-TTF based compounds, *etc.* Generally, by the time of writing the phenomenon has been well-established, uniting materials with different composition, structure, and correlation strength.

absolute zero temperature is not accessible experimentally, scaling approaches were applied. Additionally, as it was shown by Landau for liquid ${}^3\text{He}$, if the phase transition in a QCP is of the second order type, the QCP should exert its influence on the nearby regions, in particular also for $T > 0$. It is those regions in the phase diagrams that are usually considered as “near to magnetic order” or spin fluctuating regimes (see also (Sachdev 2001, Mathur, Grosche *et al.* 1998, Continentino 1993)).

An alternative approach to the QCP problem is the multi-channel Kondo model. This model was introduced in (Nozières & Blandin 1980), where the authors started with a general form of the Anderson Hamiltonian and considered the behaviour of magnetic impurities taking into account their orbital structure, crystal field and spin-orbit splitting effects. The analysis, however, was performed only for the integer valence regime due to the use of the Schrieffer-Wolff transformation. The essential point of this model is that the $c - f$ scattering process depends on the number of orbital degrees of freedom n of the c -sites and the spin S of the f -site. Then, three relevant scenarios are possible: (1) If $n = 2S$, then the localized moment is fully compensated. For $S = 1/2$ and $n = 1$ the problem reduces to the single impurity Kondo problem or the one-channel regime. (2) If $n < 2S$, then the number of electrons is not sufficient to form the local singlet and the localized moments remain not fully compensated. (3) If $n > 2S$, then the impurity is overcompensated and a critical behaviour, such as a divergence of the Kondo cloud size ξ , is expected. It was shown that regime (3) may explain the NFL behaviour in the case of, e.g., $Y_{1-x}U_xPd_3$.

In other approaches it was shown that the FL regime may be violated by disorder. According to the multi-channel Kondo model, for some combinations of n and S the FL regime becomes unstable. Then, local variations may under- or overcompensate some of the impurities, which would overall result in a modified behaviour of the system (Dobrosavljević, Kirkpatrick *et al.* 1992)

1.4.6 Superconductivity in heavy fermions

Superconductivity, as the word implies, is the dissipationless transport of electrical charge through matter. First it was discovered for several simple metals, but later many more compounds were found also to demonstrate this phenomenon. Although superconductivity was discovered by Kammerling Onnes in 1911, it remained poorly understood for almost 50 years, until the work of (Bardeen, Cooper *et al.* 1957) whose theory became known as the BCS theory. In their theory, the authors suggested two important mechanisms: (a) electrons, which obey Fermi-Dirac statistics, form bosonic quasi-particles, so-called Cooper pairs, and (b) these pairs condense into a ground state

demonstrating macroscopic phase coherence. Moreover, they showed that even a small attractive interaction would be sufficient for forming Cooper pairs and that electron-phonon interactions may cause this attraction.

It is instructive to briefly recall how the onset of superconductivity modifies some of the transport and thermodynamic quantities in simplest cases. The electrical resistivity of a hypothetical superconducting metal is shown in Fig. 1.20(a). Above the SC phase transition temperature T_c the metal behaves like a Fermi liquid, whose resistivity is described as $\rho \approx \rho_0 + AT^2$, as it was already mentioned in Sec. 1.4.5. At $T < T_c$ a coherent state is established, which is reflected in a sudden disappearance of the resistivity. The dashed blue line in this figure would have been established in the absence of superconductivity, while ρ_0 is the residual resistivity caused by crystal imperfections. The low-temperature specific heat above T_c (Fig. 1.20(b)) is dominated by the linear electronic term γ , while the phonon cubic term β is almost irrelevant in this range of temperatures. At T_c the specific heat demonstrates a jump with a subsequent decrease to zero as $C \sim Ae^{-b/k_B T}$, reflecting the presence of the SC gap in the quasiparticles density of states. Again, in the absence of superconductivity the specific heat would have followed the linear dependence towards absolute zero. As it is explained in the BCS theory, the jump has the value $(C_s - C_n)/C_n = 1.43$ (see, e.g., pp. 64-65 in (Tinkham 2004)). Simple superconductors are either Pauli paramagnets, e.g., *Al*, *Ir*, *Mo*, *Nb*,

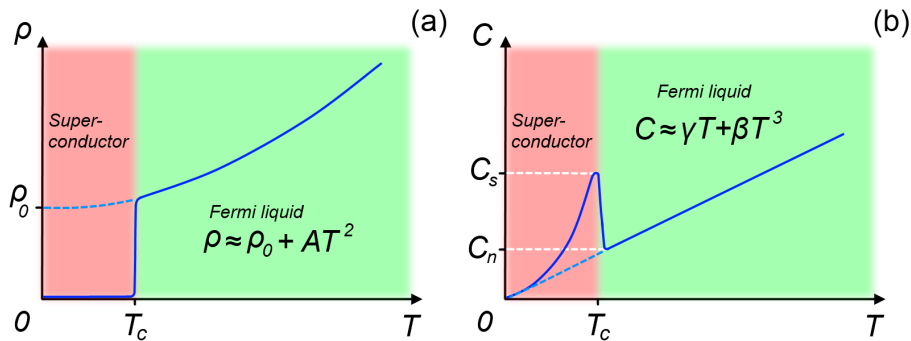


FIGURE 1.20: Low-temperature dependencies of some thermodynamic and transport quantities modified below the superconducting phase transition as expected from the BCS theory. (a) Electrical resistivity and (b) electronic specific heat. In the green shaded regions the metal behaves essentially like a Fermi liquid (also see text).

or diamagnets, e.g., *Cd*, *Hg*, *Ga*, *In*. Thus, in either case the magnetic susceptibility for these materials is temperature independent. Since superconductors demonstrate perfect diamagnetism, i.e., they expel magnetic fields up to some critical value H_c , their susceptibility becomes essentially -1 below the T_c .

The theoretical understanding, which had been much advanced with the appearance of the BCS theory, as well as focused research lead to the discovery of materials with, at first glance, properties incompatible with superconductivity within the BCS framework.

Thus, in 1979, superconductivity was found in $CeCu_2Si_2$, a member of the novel class of heavy fermion compounds at that time (Steglich *et al.* 1979). After the discovery of superconductivity in several U -based heavy fermion compounds and in copper oxides with highly unusual properties it became clear that the understanding of superconductivity was far from being complete. The superconductors which are explained by the BCS theory are usually termed as *conventional*, while the ones which do not obey the BCS theory⁴¹ are called *unconventional*.

When metals demonstrating conventional superconductivity are doped with magnetic impurities in small concentrations the superconductivity is largely suppressed. The small magnetic interactions in this case destroy the SC singlet ground state⁴². In contrast, heavy fermion superconductors, like $CeCu_2Si_2$, are local f -electron compounds with periodic localized moments and strong low-temperature antiferromagnetic on-site interactions. Hence, it was unclear how superconductivity may arise in the presence of the local Kondo singlet state⁴³ driven by antiferromagnetic spin-flip interactions. Moreover, a huge electron effective mass m^* , as was discussed in Sec. 1.4.5, affects the Fermi velocity v_F which becomes comparable to sound velocity v_s in the HF systems. Hence, there is no justification for the BCS derivation, which assumed $v_F \gg v_s$ to be satisfied for the phonon-mediated mechanism of Cooper pair formation. Additionally, heavy quasiparticles form Cooper pairs in HF, in contrast to light metallic ones in BCS superconductors. According to Londons' and Pippard's theories, which are consistent with the BCS theory, superconductors are characterized by several characteristic lengths, such as the magnetic penetration depth $\lambda \propto \sqrt{m^*/n_s}$ and the coherence length (or the smallest size of the wavepacket) $\xi_0 \propto (m^*nT_c)^{-1}$, where m^* is the quasiparticle effective mass, n_s is the density of the SC electrons, and n is the normal electrons' density. For conventional superconductors, like aluminium and tin, $\xi_0 \gg \lambda$. For HF superconductors, however, a direct consequence of large m^* is that the value of λ is much increased while ξ_0 is much reduced. This also leads to small values of the first critical field $H_{c1} \propto 1/\lambda^2$ and large values of the second critical field $H_{c2} \propto 1/\xi_0^2$, which are typically of the order of 10^{-3} and 10 *Tesla*, respectively.⁴⁴

At high temperatures heavy fermions contain free localized spins and thus are Curie paramagnets. Their effective magnetic moment is approximately given by Hund's rules. As we discussed earlier, at low temperatures, the localized moments get quenched due

⁴¹It should be said that this distinction is by far not strict and the BCS framework is widely used for unconventional superconductors. It is rather the exact coupling mechanisms that remain unknown for the unconventional superconductors.

⁴²Two electrons with opposite spins S form a Cooper pair so that its total spin $S_C = 0$.

⁴³Superconductivity was not found in the parent compound $LaCu_2Si_2$ although the La^{3+} ion has a non-magnetic configuration $4f^0$. Moreover, even a few percent substitution $Ce^{3+} \rightarrow La^{3+}$ in $CeCu_2Si_2$ suppresses SC.

⁴⁴All HF superconductors are II type superconductors.

to the peculiar hybridization between the localized f - and conduction c -states. As a result, the magnetic susceptibility saturates at a constant value. This value, however, is much larger than the Pauli susceptibility of simple metals with the enhancement factor given by (1.38).

Another observed deviation of the HF superconducting properties from the BCS theory is the symmetry of the SC order parameter⁴⁵.

Conventional BCS superconductors demonstrate a well-understood behaviour in their thermodynamic and electronic transport properties at variable temperatures around the SC transition. The HF superconductors, in contrast, very often deviate from the BCS behaviour. For example, the power law (1.39) often demonstrates exponents from as small as 0.3 for U_2Pt_2In to as large as 3 for $CeIn_3$ and is very often close to unity, as for $CeCoIn_5$ (Stewart 2001). The specific heat often demonstrates either power law or logarithmic behaviour and the Pauli susceptibility is not always temperature independent even at the lowest temperatures.

1.5 Quantum mechanical tunneling

Quantum mechanical electron tunneling effects were used in this work for studying the SC state of $CeCoIn_5$ as well as of some of its normal state properties. This section first briefly introduces the physical background for the quantum mechanical tunneling. In the main part, the tunneling phenomenon is reviewed for quasiparticle and Cooper pair tunneling between metals and superconductors.

1.5.1 The tunneling phenomenon

The tunneling phenomenon is perhaps the most often mentioned phenomenon in quantum physics, after the energy quantization principle. As it follows from its name, there is a finite probability for a quantum mechanical object to escape a potential energy trap if the energy potential walls are not infinitely high and thick. According to the de Broglie fundamental hypothesis (de Broglie 1923), formulated in the early 1920s, every freely moving particle can be associated with a characteristic plane wave of the form $\psi = e^{i\mathbf{k}\mathbf{r}}$. Later, when the Schrödinger equation was introduced for these wave states, the solutions of the equation were shown to be smooth at the edge of the potential

⁴⁵As an order parameter in superconductors one uses the value of the coupling strength of electrons into Cooper pairs 2Δ . Generally, 2Δ is a function of the wave vector \mathbf{k} , but it is independent of \mathbf{k} in the BCS theory in the case of phonon coupling, which is observed in the isotropic properties of the SC gap in many \mathbf{k} -sensitive experiments.

barrier $U(x)$ for the electron reflection problem. When the particle wave approaches the potential barrier $U(x)$, the probability amplitude $\psi^*\psi$ of finding this particle decays exponentially within the barrier. If this amplitude is non-zero at the opposite barrier side, then the probability of tunneling is also non-zero. A simple measure of this process is the transmission coefficient $D = j_L/j_R$, where j_i are given by

$$j_i = \frac{\hbar}{2mi} \left(\psi_i^*(x) \frac{d\psi_i(x)}{dx} - \psi_i(x) \frac{d\psi_i^*(x)}{dx} \right) \quad (1.41)$$

where ψ_i are the left ψ_L and the right ψ_R side wave functions. Taking into account the potential barrier shape and solving the Schrödinger equation, the transmission coefficient as a function of the particle energy can be shown to be of the form

$$D(E) = \exp \left[-\frac{2}{\hbar} \int_{x_1}^{x_2} \sqrt{2m(U(x) - E)} dx \right] \quad (1.42)$$

where m is the particle mass, x_1, x_2 are the barrier limits, and $U(x)$ is the potential barrier shape. This solution satisfies the energy and the wave vector conservation laws.

A fast success of the tunneling theory was the explanation of the anomalously high escaping rate in radioactive decay processes (Gamow 1928), the autoionization of atomic hydrogen (Oppenheimer 1928) and the electron emission from cold metals (Fowler & Nordheim 1928). In all these cases a simple solution like Eq. (1.42) yielded excellent agreement with experiment. Later, tunneling theory was applied to problems in solid state physics. The anomalous temperature independent contact resistance between two metals was explained by Frenkel in 1930 in terms of electron tunneling through a vacuum-like insulator. The success of the tunneling theory during the 1920s had a strong influence on semiconductor physics in the following several decades. It was also applied to explain the operation of solid state current rectifying diodes. In the 1950s (Esaki 1958) first observed the effect of negative resistance in a semiconductor diode, which was also in perfect agreement with the tunneling theory. Transport measurements on the Esaki diode demonstrated a spectroscopic nature of the tunneling characteristics, revealing at least approximately the electronic density of states in *Si*. Later, electron tunneling also proved to be an efficient instrument for investigating superconductivity.

1.5.2 Tunneling in the solid state

After the successful introduction of the tunneling phenomenon into semiconductor physics, its usage was also extended to superconductors and normal metals. First results on quasiparticle tunneling in superconductors were reported by Giaever (Giaever 1960). He prepared a planar tunneling diode *Al-Al₂O₃-Pb* and measured the SC energy gap of

lead at 1.6 K, which was found to be in good agreement with the, new at that time, BCS theory. Two years later Bardeen (Bardeen 1962) used Fermi's Golden Rule⁴⁶ and Oppenheimer's perturbation theory to explain Giaever's results. Different treatments based on Bardeen's calculations became known as *transfer Hamiltonian* calculations. The easiest way to approach Bardeen's derivation is probably to use Oppenheimer's perturbation theory.

Consider two independent metals whose individual electronic states are described by two independent Hamiltonians H^L and H^R . Then their time-independent Schrödinger equations will be written as

$$\begin{aligned} H^L|\psi\rangle &= E^L|\psi\rangle \\ H^R|\phi\rangle &= E^R|\phi\rangle \end{aligned} \quad (1.43)$$

For the tunneling of electrons between these metals to occur we will allow for a weak connection between them, which is described by a small perturbation term H' . Then, the total Hamiltonian of the system metal-insulator-metal will read $H = H^L + H^R + H'$. Let us assume that an electron tunnels from the left metal state $|\psi\rangle$ to one of the multiple right metal states $|\phi_k\rangle$. Hence, we are interested in the time evolution of this electronic state, which may be written as

$$|\psi(t)\rangle = a(t)e^{-itE^L/\hbar}|\psi\rangle + \sum_k a_k(t)|\phi_k\rangle \quad (1.44)$$

so that an electron from the state $|\psi\rangle$ continuously evolves into the states of the Hamiltonian H^R . The knowledge of the coefficients $a_k(t)$ will allow us to obtain the transition rate of electrons through the barrier. To calculate these coefficients, one has to insert (1.44) into the time-dependent Schrödinger equation

$$i\hbar\frac{\partial}{\partial t}|\psi(t)\rangle = H|\psi(t)\rangle \quad (1.45)$$

After simple manipulations on both sides in (1.45) and by making use of (1.43), we obtain

$$i\hbar\sum_k\frac{d}{dt}a_k(t)|\phi_k\rangle = e^{-itE^L/\hbar}(H - H^L)|\psi\rangle + \sum_k a_k(t)(E_k^R|\phi_k\rangle + (H - H^R)|\phi_k\rangle) \quad (1.46)$$

Equation (1.46) may be simplified by multiplying its both sides by $\langle\phi_j|$ and integrating over the whole phase space, which leads to

$$i\hbar\frac{d}{dt}a_j(t) = e^{-itE^L/\hbar}\langle\phi_j|H - H^L|\psi\rangle + E_j^R a_j(t) + \sum_k a_k(t)\langle\phi_j|H - H^R|\phi_k\rangle \quad (1.47)$$

⁴⁶The Fermi Golden Rule was useful as it explicitly contains the electronic density of states.

For solving (1.47) we assume that $a_k(0) = 0$ and remain small for a short time. Then, the last right-hand side term would be equal to zero during this time, but we keep the second term. For short times the solutions of (1.47) are

$$a_j(t) = \frac{e^{-itE^L/\hbar} - e^{-itE_j^R/\hbar}}{E^L - E_j^R} \langle \phi_j | H - H^L | \psi \rangle \quad (1.48)$$

while the transition probability is

$$|a_j(t)|^2 = \frac{4 \sin^2(t(E_j^R - E^L)/2\hbar)}{(E_j^R - E^L)^2} |\langle \phi_j | H - H^L | \psi \rangle|^2 \quad (1.49)$$

In order to assure that (1.49) is the main part of the transition probability, one has to further assume that the eigenfunctions of both Hamiltonians H^L and H^R are nearly orthogonal⁴⁷ so that $\langle \phi_j | \psi \rangle e^{-itE^L/\hbar} \ll a_j(t)$. Eventually, the total transition rate is found by summing (1.49) over all j and differentiating with respect to time

$$\frac{d}{dt} \sum_j |a_j(t)|^2 = 4 \frac{d}{dt} \sum_j \frac{\sin^2(t(E_j^R - E^L)/2\hbar)}{(E_j^R - E^L)^2} |\langle \phi_j | H - H^L | \psi \rangle|^2 \quad (1.50)$$

Equation (1.50) gives the total number of transitions per unit of time, i.e., the transition rate at which electrons will tunnel through the barrier, driven by the perturbation Hamiltonian H' . The form of this transition is identical to that of the Fermi Golden Rule, which was very helpful for Bardeen since one can easily express it in terms of the electronic density of states ρ^R of the Hamiltonian H^R .

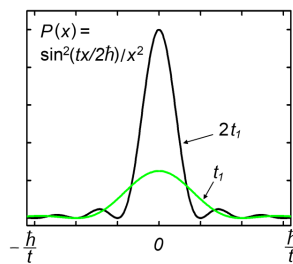


FIGURE 1.21: Behaviour of the function $P(x) = \sin^2(tx/2\hbar)/x^2$ for several times t , which demonstrates strong peaking around zero as time increases.

The density of states at energy E is defined as $\rho^R(E) = dn/dE$, where dn is the number of states within an energy interval dE . The function $P(x) = \sin^2(tx/2\hbar)/x^2$, which appears in (1.50), is strongly peaked around zero (see Fig. 1.21). When integrating $P(x)$, the most contributing part is in the energy range⁴⁸ within \hbar/t around $E_j^R - E^L = 0$, which decreases with increasing t . It is then convenient to assume that states E_j^R are evenly distributed within the small interval dE so that the summation on the right-hand side in (1.50) may be replaced by integration. Additionally, we assume that the matrix element $|\langle \phi_j | H - H^L | \psi \rangle|^2 = M(\psi)^2$ does not depend on energy within $\pm\hbar/t$ around $E^R = E^L$ so that it can be taken

⁴⁷Formally, the transition amplitude into a state $|\phi_j\rangle$ according to (1.44) is $\langle \phi_j | \psi(t) \rangle = a(t) \langle \phi_j | \psi \rangle e^{-itE^L/\hbar} + a_j(t)$ where the second term was neglected in (1.49).

⁴⁸In our case the value of energy difference $E_j^R - E^L$.

out of the integral. Taking into account these assumptions, the right-hand side of (1.50) will read

$$\int_{-\infty}^{\infty} P(E) M(\psi)^2 dn = M(\psi)^2 \rho^R(E^L) \int_{-\infty}^{\infty} P(E) dE = M(\psi)^2 \rho^R(E^L) \frac{\pi t}{2\hbar} \quad (1.51)$$

and substituting into (1.50) will result

$$\frac{d}{dt} \sum_j |a_j(t)|^2 = M(\psi)^2 \rho^R(E^L) \frac{2\pi}{\hbar} \quad (1.52)$$

which is the transition rate from the electron's single level on the left to the continuum of states of H^R around energy E^L on the right if the latter are unoccupied. Apparently, in

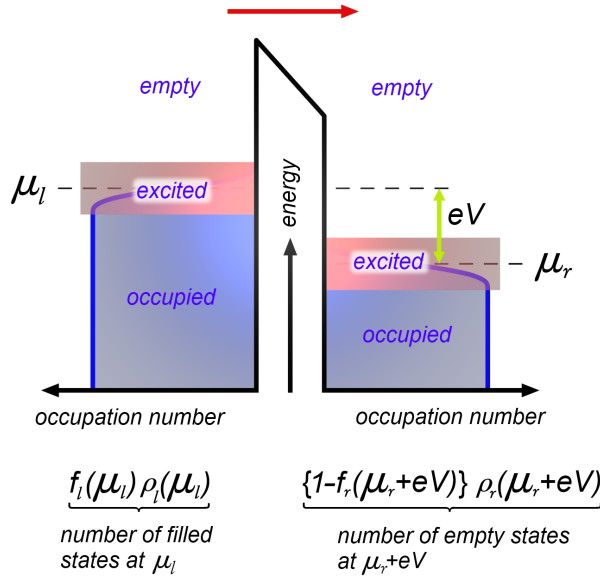


FIGURE 1.22: Schematic representation of quasiparticle tunneling between two metals at a finite temperature through a barrier at an applied voltage V , where $f(E) = [\exp\{(E - \epsilon_F)/k_B T\} + 1]^{-1}$ is the Fermi-Dirac distribution function, ρ is the density of electronic states and μ is the chemical potential. It is assumed that $\mu_r = \mu_l - eV$. See text for details.

equilibrium the net current of electrons through the barrier is zero, which means that the number of transitions left-to-right and right-to-left are equal and (1.52) may be applied symmetrically to both sides. For practical applications we are interested in the value of the current at a given bias voltage applied across the barrier, as shown in Fig. 1.22. Here, electrons tunnel from left to right. The number of states available for an electron on the right side at energy $\mu_r + eV$ and the number of occupied electronic states on the left side are given in the figure. Here, the Fermi-Dirac distribution function accounts for the appropriate statistics of electrons as well as for temperature excitations, while the investigated electronic structure is represented by the electronic density of states ρ . The total transition rate will be proportional to the transition rate (1.52), the number

of occupied states on the left, and the probability of finding an empty state at energy $\mu_r + eV$ on the right. The tunneling current is just the total rate multiplied by the electron charge e

$$I(V) = \frac{2\pi e}{\hbar} f_l(\mu_l) \rho_l(\mu_l) [1 - f_r(\mu_r + eV)] \rho_r(\mu_r + eV) M(\psi)^2 \quad (1.53)$$

The expression (1.53) is a handy approximation which tells that the current through the tunneling barrier will be a function of two electronic densities of state, one of which is presumably known, the temperature, which introduces smearing unless $kT \ll eV$, and some unknown coefficient $M(\psi)^2$, which is taken as a constant. Hence, by investigating tunneling currents at variable voltages one is able to probe the unknown electronic structure at different energies.

1.5.3 Josephson effect

Shortly after Bardeen's description of quasiparticle tunneling, a new interest in tunneling with superconductors emerged. First, the tunneling Hamiltonian was derived for an S - I - N junction by Bardeen. Just at the very same time, a young graduate student, Brian Josephson, got interested in the problem of tunneling between two superconductors. By means of perturbation Hamiltonian calculations⁴⁹ (Josephson 1962) Josephson found that there is a non-vanishing term for the current even without a voltage drop across the tunneling barrier, which was later experimentally confirmed. He considered two weakly connected superconductors⁵⁰ whose Ginzburg-Landau complex order parameters are related as

$$i\hbar \frac{\partial \psi_l}{\partial t} = U_l \psi_l + K \psi_r \quad (1.54)$$

$$i\hbar \frac{\partial \psi_r}{\partial t} = U_r \psi_r + K \psi_l$$

where K is the coupling amplitude. If $K = 0$, then (1.54) describes just two independent superconductors with respective energies U_i . If, however, a voltage V is applied between the two superconductors, their energies will differ by $U_l - U_r = q_c V$. Putting zero energy in the middle of this difference, we have $U_l = q_c V/2$ and $U_r = -q_c V/2$, where $q_c = 2e$. The complex order parameter for both superconductors is taken as

$$\begin{aligned} \psi_l &= \sqrt{\rho_l} e^{i\theta_l} \\ \psi_r &= \sqrt{\rho_r} e^{i\theta_r} \end{aligned} \quad (1.55)$$

⁴⁹An important drawback of the simple transfer Hamiltonian calculations was the complete ignorance of local effects, which may take place within the tunneling barrier or a weak link. This difficulty, however, was overcome later by treating the electrons' propagation through the barrier using Green's functions.

⁵⁰See also (Feynman, Leighton *et al.* 1965) and (Josephson 1964).

where ρ are the densities of the SC electrons in the left and right electrodes⁵¹. Substituting (1.55) into (1.54) and defining $\delta = (\theta_r - \theta_l)$ one obtains four coupled differential equations

$$\begin{aligned}\dot{\rho}_l &= \frac{2}{\hbar} K \sqrt{\rho_l \rho_r} \sin \delta \\ \dot{\rho}_r &= -\frac{2}{\hbar} K \sqrt{\rho_l \rho_r} \sin \delta \\ \dot{\theta}_l &= \frac{K}{\hbar} K \sqrt{\frac{\rho_l}{\rho_r}} \cos \delta - \frac{q_c V}{2\hbar} \\ \dot{\theta}_r &= \frac{K}{\hbar} K \sqrt{\frac{\rho_l}{\rho_r}} \cos \delta + \frac{q_c V}{2\hbar}\end{aligned}\tag{1.56}$$

The first two equations in (1.56) tell us that as the current flows the right electrode will be charged by the left one with the rate $\dot{\rho}_l = -\dot{\rho}_r$. In reality, as long as both electrodes are connected to battery terminals both densities ρ_l and ρ_r will remain unchanged as the flowing current will keep potentials constant. Hence, the superconducting DC current across the barrier will be

$$J = \frac{2K}{\hbar} \sqrt{\rho_l \rho_r} \sin \delta\tag{1.57}$$

Since ρ_l and ρ_r remain essentially the same, say ρ_0 , we may introduce some specific current $J_0 = 2K\rho_0/\hbar$ and (1.57) will then read

$$J = J_0 \sin \delta\tag{1.58}$$

which is the first Josephson relation. Now, we may look at the phase difference δ . Using the last two equations in (1.56) we may write

$$\dot{\delta} = \dot{\theta}_l - \dot{\theta}_r = \frac{q_c V}{\hbar}\tag{1.59}$$

or, integrating (1.59),

$$\delta(t) = \delta_0 + \frac{q_c}{\hbar} \int_0^t V(t') dt'\tag{1.60}$$

where δ_0 is the initial phase difference at $t = 0$. Thus, equations (1.58) and (1.60) are essential results of Josephson's work. They mean that, according to (1.60) having zero voltage applied to the tunneling junction the phase difference between the Ginzburg-Landau order parameters of the two superconductors $\delta(t) = \delta_0$ is time independent. Therefore, according to (1.58) we may have a supercurrent flowing between the two superconductors which nevertheless cannot exceed the value of J_0 , the *DC Josephson effect*. That is, applying a voltage V_0 across the junction according to (1.60), the phase

⁵¹According to the Ginzburg-Landau theory, $|\psi|^2$ describes the density of the superconducting electrons.

difference $\delta(t) = \delta_0 + V_0 q_c t / \hbar$ is not time independent any more. Thus, the total current start oscillating with a large frequency according to (1.58), the *AC Josephson effect*.

It should be noted that for currents above J_0 the two superconductors' bosonic levels⁵² will differ by the energy $\Delta E = 2eV$ (remembering that $q_c = 2e$). Hence, tunneling can now take place only as a virtual process. Subsequently, such processes are associated with emitting coherent photons with frequency⁵³ $\nu = \Delta E / h = 2eV / h$.

An effect opposite to the AC Josephson effect is also possible. It was observed by (Shapiro 1963) in experiments on exposing an *S-I-S* tunneling junction to microwave radiation. It turned out that at frequencies which are multiples of $\nu = 2eV / h$ the *V-I* characteristics have a step-like shape signaling absorption at specific energies.

For several years after the discovery of Josephson's effects they were mainly studied in the context of the tunneling through a barrier. However, the quantum mechanical nature of the effects drove interest to structures where the coupling between two superconductors was not tunneling in nature. As early as in 1964 (Anderson & Dayem 1964) Shapiro steps were observed in a double wedge weak link structure, pointing to the AC Josephson effect. Many theoretical works, such as (Waldram 1976, Likharev 1979, Lindelof 1981) followed on aiming to generalize the discovered complex nature of the Josephson effects in weak links.

1.6 Quantum interference

Though not being tunneling in nature, quantum interference effects are another manifestation of the particle-wave duality that often remarkably modify the electronic transport in solid state. Here, we will consider interference effects in both the superconducting and the normal state.

1.6.1 Cooper pair interference

It was observed in 1961 by (Deaver & Fairbank 1961) and independently by (Doll & Näbauer 1961) that the magnetic field produced by a "frozen"⁵⁴ superconducting current circulating in a loop is quantized. This quantization of the magnetic flux Φ had already

⁵²Superconductors may be viewed either in semiconductor or in bosonic representation; here, the latter is more illustrative.

⁵³Since 1992 this effect has been used for a voltage reference with accuracy up to 1 *ppb*, see, e.g., (Hamilton 2000).

⁵⁴As a direct consequence of the fact that the rate of change of the magnetic flux $\partial\Phi/\partial t$ is equal to the line integral of the electric field \mathbf{E} around a loop, i.e., $\partial\Phi/\partial t = \oint \mathbf{E} \cdot d\mathbf{s}$, which is zero in a superconductor, that circulating and persistent currents can easily be excited in superconducting loop structures.

been predicted by London in 1950, although the measurements revealed exactly half of the expected value. Even though the flux quantization has seemingly nothing to do with interference, it is exactly the instrument which allows us to probe such effects.

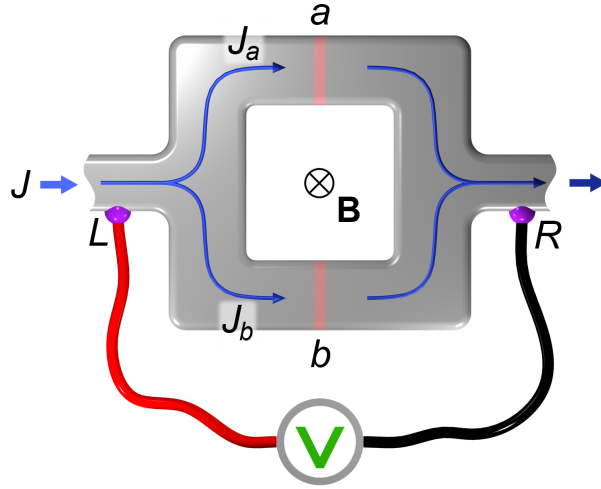


FIGURE 1.23: A schematic view of a superconducting quantum interference device (SQUID).

Consider a superconducting loop consisting of two equal current paths a and b with Josephson junctions in each (Fig. 1.23) and a magnetic field \mathbf{B} applied perpendicular to the loop plane. The current of Cooper pairs is flowing from left to right and the superconducting phase difference δ is measured between points L and R . Of course, δ does not depend on which path it is traced on, so that we may write

$$\delta = \delta_a + \frac{2e}{\hbar} \int_a \mathbf{A} \cdot d\mathbf{s} \quad (1.61)$$

$$\delta = \delta_b + \frac{2e}{\hbar} \int_b \mathbf{A} \cdot d\mathbf{s}$$

where e is the single electron charge, δ_a and δ_b are the phase differences introduced by the respective Josephson junctions. The second term in both equations is the phase accumulated by each path due to the presence of the magnetic field, characterized by the vector potential \mathbf{A} . Subtracting the first equation from the second in (1.61) gives the phase difference between the two Josephson junctions

$$\delta_a - \delta_b = \frac{2e}{\hbar} \oint_{\Gamma} \mathbf{A} \cdot d\mathbf{s} = \frac{2e}{\hbar} \Phi \quad (1.62)$$

where Φ is the magnetic flux through the loop area and integration is performed over the complete loop area. According to (1.62), we may also represent both δ_a and δ_b as

sums of some initial phase δ_0 plus some flux-induced phase

$$\delta_a = \delta_0 - \frac{e}{\hbar}\Phi, \quad \delta_b = \delta_0 + \frac{e}{\hbar}\Phi \quad (1.63)$$

But according to (1.58) the total current $J_a + J_b$ may be written using (1.63) as

$$\begin{aligned} J &= J_a + J_b \\ &= J_0 \left\{ \sin\left(\delta_0 - \frac{e}{\hbar}\Phi\right) + \sin\left(\delta_0 + \frac{e}{\hbar}\Phi\right) \right\} \\ &= J_0 \sin\delta_0 \cos\frac{e\Phi}{\hbar} \end{aligned} \quad (1.64)$$

where J_0 is the largest DC supercurrent, which may flow through both Josephson junctions. The term $\sin\delta_0$ is not known and may be thought of as a constant during measurements. Since the supercurrent may change only within $\{0, J_0\}$ we may rewrite (1.64) taking $\sin\delta_0 = 1$

$$J = J_0 \left| \cos\frac{e\Phi}{\hbar} \right| \quad (1.65)$$

What matters to us here is that the maximum total DC current J through both loop paths will be easily “tuned” by the external flux. Moreover, equation (1.65) says that the current will have its maxima at quantized values of Φ

$$\Phi = n \frac{\pi\hbar}{e} \quad (1.66)$$

where n is an integer number. This is an interesting consequence of the Josephson effect, which immediately after the prediction made by Josephson tempted scientists to verify the effect. The interference pattern following from (1.65) was experimentally observed by (Jaklevic, Lambe *et al.* 1964) on a tin loop, where the periodicity (1.66) was confirmed with good accuracy.

It has to be added that SQUID-based interferometry has important applications in both fundamental science and technology. For scientific studies, it allows for a direct access to the macroscopic wave function of electrons in their condensed state. This means that unconventional superconductivity, where such a wave function may have a non-isotropic symmetry, can be in principal investigated by this type of interferometry. In technological applications, SQUIDS are exclusively used for sensing low magnetic fields. These devices may be designed for such extreme sensitivities that even the magnetic field created by a single electron moving with a speed typical for metals can be detected⁵⁵ at a distance slightly less than 1 mm!

⁵⁵For this, however, one needs to make long averaging of the order of a few days. See “Gravity Probe B: Exploring Einstein’s Universe with Gyroscopes” at <http://einstein.stanford.edu/>

1.6.2 Weak localization and single electron interference

The interference effects appearing in the superconducting electronic state are probably the most prominent of the known electronic interference effects. However, under some circumstances, interference corrections also have to be made for the normal state. Due to their immediate connection, electronic interference most significantly affects the electronic transport properties, although the electronic DOS and the electronic specific heat are also modified (Altshuler & Aronov 1985). There are several effects of electronic interference which we review in this paragraph: single electron interference (or weak localization) and the inter-electron interference (or Aronov-Altshuler-Spivak (AAS) effect)⁵⁶.

Typically, weak localization effects are noticeable in dirty metals, that is, in the presence of strong disorder. There, electronic scattering on defects⁵⁷ may be either *elastic* or *inelastic*. In a strongly inelastic scattering event, the electron's wave function loses its phase memory. In the case of elastic scattering⁵⁸, the electron preserves its phase leaving a negligible trace on the crystal's degrees of freedom. It turns out that for dirty metals at low temperatures $\tau_\phi \gg \tau_{el}$, where τ_ϕ is the *phase relaxation time* while τ_{el} is the expected time between two subsequent elastic scatterings or the *collision time*. In this case, the approximate distance which an electron travels from a starting point still preserving its phase⁵⁹ is

$$\Delta r_\phi = l \sqrt{\frac{\tau_\phi}{\tau_{el}} \langle \cos^2 \theta \rangle} = v_F \sqrt{\frac{\tau_{el} \tau_\phi}{2}} = \sqrt{D \tau_\phi} \quad (1.67)$$

where

$$\langle \cos^2 \theta \rangle = \int_{-\pi}^{\pi} \frac{\cos^2 \theta}{2\pi} d\theta = \frac{1}{2}$$

and $l = \tau_{el} v_F$ is the electron's *mean free path* or the distance between two subsequent elastic collisions, $D = v_F^2 \tau_{el} / 2$ is the diffusion coefficient, and the cosine accounts for

⁵⁶The Aharonov-Bohm (AB) effect is also often referred to as an inter-electron interference effect, which should not be mixed with the AAS effect. The AB effect is the quantum mechanical interference between two coherent electronic waves that are modified not by the classical electromagnetic field, which can be precisely confined, but by the vector potential of the magnetic field, which was viewed as a pure mathematical trick in the early years of quantum mechanics. The AAS effect, in contrast, is related with the transport properties of solids and their electronic density of states in the presence of electronic interference effects.

⁵⁷At a typical Fermi velocity of electrons in metals, both the impurities and the ion deflections from their averaged positions may be considered as static defects.

⁵⁸In real crystals almost any scattering of an electron is associated with an energy transfer ε . By an elastic scattering we will understand here a quasi-elastic scattering with its characteristic scattering time τ so that $\varepsilon \tau \ll \hbar$. In this case, due to the uncertainty principle, one cannot know whether the electron's state was changed or not.

⁵⁹The square root in (1.67) appears due to a random walk or a diffusion process, which is proportional to $\sqrt{\text{time-of-travel}}$. See also Appendix C.

the scattering of electrons in random directions. It is the distance (1.67) or the volume $\propto \Delta r_\phi^3$ where the interference effects might take place.

The inter-electron interference effects also rely upon the electronic phase preservation but now the difference between the phases of two interfering electrons is being preserved. In this type of interference, two electrons scatter at a time $t = 0$ diffusing away in a random walk manner and may scatter again later. If their phases are not considerably changed during this diffusive motion, they may on average interfere constructively. In the case of some uncorrelated phase relaxation processes on the electrons' individual interstitial paths, the interference amplitude will be lowered.

Of course, for an improved description of the electron transport in metals at low temperatures the interference effects must be accounted for, i.e., the semiclassical Boltzmann transport equation (see, e.g., (Datta 1989)) should be corrected. But what would be the influence of these interference effects in the strongly correlated heavy-fermion state? There is no unambiguous answer to this question so far, though all the characteristic electronic times, which directly appear in the quantum interference effects, also play an essential role in the heavy-fermion state and are of great interest. For this reason, let us briefly consider the mentioned quantum interference effects and their possible implications for heavy fermions.

Weak localization

The conductivity of clean metals may be described within the Drude model where electrons are taken to be rigid particles. The applicability of this model relies upon the condition $\lambda_F \ll l$, where l is the mean free path and $\lambda_F = 2\pi/k_F$ is the wavelength of an electron at the Fermi level. In dirty metals, however, l decreases and when $\lambda_F \geq l$ the Drude model is not applicable. At strong enough disorder, electrons become fully localized so that the metal undergoes the Anderson metal-insulator transition⁶⁰. Let us consider here the clean case, i.e., $\lambda_F \ll l$. An electron in a clean metal may travel from point A to B via a number of different paths (Fig. 1.24). The total probability to find

⁶⁰The Anderson metal-insulator transition is considered for a non-interacting electron gas in contrast to the Mott metal-insulator transition caused by strong electron correlations mentioned on p. 37. Strictly speaking, the Anderson transition is a critical phenomenon only in three dimensions, while the lower dimensions do not undergo a phase transition. At $T = 0$ K in three dimensions certain structural disorder is required to fully localize single electron states, i.e., to reach the mobility edge. In smaller dimensions, in contrast, extended states only exist on a perfect lattice, i.e., even small disorder or a finite sample size cause localization of the single electron states at $T = 0$. For details see, e.g., (Thouless 1974, Lagendijk, Van Tiggelen *et al.* 2009, Gantmakher 2005) and references therein.

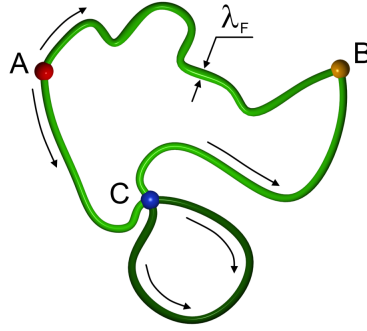


FIGURE 1.24: Several possible paths from A to B may include self-crossing ones, when an electron visits C twice.

a quantum mechanical particle in B for such a travel is

$$p = \left| \sum_i \phi_i \right|^2 = \sum_i |\phi_i|^2 + \sum_{i \neq j} \phi_i \phi_j^* \quad (1.68)$$

where ϕ_i is the wave function of the particle moving along the i -th path. Here, the first term is the classical probability and the second term is the interference term between different paths. For most path pairs due to their different lengths, and hence the arriving phases, the second term in (1.68) is averaged to zero. However, as it is shown in Fig. 1.24 in dark green, there are also paths with self-crossing. On such looped paths the electron would have to travel from C to C , the total probability of this process being also given by (1.68). Among all the possibilities for the electron to pass via such a loop, there will be of course those corresponding to the electron's motion in opposite directions, which is shown by arrows within the loop in Fig. 1.24. While for the rest of the paths the second term in (1.68) will again be averaged to zero, for these two complementary paths it will be not. Since for these paths the lengths as well as the electron's phases are identical, the probability to find the electron in C will be doubled $|\phi_i|^2 + |\phi_j|^2 + 2\Re\phi_i\phi_j = 4|\phi|^2$, as compared to a classical particle, for which in any case it is $2|\phi|^2$ (see also Appendix C). As a consequence, this increase of the time the electron spends at C leads to a decrease of the time it spends at either A or B , which is called *weak localization*. This can be immediately used for an estimation of corrections to the conductivity of metals as follows. The electron's coordinate in a crystal is as precise as its Fermi wavelength λ_F . During time t , it travels through random walk within a volume $(Dt)^{3/2}$ (see Eq. (1.67)). The total volume (the volume of the green pipes in Fig. 1.24) that the electron visits in time t is $v_F t \lambda_F^2$. Hence, the probability for the electron to revisit point C in time dt is $v_F dt \lambda_F^2 / (Dt)^{3/2}$. Eventually, corrections to the conductance in a three dimensional

sample⁶¹ will be

$$\frac{\Delta\sigma}{\sigma} = -v_F\lambda_F^2 \int_{\tau_{el}}^{\tau_\phi} \frac{dt}{(Dt)^{3/2}} = -\frac{v_F\lambda_F^2}{D^{3/2}} \left(\frac{1}{\sqrt{\tau_{el}}} - \frac{1}{\sqrt{\tau_\phi}} \right) \quad (1.69)$$

where τ_ϕ is the time in which the electron's wave function preserves its coherence or the shortest dephasing time in the system. The physical meaning of τ_ϕ can be inferred from the following considerations (see, e.g., p. 10 in (Altshuler & Aronov 1985)). Let the average electron energy transfer in the electron-phonon quasi-elastic collisions be ω and the collision rate be $1/\tau_{ph}$. Then, the electron's energy change in time t will be of the order of

$$\Delta\varepsilon(t) \simeq \omega\sqrt{t/\tau_{ph}} \quad (1.70)$$

and the phase change⁶² will be of the order of

$$\Delta\phi(t) \propto \frac{\omega t}{\hbar} \sqrt{\frac{t}{\tau_{ph}}} \quad (1.71)$$

We may determine τ_ϕ from (1.71) using the condition $\Delta\phi(\tau_\phi) \simeq 1$, which physically means that we cannot check whether the system changed its state or not until the expected action $\Delta\varepsilon\Delta t$ made on the system is less than the smallest possible action \hbar

$$\tau_\phi \simeq \left(\frac{\hbar^2\tau_{ph}}{\omega^2} \right)^{1/3} \quad (1.72)$$

When the temperature of the system is larger than or close to the Debye temperature, the phonons are by far the most effective dephasing mechanism in the system. This means that the characteristic energies of the other scattering mechanisms $\Delta\varepsilon$ would require much longer times Δt and/or many more scatterings of the electron than the electron-phonon ones in order to exert an action larger than \hbar . The situation, however, becomes very different when the temperature is lowered. The average phononic energy decreases with temperature according to the Bose-Einstein statistics $p(\varepsilon) = 1/(\exp[\varepsilon/k_B T] - 1)$, where p is the probability to find a phonon with energy ε and T is the temperature of the system. The electron-phonon relaxation time rises as $\tau_{ph} \sim T^{-3}$ (see p. 525 in (Ashcroft & Mermin 1976)). Hence, the dephasing time of electrons τ_ϕ due to scattering on phonons will rise as $\tau_\phi \sim 1/T$ according to (1.72).

The arguments above suggest that at low enough temperatures the resistivity of, say, a metal film would increase as the temperature decreases according to (1.69), with variations depending on the dimensionality of the sample. Such resistivity changes

⁶¹Generally, for any dimensionality, the denominator in (1.69) is replaced with $(Dt)^{d/2}$ and λ_F^2 with λ_F^{d-1} where d is the effective dimensionality of the sample, which is determined by the size of any of its dimensions with respect to $\Delta\tau_\phi$ given by (1.67).

⁶²According to $e^{i\phi(t)} = e^{it(\varepsilon/\hbar)}$.

were observed many times in metal films (see, e.g., review (Bergmann 1984) or (Wolf & Maret 1985)) where the increase of resistivity was successfully explained by weak localization effects.

The electron's spin degree of freedom gives rise to another remarkable interference effect. Considering the spin of the electron in (1.68) produces interference terms of the form (see pp. 13-14 in (Altshuler & Aronov 1985))

$$C = \frac{1}{2} \sum_{m=-1}^{m=+1} |\psi_{1,m}|^2 - \frac{1}{2} |\psi_{0,0}|^2 \quad (1.73)$$

where the two-particle wave functions $\psi_{s,m}$ are

$$\begin{aligned} \psi_{1,1} &= \phi_{i\uparrow}\phi_{j\uparrow} \\ \psi_{1,-1} &= \phi_{i\downarrow}\phi_{j\downarrow} \\ \psi_{1,0} &= \frac{\sqrt{2}}{2} (\phi_{i\uparrow}\phi_{j\downarrow} + \phi_{i\downarrow}\phi_{j\uparrow}) \\ \psi_{0,0} &= \frac{\sqrt{2}}{2} (\phi_{i\uparrow}\phi_{j\downarrow} - \phi_{i\downarrow}\phi_{j\uparrow}) \end{aligned} \quad (1.74)$$

While the singlet part $\psi_{0,0}$ decays in time τ_ϕ , the triplet part $\psi_{1,m}$ decays in a characteristic *spin-orbit scattering time* τ_{so} . Hence, as it was shown by (Hikami, Larkin *et al.* 1980), the corrections to the conductivity (1.69) become more complex

$$\frac{\Delta\sigma}{\sigma} = -v_F \lambda_F^2 \int_{\tau_{el}}^{\tau_\phi} \frac{dt}{h^{3-d}(Dt)^{d/2}} \left(\frac{3}{2} e^{-t/\tau_{so}} - \frac{1}{2} \right) \quad (1.75)$$

where d is the dimensionality of the sample and h its thickness. This process may even change the sign of the corrections and is called *weak antilocalization*. From (1.75) follows that when $\tau_{el} < \tau_{so} < \tau_\phi$ the correction to the conductivity is positive for paths covered by electrons in a time less than τ_{so} but is still negative for larger paths. Alternatively, when $\tau_{so} > \tau_\phi$, the correction (1.75) is only negative since $\exp(-t/\tau_{so}) \rightarrow 1$ and the spin-orbit scattering effect does not manifest itself.

On the other hand, the effects of spin-orbit scattering strongly depend on the nuclear charge (see p. 29 in (Gantmakher 2005)) as

$$\tau_{so} \sim \frac{1}{(Z\alpha)^4} \quad (1.76)$$

where Z is the atomic number and α is the fine structure constant. Hence, τ_{so} is smaller in solids with heavy ions, which is always the case for heavy-fermion compounds. For heavy fermions, as we have seen earlier, at low temperatures the heavy ions are effectively

screened due to the formation of local Kondo singlets, and the specific value of τ_{so} may strongly differ from one compound to another.

The application of a magnetic field will produce an Aharonov-Bohm phase shift of each complementary electronic wave function

$$\Delta\phi = \pm \frac{e}{\hbar} \oint_{C-C} \mathbf{A} dl = \pm \frac{e}{\hbar} \Phi \quad (1.77)$$

where index $C - C$ indicates the closed path in Fig. 1.24, \mathbf{A} is the vector potential, and Φ is the magnetic flux through the loop area. This acquired phase shift suppresses the interference effects of either sign, positive or negative. The magnetic field B applied to the electron's magnetic moment is associated with an energy of the order of $\Delta\varepsilon \simeq \mu_B B$, where μ_B is the Bohr magneton. On the other hand, we know that the electron's wave function preserves its phase until $\Delta\varepsilon \Delta t \lesssim \hbar$. Hence, the *magnetic dephasing time*, or the time after which the interference will not take place due to the electron's phase memory loss is

$$\tau_B = \frac{\hbar}{\Delta\varepsilon} \simeq \frac{\hbar}{\mu_B B} \quad (1.78)$$

and, using (1.67), the corresponding distance, below which the electron still remains "in phase" is

$$\Delta r_B = \sqrt{\frac{D\hbar}{\mu_B B}} \quad (1.79)$$

When the magnetic dephasing time becomes the smallest dephasing time in the system $\tau_B \leq \tau_{ph}$, then we may write $\tau_\phi = \tau_B$ and the corresponding corrections to conductivity may be found by integrating (1.75) with the new upper limit. Hence, by increasing the magnetic field one would suppress an either negative or positive magnetoresistance due to the weak localization effects proportionally to $B^{-1/2}$.

Inter-electron interference

The weak localization effects introduced above give a very instructive view on several relevant time scales, namely the electron-phonon relaxation time τ_{ph} , the spin-orbit relaxation time τ_{so} , and the magnetic relaxation time τ_B .

Magnetoresistance⁶³ measurements, as it was pointed out, are usually the main instrument that reveals weak localization effects. In simple metals the magnetoresistance effect is weak, typically much less than 1% with saturation in fields of the order of a

⁶³Magnetoresistance is usually defined as the normalized difference of the saturated high field resistivity to the zero field resistivity at fixed temperature, i.e., $[\rho(T, B) - \rho(T, 0)]/\rho(T, 0)$.

few Tesla⁶⁴. In heavy fermions, in contrast, the magnetoresistance may reach tens of percent (see, e.g., (Malinowski, Hundley *et al.* 2005)) although calculations considering weak localization predict that the effects should be of the same order as in simple metals⁶⁵ (Rasul 1991). The observed magnetoresistance saturates with dependencies other than for the weak localization effect and at much higher fields. In fact, the magnetoresistance phenomena in heavy fermions are very rich and not of the weak localization nature, though they may qualitatively look very similar. What, however, might be more relevant for our discussion is the inter-electron interference effects. We will get back to the perspectives later, and will now consider the effect itself.

Not only complementary waves of a single electron can interfere but also the wave functions of two different electrons. In fact they do, but one has to take into account the new respective phase memory conditions. Considering the AAS effect, one of course still has all the scattering mechanisms introduced above. Additionally, the electron-electron relaxation dynamics and localized magnetic moments introduce two more relaxation times: the electron-electron relaxation time τ_{ee} and the relaxation time on magnetic moments τ_m ⁶⁶. Let us consider the interferometer shown in Fig. 1.25(a). Here, electrical current is flowing from left to right and electrons have equal probability to travel via either arm. Let the wave functions of the two electrons at the entrance to the loop, where they split their paths, have the same complex phase $\Delta\phi^{in} = 0$, so that the interference intensity⁶⁷ attains its maximum value I_0 . Ideally, if the arms of the loop are just of the right lengths, then at the exit from the loop the electrons will also interfere constructively, i.e., $\Delta\phi^{out} = 0$ and the output intensity is I_0 . If we randomly introduced many static scatterers or defects⁶⁸ in the interferometer arms (red decaying wave), then the interference most probably would not be constructive due to uncorrelated changes of the phases of the electrons' wave functions and the intensity at the exit would be reduced to some I_1 or even to zero. Although introducing many uncorrelated scatterers we lose the interference, as long as the scatterers are static, each inducing a non-zero time averaged phase shift $\Delta\phi$, the time-averaged intensity at the exit of the interferometer may still be modulated by applying an external magnetic field B . This would introduce a phase difference between the two paths similarly to as it was done in (1.62). As a result, with a given current through the loop one would detect an oscillating voltage $\Delta V(B)$ with periodicity equal to one flux quantum $\Phi = h/e$.

⁶⁴One may insert τ_B from (1.78) into the upper integration limit in (1.69) and find that the magnetoresistance defined above is a very rapidly decaying function of the field.

⁶⁵The calculations demonstrated no enhancement of the DC conductivity although an enhancement of the AC conductivity was obtained.

⁶⁶These relaxation times are actually also relevant in the weak localization case, but we did not consider them for simplicity.

⁶⁷This is the second term in (1.68).

⁶⁸Of course, assuming that they will not dephase the electrons, i.e., $\Delta\varepsilon\Delta\tau \ll \hbar$.

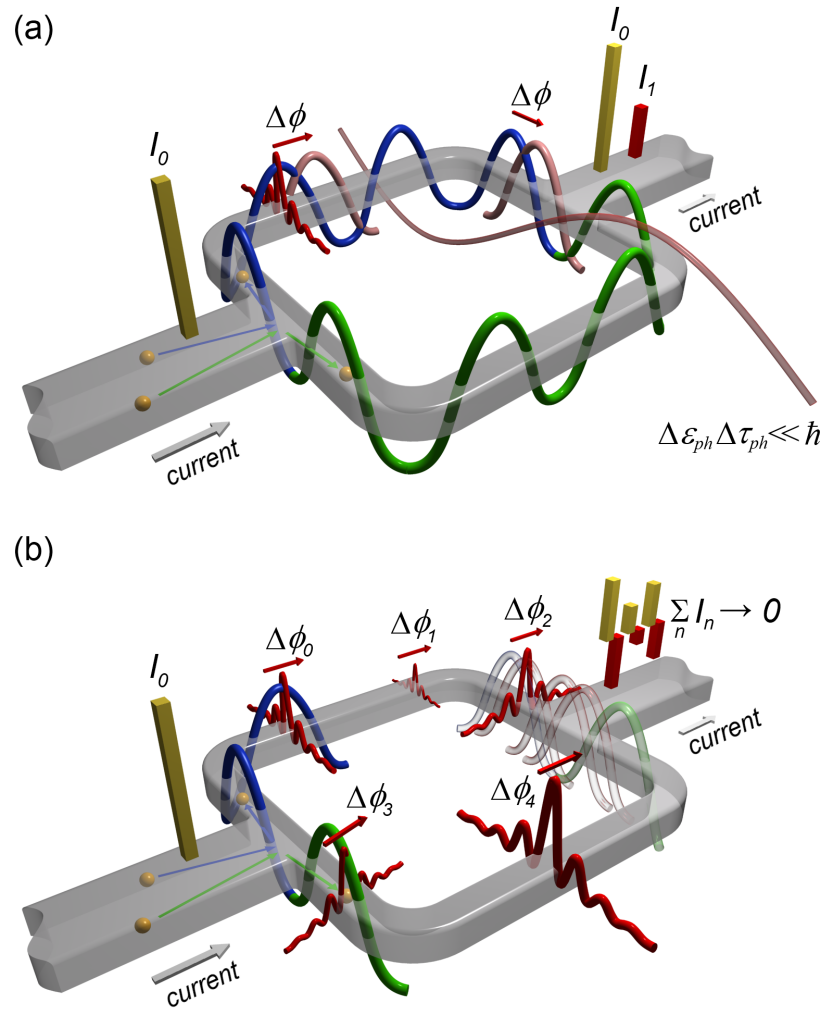


FIGURE 1.25: A hypothetical interferometer where two electron wave functions (green and blue) propagate from left to right via different loop arms. These wave functions (a) may be subject to a phase shift $\Delta\phi$ by a local static scatterer depicted by a damped red wave while the low energy phonons (long transverse reddish wave) introduce a negligibly small phase shift. The time-averaged interference will be maximal without static scatterers (yellow bars) and will be reduced in the presence of static scatterers (red bar). (b) If many dynamic local scatterers are present, the electrons' wave functions arrive to the exit (right part) of the loop with randomly modified phases. Hence, the time-averaged interference correction to the conductivity of the loop tends to zero (the sum of positive yellow and negative red bars on the right).

It should be added that if the temperature is much lower than the Debye temperature, then the phonons (the reddish long period sine wave) become an ineffective dephasing agent when compared to the other degrees of freedom. At these temperatures the electron-electron interactions become a stronger dephasing agent since the electron-electron scattering time rises as $\tau_{ee} \sim T^{-2}$, which is slower⁶⁹ than τ_{ph} (see p. 57). The electron-electron interactions do not influence the resistivity since they conserve the

⁶⁹The corresponding dephasing time due to the electron-electron interactions using (1.72) will rise as $\tau_\phi \sim T^{-2/3}$.

total momentum of electrons. These interactions, however, contribute to the electron dephasing via the energy relaxation time of the Fermi-Dirac distribution function and not via the Coulomb repulsion.

The scattering of electrons within the loop arms, however, becomes completely different if one has many dynamic scatterers in one or both interferometer arms, which are shown by red damped waves in Fig. 1.25(b). Every such dynamic scatterer introduces an uncorrelated phase shift to the electrons' wave functions. As a consequence, the interference at the exit of the loop is again lost. What is different is that by applying a magnetic field one has no chance to recover the interference pattern because adding a definite phase shift by the magnetic field to a random phase change anyway makes the waves' amplitudes at the loop's right end random. Hence, the time-averaged amplitude of the interference term at the loop's right end approaches zero and the measured voltage is related to the electrical current through the loop via Ohm's law. An important conclusion here is that by deliberately introducing defects of a specific type or by varying the interferometer circumference it is possible to catch the variation of the shortest quasiparticle phase relaxation time in the system and study its type and variation with temperature.

We may introduce a time diagram of the relevant scattering times for both single and inter-electron interferences in Fig. 1.26. In this particular diagram, one may speculate

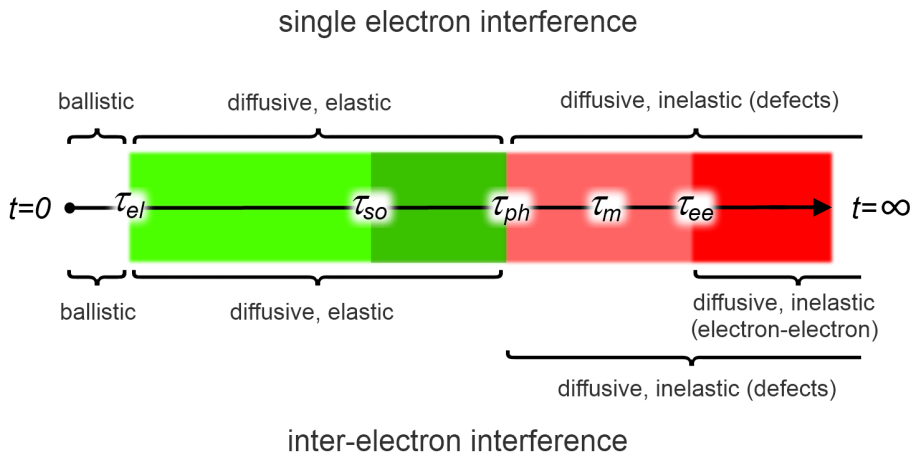


FIGURE 1.26: Several characteristic interference time scales for the single electron (weak localization effect) and for the inter-electron (Aronov-Altshuler-Spivak effect) interferences. In either case, the white area on the left covers the ballistic motion of electrons. In the green area, electrons are scattered elastically and move diffusively. The light red colour shades the times when an electron is inelastically scattered on a static defect, while the red colour denotes the characteristic time of inter-electron dephasing.

that the metallic sample is dirty enough that the elastic scattering time τ_{el} is small. The electron-phonon relaxation time τ_{ph} is much larger than τ_{el} and at the same time

is the shortest dephasing time in the system τ_ϕ . The temperature is not very low, since the electron-electron relaxation time is still larger than τ_{ph} . The electron's phase is still coherent within the time interval shaded by green, while it is incoherent in the red area. Magnetic impurities introduce the relaxation time τ_m , which is in the incoherent phase. The electron-electron relaxation time τ_{ee} may dominate and become the shortest phase relaxation time at lower temperatures. The interplay between the timescales in Fig. 1.26 partially defines the electrical conductivity in metals at all temperatures. When, however, τ_m is concerned, the interplay of interference effects and Kondo physics becomes relevant, making the analysis more complicated. While the described Gedanken experiment with an interferometer addresses the inter-electron interference, in bulk samples this effect will also modify the conductivity with similar corrections as in the weak localization case. Additionally, electron-electron interactions may modify the quasiparticles DOS around ϵ_F producing a dip, which can be probed with tunneling experiments (Gantmakher 2005, Altshuler & Aronov 1985).

Turning back to heavy fermions, one deals there with very exotic low-temperature transport phenomena, such as coherent scattering, large magnetoresistance effects, mass renormalization, unconventional superconductivity *etc.* Many of these peculiarities may be investigated by probing the characteristic electronic relaxation times. For example, the electron-phonon relaxation time τ_{ph} in heavy fermions are of great interest for time-resolved optical spectroscopy (see, e.g., (Demsar, Sarrao *et al.* 2006)). In particular, by photo-induced reflectivity experiments it was found that universally for many heavy-fermion compounds, including $CeCoIn_5$, the electron-phonon relaxation rate anomalously increases by two orders of magnitude below a certain temperature, which was related to the Kondo temperature scale⁷⁰. Such a behaviour was attributed to the largely enhanced low-energy quasiparticle DOS near ϵ_F . In the case of $CeCoIn_5$ things are rather complicated, and the analysis of many experimental results of thermal and transport measurements for $CeCoIn_5-La$ alloys (Nakatsuji, Pines *et al.* 2004) suggests the presence of two energy scales, namely the coherent heavy-fermion fluid scale at higher temperatures and the single Kondo impurity scale at lower temperatures. The description proposed by (Nakatsuji *et al.* 2004) was also supported by magnetotransport investigations on this compound (Malinowski *et al.* 2005).

It is clear that the electron-phonon relaxation time is not the shortest relaxation time for heavy fermions at low temperatures. The electron-electron interactions and the localized f -moments must introduce much shorter relaxation times at low enough temperatures. Both times were investigated for simple metals in the past (see, e.g., (Altshuler & Aronov

⁷⁰Interestingly, such an increase of τ_{ph} was reported for compounds containing rare earth ions which demonstrate mixed valence behaviour (see Sec. 1.4.2 and p.610 in (Fazekas 1999)), i.e., for compounds with Sm , Yb and Ce ions, while usual behaviour as for simple metals was reported for a Lu compound (Demsar *et al.* 2006)

1985, Bergmann 1986, Haesendonck, Vranken *et al.* 1987)) and relatively well understood in those cases. However, the models which deal with localized moments are derived within the limit $T > T_K$ (Schopfer, Bäuerle *et al.* 2003) and therefore poorly account for the RKKY interaction, whereas both the Kondo and the RKKY energy scales are essential in heavy-fermion physics. Additionally, the $c - f$ hybridization or screening of f -moments would effectively increase τ_m for the single impurity case, but the exact influence of such a screening in the case of periodic Kondo lattices is still unknown. Moreover, in the latter case partial polarization of the c -band may also decrease τ_m .

It is interesting to note that $CeCoIn_5$ is a superconductor in the clean limit (Kasahara, Nakajima *et al.* 2005) with an anomalous increase of the quasiparticle mean free path at low temperatures (Settai, Shishido *et al.* 2002). Such an increase is not expected in the Drude theory of metals. It would be also interesting to understand how this behaviour correlates with the two-fluid Kondo model which introduces disorder by defining the low-temperature single impurity Kondo energy scale. We believe that these questions may be addressed by interferometry investigations on microcrystals of $CeCoIn_5$ thin films. Even in the case of $CeCoIn_5$ with its strongly enhanced low-temperature quasiparticle mean free path, the preparation of interferometers for probing interference in the normal state requires rather small sizes of such devices. Nevertheless, these requirements can be fulfilled with existing patterning techniques.

Chapter 2

Methods and techniques

2.1 Introduction

The heart of probably any advance in physics is the different methods and techniques used either in theoretical or experimental studies. This study is no exception: we used thin film preparation, structural characterization, patterning and low-temperature transport measurement techniques. Clearly, all these steps are time-consuming, which can and does take a substantial part of the whole investigation time. Therefore, before presenting the results of our study, we have to discuss first how the studies were done.

In this chapter, we collected descriptions of the techniques used in this work. There are two reasons which motivate writing this chapter. First, one would like to provide many technical details which are important themselves but can make the perception of the physical results more difficult if discussed together. Second, understanding of the results of the $CeCoIn_5$ and $CeIn_3$ thin film growth studies and of the structural analysis of these films performed using x-rays requires understanding of both the growth and x-ray diffractometry techniques which are explained here.

The chapter starts with a description of the essential details of the growth techniques, equipment, and preparation for growth. The usage of vacuum for thin film growth is motivated next, which is followed by a description of a typical thin film growth procedure in an MBE system. The following description of the thin film characterization steps is mainly focused on the x-ray diffraction methods. In this part, we discuss the basic diffraction physics and diffractometry techniques, the intensity of Bragg reflections in diffractograms, the particular diffractometer used in this work, its scanning regimes with basic sample alignment methods, and the line profile analysis (LPA) method. In the last sections we briefly discuss the low-temperature equipment, peculiarities of small electric signal measurements, and the lock-in measurement technique.

2.2 Preparation for thin film growth

Thin film growth starts in fact before the first molecules of a specific kind are deliberately deposited on the substrate's surface. It starts with the preparation of the substrates outside of the growth system, their cleaning and mounting on a substrate carrier, which is briefly described here. Also we will describe the essential characteristics of the vacuum system and its equipment, which were used for thin film growth and *in-situ* characterization.

2.2.1 Molecular beam epitaxy system

The main instrument used in this work for thin film growth was the molecular beam epitaxy (MBE) system shown in Fig. 2.1. The main parts of this system are: the linear transfer chamber, the metal MBE chamber (bottom photograph), the organic molecular beam deposition (OMBD) chamber, the gold and aluminium sputtering chambers (behind the OMBD chamber in the top photograph), and the load lock chamber. All chambers have individual two/three stage pumping systems. The MBE is built in a star logical connection scheme where the transfer chamber is connected to the growth chambers. The chambers are interconnected within the MBE system via vacuum valves, which allow for autonomous work of each chamber. The MBE system features a common for all chambers sample transportation system, which is operated manually without disturbing the vacuum.

The load lock chamber is the smallest chamber within the MBE system. This chamber is used for loading/unloading samples. It is equipped with a rotary holder which allows operations with up to three standard sample holders at a time. The sample holders with mounted substrates can be baked-out for degassing inside the load lock chamber before being transported into the next chamber. The typical bake-out procedure is performed at a temperature of ~ 300 °C for not less than ~ 30 minutes.

After degassing the substrate holder in the load lock chamber, it is transferred through the transfer chamber into the metal MBE chamber for thin film growth (see Fig. 2.1). The metal MBE chamber is equipped with up to three high-temperature water cooled Knudsen effusion cells for producing fluxes of *Ce*, *Co*, and *In* and a FerroTec EV1-8 electron beam evaporator for producing *Co* flux. It also contains a reflection high-energy electron diffraction (RHEED) setup with a luminescent screen for *in-situ* growth quality control. For post growth quality control of the thin films a low-energy electron diffraction (LEED) setup is used. The chamber is pumped by a three-stage pumping system: a Pfeiffer TMU1001-P turbomolecular pump, a Pfeiffer TC100 booster pump

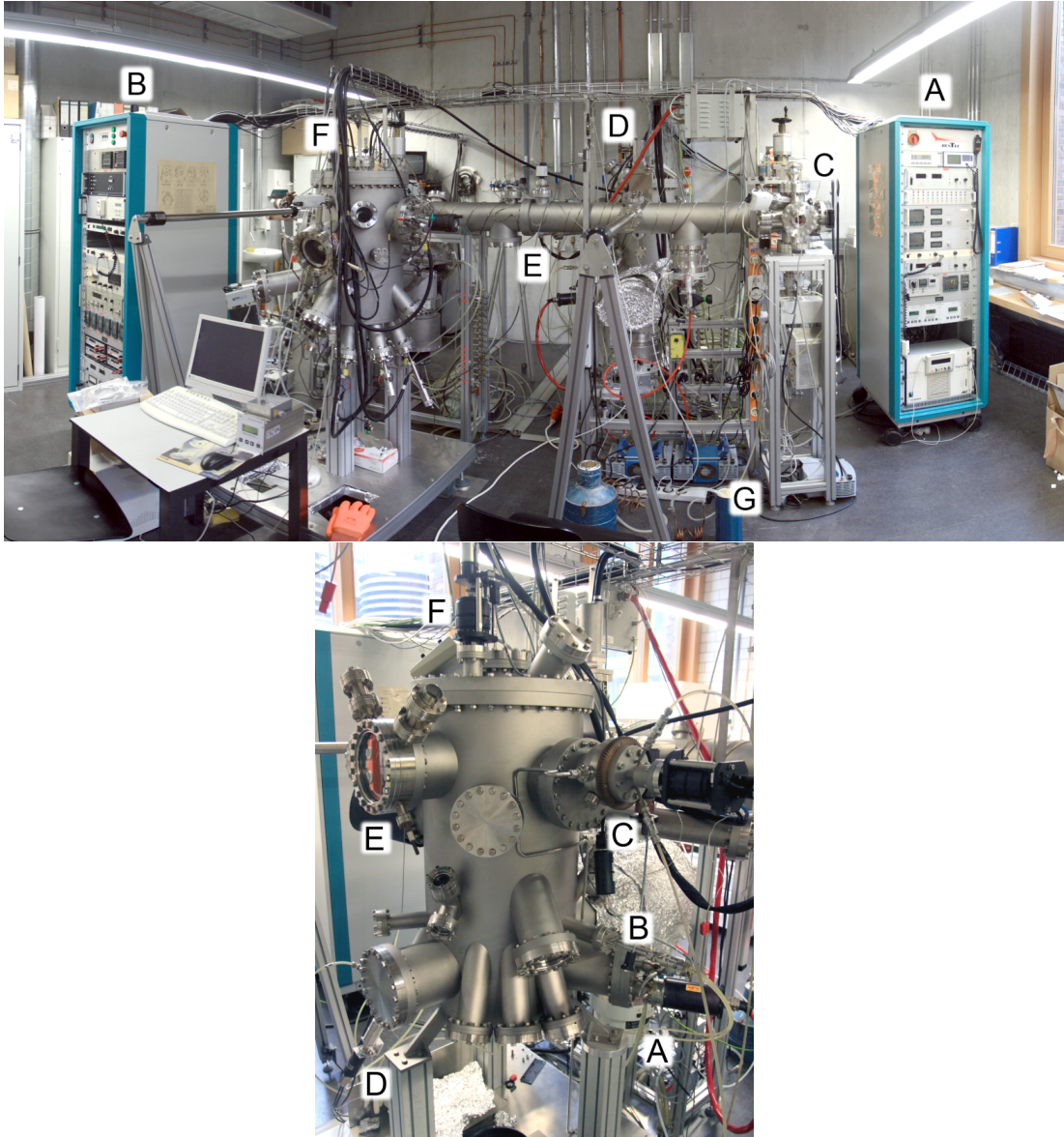


FIGURE 2.1: A complete MBE system (top figure). Here A and B are electronic controls for the metal MBE chamber D and for the organic molecular beam deposition chamber F. C is the load-lock chamber, E is the transfer chamber, and G are the membrane vacuum pumps. The metal MBE chamber (bottom figure). Here A is the turbomolecular vacuum pump, B is the electron beam evaporator, C is the sample manipulator, D is one of the Knudsen evaporation effusion cells, E is the LEED, and F is the sample's shutter manipulator.

and a Vacuubrand MD4 membrane pump. Such a combination allows to achieve the base pressure of 1×10^{-11} *mbar*. This pressure, however, does require a bake-out procedure of the complete metal MBE chamber with running pumps. This procedure typically takes not less than 20 hours at a temperature of ~ 150 °C.

Within the metal MBE chamber, the sample holder is kept face down (like in Fig. 1.1) in a special slot, which is also equipped by a heater. This heater is able to warm the

sample up to¹ 1000 °C via Joule heating delivered by a tungsten filament. The sample temperature is monitored by a thermocouple located close to the tungsten filament and is controlled by a closed-loop controller using a standard PID (proportional integral derivative) algorithm with temperature variations during thin film growth not more than 1 °C. The substrate surface temperature may differ from the PID controlled one by a few ten degrees.

The Knudsen effusion cells used in the metal MBE system utilize Joule heat for warming up the source materials (see Fig. 2.2). The effusion cells are mounted to the appropriate metal MBE chamber water-cooled ports so that the produced material fluxes are pointed from bottom to top in the direction of the substrate (as is shown in Fig. 1.1) The crucible

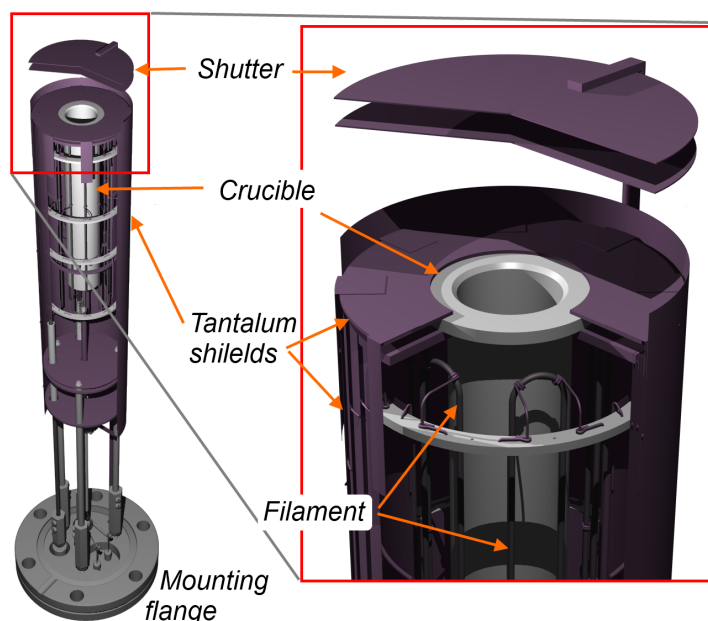


FIGURE 2.2: Schematic view of a Knudsen effusion cell. The grey parts within the effusion cell are made of ceramics, while the pink parts are made of tantalum foil and wires. The shutter rotation mechanism is vacuum sealed on the outer face of the mounting flange.

in Fig. 2.2 contains the source material, which is melted during thin film growth for obtaining the desired vapour pressure. The temperature of the crucible is monitored by a thermocouple located below the crucible and controlled by a standard closed-loop PID controller. The variation of this temperature during growth is not more than 1 °C. However, it should be emphasized that due to local temperature gradients within the effusion cell the temperature on the surface of the melted material within the crucible may be less than the controlled temperature by a few ten degrees of Celcius. During the warm-up of the effusion cells the vapors of the melted materials can be blocked on

¹The maximal allowed temperature depends on the substrate holder material.

their ways to the substrate surface by both the effusion cell shutter (see Fig. 2.2) and the sample's shutter located in the vicinity of the substrate surface.

The electron beam evaporator used for producing the *Co* flux for *CeCoIn₅* thin film growth utilizes a high-energy focused electron beam² for local melting of the *Co* target material which is located in a tungsten crucible. The produced flux rate is controlled by a programmable electronic controller which operates in a closed-loop system. As a feedback, the controller uses the measured flux rate in the vicinity of the evaporator by a gold-coated quartz crystal. The resonant oscillation frequency of the quartz crystal for the employed model is 6 *MHz*, which is decreased as new material is deposited on the quartz surface. The exact flux rate at the substrate surface, however, is not controlled directly and may be obtained only implicitly³.

It was emphasized that the exact temperatures of the source materials within the effusion cells are not exactly known. Thus, the theoretical estimation of the desired material temperatures (see p. 15) is complicated by the temperature uncertainties and can be used only as a first calibration step. As the ratio between the flux rates of the constituent components, e.g., *Ce:Co:In* as 1:1:5 for *CeCoIn₅*, should be maintained stoichiometric for better crystallinity of the *CeCoIn₅* phase⁴, further calibration is required. As the second calibration step, the flux ratios, i.e., the effusion cell regulated temperatures, were approached experimentally using indirect calibration methods: x-ray diffraction for crystallographic phase analysis and the energy dispersive x-ray spectroscopy (EDXS) for element composition analysis.

The *CeCoIn₅* and *CeIn₃* thin films in this work were grown either using only Knudsen effusion cells or using two Knudsen effusion cells and the electron beam evaporator (only for *CeCoIn₅*). The mentioned calibration procedure of the effusion cell fluxes was performed in either case. In the second case, typically a flux rate of 0.2 Å/s of *Co* was programmed to the electron beam controller and the effusion cell fluxes were calibrated for matching the desired ratio between all three fluxes.

2.2.2 Substrate preparation

For thin film growth in this work we used monocrystalline substrates of the following materials and out-of-plane crystallographic orientations:

²With typical acceleration voltage of 6.8 *keV* and beam current of 10-25 *mA*, depending on the desired flux rate.

³As a rule of thumb, the flux rate at the substrate surface is few times less than the controlled flux rate at the quartz crystal monitor.

⁴The best film crystallinity needs not to occur at a stoichiometric ratio of the fluxes. Thus, bulk *CeCoIn₅* demonstrates better crystallinity when it is grown with excess of *In* by the *In*-flux growth method (Petrovic, Pagliuso *et al.* 2001).

- $\alpha\text{-Al}_2\text{O}_3$ with orientations (0001), (11 $\bar{2}$ 0), and (1 $\bar{1}$ 02)
- MgO with orientations (100) and (111)
- MgF_2 (001)
- SrTiO_3 with orientations (100) and (111)
- Si (100)- SiO_2

The as-supplied substrates were of $10 \times 10 \text{ mm}^2$ surface area and $450 \mu\text{m}$ thickness. The substrates' surfaces were epitaxially polished at the supplier facilities (CrysTec company) and cut out of single crystals grown by the Czochralski, arc fusion or Edge-Defined Film-Fed growth methods with angular accuracy⁵ not worse than 1 degree. For practical reasons, when smaller substrates were also suitable, e.g., the growth for calibration of the fluxes, they were cut each in four smaller pieces with dimensions of about $4.5 \times 4.5 \text{ mm}^2$. The cutting was done with a precision wire saw Sommer Well 3241-2 with a diamond wire of 0.25 mm diameter. Wet wire cutting was used in order to reduce the risk of scratches on the substrates' polished surfaces.

The substrates were chemically cleaned before use. While the exact cleaning procedure may vary among different laboratories, what is truly important is to carry it out in a reproducible manner. The following procedure of cleaning was utilized in this work:

1. Cleaning with acetone and ultrasound for not less than 10 *min*
2. Rinsing with bi-distilled deionized water without ultrasound
3. Cleaning with acetone and ultrasound for not less than 3 *min*
4. Cleaning with bi-distilled deionized water with ultrasound for not less than 3 *min*
5. Cleaning with isopropyl alcohol and ultrasound for not less than 3 *min*
6. Quick drying by blowing acetone vapour against the substrate surface under well ventilated conditions

The acetone and isopropyl alcohol used for the substrate cleaning had purity better than 99.8%. The water quality was specified by residues on evaporation with value less than 1 mg/l . A special clean set of small laboratory instruments was used for handling the substrates. Individual clean glasses were assigned to each step from the given list above, while each glass was used for cleaning one substrate at a time. The substrates'

⁵By the angular accuracy we mean here the angle between the normal to the optical plane of the substrate and the specified crystallographic out-of-plane orientation. See also Sec. 3.3.2 and p. 95.

drying in the last step has to be done quickly for preventing substrate contamination by dry residues. The high evaporation rate of acetone helps to speed up this drying and removes residues with its vapour.

2.2.3 Transfer into the growth chamber

After a substrate has been cleaned, it is prepared for being mounted on a substrate holder and then transferred into the MBE system. The substrate holders used in this work⁶ are shown schematically in Fig. 2.3. They differed by material, which can be stainless steel, inconel alloy or molybdenum. In this work we mainly used the stainless steel holders in order to reduce uncorrelated variations from growth to growth. As it is shown in Fig. 2.3, the substrate can be mounted on the holder in several ways, e.g., by gluing or by clamping. When the substrates were mounted with glue, the following

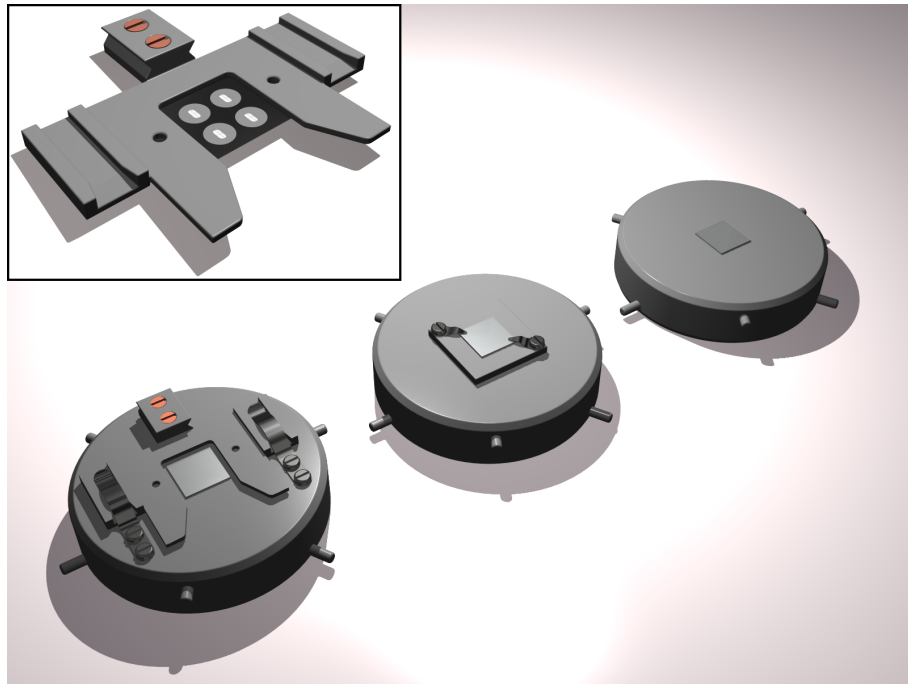


FIGURE 2.3: Schematic view of the substrate holders used in this work for the thin film growth in the MBE system (from right to left): a standard steel holder with a substrate ($10 \times 10 \text{ mm}^2$ on all holders in the figure) mounted with glue; a modified steel holder with a substrate mounted via steel clamps; a holder with a substrate mounted with glue, which supports a carrier for non-contact shadow masks (the masks are absent in the figure). The positioning of the mask carrier on the substrate holder is facilitated via guiding pins (not visible in the figure) with $100 \mu\text{m}$ of approximate lateral accuracy. The inset demonstrates schematically the shadow mask carrier with four attached shadow masks. The carrier supports up to four interchangeable shadow masks. The distance substrate-to-mask is fixed at approximately $100 \mu\text{m}$ if a $450 \mu\text{m}$ thick substrate is used.

compounds were used: PELCO Conductive Liquid Silver Paint (16031 MSDS) or two

⁶Yet another modified substrate holder was used for multiple growth, which is described in Sec. 3.2.2.

component, silver filled, and electrically conductive epoxy adhesive resin (ECCOBOND 56 C) with Catalyst 9 as a curing agent. Both glues are good electrical conductors and thus should be good thermal conductors as well. Nevertheless, the thermal coupling between the substrate and the holder may vary from growth to growth due to the poor reproducibility of the manual processing. The corresponding variations of the substrate temperatures due to variable thermal coupling were found to have a strong influence on the $CeIn_3$ and $CeCoIn_5$ thin film growth.

For improved reproducibility of the films' morphology the clamping substrate mounting method was used. Thus, the clamping system improved the reproducibility of the substrate-to-holder thermal coupling and reduced the degassing requirements under high vacuum conditions, when compared with the glue-based mounting methods.

When the substrate is mounted on the holder, it is transferred into the load lock MBE chamber for the subsequent degassing procedure, as was described earlier.

2.3 Thin film growth

The discussion here will briefly cover the vacuum concept with some calculations and the vacuum equipment in general. Later, we will discuss the growth procedure itself.

2.3.1 Vacuum concept

Thin films can be grown via a number of different techniques. The technique based on the usage of vacuum systems (e.g., MBE, sputtering, ion/electron beam induced depositions, chemical vapour deposition (CVD), pulsed-laser deposition (PLD) *etc.*) is one possibility, which requires understanding of both the motivation of using these systems and the essential physics involved. On the one hand, the vacuum systems employ vacuum in a growth chamber for minimizing the ratio between the number of unwanted molecules and the supplied vapour or flux. On the other hand, in ultra high vacuum (UHV) conditions the continuum dynamics framework cannot be used for describing the gas flows. In these conditions, statistical mechanics has to be used instead. In order to estimate which regime is realized under given conditions one uses the Knudsen number, which is defined as the dimensionless ratio of the gas molecules' mean free path λ to the characteristic length scale⁷ L as

$$K = \lambda/L \tag{2.1}$$

⁷The length scale here is determined by the linear dimensions of the volume in which the gas molecules are considered.

For $K \ll 1$ continuum dynamics is used for describing the gas flows⁸, while for $K \gg 1$ one uses statistical mechanics.

2.3.2 Gas kinetics

Let us estimate typical quantities, like the surface arrival rate, mean free path of gas molecules, and monolayer arrival time, which are important in UHV systems. The arrival rate of molecules on the substrate surface R is given within the kinetic theory of gases (see, e.g., (Lafferty 1998)) as

$$R = nv/4 \quad (\text{collisions}/(m^2 \cdot s)) \quad (2.2)$$

where $v = (8k_B T/\pi m)^{1/2}$ is the mean velocity of the gas molecules, T is the gas temperature, k_B in the Boltzmann constant, and m is the molecular mass. The molecular density n in (2.2) can be expressed at low pressures as

$$n = p/k_B T \quad (2.3)$$

where p is the gas pressure. Plugging these expressions for v and for n into (2.2) gives

$$R = p/(2\pi m k_B T)^{1/2} \quad (\text{collisions}/(m^2 \cdot s)) \quad (2.4)$$

Let us insert numbers into (2.4) for CO molecules and find the arrival rates at different pressures. Using the CO molecular weight 28, the respective molecular mass is $m = 28 \times 1.6605 \times 10^{-27} \text{ kg} = 4.65 \times 10^{-26} \text{ kg}$. If we use the temperature $T = 300 \text{ K}$, we arrive at the following results:

Observed in/at	Pressure ($Pa/mbar$)	Arrival rate (collisions/ $(m^2 \cdot s)$)
Sea level	$1 \times 10^5/1 \times 10^3$	2.87×10^{27}
Mesosphere	$0.275/2.75 \times 10^{-3}$	7.91×10^{21}
High vacuum	$1 \times 10^{-4}/1 \times 10^{-6}$	2.87×10^{18}
Ultra high vacuum	$1 \times 10^{-8}/1 \times 10^{-10}$	2.87×10^{14}

The obtained arrival rates are still very large even under high vacuum conditions and may have great influence on the growth kinetics, especially during the surface nucleation growth period. Now, for example, if we put numbers into (2.3) at $T = 300 \text{ K}$, we will

⁸The Navier-Stokes equations are used.

get the following molecular densities:

Observed in/at	Pressure ($Pa/mbar$)	Density ($1/m^3$)
Sea level	$1 \times 10^5/1 \times 10^3$	2.41×10^{25}
Mesosphere	$0.275/2.75 \times 10^{-3}$	6.64×10^{19}
High vacuum	$1 \times 10^{-4}/1 \times 10^{-6}$	2.41×10^{16}
Ultra high vacuum	$1 \times 10^{-8}/1 \times 10^{-10}$	2.41×10^{12}

There are still about 2.5 million molecules in each cubic centimeter even under UHV conditions! Let us now estimate the mean free path for molecules of residual gases in the MBE chamber. According to Rudolf Clausius (Clausius 1857), the mean free path of molecules with high velocities can be written as

$$\lambda = \frac{f}{\sigma n} \quad (2.7)$$

where σ is the effective cross sectional area for collisions and f is a proportionality coefficient. Using the Maxwell distribution function of velocities, it is possible to show that $f = 1/(\sqrt{2}\pi)$. When (2.7) is combined with the expression for f we obtain

$$\lambda = \frac{1}{\sqrt{2}\pi\sigma n} = \frac{0.2251}{\sigma n} \quad (2.8)$$

The cross section of CO molecules is $\sigma = d_{CO}^2$, where $d_{CO} = 0.316 \text{ nm}$ is the CO molecule diameter. Using (2.8) we may estimate the molecules' mean free path at $T = 300 \text{ K}$ and several pressures:

Observed in/at	Pressure ($Pa/mbar$)	Mean free path
Sea level	$1 \times 10^5/1 \times 10^3$	$\sim 100 \text{ nm}$
Mesosphere	$0.275/2.75 \times 10^{-3}$	$\sim 35 \text{ mm}$
High vacuum	$1 \times 10^{-4}/1 \times 10^{-6}$	$\sim 100 \text{ m}$
Ultra high vacuum	$1 \times 10^{-8}/1 \times 10^{-10}$	$\sim 1000 \text{ km}$

As we see, in the 10^{-6} mbar region the mean free path is already larger than typical dimensions of an MBE chamber and a laminar gas flow regime may already be established in these conditions. If the chamber characteristic length scale L is of the order of 1 m , the Knudsen number under UHV conditions $K \sim 1 \times 10^6$ and under high vacuum $K \sim 1 \times 10^2$. At pressures $\sim 10^{-6} \text{ mbar}$ and lower, one should use statistical mechanics and can neglect the effects specific to continuum dynamics such as turbulence⁹.

⁹In the case of long traveling distances, like in high-energy particle accelerators, the restrictions on the mean free path are much more narrowed and not a single collision must occur on the particle's traveling trajectory.

If one is concerned only with producing laminar fluxes of constituent elements for a deliberate transfer of molecules to the substrate surface, high vacuum conditions are already sufficient. Why then do we use UHV conditions for growing films? The reason is the monolayer (ML) arrival time τ_r . Let us assume that the residual gas molecules collide with the substrate's surface at the rate R and adsorb on that surface. The time required to create one atomic monolayer is called the monolayer arrival time $\tau_r = N_0/R$, where N_0 is the number of molecules per one atomic monolayer per unit area. Here, an atomic monolayer refers to a close packed layer of CO molecules with the diameter d_{CO} mentioned above. The atomic density of such packing will then be of the order of $1 \times 10^{19} \text{ atoms/m}^2$. Using the values from (2.5), we obtain the values of τ_r at several pressures

Observed in/at	Pressure ($Pa/mbar$)	ML arrival time	
Sea level	$1 \times 10^5/1 \times 10^3$	$\sim 3.5 \text{ ns}$	
Mesosphere	$0.275/2.75 \times 10^{-3}$	$\sim 1.3 \text{ ms}$	(2.10)
High vacuum	$1 \times 10^{-4}/1 \times 10^{-6}$	$\sim 3.5 \text{ s}$	
Ultra high vacuum	$1 \times 10^{-8}/1 \times 10^{-10}$	$\sim 10 \text{ hours}$	

Hence, if typical thin film growth time is one hour, then high vacuum conditions are not suitable for clean experiments and UHV conditions are desired. At lower pressures, i.e., under UHV conditions, the residual gases ML arrival time τ_r is so large that we can almost always neglect the influence of the residual gas molecules on the thin films growth dynamics. At higher pressures, i.e., under high vacuum conditions, the substrate surface will be bombarded by the residual, i.e., unwanted, gas molecules at even higher rates than the arrival rate of the desirable molecules¹⁰. Thus, the growth dynamics of the desired chemical and crystal phases becomes essentially complex. The growth of different chemical and crystal phases may become not a function of the deliberate variations, but rather a stochastic function of local variations on the substrate surface. At the nucleation growth stage, such variations lead to formation of structurally and chemically dissimilar growth centers, which eventually evolve into a discontinuous thin film surface morphology.

2.3.3 Vacuum calculations

Consider a vacuum growth chamber with volume V and pressure p inside. The vacuum is produced by a pumping system with performance S_0 measured in *liters/second*. We

¹⁰See also Sec. 2.3.5.

may write the equation which relates these quantities and time as

$$V \frac{dp}{dt} + S_0 p = Q \quad (2.11)$$

called the *pump-down* equation. Here, Q is the chamber's leak rate measured in *mbar · liter/s*. This rate consists of real leaks through holes, degassing of the walls and parts inside the chamber or the trapped volumes (virtual leaks). We can solve this linear differential equation if all its variables except the pressure are fixed. The essential solutions are

1. If the leak rate Q is negligible, i.e., at short times after starting the pump, then $p = p_0 \exp(-t/\tau)$, where $\tau = V/S_0$. The time it takes to lower the pressure from p_1 down to p_2 is $\Delta t = (V/S_0) \ln(p_1/p_2)$. In practice, this regime is valid for times of the order of minutes.
2. The long pumping time pressure limit $p = Q/S_0$ is governed by the leak rate Q , which is a well-known relation in the vacuum systems community. The pressure p obtained here is the lowest achievable pressure within the growth chamber.

It has been known for many years that for a well designed (i.e., without holes, trapped volumes *etc.*) UHV system the lowest pressure is limited mainly by degassing of the chamber walls and internal parts. Hence, reducing the internal surface area without reducing the functionality of the whole system is essential. Let us consider a chamber with a typical leak rate per 1 m^2 (Chen & Liu 1986) $q = 6 \times 10^{-7} \text{ mbar} \cdot l / (s \cdot m^2)$, pumping speed $S_0 = 920 \text{ l/s}$ and an internal surface area¹¹ of 2 m^2 . Then, without accounting for the chamber's geometry, the ultimately lowest pressure in such a chamber will be $p = 1.3 \times 10^{-9} \text{ mbar}$. If, however, slow degassing within the chamber contributes to the value of q , call it "virtual leak", the value of q will be decreasing during pumping. This process can last thousands of pumping hours until the virtual leaks diminish and only leaks through holes contribute to q . This process can be substantially speeded up by warming the chamber's walls, i.e., baking it out. As it is reported in (Chen & Liu 1986), by backing out such a chamber with the mentioned value of q at 200 °C for 8 hours the leak rate can be decreased by two orders of magnitude down to $q \simeq 6 \times 10^{-9} \text{ mbar} \cdot l / (s \cdot m^2)$. Thus, the ultimately lowest pressure of such a chamber pumped with a rate $S_0 = 920 \text{ l/s}$, according to the solution of (2.11), will be $p = 1.3 \times 10^{-11} \text{ mbar}$, which can be reached in just 10 hours.

¹¹Here $Q = qA$, where A is the chamber's internal surface area.

2.3.4 Tube conductance

The pressures calculated above are valid for the perfect case but not for real systems. In our calculations we did not take into account the geometry of the vacuum system, i.e., the diameters and lengths of its tubes. A real vacuum system, however, contains tubes of finite diameters, which requires introducing their finite gas conductances. The tube conductance C is defined as the flow rate g in $mbar \cdot l/s$ divided by the pressure difference $p_2 - p_1$ at the ends of the tube in $mbar$:

$$C = \frac{g}{p_2 - p_1} \quad (2.12)$$

When a high vacuum turbomolecular pump is connected to the vacuum chamber through a given tube with conductance C , its effective pumping rate is given by

$$S^{-1} = \sum_i C_i^{-1} + S_0^{-1} \quad (2.13)$$

where C_i are the conductances of all serially connected tubes. Alternatively, when several tubes are connected in parallel, their conductances are summed $C = \sum_i C_i$ before applying (2.13). Thus, there is always a compromise between increasing the tubes' diameters within a vacuum system and keeping the total volume of the vacuum system as small as possible¹². It can also be emphasized that pressure measurements in the vacuum system are also affected by the finite conductance of the tubes. Hence, placing a pressure gauge close to the vacuum pump will give somewhat more pleasing numbers, although the pressure in the vicinity of the sample may be somewhat higher.

2.3.5 Growth procedure

After a sample has been transferred into the metal MBE chamber, it is ready for thin film growth. At this step one needs to rise the temperatures of the effusion cells and the substrate. Typical numbers for the growth processes are given in Appendix E. The warm-up rate of the effusion cells is limited by the risk of breaking the crucibles due to the difference in thermal expansion coefficients of the crucible and of the material it carries. This risk becomes larger at the melting transition temperature of the source material due to the fast change of its volume. A typical time for warming up the effusion cells is $\sim 60-90 \text{ min}$ for a temperature span of $\sim 1000 \text{ }^\circ\text{C}$. The sample, in contrast, can be warmed up faster (typically 20 min for $\Delta T = 500-550 \text{ }^\circ\text{C}$) since no melting transitions and no brittle materials are usually involved. It is also reasonable to allow the sample to additionally degas, which improves the growth chamber's pressure.

¹²For details see, e.g., (Hoffman, Singh *et al.* 1998) or (Dushman 1962).

When an electron beam evaporator is used, the time required for obtaining a stable flux is reduced. Since the evaporator uses a massive tungsten crucible, the risk of damage is much reduced. A typical warm-up time for the electron beam evaporator is $\sim 30 \text{ min}$.

As it was already noted earlier, the fluxes produced by the effusion cells can be blocked by individual shutters. The electron beam evaporator was not equipped with such a shutter. Thus, during the warm-up procedure the second shutter located in the vicinity of the sample must be kept closed. When the desired effusion cells temperatures are reached, the individual cell shutters are opened to stabilize their fluxes ($\sim 15 \text{ min}$), while the sample shutter is still closed. No growth has been established so far, although residual molecules of the constituent elements may reach the substrate surface and, depending on the gas pressure within the chamber, can deposit there.

Nominally, the growth starts by opening the sample's shutter and so letting the fluxes directly reach the substrate surface. The typical pressure seen by the pressure gauge within the growth chamber at this step is $\sim 5\text{-}20 \times 10^{-9} \text{ mbar}$, which is almost unchanged during one hour of growth¹³. The film's growth rate cannot be easily changed due to the mentioned uncertainties of the source material temperatures and therefore is pre-programmed by the flux ratio calibration procedure. The thickness of the thin films was controlled by the growth time, which is typically $\sim 300 \text{ nm}$ per 1 hour growth. This thickness corresponds to a film growth rate of about 0.8 \AA/s or about 12.5 seconds for the arrival of one atomic monolayer of CeCoIn_5 with (001) out-of-plane crystallographic orientation.

The growth ends by closing the sample's and effusion cells' shutters, cooling down the effusion cells and the sample, and stopping the electron beam evaporator.

2.4 Characterization

Apparently, when a thin film is obtained, its quality has to be analyzed. Such an analysis is usually a multi-stage task, since no single technique can give a complete characterization of the film's quality. Moreover, statistical quality variations in films grown even under nominally identical conditions poses additional requirements on the analytical interpretations of the results. By the quality of a thin film we mean the chemical phase purity of the film, the crystallographic phase purity of this chemical

¹³Carrying out calculations for Ce , Co , and In as in Sec. 2.3.2 at $T = 300 \text{ K}$, their arrival rates are $R(\text{Ce}) = 6.4 \times 10^{15}\text{-}1.4 \times 10^{16} \text{ collisions}/(\text{m}^2 \cdot \text{s})$, $R(\text{Co}) = 1.0 \times 10^{16}\text{-}2.3 \times 10^{16} \text{ collisions}/(\text{m}^2 \cdot \text{s})$, and $R(\text{In}) = 7.1 \times 10^{15}\text{-}1.6 \times 10^{16} \text{ collisions}/(\text{m}^2 \cdot \text{s})$. The monolayer arrival times are $\tau_r(\text{Ce}) \simeq 270\text{-}590 \text{ s}$, $\tau_r(\text{Co}) \simeq 200\text{-}790 \text{ s}$, and $\tau_r(\text{In}) \simeq 170\text{-}670 \text{ s}$. The arrival times are smaller than the $\sim 15 \text{ minute}$ flux stabilizing time, so the first nucleation of Ce , Co , and In molecules and their compounds should already be established on the substrate surface even before the sample's shutter is opened.

phase ($CeCoIn_5$ and $CeIn_3$ in our case), the film's surface morphology (see Sec. 1.3.2), the crystallographic defect types and their density *etc.* That is, literally, the highest quality would correspond to a monocrystalline film without crystallographic defects.

Each of the quality factors was monitored by a specific technique. Reflection high-energy electron diffraction (RHEED) was used regularly for *in-situ* monitoring of the films' crystallinity. The surface morphology monitoring of the thin films was performed with a Leica DM4000M optical microscope equipped with selectable optical polarizer/analyzer crystals. The optical magnification range used for observations was 50 to 1000 times. Although the optical microscopy gives important information, some information can already be obtained with the naked eye. In the case of $CeCoIn_5$ and $CeIn_3$ systems, the elemental residues on the film's surface start oxidizing in air and one easily detects the film's surface colour variation¹⁴.

We used atomic force microscopy (AFM) (Easy Scan 2 AFM system from Nanosurf) as yet another technique for analyzing the thin films' surface morphology¹⁵. With this technique we obtained three-dimensional information about the films' surfaces with spatial resolution of 1.1 nm and height resolution of 0.21 nm. The films' thickness was measured with this technique by taking height profiles across the areas where the film had been mechanically removed down to the substrate surface.

Another technique used in this work to analyze the surface morphology of the thin films with high spacial resolution was scanning electron microscopy (SEM)¹⁶. The SEM was also employed for quantitative analysis of the thin films' elemental composition with energy dispersive x-ray spectroscopy (EDXS). Focused ion beam induced deposition (FIBID) and focused ion beam milling (FIBM) were used to micropattern $CeCoIn_5$ and $CeIn_3$ thin film microcrystals for subsequent low-temperature electrical transport measurements. For this purpose, the microcrystals were contacted via *W-C* composite nanowires, which demonstrate metallic conductivity down to the lowest temperatures measured, prepared with FIBID¹⁷. The FIBM was additionally employed to electrically isolate these microcrystals as well as to prepare superconducting quantum interference devices (SQUID) on $CeCoIn_5$ thin film microcrystals.

The x-ray diffractometry was used in this work to obtain the most important characterization information, namely for both qualitative and quantitative analysis of the crystallographic phases of the as-grown $CeCoIn_5$ and $CeIn_3$ thin films. With this technique we also estimated the relative defect concentration in the $CeCoIn_5$ phase using

¹⁴In our case, the films' surface colours ranged from grey metallic (no *In* or *Ce* residues) to yellowish or violet, reflecting the presence of *Ce* or *In* oxides, respectively.

¹⁵The non-contact dynamic mode was used.

¹⁶A dual beam FEI Nova NanoLab 600 scanning electron microscope was used.

¹⁷In the following we will refer to these composites as *W-IBID*.

the line profile analysis (LPA) and the Williamson-Hall plot method, which was automated with a software developed during this work. We analyzed the relations between the $CeCoIn_5$ (001) crystallographic orientation and a selected substrate crystallographic orientation by taking polar plot scans. The grazing incidence diffraction (GID) was used to analyze the in-plane preferential orientation of the $CeCoIn_5$ thin films. This improved our qualitative understanding of the $CeCoIn_5$ thin films growth at initial growth stages (see also Sec. 1.3.2).

While the orientational analysis will be addressed in the next chapter, here we will consider the basic principles of x-ray crystallography. Then follows a description of the LPA method.

2.4.1 X-ray diffractometry

It is known from optics that scattering of electromagnetic waves on periodic lattices may demonstrate diffraction effects under certain conditions. Under these conditions, the intensity pattern produced by the reflected electromagnetic waves demonstrate a series of spatially modulated minima and maxima due to destructive and constructive interference effects. For an instrumental observation of the interference effect, the wavelength of the employed electromagnetic waves must be comparable to the separation between the scattering centers. If this separation is of the order of inter-atomic distances, i.e., in the sub-nanometer range, according to the de Broglie relationship one has to use photons with energies of about 10 keV, i.e., x-rays.

In this section we give a sketch of the x-ray diffractometry technique, which is, probably, one of the most important techniques available to a thin film investigator. We will describe its main principles as well as the particular diffractometer used in this work together with the basic alignment procedure.

Individual scatterers

When an interaction of the electromagnetic waves with an individual scatterer is considered, the following effects may arise. The *photoionization* effect consists of ejecting one or more electrons from an atom, ion or molecule by an incident photon. For the effect to occur the photon frequency should reach a material specific threshold value, which is much lower than typical x-ray energies. The second effect is *Compton scattering*, during which a part of the incident photon energy is transferred to an electron, i.e., an inelastic scattering takes place. The effect we are interested in, is the elastic *Thomson scattering*.

An elastic scattering event is demonstrated in Fig. 2.4, where the incident electromagnetic wave exerts a force on a *charged* particle, an electron in this case with charge q , and forces it to oscillate in the plane of the electric field \mathbf{E} (the up and down arrows in the figure) with a frequency identical to that of the incident wave. This oscillating charge becomes a source of polarized secondary electromagnetic radiation with no restrictions on the direction of the scattered wave vector. The measured intensity of the scattered

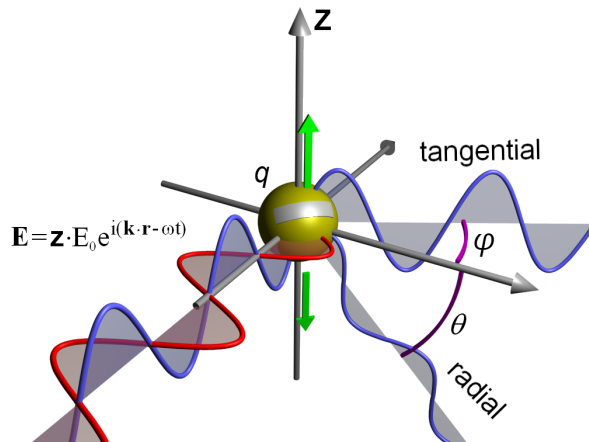


FIGURE 2.4: Elastic scattering of the electromagnetic wave on a charged particle. The secondary light is polarized in the direction of \mathbf{E} of the incident light and has the tangential ($\theta = 0$) and radial ($\theta \neq 0$) components.

wave will strongly depend on its polarization seen by the observer. For a tangentially polarized wave, i.e., $\theta = 0$, the measured intensity will be equal to that of the incident wave. If a radially polarized wave is considered, i.e., $\theta \neq 0$, the measured intensity I will be proportional to $(1 + \cos^2 \theta)/2$, which defines the polarization factor described in one of the following sections.

Scattering on a periodic lattice

When it comes to scattering of electromagnetic waves on periodically arranged scattering centers, the effects of spatial modulation of the re-emitted light intensity become strong, i.e., a diffraction pattern occurs. Generally, two equivalent mathematical descriptions are used for explaining x-ray diffraction effects on crystals. These are the Laue (Friedrich, Knipping *et al.* 1912) and the Bragg (Bragg & Bragg 1913) formulations, which are both based on conditions of constructive interference.

Max von Laue *et al.* considered a periodically arranged one-dimensional array of atoms with translational vector \mathbf{a} , which is shown in Fig. 2.5(a). The incident and diffracted beams are represented by the unit vectors \mathbf{S}_0 and \mathbf{S}_a respectively so that $\angle(\mathbf{S}_0, \mathbf{a}) = \alpha_i$ and $\angle(\mathbf{S}_a, \mathbf{a}) = \alpha_o$. Laue formulated his condition for the occurrence of constructive interference between the diffracted beams as the requirement that the geometrical path

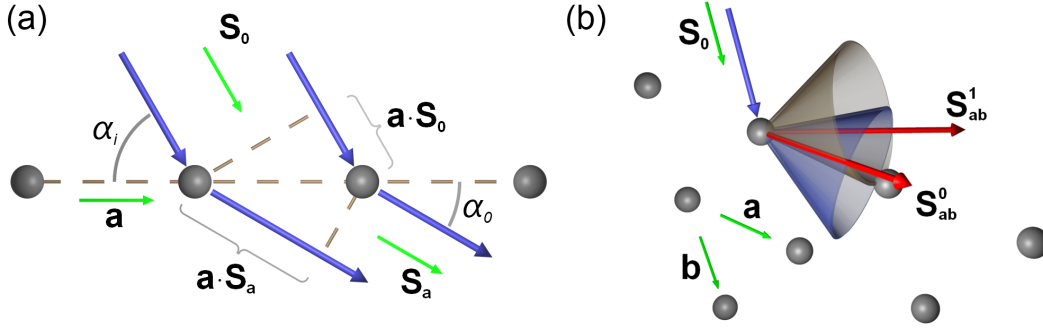


FIGURE 2.5: (a) The diffraction of x-rays on a one-dimensional chain of equally spaced scatterers with the translation of vector \mathbf{a} . The incident beams \mathbf{S}_0 and the scattered beams \mathbf{S}_a are shown by blue arrows. The angles of incoming and outgoing beams are α_i and α_o respectively. (b) The diffraction of x-rays on a periodic two-dimensional array of scatterers with translational vectors \mathbf{a} and \mathbf{b} . The red vectors \mathbf{S}_{ab}^0 and \mathbf{S}_{ab}^1 visualize solutions of a system of Laue equations (see text).

difference between a pair of incident and a pair of diffracted beams has to be an integer number of wavelengths λ . This can be written in a vector form as

$$\mathbf{a} \cdot \mathbf{S}_a - \mathbf{a} \cdot \mathbf{S}_0 = \mathbf{a} \cdot (\mathbf{S}_a - \mathbf{S}_0) = n\lambda \quad (2.14)$$

where n is an integer number. The solutions of (2.14) are an infinite number of vectors \mathbf{S}_a , which form a three-dimensional cone with its apex centered at the scattering atom and its axis being aligned with \mathbf{a} . If a one-dimensional chain of scatterers is propagated periodically, then a two-dimensional array is formed (see Fig. 2.5(b)) from a set of two chains with two unit vectors \mathbf{a} and \mathbf{b} . In this case, solutions of a system of two coupled equations of the type of (2.14) have to be found. These solutions are essentially the intersections of two cones, which are shown by red vectors \mathbf{S}_{ab}^0 and \mathbf{S}_{ab}^1 in Fig. 2.5(b). These directions correspond to the largest observable intensities of the diffracted waves. In a three-dimensional crystal lattice, one finds the directions of maximal intensity by solving a system of three coupled Laue equations

$$\begin{aligned} \mathbf{a} \cdot (\mathbf{S}_a - \mathbf{S}_0) &= h\lambda \\ \mathbf{b} \cdot (\mathbf{S}_b - \mathbf{S}_0) &= k\lambda \\ \mathbf{c} \cdot (\mathbf{S}_c - \mathbf{S}_0) &= l\lambda \end{aligned} \quad (2.15)$$

where h , k , and l are independent integer numbers. These equations may be rewritten as¹⁸

$$\begin{aligned} \mathbf{a} \cdot \mathbf{Q} &= h \\ \mathbf{b} \cdot \mathbf{Q} &= k \\ \mathbf{c} \cdot \mathbf{Q} &= l \end{aligned} \quad (2.16)$$

where $\mathbf{Q} = (\mathbf{S} - \mathbf{S}_0)/\lambda$ has been normalized by $1/\lambda$ and has the unit of m^{-1} . We are interested in simultaneous solutions of (2.16) such that $\mathbf{S}_a = \mathbf{S}_b = \mathbf{S}_c = \mathbf{S}$.

Let us now consider a three-dimensional lattice of periodically arranged scatterers with base vectors \mathbf{a} , \mathbf{b} , and \mathbf{c} , which are linearly independent. Since our choice of \mathbf{Q} is not restricted, let us consider only those directions of \mathbf{Q} , which are collinear to the vector $\mathbf{c}^* = \mathbf{a} \times \mathbf{b}$, i.e., to the normal of the (\mathbf{a}, \mathbf{b}) -planes¹⁹, as it is shown in Fig. 2.6. Our restrictions on the directions of the scattering vector \mathbf{Q} are also identical to equalizing the angles of incident and diffracted rays $\alpha_i = \alpha_o$, measured from \mathbf{S}_0 and \mathbf{S} to the (\mathbf{a}, \mathbf{b}) -plane, which we will call θ . Increasing the value of angle θ from zero on keeps increasing the modulus of \mathbf{Q} , which at some value will satisfy the Laue equations (2.16). That is, the projection of \mathbf{Q} on \mathbf{c} will become an integer number l or, using (2.16) and notations from Fig. 2.6,

$$|\mathbf{Q}| = \frac{l}{|\mathbf{c}| \cos \varphi} \quad (2.17)$$

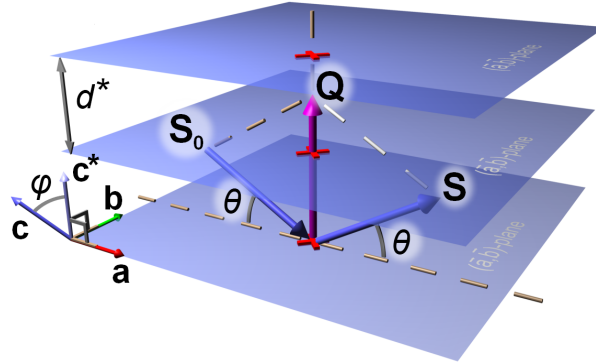


FIGURE 2.6: The scattering vector \mathbf{Q} in the reciprocal space representation. The semi-transparent planes represent the reciprocal space planes, their intersections with vector \mathbf{Q} being shown by red crosses. The planes are equally spaced by $d^* = 1/d$, where d is the distance between atomic planes in real space. Vectors \mathbf{a} , \mathbf{b} , and \mathbf{c} are the real space base vectors and vector \mathbf{c}^* is one of the base vectors in reciprocal space, i.e., $\mathbf{c}^* \perp (\mathbf{a}, \mathbf{b})$ and $|\mathbf{c}^*| = d^*$.

¹⁸Curiously, one may recall from a geometry course that the equations written in this form are nothing else but the equation of a plane in three dimensions of the form $\mathbf{n} \cdot \mathbf{p} = m$. Here, \mathbf{n} is the plane normal unit vector, \mathbf{p} is any vector lying in the plane, and m is the coordinate along \mathbf{n} , at which the plane intersects an axis parallel to \mathbf{n} . That is, if $m = 0$, then the plane passes through the origin.

¹⁹For cubic, tetragonal, and orthorhombic crystal systems this normal will be collinear with \mathbf{c} , though generally this is not the case.

where φ is $\angle(\mathbf{Q}, \mathbf{c}) = \angle(\mathbf{c}, \mathbf{c}^*)$. Equation (2.17) is valid for arbitrary crystal symmetry. However, for the simple case of orthogonal base vectors (2.17) reduces to $|\mathbf{Q}| = l/|\mathbf{c}|$, since $\varphi = 0$. In this case, constructive interference is observed only when the modulus of the vector \mathbf{Q} is an *integer number* times the *reciprocal* value of the inter-planar distance $1/|\mathbf{c}|$. Since the angle φ is not zero for non-orthogonal crystal lattices, we may construct a new universal set of base vectors²⁰

$$\begin{aligned} \mathbf{a}^* &= \mathbf{b} \times \mathbf{c}, & |\mathbf{a}^*| &= 1/(|\mathbf{a}| \cos \angle(\mathbf{a}, \mathbf{a}^*)) \\ \mathbf{b}^* &= \mathbf{c} \times \mathbf{a}, & |\mathbf{b}^*| &= 1/(|\mathbf{b}| \cos \angle(\mathbf{b}, \mathbf{b}^*)) \\ \mathbf{c}^* &= \mathbf{a} \times \mathbf{b}, & |\mathbf{c}^*| &= 1/(|\mathbf{c}| \cos \angle(\mathbf{c}, \mathbf{c}^*)) \end{aligned} \quad (2.18)$$

which define a new three dimensional space called *reciprocal space* with dimensions of m^{-1} . Now, irrespective of the crystal structure, constructive interference is observed only for integer-valued coordinates h, k and l of the scattering vector $Q = (h\mathbf{a}^*, k\mathbf{b}^*, l\mathbf{c}^*)$ in this space. The integers h, k and l are called *Miller indices*, which are common notations of crystal planes in Bravais lattices (Hahn 2006, Ashcroft & Mermin 1976).

In an alternative approach, Sir William Lawrence Bragg considered x-rays being specularly scattered from the *planes* formed by periodically arranged atoms. Though physically this idea is not completely correct since every atom represents an individual source of secondary emitted waves, it turned out that it gives correct results which can also be derived from Laue's equations. Following Bragg, let us consider incoming x-ray beams \mathbf{S}_0 (see Fig. 2.7) that are specularly reflected (\mathbf{S}) from the set of atomic planes spaced by d . Similarly to Laue's conditions of constructive interference, the Bragg condition

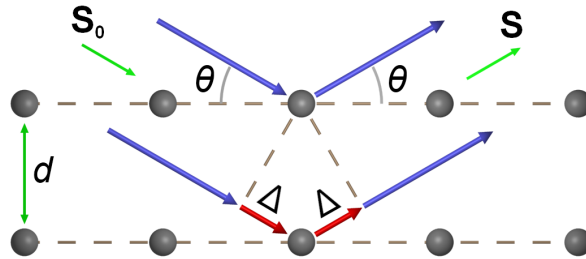


FIGURE 2.7: Diffraction of specularly reflected x-rays from a set of regularly spaced atomic planes according to Bragg's law. 2Δ is the geometrical path difference between the two ray paths. d is the inter-planar distance in real space.

defines the geometrical path difference between two ray paths, which is $2\Delta = 2d \sin \theta$ according to Fig. 2.7. When the geometrical path becomes equal to an integer multiple n

²⁰The set of base vectors in (2.18) forms a right-handed coordinate system, which is required for correct switching between the direct and reciprocal spaces. For details see, e.g., Sec. 1.1.3 in (Hahn 2006) vol. B.

of the wavelength λ , constructive interference between the outgoing waves is established

$$2d \sin \theta = n\lambda \quad (2.19)$$

which is called Bragg's law and the angle θ is commonly referred to as the Bragg angle. The law says that it is possible to select such a direction of the incident rays \mathbf{S}_0 with respect to the crystallographic or atomic planes that the specularly reflected rays will interfere constructively, resulting in large intensity in the selected direction. Performing a "scan" by varying angle θ will result in a series of *Bragg reflections*, each at its own unique angle θ . The values of θ of these Bragg reflections are related to the unknown value of d through (2.19), which gives a straightforward method to measure the inter-atomic distances using diffractions of mono- or polychromatic x-rays.

The Laue equations and the Bragg law can be derived from one another. Let us demonstrate this by considering the diagram in Fig. 2.8. The balls represent integer-valued

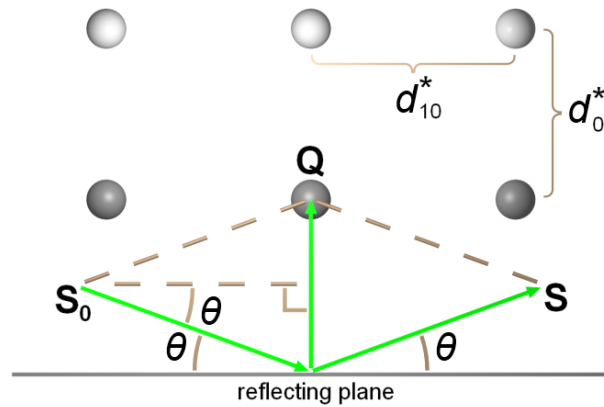


FIGURE 2.8: Demonstration of the scattering vector \mathbf{Q} in reciprocal space. Balls are the integer-valued coordinates in this space. d^* are the reciprocal inter-planar distances.

coordinates in reciprocal space derived earlier from the Laue equations. The distances d^* are the reciprocal inter-planar separations in real space with the lower indices coding different stacking directions of atomic planes in real space. Now, as it is shown in the figure, the length of \mathbf{Q} is

$$|\mathbf{Q}| = 2 \frac{1}{\lambda} \sin \theta = d^* = \frac{1}{d} \quad (2.20)$$

Regrouping, (2.20) becomes

$$2d_{hkl} \sin \theta = \lambda \quad (2.21)$$

which is the Bragg law for the 1-st diffraction maximum, where d_{hkl} is the inter-planar distance between the (hkl) planes in real space. As it was shown, the Bragg law is a special case of the three Laue equations. In practice, the Bragg law is used more often due to its easier visual representation and its straightforward connection to the mathematical description of crystallographic symmetries.

Diffractometry

The x-ray diffraction laws, which were considered above, made it possible to develop a number of techniques to study the crystal structure of monocrystalline, powder, and thin film samples as well as biological objects like proteins or viruses in a crystallized form. The Laue and Bragg formulations can be employed in two ways, either by using a polychromatic x-ray source and fixing the sample's position or by using a monochromatic x-ray source and varying the sample's angular position.

In the Laue geometry, i.e., using a polychromatic x-ray source with wavelengths from λ_{min} to λ_{max} , the sample is fixed at the center of a cylindrical chamber and exposed to x-ray radiation. Each crystallographic plane will “pick out” its own wavelength which satisfies the diffraction laws. As a result, all diffracted intensities in all possible directions are registered by a screen located on the inner surface of the cylindrical chamber.

The second group of methods, which is commonly referred to as powder diffraction, uses a source of monochromatic or synchrotron radiation which is combined with sample rotation. These methods are by far the most commonly used ones for powder or thin film analysis. While the Laue method is a powerful tool for fast identification of crystal symmetry, the methods of the second group are most commonly used for crystalline phase determination, distinction between crystalline and amorphous phases, determination of the preferred orientation or mosaicity. When combined with modern data processing the powder and related diffraction methods are particularly powerful for lattice parameter and microstructure measurements, such as crystallite size, strain, crystal defects *etc.* determination.

The vast majority of modern x-ray investigations of thin films, powder, and bulk samples are made with computerized diffractometers. In the following we will discuss briefly the beam focusing and conditioning methods. The most common focusing geometry applied in modern diffractometers is the Bragg-Brentano geometry, whose typical arrangement is shown in Fig. 2.9. The x-ray beam source, the sample surface, and the detector receiving slit lie on the focusing circle. Naturally, the x-rays are divergent at the focus F and need to be collimated. Soller slits decrease the divergence of the beam in the plane perpendicular to the figure, i.e., axial divergence. Due to the fact that for x-rays the refractive index of all materials is slightly less than unity it is impractical to use focusing lenses. Therefore, the beam shaping is done by slits and multi-coated mirrors, the latter being able to reflect all incident intensity above a critical angle. Ideally, the sample surface should be a spherical segment in order to refocus all reflected beams into the detector. However, due to the small dimensions of a typical sample, the additional divergence of the beam, introduced by the sample's flat surfaces, is usually neglected.

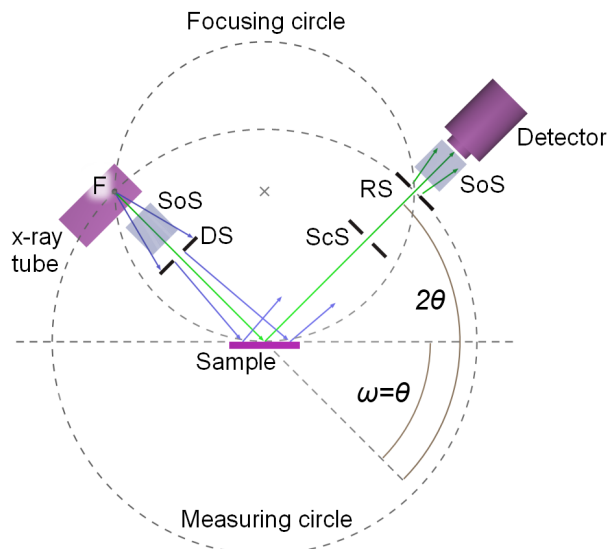


FIGURE 2.9: Bragg-Brentano or self-focusing geometry of a diffractometer. The primary side consists of the focus of the x-ray source F, the soller slit SoS, and the divergence slit DS. The secondary side consists of the scattering slits ScS, the receiving slit RS, and the detector. The sample surface is flat, which introduces additional divergence. The F, the sample surface, and the RS are always located on the focusing circle so that the beam is refocused into the detector.

The diffractometers are often equipped with a monochromator or a Göbel mirror for additional collimation of the x-ray beam.

The diffractometers with the Bragg-Brentano geometry allow for various kinds of crystallographic analysis. Several of their possible operational regimes used in this work will be described in one of the following sections. Briefly, in all these regimes one is concerned with probing diffracted intensities for a selected volume of reciprocal space. Further information can also be extracted from the shapes and relative intensities of the observed Bragg reflections.

Intensity of Bragg reflections

The x-ray diffraction pattern obtained on a Bragg-Brentano diffractometer is in most cases a plot of intensities versus the Bragg angle. This pattern can be analyzed on several complexity levels. The analysis of the reflections' positions and their relative intensities gives the first qualitative information on the sample's phase composition. Additional information can be obtained from the reflections' shapes as well as their variations along the Bragg angle. For such an analysis, one has to understand first the source of the Bragg reflection intensity.

Generally, the energy dE received by the x-ray detector in time dt is

$$dE = I(\mathbf{S})dsdt \quad (2.22)$$

where vector \mathbf{S} pointing in the scattering direction has the same meaning as in the previous section, $I(\mathbf{S})$ is the intensity function, and ds is the detector surface element. The diffracted intensity $I(\mathbf{S})$ is influenced by several factors which are structure, instrument, and the Bragg angle dependence. Briefly, those factors are classified as follows.

The *atomic form factor* f . In the beginning of this section we described an elastic, or Thomson, scattering event of a photon on a charged particle. Every atom consists of a positively charged nucleus, which we will neglect due to its negligibly small scattering cross-section, and negatively charged electrons distributed around the nucleus. Although we cannot predict the positions of these electrons as a function of time it is possible to approximately calculate the probability of finding an electron in a certain volume around the atomic nucleus, which would vary from one atom to another (see, e.g., (Rez, Rez *et al.* 1994)). Consider an isolated atom shown in Fig. 2.10 whose electrons scatter two initially phase-coherent photons approaching the atom along direction \mathbf{S}_0 at two random positions “within” the atom. Since we are dealing with sub-nanometer photonic wavelengths, the two scattered waves can be substantially dephased, depending on the scattering positions and the scattering angle, which are essentially stochastic variables. When we now collect the intensities of the diffracted waves from a large number of such random scattering events in a real-life measurement, we will be able to plot the registered intensity, which is schematically shown by yellow bars in Fig. 2.10, as a function of the scattering angle θ . The angular dependence of the diffracted intensity gets stronger with increasing atomic number. Today, instead of performing rather complex calculations of

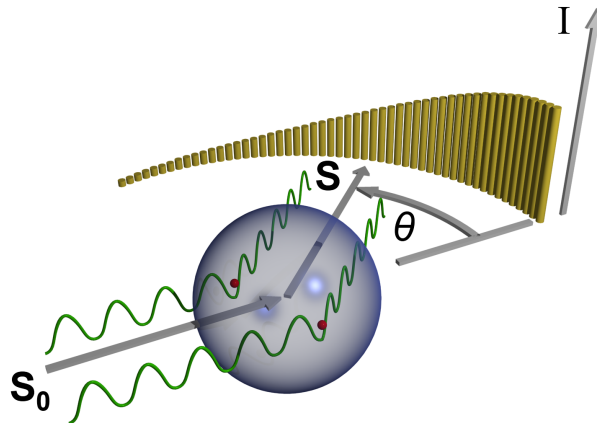


FIGURE 2.10: Diffraction of electromagnetic waves on an isolated atom.

the angular dependence of the diffracted intensity, one can use tabulated coefficients

(see, e.g., (Maslen, Fox *et al.* 2006)) a_i , b_i , and c of the polynomial

$$f(\sin \theta/\lambda) = \sum_{i=1}^4 a_i \exp(-b_i \sin^2 \theta/\lambda^2) + c \quad (2.23)$$

where θ is the Bragg angle and λ is the wavelength in angstroms²¹.

The *structure factor* F . The structure factor combines the phase shifts of the scattered waves from all atoms within an elementary unit cell and the Laue conditions for constructive interference. Thus, the structure factor for the reflection from the (hkl) plane of a crystal is written as

$$F(hkl) = \sum_{n=1}^N f_n \exp(i\phi_n) = \sum_{i=1}^N f_n \exp(2\pi i[hx_n + ky_n + lz_n]) \quad (2.24)$$

where ϕ_n is the phase of the scattered wave introduced by the n -th atom. x_n, y_n, z_n are the fractional coordinates of the n -th atom within the unit cell²², and h, k, l are integer numbers. Here, the phases ϕ_n are dot products between the scattering vector $\mathbf{Q} = (h, k, l)$ and the radius vector of the n -th atom $\mathbf{r}_n = (x_n, y_n, z_n)$. Since we are interested only in the scattering vectors \mathbf{Q} that already satisfy the Laue conditions, we only took integer-valued coordinates, even though any scattering vector could be considered in (2.24). The intensity of a given reflection is proportional to the squared structure factor $I \propto |F(hkl)|^2$. The structure factor is a combination of the atomic composition of a unit cell and its symmetry that creates a unique fingerprint of every compound as an x-ray diffraction pattern.

The *multiplicity* m . The multiplicity is defined as the number m of lattice planes with identical inter-planar distances d_{hkl} but with different combinations of (hkl) . Reflections from every such (hkl) plane will be eventually observed at identical Bragg angles θ , which amplifies the integral measured intensity in this direction. For example, for a simple cubic symmetry in a powder diffraction analysis the reflections (100), (010), and (001) will be seen at identical Bragg angles. Hence, it is sufficient to account only for the reflection (100) with multiplicity of 3.

The *geometry factor*. The integral intensity of every Bragg reflection is spread over a cone with angle 2θ (see Fig.2.7). The intensity from a given plane seen by a detector is then a function of the Bragg angle, since the total intensity will be spatially redistributed over the cone circumference. One accounts for this effect by introducing the geometry factor $G = \cos \theta / \sin 2\theta$.

²¹To be precise, the atomic factor also depends on temperature, which can be accounted for using the Debye-Waller corrections to the coefficients in (2.23).

²²Fractional coordinates are determined with respect to the three unit cell translational vectors and range from 0 to 1.

The *texture factor* T_{hkl} . If thin film crystallites are not oriented randomly but have some preferred orientation, then the measured intensity from the preferred (hkl) planes will be enhanced with respect to other planes compared to powder diffraction analysis. This is accounted for in the texture factor T_{hkl} , which appears as a weighing coefficient for every (hkl) reflection and is unity in powder diffraction analysis.

The *polarization factor*. As it was pointed out on p. 81, an electromagnetic wave scattered on a charged particle will be polarized. Thus, the initially circularly polarized²³ incident electromagnetic wave will be partially polarized after being reflected from a crystallite. This reflected wave will then redistribute its intensity between the tangential and the radial waves. We may write the polarization factor which reduces the registered intensity with increasing scattering angle as

$$C = \frac{1}{2} + \frac{1}{2} \cos^2 2\theta \quad (2.25)$$

The first term here stands for one half of the intensity of the tangentially polarized wave, which does not depend on the Bragg angle. The second term stands for the second half of the intensity brought by the radially polarized wave. This part of the reflected wave is always polarized in the plane of the reflection, which decreases the intensity seen by the detector as a function of the Bragg angle (see also (Kirkpatrick 1927)).

The *absorption factor*. It is known from optics that electromagnetic waves are absorbed while traveling through matter. According to the Lambert-Beer law, the intensity of the electromagnetic wave I_0 will be attenuated at the traveling distance l within a solid as $I_0 \exp(-\mu l)$, where μ is called a linear absorption coefficient. This coefficient varies with the atomic weight number, having the largest values in heavy elements, which implies strong attenuation in, e.g., $CeCoIn_5$ thin films. The absorption also depends on the wavelength of the incident wave and for the $Cu-K_\alpha$ line typical values of $\mu = 10^5$ - 10^7 m^{-1} would give penetration depths $z = 0.1$ - $10 \text{ }\mu\text{m}$, depending on the considered elements. The penetration depth z is defined here as the depth at which the intensity of the x-rays I_0 is reduced by a factor of e . From geometrical considerations the larger the incidence angle, i.e., the Bragg angle, the deeper the penetration of x-rays into the sample with maximum penetration depth at 90° . According to this, at small incidence angles a smaller crystal volume contributes to the intensity of constructively interfering x-rays and a larger crystal volume at large incidence angles. Thus, the intensity collected by the x-ray detector is the intensity of the incident beam multiplied by the absorption

²³Usually, x-ray tubes produce an equal combination of horizontally and vertically polarized waves, see, e.g., (Kirkpatrick 1927).

factor A , which is introduced as

$$A = 1 - \exp\left(-\frac{2\mu t}{\sin\theta}\right) \quad (2.26)$$

where t is the film thickness.

It is now possible to combine the discussed factors, which modify the diffracted intensity, into one expression. After integrating with (2.22) and introducing some simplifications (see pp. 29-36 in (Birkholz, Fewster *et al.* 2006)) one gets the following commonly used practical expression

$$I = K \cdot m \cdot T_{hkl} \cdot L \cdot G \cdot F(hkl)^2 \cdot A \quad (2.27)$$

where K is a scaling factor justifying the absolute values of the measured intensity and incorporating diffractometer factors.

Using the simplified expression (2.27), one may understand and simulate the intensities of the Bragg reflections for a given sample composition, crystallinity *etc.* What is still lacking for better understanding of x-ray patterns is the knowledge about factors influencing the peak positions. According to (2.21), there is a direct correspondence between the Bragg angle and the respective inter-planar distance d_{hkl} . However, there are several factors that limit the accuracy of the Bragg angle determination. The Bragg angle registered by a diffractometer $2\theta_{hkl}$ consists of the theoretically expected angle plus some corrections due to the specific sample properties giving rise to the reflection shift $2\theta_{hkl}^0$ and the instrumental error $\Delta 2\theta_{hkl}$, i.e., $2\theta_{hkl} = 2\theta_{hkl}^0 + \Delta 2\theta_{hkl}$. The main instrumental factors affecting the accuracy are *zero shift*, *height misalignment*, *flat sample*, *axial divergence* of the beam, *etc.* The zero shift is undoubtedly the largest instrumental factor in practice which must be accounted for in every analysis. If, however, an analysis with higher accuracy is desired, other sources of instrumental uncertainties must be estimated in order to deduce the measurement error. A detailed classification and description of these instrumental errors can be found in (Birkholz *et al.* 2006) or in (Pecharsky & Zavalij 2009). In practice, typical values for $\Delta 2\theta_{hkl}$ may be as large as 0.02° for a typical well-aligned diffractometer. This shift tends to be larger at small and large Bragg angles, while having the lowest values at around $2\theta = 90^\circ$.

Diffractometer used in this work

A Bruker D8 Discover diffractometer, shown in the left panel of Fig. 2.11, was used in this work for all x-ray measurements. It utilizes the parallel beam focusing geometry²⁴.

²⁴For difference between the Bragg-Brentano and the parallel beam optics see, e.g., (Verman & Kim 2004) and references therein.

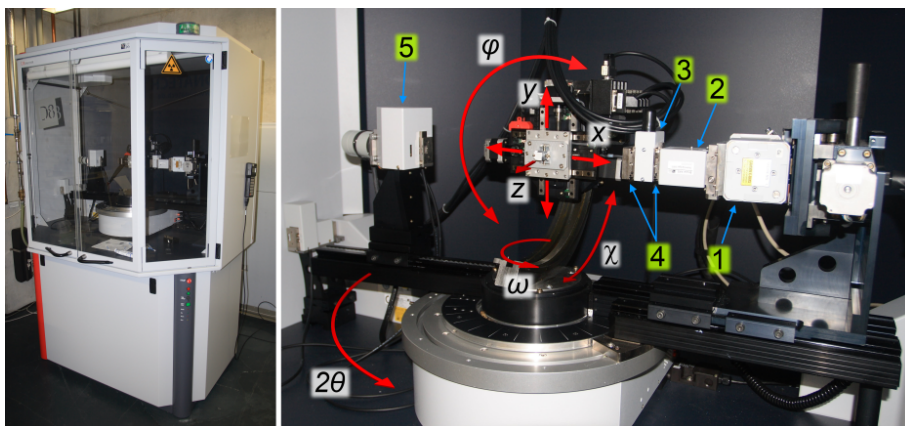


FIGURE 2.11: Photograph of the Bruker D8 Discover diffractometer used in this work. The degrees of freedom of the diffractometer are shown in the right panel. See text for details.

The primary optics side (right panel of Fig. 2.11) consists of a *Cu* x-ray source tube (1), which operates at 40 *kV* of accelerating voltage, a tilted gradient multilayer (Göbel) mirror (2), which reduces substantially the x-ray beam divergence (this is why this beam optics is termed as the parallel beam optics), and divergence slits (4). The variable slit (3) is controlled by a microprocessor and allows for automatic adjustment of the slit aperture as a function of the Bragg angle θ such that a constant width (1, 10 or 20 *mm*) of the sample is exposed to x-rays independent of the Bragg angle. The height of the conditioned x-ray beam cross-section, measured vertically in Fig. 2.11, is limited by the aperture height of the variable slit and by the manually exchangeable divergence slits at a value of approximately 20 *mm*. The width of the manual divergence slits, which condition the beam in *z* direction in Fig. 2.11, can range from 6 *mm* down to 0.15 *mm*, resulting in an opening angle from 3° down to 0.025° , respectively. The radius of the measuring circle²⁵ was set to 500 *mm*.

The secondary optics side (5) consists of a scintillation counter with a beryllium window and two beam conditioning subsystems one of which can be set active at a time. The first beam conditioning subsystem is a variable slit subsystem synchronized with the Bragg angle. The second subsystem is a triple reflective *Ge* (220) crystal-based monochromator. The receiving slit on the secondary side shares the same set of exchangeable slits as the divergence slits on the primary side. Thus, possible slit widths range from 6 *mm* down to 0.15 *mm* resulting in opening angles of the secondary optics from 1.8° down to 0.015° , respectively.

The names of the diffractometer axes are shown in the right panel of Fig. 2.11. The absolute accuracy of the ω and 2θ axes drives of the Bruker D8 Discover diffractometer is 0.005° , with reproducibility of 0.0001° , as guaranteed by the manufacturer. The

²⁵See also Fig. 2.9.

accuracy of the x and y axes drives is 0.001 mm , and of the z drive 0.0005 mm . The parallel beam optics of the D8 Discover is also suitable for grazing incidence diffraction measurements. For all scanning regimes utilizing the ω and 2θ axes, the positions of these axes are incremented in a step-like manner with an adjustable step integration time to fulfill the signal-to-noise level requirements.

Scanning regimes and alignments

Several scanning regimes were used in this work for characterization of the $CeCoIn_5$ and $CeIn_3$ thin films. These regimes are

- $\theta/2\theta$ regime
- ω -scan regime
- Grazing incidence diffraction (GID)
- φ - $\theta/2\theta$ scanning maps

The most commonly used regime is perhaps the $\theta/2\theta$, for which the diffracted intensity is registered while rotating the 2θ and ω axes in a step-like manner so that $\omega = 2\theta/2$ (see Fig. 2.9 and Fig. 2.11). In the ω -scan regime, the diffracted intensity is registered while the 2θ axis is fixed at a theoretically expected position²⁶ and the ω axis is varied around the $2\theta/2$ position. By taking x-ray diffraction data with one of the aforementioned regimes or by combining both, only atomic planes lying perpendicularly to the goniometer axis (axis z in Fig. 2.11) are probed. Alternatively, in the GID regime, it is possible to sample atomic planes lying parallel to the goniometer axis. For this regime, both the ω and the 2θ axes are fixed at the theoretically expected values for the tested (hkl) plane, while the diffracted intensity is registered as angle φ is varied²⁷. It has to be stressed that this regime is much more sensitive to the beam conditioning than the previous two regimes. This is so because the angle of incidence of x-rays onto the sample surface has to be not much larger than the angle of total reflection²⁸, which is usually less than 1° . For a φ - $\theta/2\theta$ scanning map a set of $\theta/2\theta$ scans are performed for different values of angle φ . With proper alignment of the sample, it is possible with this type of a scan to probe the relationship between the selected substrate crystallographic orientation or

²⁶This value of 2θ corresponds to a certain (hkl) reflection of a crystalline sample under investigation and can be found using special software, diffraction tables, or simply calculated by hand from the Bragg law and known unit cell dimensions of the investigated substance.

²⁷Typically, for one complete revolution.

²⁸On the one hand, we select a small angle of incidence in the GID geometry to increase the coherently scattering sample volume seen by the x-ray beam, which increases the scattered intensity. On the other hand, we cannot make this angle too close to the total reflection angle, because the reflected beam intensity will be dramatically decreased.

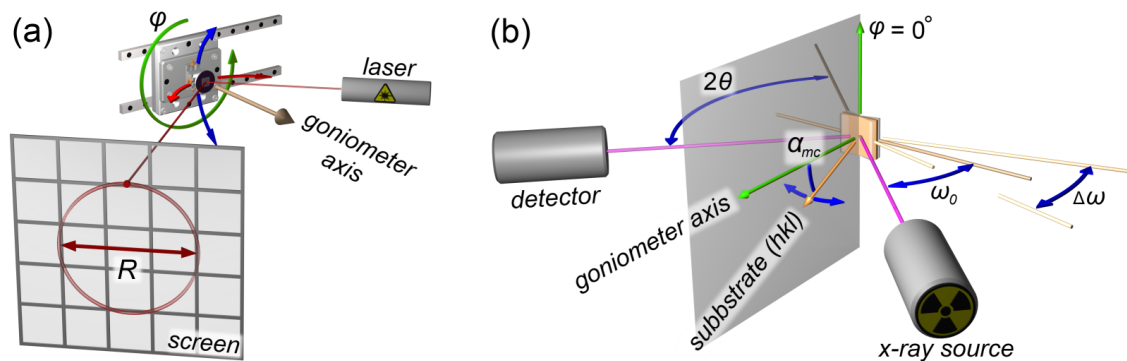


FIGURE 2.12: (a) Alignment of the sample's optical plane with the goniometer plane of rotation with the help of a laser beam which is reflected to a screen. (b) Optional second alignment step done with the help of an x-ray beam and a known substrate Bragg reflection.

the normal to the substrate optical surface and the selected crystallographic orientation of the $CeCoIn_5$ thin film crystallites. The result of such measurements can be presented as colour maps of intensities in the coordinates φ - $\theta/2\theta$, which are analyzed in Sec. 3.3.2. Here, we will present sample alignment procedures for the discussed scanning regimes.

Typically, all these regimes, except for GID, involve one or two alignment steps as shown in Fig. 2.12. In the first alignment step, a laser beam and a reflective screen are used (see Fig. 2.12(a)). The laser beam is essentially parallel to the laboratory floor. At the initial position, when $\varphi = 0^\circ$, the laser beam is reflected from the sample surface towards the screen where a laser spot is observed. When the angle φ is varied, the precession of the normal to the sample's optical surface around the goniometer axis will be reflected in an elliptical trajectory of the laser spot on the screen. The length of the ellipse's longer axis R and the distance screen-to-sample will define the laser alignment angular accuracy²⁹. By adjusting manually the sample's tilt along the directions shown by the blue and red arrows in Fig. 2.12(a) for several values of angle φ , it is possible in our setup to align the sample's optical plane with the goniometer axis with an accuracy not worse than $\delta = 0.0477^\circ$.

While a carefully performed laser alignment is the only alignment required for the φ - $\theta/2\theta$ scanning regime, optionally, for the other regimes where no dependency on φ is involved an additional alignment may be performed. For this alignment procedure, the x-ray beam and a known substrate Bragg reflection are used. 2θ and ω_0 are set to their theoretically expected values for the known substrate reflection. Then, an ω -scan is performed, i.e., the angle ω is varied around $\omega_0 = 2\theta/2$ within small limits $\pm\Delta\omega/2$ while the angle φ is fixed (see Fig. 2.12(b)). As a result, one finds a new value $\omega' \neq \omega_0$ which corresponds to the maximal diffracted intensity within the probed limits $\Delta\omega$. The

²⁹The distance sample-to-screen in this particular case was 3 m and the accuracy of the manual adjustment allowed to obtain $R \leq 2.5 \times 10^{-3}$ m.

difference $|\omega' - \omega_0|$ contains manual alignment errors and the substrate miscut α_{mc} . The latter is compensated *only* for a given value of φ which is commonly set to zero in this step. As it is shown in Fig. 2.12(b), a specific substrate (hkl) reflection will be aligned with the vertical plane shown in grey colour, so that the angle α_{mc} is not sensed by $\theta/2\theta$ and ω scans as long as φ angle is not varied.

2.4.2 Line profile analysis

Shortly after the discovery of the diffraction laws it was noted that the shapes of Bragg reflections contain rich information about the sample structure. In 1918 Scherrer introduced an expression relating the average crystallite size with the already known broadening of the Bragg reflections in $\theta/2\theta$ x-ray diffractograms (Scherrer 1918a). The physical reason for this type of broadening is the finite size of the coherently scattering crystal volume. Later, it turned out that microstrain fields³⁰ and structural defects also cause broadening of Bragg reflections due to inter-atomic distance variations. It was also established that the reflection broadening due to size effects is described by the Cauchy function, while that due to microstructural defects by the Gaussian function.

Line profile analysis (LPA) (Cheary & Coelho 1992, Scardi & Leoni 2006, Snyder, Fiala *et al.* 1999) is a collection of computational and analytical methods that allow to discriminate the crystallite size broadening and the broadening caused by microstructural defects by analyzing the shape of Bragg reflections. LPA can be applied to monocrystalline, polycrystalline or powder samples. In this work, we used LPA methods to analyze the relative strain in the $CeCoIn_5$ thin films. The complete LPA procedure is rather time-consuming when not automatized. For this reason, the LPA was performed with an interactive software developed during this work. It uses a provided $\theta/2\theta$ profile to construct a Williamson-Hall plot for a selected set of Bragg reflections. The strain and size broadening coefficients are then obtained.

Model functions

In LPA, we use model parametric functions or their weighed mixture to numerically fit a given Bragg reflection profile. When the numerical fitting is complete, the experimentally measured intensity as a function of the Bragg angle can be recovered as

$$I(2\theta) = I_0 f(2\theta - 2\theta_0, 2\omega, \dots) \quad (2.28)$$

³⁰The term *microstrain* stems from the typical dimensions in which it is established. The microstrain dimensions are much smaller than the attenuation coefficient $1/\mu$ that causes broadening. For macrostrains whose dimensions exceed $1/\mu$ positions of Bragg reflections will be shifted. The LPA deals only with reflection shape effects, i.e., with microstructural defects.

where $2\theta_0$ is the centroid peak position, 2ω is the full width at half maximum (FWHM), I_0 is the reflection's maximal intensity. Besides $2\theta_0$, 2ω , and I_0 , f may also depend on some other parameters of the reflection's shape. As it was pointed out, the Cauchy shape function and the Gauss shape function are used

$$f_C(2\theta) = \frac{1}{1 + \frac{(2\theta - 2\theta_0)^2}{\omega^2}} \quad (2.29)$$

$$f_G(2\theta) = \exp\left[-\frac{\ln 2 (2\theta - 2\theta_0)^2}{\omega^2}\right]$$

To unify the analysis, 2ω in (2.29) is replaced by the *integral breadth*, which is the width of a rectangle having the same height and area as those of the Bragg reflection it replaces

$$\beta = \frac{1}{I_0} \int_{-\infty}^{\infty} I(2\theta) d2\theta \quad (2.30)$$

As demonstrated in Fig. 2.13, if a Gauss type curve and a Cauchy type curve had identical values of 2ω , then, due to its larger tails, the Cauchy type curve would have a larger integral breadth, i.e., $\beta_C > \beta_G$.

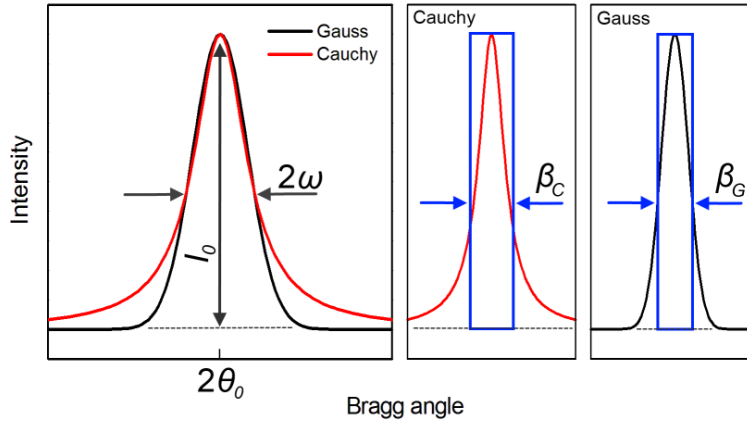


FIGURE 2.13: Left panel demonstrates the difference between the Gauss and Cauchy shape functions for identical values of FWHM 2ω . The right two panels demonstrate the concept of an integral breadth (blue rectangles of widths β_C and β_G) and its different values for the two functions shown in the left panel. The area of either rectangle equals to the area under the corresponding curve.

Since it is very rare that a measured Bragg reflection is adequately fitted by either of those functions, their weighed mixture is usually used. Several functions based on such a weighed mixture are commonly employed, namely, Pearson VII, Voigt, or pseudo-Voigt (Birkholz *et al.* 2006), which all allow fits of comparable quality. For the LPA in this work, the Pearson VII function was employed

$$f_P(2\theta) = \frac{1}{[1 + (\sqrt{2} - 1)(2\theta - 2\theta_0)^2/\omega^2]^m} \quad (2.31)$$

The Cauchy function is obtained from (2.31) for $m = 1$, while the Gauss function results for $m \rightarrow \infty$. Hence, m is a single parameter that allows smooth variation of the relative weight of either of the two model functions in one expression. The integral breadth of the line shape given by (2.31) may be approximated as

$$\beta = \frac{\pi 2^{2(1-m)} \Gamma(2m-1)}{(2^{1/m} - 1) [\Gamma(m)]^2} \omega \quad (2.32)$$

where $\Gamma(x)$ is the gamma function, for which the approximation

$$\Gamma(x) = \frac{2\pi}{x} \left(\frac{1}{e} \left[x + \frac{1}{12x - 1/(10x)} \right] \right)^x$$

was used (see (Nemes 2010)). The values of β obtained by fitting (2.31) to the measured Bragg reflections are used in the Williamson-Hall plot analysis, which is described at the end of this section.

Instrumental line profile

When an idealized diffractometer is assumed, then the broadened nature of Bragg reflections is only due to sample characteristics. Real instruments, however, are always sources of an instrumental broadening (Alexander 1954). Thus, the measured intensity $h(2\theta)$ is a convolution of the sample function, which we can approximate by the model function $f(2\theta)$, and the instrumental line profile $g(2\theta)$, so that $h(2\theta) = f(2\theta) * g(2\theta)$. The instrumental function $g(2\theta)$ depends on beam divergences, receiving slit width, misalignments, x-ray tube wavelength composition, flatness of the sample surface, *etc.* The exceptionally small divergence of the parallel beam optics of the diffractometer used in this work and a much smaller FWHM of the Bragg reflections measured on monocrystalline sapphire samples than of those measured on $CeCoIn_5$ thin films³¹ allows us to neglect the influence of the instrumental line profile on the measured $CeCoIn_5$ diffractograms. Nevertheless, when such an analysis is obligatory, the fundamental parameters profile fitting (FPPF) method may be used (Cheary & Coelho 1992) which employs measurements on a standard sample.

The multi-component nature of the K -line characteristic emission spectrum of the Cu anode x-ray source was accounted for in this work during the numerical fitting of the measured diffractograms. This was required since no monochromator was used during

³¹From numerical fitting, the FWHM of the (110) Bragg peak of a monocrystalline Al_2O_3 substrate for the $Cu-K^{\alpha 1\alpha}$ line was found to be 0.026° , while the FWHM of the (001) Bragg peak of $CeCoIn_5$ for the same characteristic line was found to be not less than 0.06° and at least 0.12° for the $CeCoIn_5$ (006) peak. The measurements were done at identical instrument configurations.

the x-ray data acquisition on the $CeCoIn_5$ thin films in order to maintain a high counting rate and signal-to-noise ratio within a reasonable time period. It is known that the Cu characteristic K^α line is a quartet (Hölzer, Fritsch *et al.* 1997, Thompson, Vaughan *et al.* 2001), whose components' wavelengths and their relative intensities are summarized in Table 2.1³². The reflections corresponding to the $Cu-K^\beta$ lines were also observed

TABLE 2.1: Parameters of the characteristic $Cu-K^\alpha$ lines.

Emission line	Energy (eV) / Centroid wavelength λ (Å)	Relative intensity I_0
$K^{\alpha_{1a}}$	8047.837 / 1.54054	0.957
$K^{\alpha_{1b}}$	8045.367 / 1.54101	0.090
$K^{\alpha_{2a}}$	8027.993 / 1.54435	0.334
$K^{\alpha_{2b}}$	8026.504 / 1.54463	0.111

in our diffractograms but neglected because these reflections are well apart from the K^α reflections whose line shapes are therefore not modified. The four K^α lines decompose every measured $CeCoIn_5$ (hkl) reflection line profile into four principal reflections. Each principal reflection corresponds to a single $CeCoIn_5$ (hkl) plane but different $Cu-K^\alpha$ lines. Thus, the measured intensity is a sum of four line shapes which are individually numerically fitted by the corresponding line shape functions (2.31) each having an individual centroid position $2\theta_0$ and initial intensity I_0 given by the data from Table 2.1. Although the number of fitting parameters is dramatically increased due to the presence of 4 line shapes, the fitting algorithm makes use of fixed relative wavelengths and relative intensities within a group of four principal reflections³³. The fitting procedure requires an approximate position of some reference line which was always taken to be the $K^{\alpha_{1a}}$ line. The appropriate positions of the other principal reflections are calculated using the expression

$$\theta_i = \arcsin \left(\frac{\lambda_i}{\lambda_0} \sin \theta_0 \right) \quad (2.33)$$

where λ_0 and θ_0 are the wavelength and the angular position corresponding to the $K^{\alpha_{1a}}$ line, and λ_i runs over the remaining K^α wavelengths for which a corresponding reflection position θ_i has to be found.

³²Fast switching between wavelength λ and energy E may be done via the relation λ [Å] = 12398/ E [eV].

³³Small variations of the ratios between the intensities and the wavelengths within the K^{α_1} and K^{α_2} doublets around the theoretical values were allowed in order to accommodate a possible variation of these values for the particular diffractometer.

Scherrer equation and crystallite shapes

An x-ray diffraction pattern is mostly defined by the structure factor (2.24) which contains the three Laue conditions and coordinates of the atoms in the unit cell. Thus, the diffracted intensity is the result of interference between N scatterers for which a summation in (2.24) is performed. Then, the sum in (2.24) can be extended to M unit cells. By varying M it can be shown that the shape of Bragg reflections becomes the narrower the larger the number of unit cells. Following these considerations, Scherrer obtained in 1918 a formula relating the dimensions of a coherently scattering crystallite with the FWHM of its Bragg peaks (Scherrer 1918b). This formula may be written in terms of the previously introduced integral breadth as

$$D_{cube} = \frac{K_S \lambda}{\beta_S \cos \theta_0} \quad (2.34)$$

where β_S is the integral breadth in radians and D_{cube} is the length scale of a cube-shaped crystallite. An important implication of this formula is that the widths of the reflections within a set of Bragg reflections are inversely proportional to the cosines of the Bragg angles. To account for the deviation of the crystallite shape from a cube, a shape parameter K_S is introduced into the Scherrer formula, which, however, does not change the result qualitatively.

Size and strain broadening, Williamson-Hall plots

The strain fields, caused by crystallographic defects through small local variations of inter-planar spacings $d \pm \Delta d$, affect the line shape of Bragg reflections. According to the Bragg law (2.19), for such a small variation of an inter-planar spacing around its relaxed value the diffraction condition will already be satisfied for a limited number of planes at vectors $\mathbf{Q}_{hkl} \pm \Delta \mathbf{Q}$. This will cause overlapping of the diffracted intensities within a broadened range of angles and smoothening of the Bragg reflections. One of the aims of LPA is to relate the distribution of the microstrain fields with the shape of the Bragg reflections. The problem is generally difficult due to the large variety of defect types a crystal structure may contain since each type has its own fingerprint on the line shape of the Bragg reflections. The analysis can be simplified if the shape evolution within a single family of Bragg reflections is known. However, other systematic variations of the line shape within this family, caused by instrumental factors as well as by the sample's properties unrelated to defects, have to be estimated.

In spite of the complex nature of the Bragg reflections broadening, it is possible to single out several key features of the strain-induced broadening that distinguish it from

the other broadening types. Strain is characterized by a dimensionless quantity $\varepsilon = \Delta d/d$. The relation between the reflection broadening and the strain can be obtained by differentiating the Bragg equation (2.19)³⁴

$$\frac{\Delta d}{\Delta(2\theta)} = \frac{n\lambda \cos \theta_0}{4 \sin^2 \theta_0} = \frac{d}{2 \tan \theta_0} \quad (2.35)$$

Clearly, the variation $\Delta(2\theta)$, which is intimately related to the variation of the interplanar spacing Δd , is associated with the integral breadth β . Using the expression for strain introduced in the text above and (2.35), we can write

$$2K_D \varepsilon_{rms} \tan \theta_0 = \beta_D \quad (2.36)$$

where coefficient K_D is introduced to account for the different nature of strains, β_D is the Bragg reflections broadening due to defects, and ε_{rms} is the root mean square of the strain distribution ε .

By now, we have introduced two types of Bragg reflection broadening: due to size and due to strain. Thus, we can write the total broadening as

$$\beta_{2\theta} = \beta_S + \beta_D \quad (2.37)$$

If the size and strain integral breadths in (2.37) are replaced by those defined in (2.34) and (2.36) we will arrive at

$$\beta_{2\theta} = \frac{K_S \lambda}{D \cos \theta_0} + 2K_D \varepsilon_{rms} \tan \theta_0 \quad (2.38)$$

Equation (2.38) was proposed by Williamson and Hall (Williamson & Hall 1953) for discriminating between the size and the strain broadening effects. Multiplying both sides of (2.38) by $\cos \theta_0/\lambda$, we obtain

$$\beta_{2\theta} \frac{\cos \theta_0}{\lambda} = \frac{K_S}{D} + K_D \varepsilon_{rms} \frac{2 \sin \theta_0}{\lambda} \quad (2.39)$$

When this is plotted as $\beta \cos \theta_0/\lambda$ versus $2 \sin \theta_0/\lambda$, (2.39) is nothing else but an equation of a straight line, which is schematically shown in Fig. 2.14.

Two essential quantities are obtained from the Williamson-Hall plot: the average crystallite dimension parameter K_S/D and the average microstructural strain parameter $K_D \varepsilon_{rms}$. The blue solid line in Fig. 2.14 is a linear fit to the integral breadths for a set of Bragg reflections (red crosses) obtained from the previous analysis. The schematic plot demonstrates data points only within one family of crystallographic planes, namely

³⁴Due to the unfortunate coincidence between the notations for the inter-planar distance in the Bragg law and the differential operator, we use here Δ for the latter.

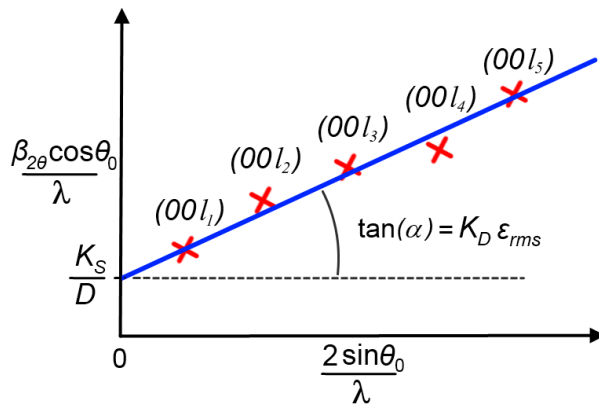


FIGURE 2.14: Schematic Williamson-Hall plot. $K_D \epsilon_{rms}$ and K_S/D are determined from a linear fit (blue solid line) to hypothetical experimental data (red crosses). These two values are recognized as the average strain and the average crystallite size parameter (see text).

for the $\{00l\}$ family. In this case, the position of each data point in a plot is defined by the same strain field or the same set of fields. Thus, the increase of the broadening with the increase of the reflection index is solely due to the angular dependence of a particular set of strain fields, which was derived from the Bragg law. In case of data shortage one can use Bragg reflections from different families of planes with some further analysis, assuming a specific model of the microstructural defects.

2.5 Low-temperature measurements

The growing of thin films, their structural and compositional characterization, even the investigations of the structural defects all served in this work for careful analysis of the films' properties prior to the investigations of their electronic transport properties. We were interested in the temperature-dependent transport properties of $CeCoIn_5$ and $CeIn_3$ thin films. When performed on a thin film or a microcrystal patterned as a tunneling diode or a SQUID, transport measurements can reveal essential electronic properties of the studied materials. In this work, the electronic transport studies were focused on quantum mechanical tunneling phenomena. Nevertheless, simple temperature-dependent resistivity measurements were often also performed for better sample characterization.

A 4He and a 3He cryostat were used for low-temperature measurements. The 4He cryostat used in this work features a variable temperature insert (VTI) allowing to span the temperature range of 1.6-300 K. It is equipped with a superconducting magnet for measurements in magnetic fields up to 9 T. The cryostat design is simple, suits well for fast measurements and allows for simple sample exchange, but on the other hand

it has limited temperature stability due to its specific design. Temperatures between 4.2 K and room temperature are controlled by a microprocessor controlled heater and the manually controlled Helium pumping rate³⁵. Temperatures below 4.2 K are achieved by lowering the pressure of 4He vapour around the sample using a manually controlled needle valve.

The 3He cryostat has a top-loading VTI, which gives access to a sample temperature range of 0.28-100 K in the fully loaded position of the top-loading probe (TLP). Measurements above 100 K are performed by varying the loading positions of the insert. The cryostat is equipped with a superconducting magnet for measurements in magnetic fields up to 11 T . Generally, the operation of a 3He cryostat is more sophisticated than that of a 4He cryostat, but the former gives access to much lower temperatures and has much better low-temperature stability. Above approximately 1.7 K the temperature can be kept constant arbitrarily long, while the stability at lower temperatures relies on the availability of the condensed 3He in the sample pot³⁶.

The typical construction of a 3He cryostat is shown in Fig. 2.15. The sample is located at the bottom end of the TLP (G). The TLP chamber is *always* kept evacuated from air. Additionally, it is thermally shielded by the inner vacuum can (IVC) (K). The advantageous ability of the 3He type cryostat to achieve much lower temperatures compared to the 4He type cryostat is realized through condensation and controlled vaporization of 3He . Let us briefly consider the essential internal parts of the 3He cryostat.

The *sorption pump* J is made of porous charcoal which stores the gaseous 3He . It can absorb gases when being cooled down and, respectively, desorb gases when being warmed up. The temperature of the pump during the stand-by mode of the cryostat is close to the temperature of liquid 4He , though in practice it is a bit higher due to thermal coupling to the slightly warmer TLP rod³⁷. When the cryostat is in use, the temperature of the charcoal is increased up to 30 K , which rises the pressure of the gaseous 3He within the VTI chamber up to a few hundred millibars. The temperature of the pump is maintained both by an electronically controlled individual resistive heater and by the manually controlled pumping rate of the 4He vapour through the charcoal body.

The *1K-pot* I is essentially a fridge used for condensation of gaseous 3He which is thermally coupled to the sample chamber. In the stand-by mode, its temperature is close to that of the sorption pump. During operation, the 1K-pot is cooled down. Its

³⁵Vaporized 4He is pumped through the sample space thus cooling the sample.

³⁶Sample pot and 3He -pot can be used interchangeably.

³⁷The TLP rod in turn is thermally coupled to the environment via the top flange and, weakly, to the internal dewar D with liquid 4He . Due to very weak thermal conductance of the long and specially constructed TLP, nevertheless, its lower parts remain cold.

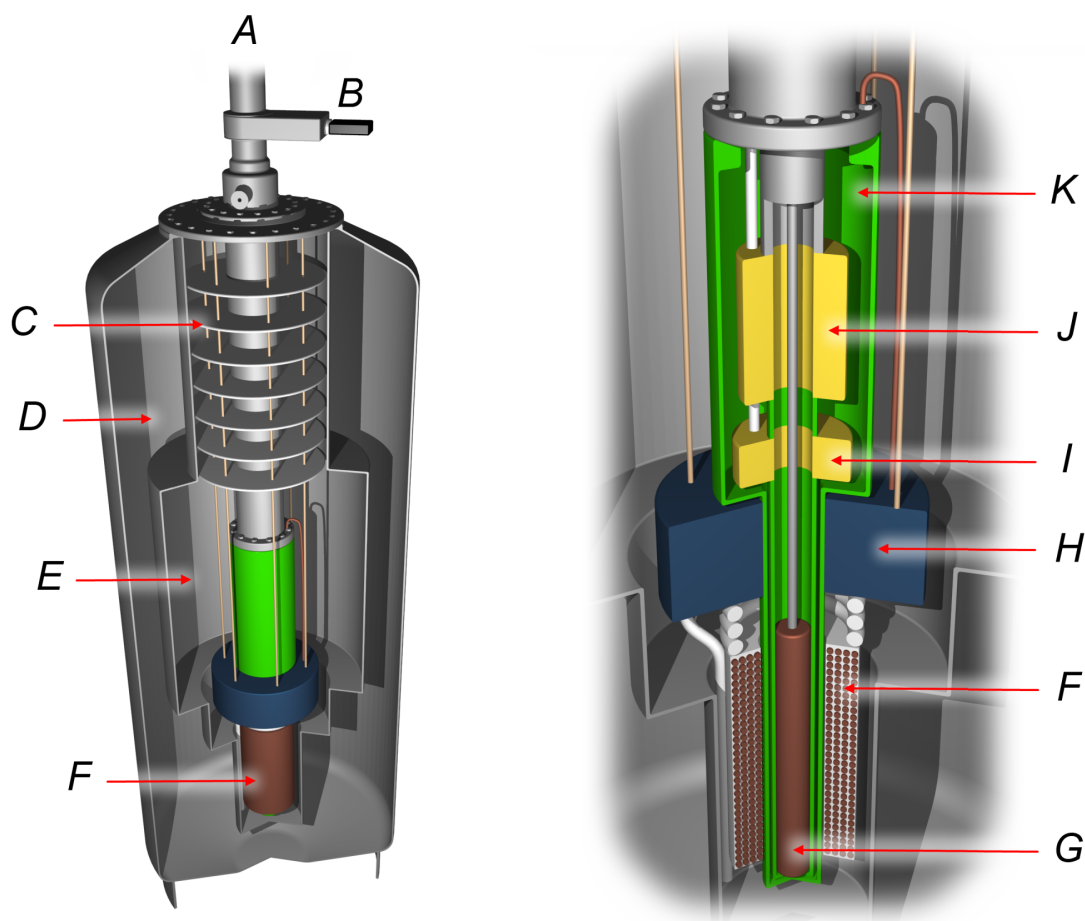


FIGURE 2.15: Schematic representation of a typical ^3He cryostat internal construction. The cryostat consists of an external part of the evacuated TLP chamber *A*, the vacuum gate *B*, the radiation shields *C*, the outer vacuum can *D*, the ^4He dewar *E*, the SC magnet *F*, the top loading probe *G*, the λ -cooler *H*, the 1K-pot *I*, the sorption pump *J*, and the inner vacuum can *K*.

temperature is controlled similarly to that of the charcoal pump via an individual heater and the pumping rate of ^4He vapour through it.

The ^4He dewar *E* stores about 60 liters of liquid ^4He . It is thermally shielded from the environment by the evacuated outer chamber *D*. A system of radiation shields *C* is used to minimize thermal coupling of the dewar and other cold parts within the cryostat to the environment through the upper mounting flange.

The *superconducting magnet* *F* located at the bottom of the cryostat is immersed into the liquid ^4He which maintains the magnet coils at low temperature. At 4.2 K, it can produce up to 9 T of magnetic field measured at the TLP sample slot *G*. If a higher magnetic field is required, the magnet can be further cooled down by a λ -cooler *H*. The magnetic field is controlled by a superconducting magnet controller (Scientific Magnetics SMC-120-10) with a step of not less than 0.1 mT up to 9 T. The measurements with

fields up to 200 mT with a step of as small as 5 μT were performed by controlling the SC magnet current with a Keithley Source Meter 2400. Alternatively, an Oxford Instruments IPS 120-10 SC magnet controller was used for fields up to 9 T and field steps as small as 10 μT .

During the cooling down operation of the 3He cryostat, its charcoal pump is warmed up and the pressure of the 3He vapour within the TLP rises. Next, the temperature of the 1K-pot is lowered and when it is low enough³⁸, the 3He starts to condense and is collected in the 3He -pot, right around the sample. After the condensation procedure has been completed³⁹, the temperature of the charcoal pump is decreased and it starts to pump the 3He vapour, thus lowering its pressure within the TLP chamber and, as a consequence, the temperature of the remaining liquid 3He and the sample.

By pumping the liquefied 3He 280 mK , measured at the sample position, can be achieved⁴⁰. This temperature may be maintained for as long as 12 hours or as short as a few minutes, which strongly depends on the amount of liquid 3He in the 3He pot and the heat dissipations produced by the measuring procedures.

2.5.1 Low-level electrical measurements

The small sample dimensions, the low energy scale being probed, and the low temperatures restrict the electrical signals used for transport measurements to low levels. Voltages and currents in the micro and sub-micro ranges needed to be measured. In order to sense such small signals, one needs both an appropriate measuring setup and some knowledge of low-level signal measuring techniques.

The transport measurements in this work were done using mainly the four-terminal method, which allows to sense the voltage drop associated only with the sample. Two setups were used:

- A programmable DC current/voltage source (Keithley 2400 type) and a DC nanovoltmeter (Agilent 34420A)
- A dynamic resistance measurement setup based on a lock-in amplifier (Stanford SR830) and a DC nanovoltmeter (Agilent 34420A)

³⁸The thermodynamic equilibrium between the liquid and its vapour is given by vapour pressure charts, which are shown for 4He and 3He in Appendix B.

³⁹The longer the condensation process the more cooling work can be done at the lowest achievable temperature.

⁴⁰Temperatures as low as 7 mK can be reached with a similar principle by using a controlled mixture of 3He and 4He gases, which is realized in so-called *dilution refrigerators*.

The first setup was used for temperature-dependent resistivity measurements and for voltage/current controlled voltage-to-current (V - I) characteristic measurements described in Sections 3.2.2, 3.2.3, 3.4.1. The second setup was used for transport measurements on SQUID devices and tunneling diodes described in Section 3.4.2-3.4.4. All measuring devices as well as the SC magnet controller and the temperature controller (Lake Shore Temperature Controller Model 340) were controlled via a PC with self-written software in Python script language.

The electrical measurements in this work were performed on samples that are mostly low resistive. Thus, the samples are low voltage sources from the electrical point of view, which defines possible sources of errors. These error sources can be the following: offset voltages, noise, and common mode currents.

The offset voltages are the most common sources of systematic errors in low-level measurements produced by the measuring equipment. Ideally, no voltage should be read when the voltmeter terminals are shorted. In reality, however, a non-zero voltage will be registered. The reasons for this small voltage offset are thermoelectric effects, radio frequency interference, current/voltage offsets introduced by the input stages of the meter itself⁴¹. A *thermoelectric* voltage is generated under a temperature gradient across the contacts between electrical wires made of dissimilar materials. This voltage occurs due to different Seebeck coefficients of the two materials⁴² and should be considered for low-temperature measurements where large temperature gradients appear along the measurement wires. This effect, however, can be minimized by minimizing the temperature gradients along the electrical contacts between different materials. The measuring devices should be kept far from heat sources/sinks and allowed to reach their steady temperature. These errors can also be reduced during measurements by reversing the polarity of the current source and averaging the two measured values⁴³, which is called the *current-reversal method*.

Another source of voltage offsets can be *interference effects* with radio frequencies. The interferences may be caused by signals such as radio broadcasting, switching mode power supplies or transformers, fluorescent lamp power supplies, *etc.* Usually, these offsets are small but nevertheless must be considered for very sensitive measurements. Additionally, non-ohmic contacts within the electrical scheme will act as rectifiers for radio frequency noise, hence introducing non-zero and, possibly, non-linear DC voltage shifts. To reduce these effects, all possible sources of radio frequencies should be minimized, the wires

⁴¹These are generally not constant and vary with the device's temperature, with temperature gradients within the device, over the lifetime of the device, in the presence of external magnetic fields *etc.*

⁴²It can be less than $0.2 \mu\text{V}/^\circ\text{C}$ for a crimped Cu-Cu contact or as large as $1000 \mu\text{V}/^\circ\text{C}$ for a Cu-CuO interface.

⁴³The thermal time constant of the measured circuit must be large in comparison to the voltmeter response time, otherwise the error will not be compensated as expected.

and contacts should be shielded with materials with high relative magnetic permeability coefficients. Alternatively, at the expense of the measurement response time, capacitive filtering may be used.

Voltmeters themselves are also sources of offset voltages. The input stage of a voltmeter has non-ideal behaviour, such as non-zero input current, input current offset⁴⁴, voltage offset at the inputs *etc.* These sources are not permanent and are continuously changing under the influence of aging effects, temperature, the signal strength being detected *etc.* However, offsets of this type may be accounted for right before sensitive measurements by using a relative zero function, which is usually present in all laboratory voltmeters.

Another source of inaccurate readings is the intrinsic noise in electrical conductors generated by the non-zero thermal energy of electrons, which is called the Johnson-Nyquist noise. Though this noise is typically small, for sensitive measurements it should be estimated for its possible influence. The root mean square voltage noise V_n is related with the resistance R , the absolute temperature T , and the noise bandwidth Δf in Hz as

$$V_n = \sqrt{4k_B T R \Delta f} \quad (2.40)$$

where k_B is the Boltzmann constant $1.38 \times 10^{-23} J/K$. For a resistor of $100 k\Omega$, $T = 300 K$, and a typical voltmeter bandwidth (Belen’kii 1968) of $8 kHz$, $V_n = 3.6 \mu V$. The thermal voltage noise associated with an RC circuit is given by (Sarpeshkar, Delbruck *et al.* 1993)

$$V_n = \sqrt{4k_B T / C} \quad (2.41)$$

where C is the capacitance of the circuit. Fluctuations of electrical current can also be obtained in a similar way. Reducing the temperature of highly resistive parts of a meter or reducing its bandwidth would reduce the noise. The reduction of the voltmeter’s bandwidth can be achieved by increasing the integration time, which, however, will increase the response time. On the other hand, the increased response time will increase non-zero offsets due to thermal voltages and other longer period fluctuations.

Lock-in measurements

We saw in (1.53) from the previous chapter that the electrical current through a tunneling barrier is proportional to the voltage drop across this barrier times the number of available electronic states. Thus, the differential dI/dV should be proportional to the

⁴⁴That is, the positive and the negative inputs of the differential amplifier and the input stage of the voltmeter are subject to different input currents. This non-zero current difference, which depends on the resistance connected to the input terminals of the voltmeter, will cause a corresponding voltage drop, which is further amplified at the following stages of the voltmeter.

electronic density of states. Of course, one can obtain the dI/dV characteristic by measuring an $I(V)$ curve and differentiating it numerically. However, such differentiation is not accurate. Indeed, if we measure the $I(V)$ curve using a simple DC current source and a voltmeter, for the numerical differentiation we will have to use small differences between the values of the nearby data points. These small differences will have to be calculated using a large common mode signal. On the other hand, the noise, which is inevitably present in the measured data, will be the larger the larger the signal becomes. Thus, in practice we cannot provide the required accuracy for numerical differentiation of the measured $I(V)$ curves.

Fortunately, there exists a setup for a direct measurement of the n -th harmonic of the initial $I(V)$ curve, which is generally called the *lock-in* technique. The setup that we used in our work to measure dynamic resistance/conductance curves is schematically shown in Fig. 2.16. The sample, depicted as an orange filled box, has resistance R , which is

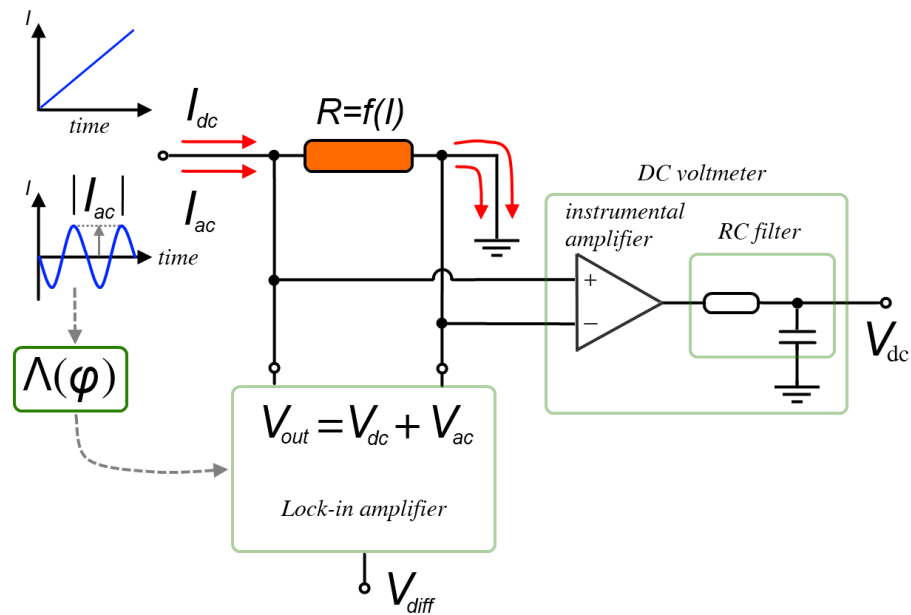


FIGURE 2.16: The general idea of the lock-in measurement setup.

a function of the electrical current I . Imagine that we have two sources of electrical current, whose time dependencies are shown to the left. One is a source of a direct current I_{dc} and the other is a source of an alternating sine wave current I_{ac} with known amplitude and frequency⁴⁵. We propagate these two currents through the sample. The corresponding voltage drop across the sample is measured by both a DC voltmeter and a lock-in amplifier. Assume that the low-pass RC filter of the DC voltmeter has a cut-off frequency much lower than the frequency of I_{ac} so that the voltage measured here, V_{dc} , is proportional to I_{dc} only. The lock-in amplifier does not have such a filter and senses

⁴⁵In our setup both current sources were approximated by voltage sources with serially connected resistors whose values are large compared to the sample resistance. For calculation details see Appendix A.

both voltage drop V_{ac} corresponding to I_{ac} and V_{dc} corresponding to I_{dc} . Additionally, assume that we continuously inform the lock-in amplifier about the phase of I_{ac} using the following logic function

$$\Lambda(\varphi) = \begin{cases} 1 & \text{if } I_{ac} > 0 \\ 0 & \text{if } I_{ac} \leq 0 \end{cases} \quad (2.42)$$

Let us consider now the simplified internal construction of the lock-in amplifier shown in Fig. 2.17. The combined voltage $V_{ac} + V_{dc}$ is sensed at (i) by the unity gain differential amplifier. The signal is then transmitted to a switch box, which automatically switches between positions A and B controlled by the logic function $\Lambda(\varphi)$, as it is shown in the figure. After the switch, the voltage at (ii) is either transmitted without changes or

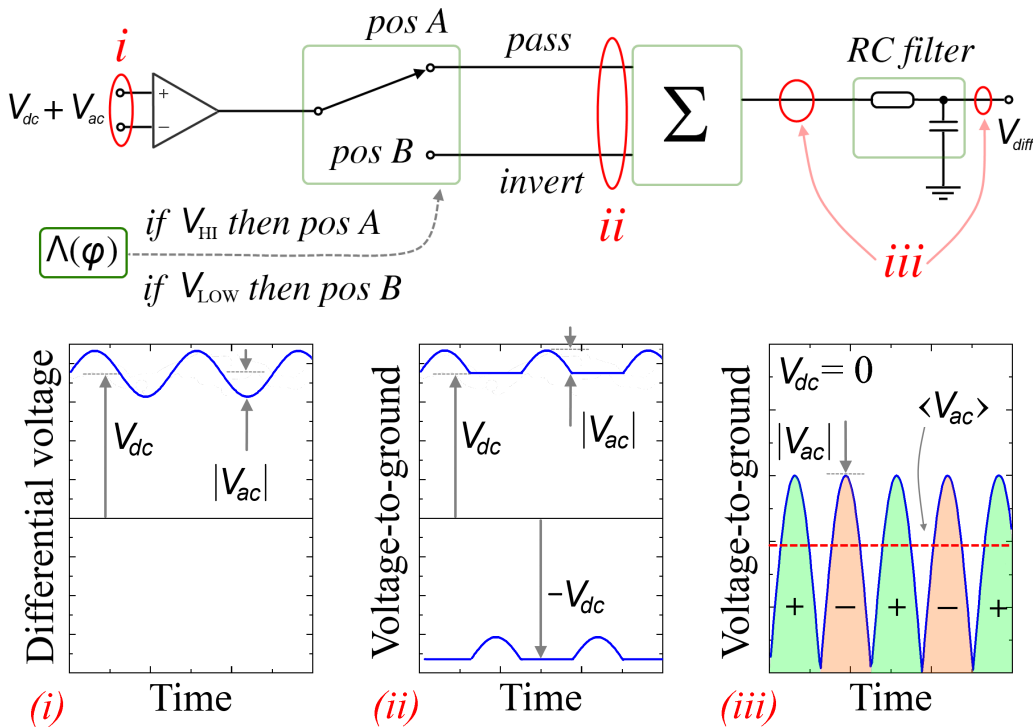


FIGURE 2.17: Demonstration of the signal conditioning within a lock-in amplifier (upper scheme) with the respective schematic view of the signal waveforms (lower graphs).

inverted. Both signals are then added together within the summing box, which cancels out any V_{dc} component. Thus, only a rectified V_{ac} signal is transferred to the low-pass RC filter in (iii), where it is smoothed out and the DC voltage V_{diff} is read at its output. It can be shown that the ratio between the amplitudes V_{ac}/I_{ac} (or their averaged values) at a given DC current bias I_{dc} is the steepness of the function $V_{dc} = f(I_{dc})$ at this DC

current bias⁴⁶. Thus, this ratio is the first derivative dV/dI or the differential resistance

$$dR = \frac{\langle V_{ac} \rangle}{\langle I_{ac} \rangle} = \frac{V_{diff}}{\langle I_{ac} \rangle} \quad (2.43)$$

Hence, the described setup allows to measure differential signals on large common mode signals with largely improved sensitivity compared to the traditional DC based measurements.

⁴⁶It is similar to a transistor used as a voltage amplifier, whose amplification ratio is given by the steepness of the load line.

Chapter 3

Overview of experimental results

3.1 Introduction

In this chapter, we will discuss the main results of our growth and electronic transport studies on $CeCoIn_5$ and $CeIn_3$ thin films. Many of the technical details of growth, preparation, structuring, and measuring techniques, which otherwise might have appeared in great numbers in each section, are omitted to keep the discussion more physical than technical. Nevertheless, since these details or recipes, many of which were obtained through tedious time-consuming optimizations, validate our results, the reader is referred, when required, to Appendix E for growth and structuring settings, Appendix A for settings of the lock-in measuring setup, and Appendix D for x-ray diffraction tables. The discussion will use the physical concepts from Chapter 1 and the methodological concepts from Chapter 2. In several cases, detailed descriptions of non-trivial structuring steps are presented as well to justify the obtained physical results.

The chapter is divided into three parts. First, we discuss the $CeIn_3$ thin film growth and electronic transport studies, including the $CeIn_3$ thin film microcrystal study. The second part focuses on the $CeCoIn_5$ thin film growth. In particular, we carry out orientational and microstrain analysis of the $CeCoIn_5$ thin films using x-ray diffractometry, which was not done for the $CeIn_3$ thin films. Finally, we will discuss in detail electronic transport measurements on microbridges prepared on $CeCoIn_5$ thin film microcrystals.

One should note that the results on the $CeCoIn_5$ microbridges presented in the last section are analyzed mainly for the superconducting regime. However, a well-reproducible peculiar behaviour of the dynamic conductance characteristics of these $CeCoIn_5$ microbridges is also observed in the normal state up to approximately 10 K in magnetic fields up to 8 T applied along the $CeCoIn_5$ c -axis. Due to the specific patterned geometry of these microbridges on the one hand and the complex low-temperature electronic

properties of $CeCoIn_5$ on the other, we are not able to provide a unified explanation of the normal state peculiarities at the moment of writing. Therefore, some representative normal state characteristics will be shown in Appendix F but not discussed in the main text.

3.2 $CeIn_3$ growth study

3.2.1 Surface morphology

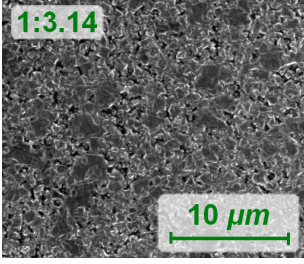
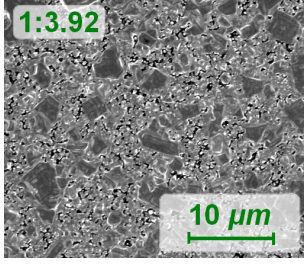
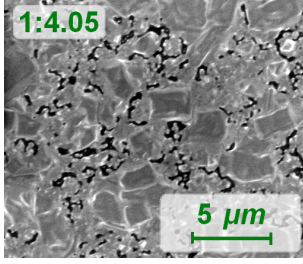
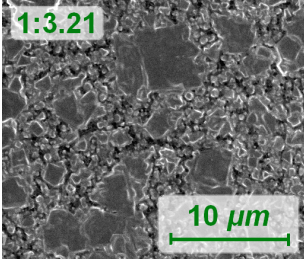
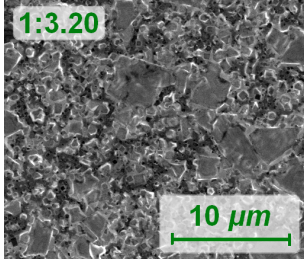
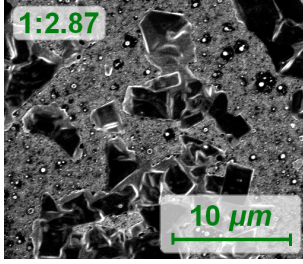
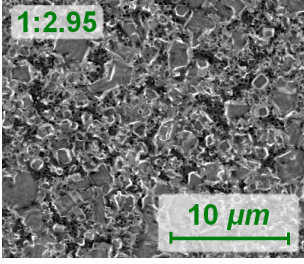
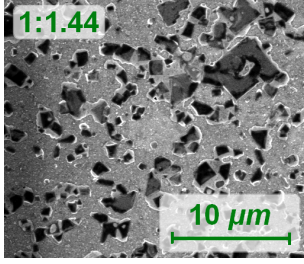
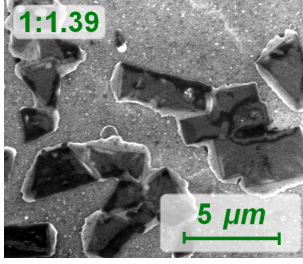
The $CeIn_3$ growth study included systematic investigations of the influences of the substrate type used for growth, the nominal substrate temperature T_s , and the substrate holder material on the $CeIn_3$ films' surface morphology. To compare the quality of different films we used their structural and phase purities, which were established using x-ray diffractometry and energy dispersive x-ray spectroscopy (EDXS) techniques. The variation of the $CeIn_3$ thin film surface morphology for several substrates and substrate holder materials as seen with a scanning electron microscope (SEM) are shown in Table 3.1 for $T_s = 500\text{ }^\circ C$ and in Table 3.2 for $T_s = 600\text{ }^\circ C$. The x-ray diffraction data taken for these two sample sets are presented in Tables 3.3 and 3.4 for $T_s = 500\text{ }^\circ C$ and $T_s = 600\text{ }^\circ C$, respectively¹. The molar ratios $Ce:In$ determined with EDXS analysis for each sample are shown in the tables. Here, the holders named "Inconel 1" and "Inconel 2" are nominally identical. The samples shown in the tables below were grown using the growth parameters obtained after the calibration of the effusion cell fluxes² (see also Sec. 2.2 and Sec. 2.3.5). The EDXS analysis was performed using 10 kV of accelerating voltage for the primary electrons. The quantification analysis was done using the $Ce^{L\alpha}$ (4.839 eV) and $In^{L\alpha}$ (3.286 eV) characteristic lines when the smallest peak among the analyzed spectral lines reached the intensity of 1000 counts. The accuracy of the quantification analysis was estimated as 3%, based on the average data scattering for a single sample.

Let us first analyze the samples grown at the nominal substrate temperature $T_s = 500\text{ }^\circ C$ (Table 3.1 and Table 3.3). The surface morphologies of these films are discontinuous for all substrate and holder types. Although one expects no or small influence of the holder material on the films' surface morphology and composition, strong variations were systematically observed. The smallest variations of both the nucleation strength and the $Ce:In$ ratio were observed for $a-Al_2O_3$ substrates, when compared to the films grown on $c-Al_2O_3$ and MgO (100). The $CeIn_3$ thin films grown on $a-Al_2O_3$ also demonstrate

¹For identification of the Bragg reflections, please, refer to Appendix D.

²The same inconel holder was used for all test growths.

TABLE 3.1: SEM micrographs of the surface morphology of $CeIn_3$ thin films grown at the nominal substrate temperature $T_s = 500\text{ }^\circ\text{C}$ using several combinations of the substrate type and the substrate holder material. The molar ratio $Ce:In$ obtained for each sample with EDXS analysis is shown in the left top corner of the respective figure.

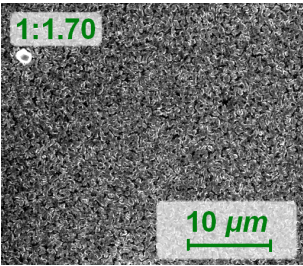
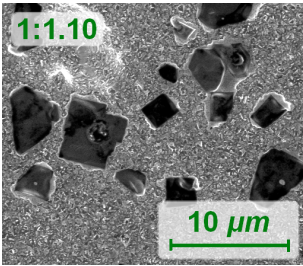
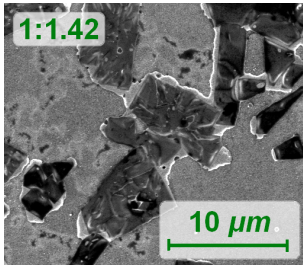
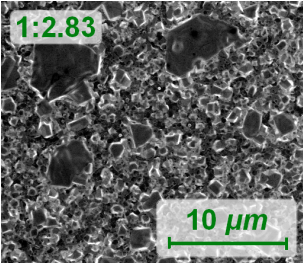
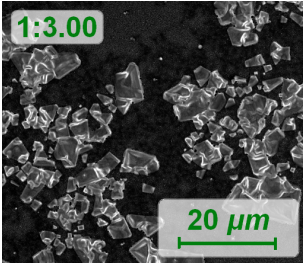
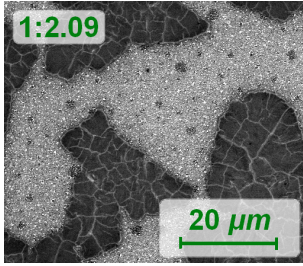
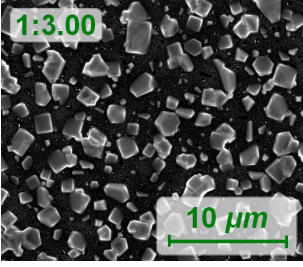
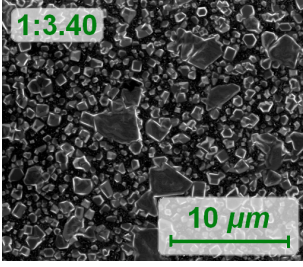
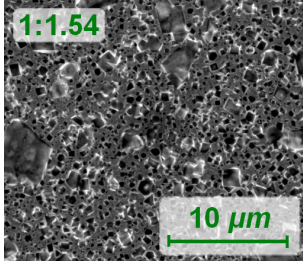
		Substrate		
		$\alpha\text{-Al}_2\text{O}_3$	$c\text{-Al}_2\text{O}_3$	MgO (100)
Holder material	Steel			
	Inconel 1			
	Inconel 2			

slightly better phase purity as seen in the x-ray diffraction analysis (see Table 3.3) when compared to the other two substrate types.

The smallest variation of the nucleation strength is observed when the steel holder is used, though the $Ce:In$ ratio and the purity of the $CeIn_3$ phase according to the x-ray diffraction data (Table. 3.3) strongly vary between the substrate types. It is known that the thermal conductivity of steel is by about 10% larger than that of inconel alloy (Sweet, Roth *et al.* 1987). This difference would result in a stronger temperature gradient over the inconel holders than over the steel holder. Thus, when two substrates are mounted on a steel holder and on an inconel holder that are both kept at nominally identical temperatures³ T_s , both substrate temperatures T_s^a will be reduced although the first substrate will stay at a slightly larger temperature than the second one. If one uses

³In our system, the temperature is monitored at the back side of the holder via a thermocouple radiatively coupled to the sample holder. See also Sec. 2.2.

TABLE 3.2: SEM micrographs of the surface morphology of $CeIn_3$ thin films grown at the nominal substrate temperature $T_s = 600 \text{ }^\circ\text{C}$ using several combinations of the substrate type and the substrate holder material. The molar ratio $Ce:In$ obtained for each sample with EDXS analysis is shown in the left top corner of the respective figure.

		Substrate		
		$\alpha\text{-Al}_2\text{O}_3$	$c\text{-Al}_2\text{O}_3$	MgO (100)
Holder material	Steel			
	Inconel 1			
	Inconel 2			

glue to mount the substrates (see Sec. 2.2.3), the variations of T_s^a also become non-systematic. Depending on the sensitivity of $CeIn_3$ films to the growth conditions, both systematic and non-systematic variations of T_s^a can cause the observed variations of the films' quality.

Let us consider now the samples grown at the nominal substrate temperature $T_s = 600 \text{ }^\circ\text{C}$ (Table 3.2 and Table 3.4). The value of T_s is now increased by about 13% over that corresponding to the previous set of samples. Such an increase will make the systematic variation of T_s^a between different holder materials stronger. For a stronger variation of T_s^a one should expect stronger variation of the $CeIn_3$ thin films surface morphology. Indeed, as we see in Table 3.2, the variation of the surface morphology is now stronger than in the previous set of samples for all holder materials. According to the EDXS data, the samples within the second set grown on the steel holder demonstrate

TABLE 3.3: X-ray diffraction patterns of $CeIn_3$ thin films grown at the nominal substrate temperature $T_s = 500$ °C using several combinations of the substrate type and the substrate holder material. The molar ratio $Ce:In$ obtained for each sample with EDXS analysis is shown in the left top corner of the corresponding figure. In all diffractograms the ordinates represent the signal intensity in counts and the abscissas represent the Bragg angle.

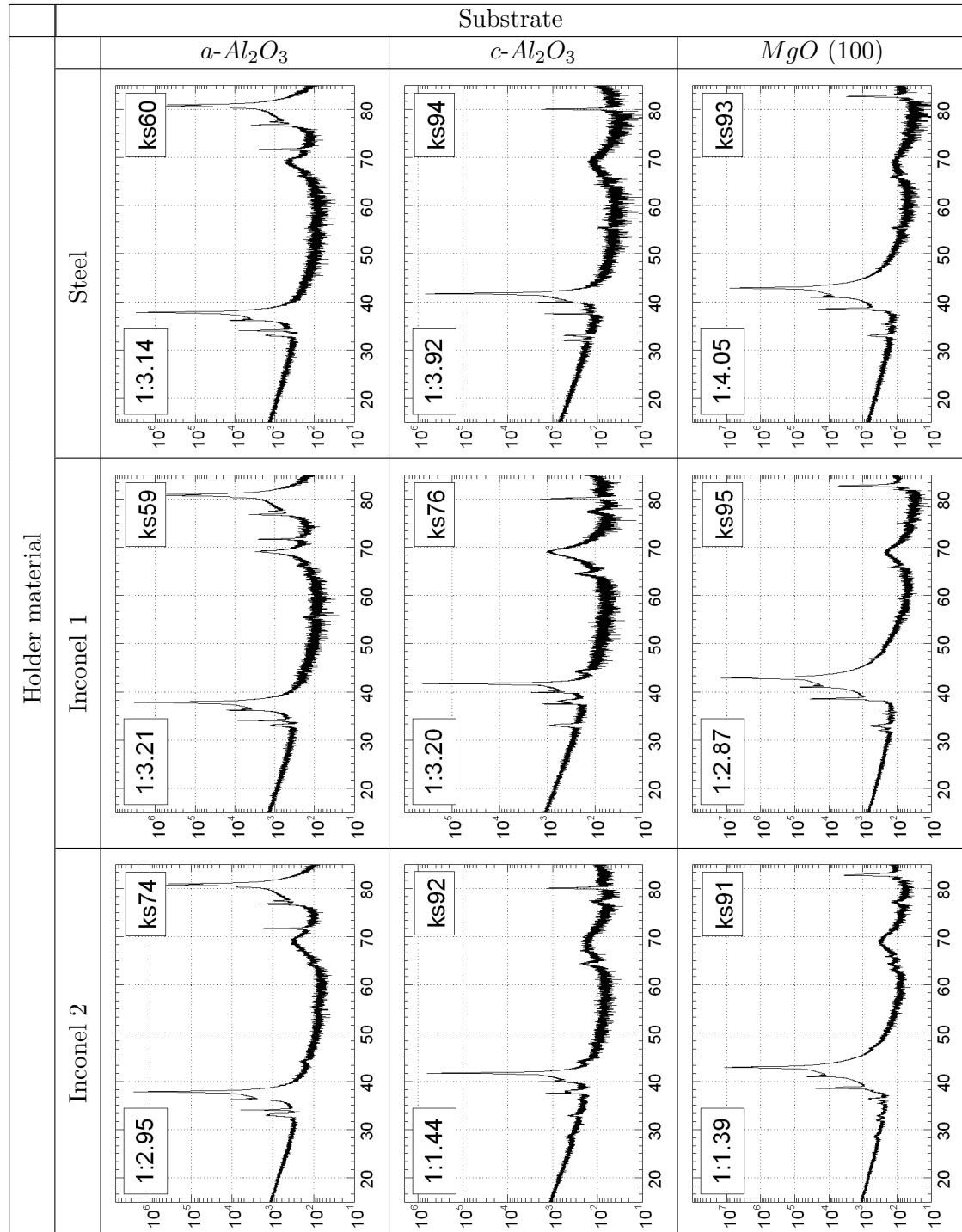
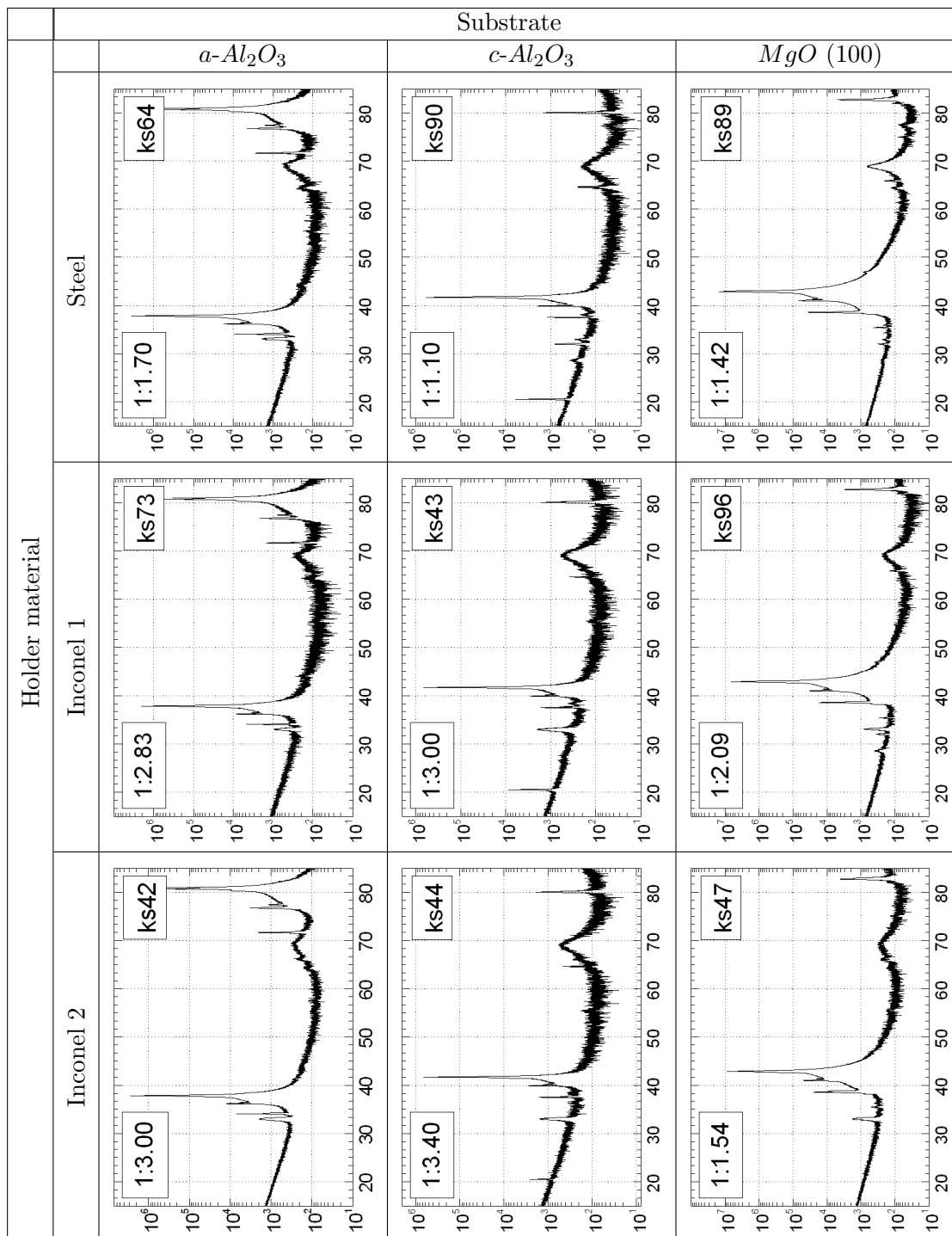


TABLE 3.4: X-ray diffraction patterns of $CeIn_3$ thin films grown at the nominal substrate temperature $T_s = 600\text{ }^\circ\text{C}$ using several combinations of the substrate type and the substrate holder material. The molar ratio $Ce:In$ obtained for each sample with EDXS analysis is shown in the left top corner of the corresponding figure. In all diffractograms the ordinates represent the signal intensity in counts and the abscissas represent the Bragg angle.



large deficiencies of In (large $Ce:In$ ratios). This suggests an enhanced desorption rate of In molecules from the substrate surface during growth. Since In has a smaller vaporization enthalpy than Ce , even a small variation of the substrate temperature T_s^a in the used temperature range will increase more strongly the desorption rate of In molecules than that of Ce molecules, which results in an enhanced ratio $Ce:In$. As we discussed above, for the inconel holders one expects lower values of T_s^a than for the steel holder. Thus, when the inconel holders are used, the desorption rate of In molecules from the substrate surface will be less than in the case of the steel holder. This would result in smaller ratios $Ce:In$ for the inconel holders, which is reflected in the data. In spite of the large ratios $Ce:In$ for the samples grown on the steel holder within the second set, all the samples grown on $\alpha-Al_2O_3$, including the one grown using the steel holder, have the best purity according to the x-ray diffraction data (Table 3.4).

For either sample set, holder material, and substrate type, the $CeIn_3$ [$Pm\bar{3}m$] {111} phase, if present, dominates over other $CeIn_3$ crystallographic orientations as seen in the x-ray diffraction data. Among the weaker reflections in the case of $c-Al_2O_3$ and MgO (100), $CeIn_3$ {011}, $CeIn_3$ {001}, $CeIn_3$ {113}, In [$I4/mmm$] {011}, Ce_2In [$P6_3/mmc$] {110} were found. The presence of In [$I4/mmm$] in the x-ray diffraction patterns indicates that In crystallites exist in the film, are sufficiently well protected from ambient air, and are not oxidized. This, in turn, suggests that In tends to crystallize separately at the initial stages of growth.

The performed study demonstrated difficulties associated with the $CeIn_3$ thin film growth. In spite of working under UHV conditions and using clean constituent material sources, the films' quality is still very sensitive to small uncontrollable variations of the growth parameters. Strong variability of the $CeIn_3$ thin films quality was observed even for nominally identical growth conditions, suggesting the high sensitivity of the $CeIn_3$ growth dynamics to these conditions. The films grown on $\alpha-Al_2O_3$ substrates at the nominal substrate temperature $T_s = 500$ °C using the steel holder demonstrate the best reproducibility of their quality among the tested combinations.

3.2.2 Simultaneous growth

The results of the previous study suggest that the uncontrollable variations of the growth parameters (e.g., the real substrate temperature T_s^a , the variations in fluxes of constituent elements, the substrate surface contamination level *etc.*) are strong enough to substantially modify the $CeIn_3$ thin films' morphology.

In the study discussed in this subsection, we focused on the influence of the substrate temperature T_s^a on the surface morphology of the $CeIn_3$ thin films and their transport

properties (see also (Foyevtsov, Reith *et al.* 2010)). Taking into account the lack of reproducibility observed in the previous study, here, each sample set was grown in a single growth process with variable T_s^a between different samples within a set. In this case, a substrate holder should accommodate several substrates, each having its own temperature, while all other growth parameters are essentially identical for all samples. Such a holder was constructed as shown schematically in Fig. 3.1. The holder consists of a standard stainless steel base (see Fig. 2.3) with a spot-welded spiral made of stainless steel as well. The spiral, on which substrates are glued, is welded to the base at one of its ends while the other end remains free and is lifted above the base surface. The nominal temperature of the base $T_s^{(0)}$ is assumed to be constant, i.e., it is the heat source for the spiral part. The spiral part exchanges heat with the base plate via thermal conduction through its welded end and via radiative coupling according to the Stefan-Boltzmann law. This geometry suggests a variation of temperature along the spiral. Such a temperature profile was simulated for an ideal case using the finite element method as implemented in the heat transfer module of the Comsol Multiphysics software package. The thermal conductivity of the metal of $44.5 \text{ W}/(\text{m} \cdot \text{K})$ and a surface emissivity of 0.4 were used for the simulations. The resulting temperatures as a function of coordinate along the spiral starting at the welded end are shown in Fig. 3.1. The solid and the broken lines correspond to the expected temperature profiles for $T_s^{(0)} = 550 \text{ }^\circ\text{C}$ and $T_s^{(0)} = 600 \text{ }^\circ\text{C}$, respectively. The circles indicate approximate positions of the substrates along the spiral. The substrates were mounted using silver colloidal liquid, as described earlier in Sec. 2.2.3.

Two sample sets, with three samples in each, were grown on $\alpha\text{-Al}_2\text{O}_3$ substrates with the spiral holder at $T_s^{(0)} = 550 \text{ }^\circ\text{C}$ and $T_s^{(0)} = 600 \text{ }^\circ\text{C}$. SEM micrographs of the resulting

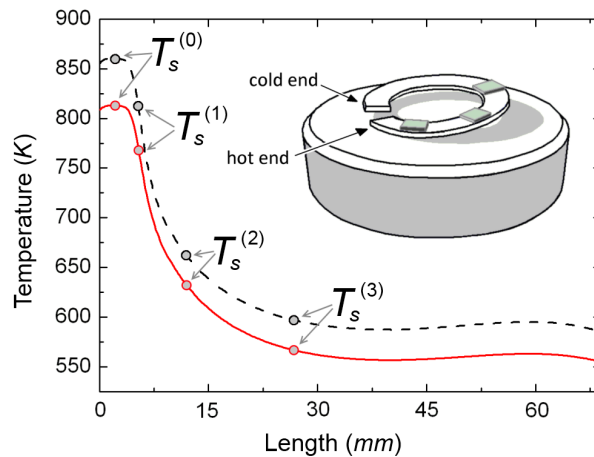


FIGURE 3.1: Spiral holder used for simultaneous thin film growth with variable substrate temperature. The plot demonstrates simulated temperature profiles along the spiral for two hot-end temperatures, $T_s = 550 \text{ }^\circ\text{C}$ and $T_s = 600 \text{ }^\circ\text{C}$.

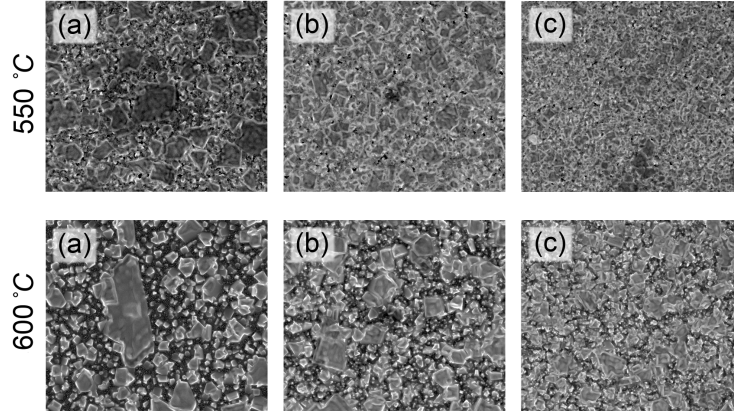


FIGURE 3.2: The SEM micrographs of the films surface morphology from the two sample sets for $T_s^{(0)} = 550 \text{ }^\circ\text{C}$ and $T_s^{(0)} = 600 \text{ }^\circ\text{C}$. (a) correspond to the highest substrate temperature within each set, i.e., to $T_s^{(1)}$, (b) correspond to $T_s^{(2)}$, and (c) correspond to the lowest substrate temperature $T_s^{(3)}$. The area of each micrograph is approximately $25 \times 20 \text{ } \mu\text{m}^2$.

surface morphologies are shown in Fig. 3.2. Morphologically, the $T_s^{(0)} = 550 \text{ }^\circ\text{C}$ samples are more densely packed by microcrystals, while the $T_s^{(0)} = 600 \text{ }^\circ\text{C}$ samples are less dense. A comparison with the previous growth study reveals similar trends for the packing density as a function of temperature, while the surface morphology variation is more systematic in this experiment. The $Ce:In$ molar ratio was found to be 1:3 for all samples within the accuracy of the EDXS analysis, which contrasts to the previous growth study. The x-ray diffraction analysis also suggests the presence of mainly the $CeIn_3$ {111} phase (see Fig. 3.3). The x-ray diffractograms for the samples within each set are very similar and only one pattern is shown for each series in Fig. 3.3. Such a reproducibility of x-ray diffractograms within each set, in contrast to the results discussed in the previous section, suggests that the uncontrollable deviations of growth conditions had identical influences on the thin film growth within one set and that the variations of the surface morphology that we see are due to variations of the substrate temperature. It is clear from Fig. 3.3 that the volume fraction of the $CeIn_3$ phase, which is proportional to the area of the Bragg reflection, is larger for the set grown at $T_s^{(0)} = 600 \text{ }^\circ\text{C}$. Additionally, for this set the $CeIn_3$ (200) reflection appears.

We performed temperature-dependent electronic transport measurements on each sample from these two sets. The measured electrical resistance curves shown in Fig. 3.4(a) and (b) correspond to the samples from the $T_s^{(0)} = 550 \text{ }^\circ\text{C}$ and $T_s^{(0)} = 600 \text{ }^\circ\text{C}$ sets, respectively. All the samples demonstrate metallic conductivity despite the apparently isolated microcrystals morphology of the samples grown at the highest T_s , i.e., at $T_s^{(1)}$. Assuming a film thickness of 300 nm , their resistivity is at most 3 times larger than the $CeIn_3$ bulk resistivity (Walker, Grosche *et al.* 1997, Shishido, Shibauchi *et al.* 2010).

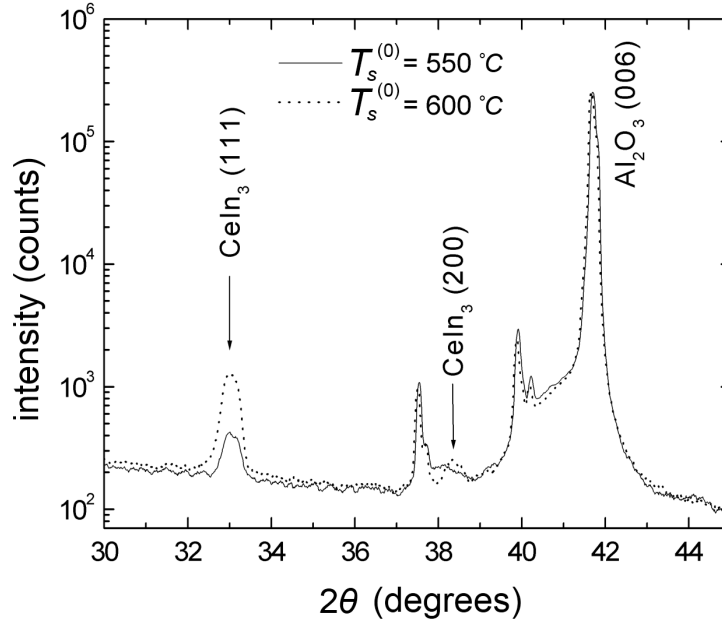


FIGURE 3.3: X-ray diffractograms of $CeIn_3$ thin films grown in two series as described in the text. The diffractograms are identical within each series and only one typical dataset is shown for every series.

Let us first discuss the samples from the $T_s^{(0)} = 550\text{ °C}$ set. The resistance curve of the sample grown at the lowest substrate temperature within this set, $T_s^{(3)}$, demonstrates a broad peak at about 50 K , which is a characteristic feature of all heavy-fermion compounds and corresponds to the crossover from an incoherent to a coherent Kondo scattering. This peak gets substantially reduced as the temperature $T_s^{(i)}$ increases. This change suggests that the weight of the $CeIn_3$ contribution to the total resistivity decreases as $T_s^{(i)}$ increases. All the curves demonstrate a kink at about 10 K , which corresponds to the antiferromagnetic transition of $CeIn_3$, i.e., the Néel temperature T_N . The low-temperature part of the resistivity is shown in the inset of Fig. 3.4(a). Here, one finds another kink at about 3.3 K , which most probably corresponds to the SC transition of In . The kinks, as opposed to the Kondo peak at 50 K , become more pronounced as $T_s^{(i)}$ increases. The residual resistance ratio RRR (R_{200K}/R_{4K}) decreases with decreasing $T_s^{(i)}$ from 3.12 for the highest temperature, $T_s^{(1)}$, to 2.04 for the lowest one, $T_s^{(3)}$. The sample grown at the highest substrate temperature $T_s^{(1)}$ becomes superconducting below 3 K . Analyzing the evolutions of the Kondo peak and of the transition at 3.3 K with variation of $T_s^{(i)}$, a few conclusions can be made. First, the films contain an In impurity phase, which conducts current in parallel with the $CeIn_3$ phase. The volume distribution between the $CeIn_3$ and the In phases shifts towards the In phase as the substrate temperature increases. Second, the fact that the sample grown at the highest temperature $T_s^{(1)}$ becomes superconducting suggests percolation of the In phase through the whole film. Although according to the EDXS analysis the $Ce:In$ ratio for

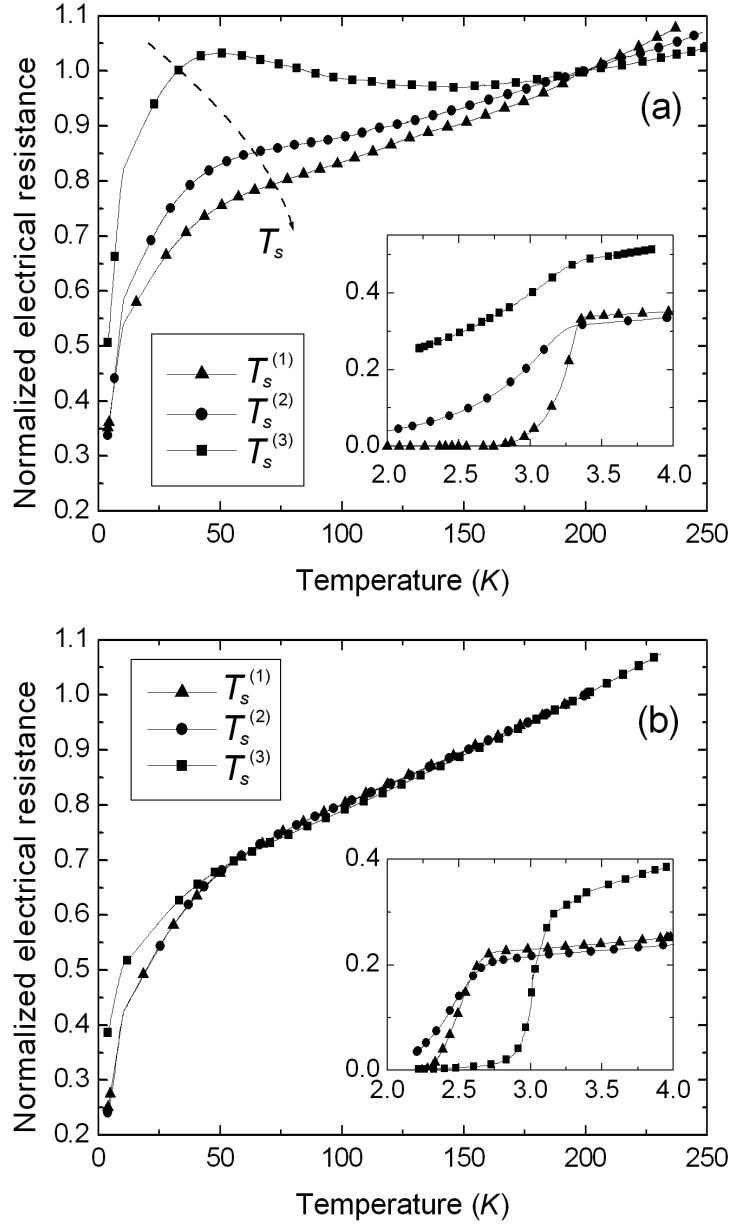


FIGURE 3.4: Temperature-dependent resistance measurements on $CeIn_3$ thin films (a) for the series $T_s^{(0)} = 550$ °C and (b) for the series $T_s^{(0)} = 600$ °C.

all the films within the two sets is very close to the stoichiometric one, it is possible that In forms its own crystals as a result of its high surface diffusivity in comparison to Ce . These In crystals may conduct current or even percolate through the film, which can already take place at 2% volume fraction (Balberg & Binenbaum 1987). As a result, the stronger the In islands overlap the stronger the linear component caused by In in the temperature dependence of the resistivity of the films. The evolution of the RRR also supports this idea, since bulk In samples of high purity tend to show a higher value of $RRR \approx 5000$ (Meissner & Zdanis 1958) than $RRR \approx 100$ of high purity bulk $CeIn_3$ samples (Grosche, Walker *et al.* 2001, Settai, Kubo *et al.* 2005).

The strong evidences for the presence of an In phase in the thin films, however, do not contradict the fact that no In Bragg reflections were found in the x-ray diffractograms. First, in particular for In the substrate-adatom interaction is weaker than the adatom-adatom interaction. Consequently, the crystal volume of In should be distributed between different crystallographic orientations, which may substantially reduce the intensity of the corresponding Bragg reflections. Second, as it was mentioned, even a small amount of In could be sufficient for percolation, which makes the observation of In Bragg reflections unlikely.

The samples grown at $T_s^{(0)} = 600\text{ }^\circ\text{C}$ demonstrate similar electrical resistance properties (see Fig. 3.4(b)). The shoulder around 50 K is suppressed even stronger. The transitions at around 3 K are more abrupt and now two samples become superconducting. Their temperature dependences of resistivity suggest a stronger influence of the In impurity phase and higher probability for its percolation. The RRR value, as in the previous case, decreases with decreasing $T_s^{(i)}$: from 4 for the hottest sample down to 2.6 for the coldest one. The absolute values of the RRR are larger than in the previous set, which also supports the assumption of a larger contribution of In to the resistivity.

The surface morphology of the $CeIn_3$ thin films demonstrates a systematic variability, as one would expect from the consistent variations of just one growth parameter, the substrate temperature in this case. The x-ray diffraction data of the films demonstrate no detectable variation within one set. Nevertheless, according to the simulated temperature profile along the spiral, the ranges of the substrate temperature $T_s^{(i)}$ variations from the two sets overlap and therefore one would expect consistently overlapping results in the variation of the x-ray and the resistivity data from both sets, which however is not the case. This, in turn, might be explained by still uncontrollable variations of some growth parameters from one set to another. In this case, one may observe logical variability within each set, but poor coherence between the results from different sets.

3.2.3 Microcrystal measurements

Considering the results described in the previous two sections and the results reported in literature, we can speculate that the surface morphology of the $CeIn_3$ and, anticipating results from the $CeCoIn_5$ growth study from Sec. 3.3.1, $CeCoIn_5$ thin films cannot be sufficiently improved within the existing degree of control of the growth parameters. On the other hand, to perform planar tunneling spectroscopy studies on these compounds one would require smooth epitaxial films. In order to nevertheless proceed in this direction, we decided to use individual $CeIn_3$ or $CeCoIn_5$ thin film growth domains to be selectively patterned as planar tunneling diodes. The $CeIn_3$ and $CeCoIn_5$ thin film

growth domains are microcrystals with a preferred crystallographic orientation, which are also large enough to demonstrate bulk SC properties.

In this section we describe the preparation of and transport measurements on an individual $CeIn_3$ thin film microcrystal. For the transport measurements, a suitable $CeIn_3$ film was pre-patterned with ultra-violet (UV) photolithography and then micropatterned using SEM techniques. During the micropatterning, a selected microcrystal was electrically isolated from the remaining conductive thin film⁴ and connected via metallic wires for electrical measurements.

The preparation steps are schematically shown in Fig. 3.5. A $5 \times 5 \text{ mm}^2$ $\alpha\text{-Al}_2\text{O}_3$ substrate was mounted on a standard stainless steel holder⁵ with colloidal silver liquid. Four 20 nm thick Cr contact pads spaced by 20-50 μm were deposited⁶ using the non-contact stencil mask shown in Fig. 3.5(a).

In the next step, the $CeIn_3$ thin film was grown using the stencil mask shown in Fig. 3.5(b). This mask had a window with a diameter of 50 μm ⁷. Evidently, the presence of the stainless steel mask in the vicinity of the substrate surface influences the gas kinetics and the real substrate temperature T_s^a . In order to account for this influence, several test growths were performed first to optimize the growth parameters.

In the third step (Fig. 3.5(c)), the sample was mounted on a standard printed circuit board (PCB) holder and the four Cr pads were wired to the PCB pins with gold wires of 30 μm in diameter using colloidal silver liquid (on the Cr pads) and soldering (on the PCB pins).

Then, the sample was transferred into the SEM chamber for microstructuring. There, a suitable $CeIn_3$ microcrystal was selected (Fig. 3.6(a)) and electrically isolated (Fig. 3.6(b)) by milling a net of channels around it down to the insulating substrate using the focused ion beam milling (FIBM). In the last step, the microcrystal was electrically connected to the Cr pads via the conducting film residues and W-C nanowires prepared with the focused ion beam induced deposition (FIBID) technique (Fig. 3.6(c)). The electrical connections to the microcrystal were tested *in-situ* by sending a small current through different contact pairs.

⁴The $CeIn_3$ films demonstrate good metallic conductance almost independently of their surface morphology. Many samples preserve their conductivity even after months of being oxidized in air under ambient conditions, whereas some of them become isolating.

⁵The holder was equipped with a mask clamping system as shown in Fig. 2.3, with a mask-to-substrate distance of about 100 μm .

⁶For details see Appendix E.

⁷Since the fluxes of the constituent elements fall on the substrate surface at an angle of 28° measured to the surface normal, the shadowing effect had to be accounted for by making due alignments under an optical microscope in order to grow the $CeIn_3$ film in between the four Cr pads.

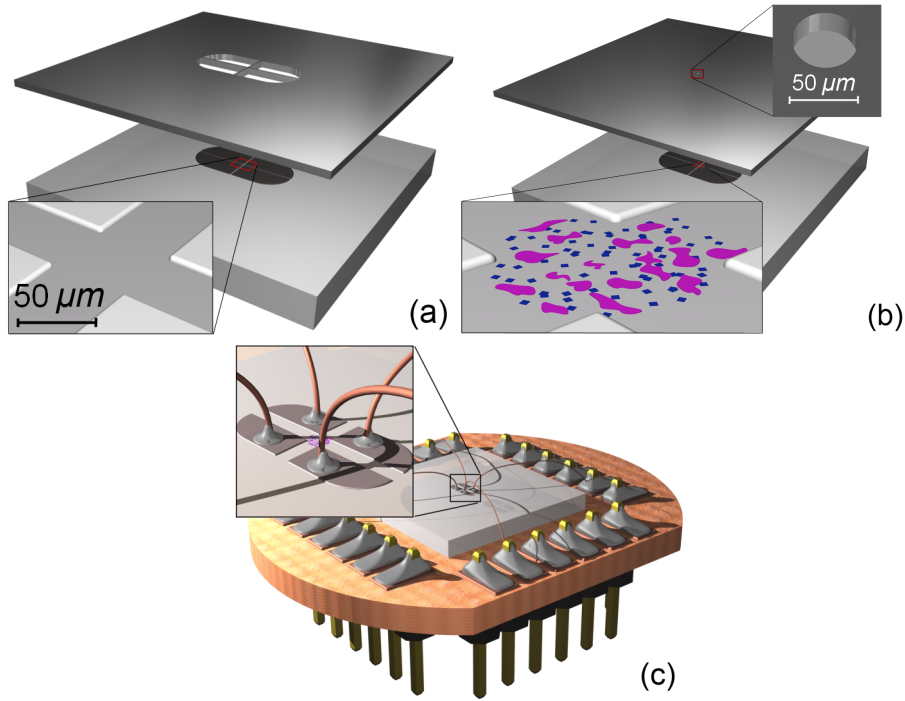


FIGURE 3.5: Pre-patterning of a $CeIn_3$ thin film for microcrystal measurements. (a) Four-window shadow mask for sputtering four Cr contact pads spaced by 20-50 μm . (b) $CeIn_3$ film grown using a single-window shadow mask. (c) The sample is mounted on a standard PCB holder and wired from the Cr contact pads to the PCB pins with 30 μm thick gold wires.

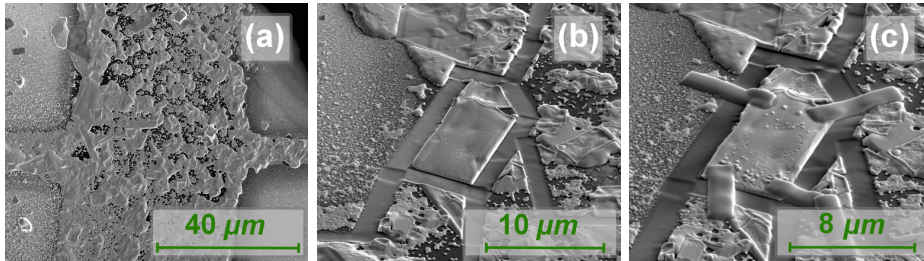


FIGURE 3.6: (a) SEM micrograph of the Cr contact pads and the grown $CeIn_3$ thin film. (b) $CeIn_3$ microcrystal isolated with the FIBM. (c) $W-C$ FIBID nanowires connecting the microcrystal and the Cr contact pads.

The temperature dependence of resistance for this $CeIn_3$ microcrystal (Fig. 3.7) was measured in a 4He cryostat with the four-terminal method using a small constant direct current. The resistance curve demonstrates typical features expected for HF. A resistance minimum is observed at 204 K , the characteristic maximum at 45 K , and the Néel antiferromagnetic transition at 10.1 K . The RRR (R_{200K}/R_{4K}) of the microcrystal is 1.1. The curve is qualitatively similar to the $T_s^{(3)}$ curve (the lowest temperature within the set) from the $T_s^{(0)} = 550$ $^{\circ}C$ set in the simultaneous growth study. However, the resistance measured on the microcrystal has a few distinct features. First, the minimum of the electrical resistance for the microcrystal is observed at 204 K , which coincides with the corresponding temperature in bulk $CeIn_3$ crystals (Tchokonté, Tshabalala

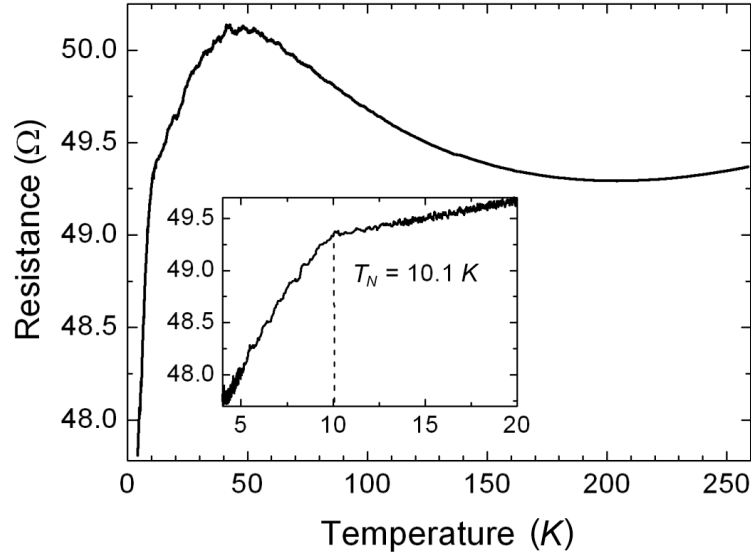


FIGURE 3.7: Electrical resistance measured as a function of temperature on the $CeIn_3$ microcrystal. T_N denotes the Néel temperature.

et al. 2010, Elenbaas, Schinkel *et al.* 1980), whereas in the simultaneous growth study this minimum was found at 150 K. Second, the RRR of the microcrystal is reduced by a factor of about 2 in comparison to the thin film. Third, the microcrystal does not demonstrate a resistance drop at 3 K observed before in the thin films and associated with the In SC transition. The lower value of the microcrystal RRR , compared with the thin films RRR , should correspond to the intrinsic RRR value of the $CeIn_3$ crystallite, which is not enhanced by impurities as it was suggested for the films. The resistivity of the microcrystal at room temperature calculated with the Van der Paw method (Van Der Pauw 1958) assuming a thickness of 300 nm (measured with AFM, see Sec. 2.4) is $6.7 \times 10^{-7} \Omega m$, which is about two times larger than the bulk value. The higher value of the resistivity and the lower value of the RRR (the RRR for bulk $CeIn_3$ is about 15-20) suggest an inferior crystal quality of this MBE grown $CeIn_3$ thin film microcrystal.

In conclusion, the temperature dependence of the electrical resistivity measured on an oriented $CeIn_3$ thin film microcrystal demonstrates closer similarity to that of $CeIn_3$ bulk crystals when compared to $CeIn_3$ thin films. On the other hand, the crystal quality of the characterized $CeIn_3$ crystallite is poor in comparison with the $CeIn_3$ bulk crystals.

3.3 $CeCoIn_5$ growth study

3.3.1 Variations and lack of repeatability

$CeCoIn_5$ and $CeIn_3$ thin films demonstrate similar growth peculiarities. Several thin film groups invested substantial efforts into improving the films' quality, which however did not result in any significant improvements. According to the reports, several growth methods were used to prepare $CeCoIn_5$ thin films, such as evaporative methods (Izaki, Shishido *et al.* 2007, Soroka, Blendin *et al.* 2007), magnetron sputtering and co-evaporation methods (Zaitsev, Beck *et al.* 2009), and the pulsed laser deposition method (Hänisch, Ronning *et al.* 2010). Typically, oxidic substrates were used, such as MgO (100), MgF_2 (001), $r-Al_2O_3$, and $a-Al_2O_3$, which in some cases were finished with a Cr or Nb buffer layer. The best results were reported for nominal substrate temperatures 300-600 °C. As we already discussed in Sec. 3.2.1 (p. 114), these temperatures are about 1.5 times higher than the In melting temperature, which implies poor adhesion and high desorption rates of In . As a consequence, to obtain films with better quality one may need to increase the In flux rates away from stoichiometric ratios. Still, a substantial part of In can be segregated stimulating strongly discontinuous growth of $CeCoIn_5$ and $CeIn_3$ thin films. In the mentioned reports, the $CeCoIn_5$ films were strongly c -axis oriented with no in-plane ordering. Various admixtures of other $CeCoIn_5$ crystallographic orientations as well as of some concomitant compounds (e.g., CeO_2) were also reported.

After about three hundred attempts to optimize the growth parameters of $CeCoIn_5$ thin films that had been made in our group, the films remained strongly nucleated, phase impure, with no in-plane preferential orientation, and with substantial quality variations from growth to growth. It should be noted that an in-plane crystallographic preferential orientation, i.e., long range ordering of the $CeCoIn_5$ crystallites, is a prerequisite to the epitaxial growth, which is, in turn, required for planar tunneling experiments. In the subsequent study, we rearranged the existing MBE setup for producing a Co flux by an electron beam evaporator (see also Sec. 2.2). This qualitatively new setup was re-calibrated using the electron beam evaporator and the Ce and In Knudsen effusion cells.

We used $a-Al_2O_3$ substrates to grow $CeCoIn_5$ thin films motivated by the relatively better results obtained with this substrate type in the $CeIn_3$ growth study (Sec. 3.2.1). Several test growths were also performed on $Si-SiO$, MgF_2 (001), and $SrTiO_3$ (100) substrates, which however showed no evident improvements of the films' quality. We used a standard stainless steel holder together with silver liquid glue or composite bond for substrate mounting. The clamping mounting system described in Sec. 2.2.3 was

exclusively used for later growths. Films of the best quality were obtained with nominal substrate temperatures⁸ in the range of 500-600 °C. The samples discussed in this section were grown at the nominal substrate temperature of 550 °C.

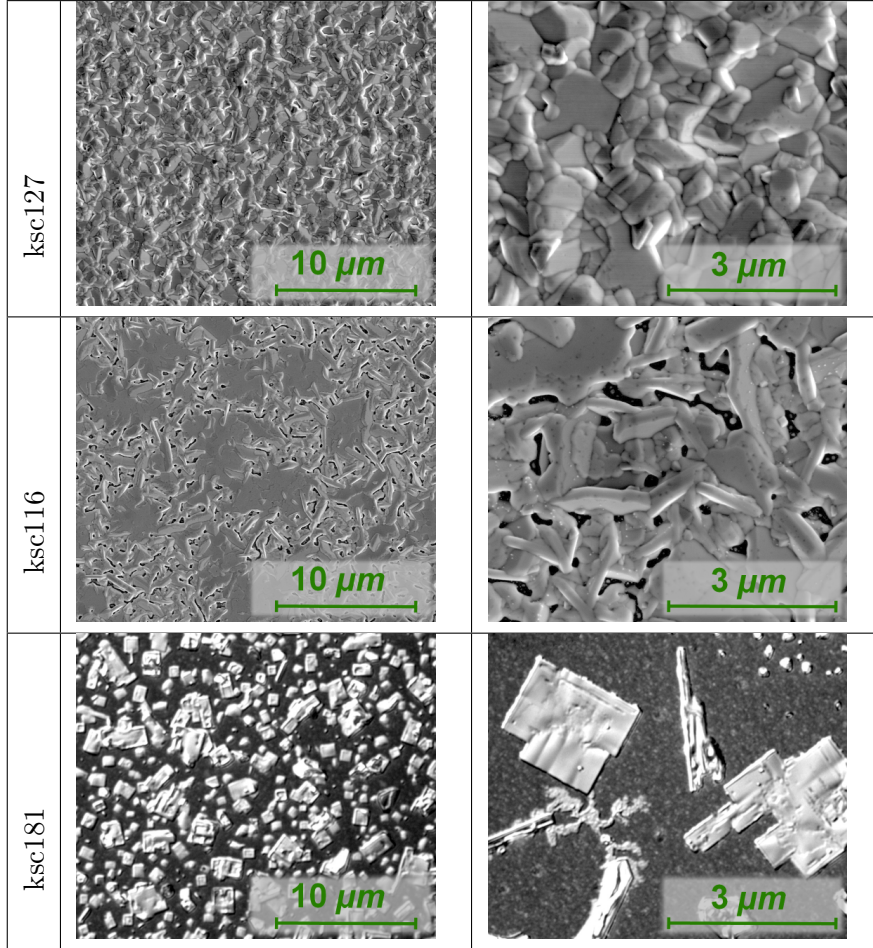
The typical surface morphology of the *CeCoIn₅* films grown in the modified MBE system is similar to that of the *CeCoIn₅* films grown using 3 Knudsen effusion cells. At the same time, the reproducibility of the new films was slightly improved, which is possibly a result of using the substrate mounting clamping system and of an improved film-substrate interaction as described in the following. The variation of the surface morphology of the *CeCoIn₅* films that were grown under nominally identical conditions but have different thicknesses is shown in Table. 3.5. The x-ray diffraction data taken on these samples are presented in Fig. 3.8. The three *CeCoIn₅* films are strongly *c*-axis oriented, as follows from the x-ray diffraction patterns. The *CeCoIn₅* {001} and *CeCoIn₅* {010} Bragg reflection families appear in all three films⁹, although the relative intensity of the latter is weaker than the theoretically predicted value for powder diffraction data (see Appendix D). Several concomitant phases, such as *CeIn₃*, *Co*, and *Ce₃In*, were also identified (see details in Fig. 3.8). While the *CeCoIn₅* {010} crystallographic phase is hardly detectable in the 30 *min* sample, one can observe it clearly in the 60 *min* and 120 *min* samples. This implies that the *CeCoIn₅* {010} phase poorly nucleates on a clean substrate surface.

For all three films, the FWHM of the *CeCoIn₅* (003) reflection in the ω -scan (rocking curve) is approximately 0.75°, which is a few times less compared to the *CeCoIn₅* films grown using 3 Knudsen effusion cells and to the works cited at the beginning of this section. The smaller the FWHM value of a given reflection in the w -scan the narrower the orientational distribution of the probed crystallographic planes (the *CeCoIn₅* {001} planes in our case). That is, the observed reduction of the FWHM can be interpreted as a result of improved substrate-film interaction and tendency to epitaxial growth. The suggested enhancement of the substrate-film interaction may also lead to an improved selectivity of planar orientations of the *CeCoIn₅* crystallites, which was absent in the previous studies. We can analyze these preferred in-plane orientations using grazing incidence diffraction (GID) (see Sec. 2.4.1). Typical results of the GID measurements on the new set of *CeCoIn₅* films are shown in Fig. 3.9. While in the standard $\theta/2\theta$ regime we collect diffracted intensity from the crystallographic planes which are stacked parallel to the substrate surface, in the GID regime the intensity is collected from planes stacked normally to the substrate surface. The resulting pattern is typically shown for

⁸For detailed information on the thin film growth parameters see Appendix E and Sec. 2.2.

⁹We use the notation (*hkl*) for denoting a specific crystallographic plane and {*hkl*} for denoting a family of symmetrically equivalent planes.

TABLE 3.5: SEM micrographs (ksc127 and ksc116) and optical microscope photographs (ksc181) demonstrating the typical morphology of $CeCoIn_5$ thin films grown in the modified MBE system (see text). The films were grown under nominally identical conditions but with different thickness. The sample shown in the bottom row has the smallest thickness. For every next row to the top the thickness is doubled. The corresponding growth times (from bottom to top) are 30 min, 60 min, and 120 min respectively.



one complete revolution around the goniometer axis, i.e., for $\Delta\varphi = (-\pi; \pi)$. The crystallographic symmetry of the probed sample, its texture and crystallinity will define the number¹⁰, the relative positions, and the intensity of the reflections seen by the detector. The measurements of the GID patterns were performed in two steps: first, with settings for a selected substrate reflection and, second, with settings for a selected $CeCoIn_5$ reflection without unmounting the sample, i.e., preserving the relative orientation between the substrate and the film reflections.

¹⁰If crystallographic planes of the $\{001\}$ family of a hexagonal structure are probed, two reflections spaced by π will be detected in one revolution.

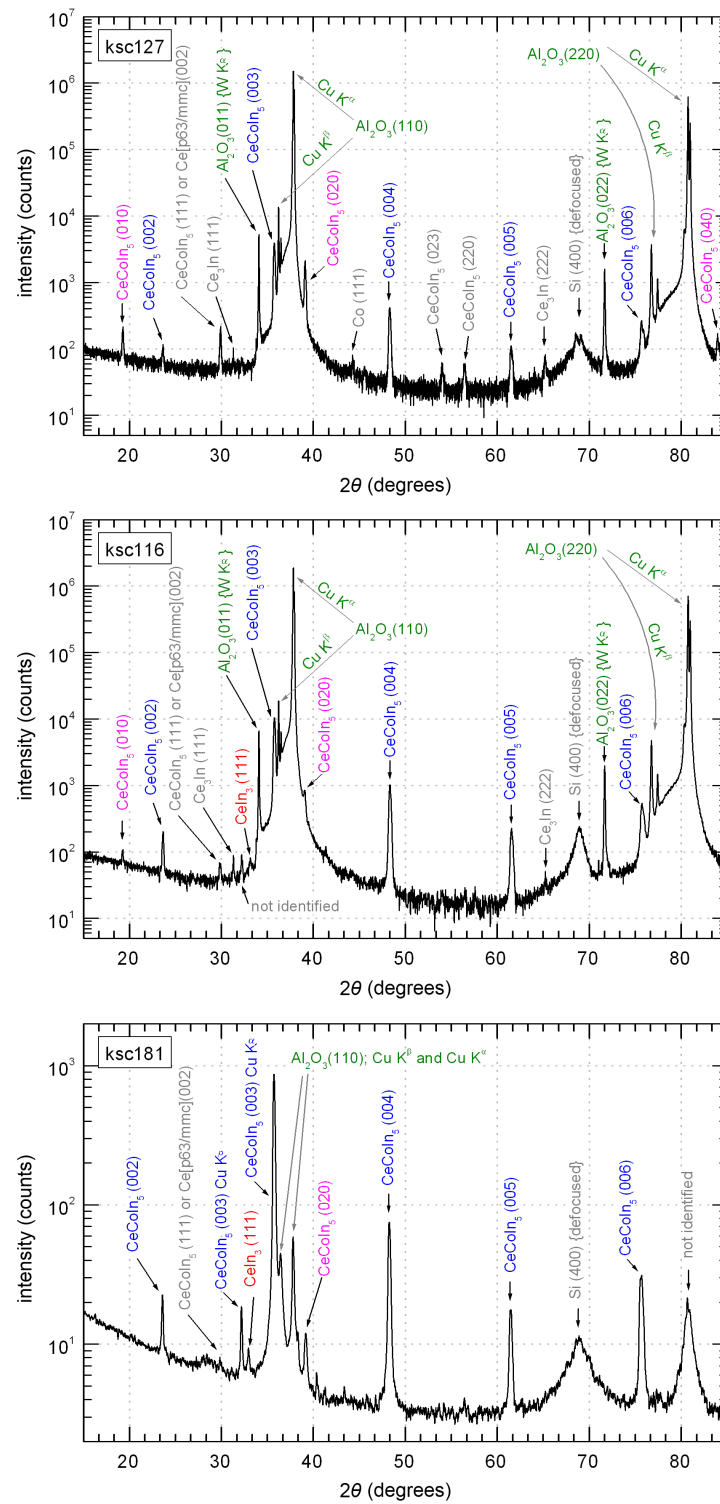


FIGURE 3.8: X-ray diffractograms of three typical $CeCoIn_5$ thin films of different thicknesses. The pattern shown in the lowest figure corresponds to the sample with the smallest thickness. The thickness is doubled for every next pattern to the top. The corresponding growth times (from bottom to top) are 30 min, 60 min, and 120 min, respectively. The bottom diffractogram was measured with single step alignment (see text).

The two sharp peaks seen in both diffractograms in Fig. 3.9 correspond to the sapphire substrate (006) Bragg reflections while the four broad reflections correspond to the $CeCoIn_5$ (020) Bragg reflections. Clearly, the FWHM of the substrate reflections is due to the broadening introduced by diffractometer settings, which is negligibly small in this case. The $CeCoIn_5$ microcrystals demonstrate long range planar ordering, i.e., they are aligned along a preferred substrate crystallographic direction. However, the finite FWHM value of the $CeCoIn_5$ (020) reflections indicates that the alignment of the $CeCoIn_5$ microcrystals is not perfect. The mean deviation of the $CeCoIn_5$ microcrystals' orientations from their averaged orientation, which is equivalent to the FWHM in this scanning geometry, is 13.5° . Moreover, according to the data this averaged orientation is along the substrate $\{001\}$ crystallographic direction. The GID measure-

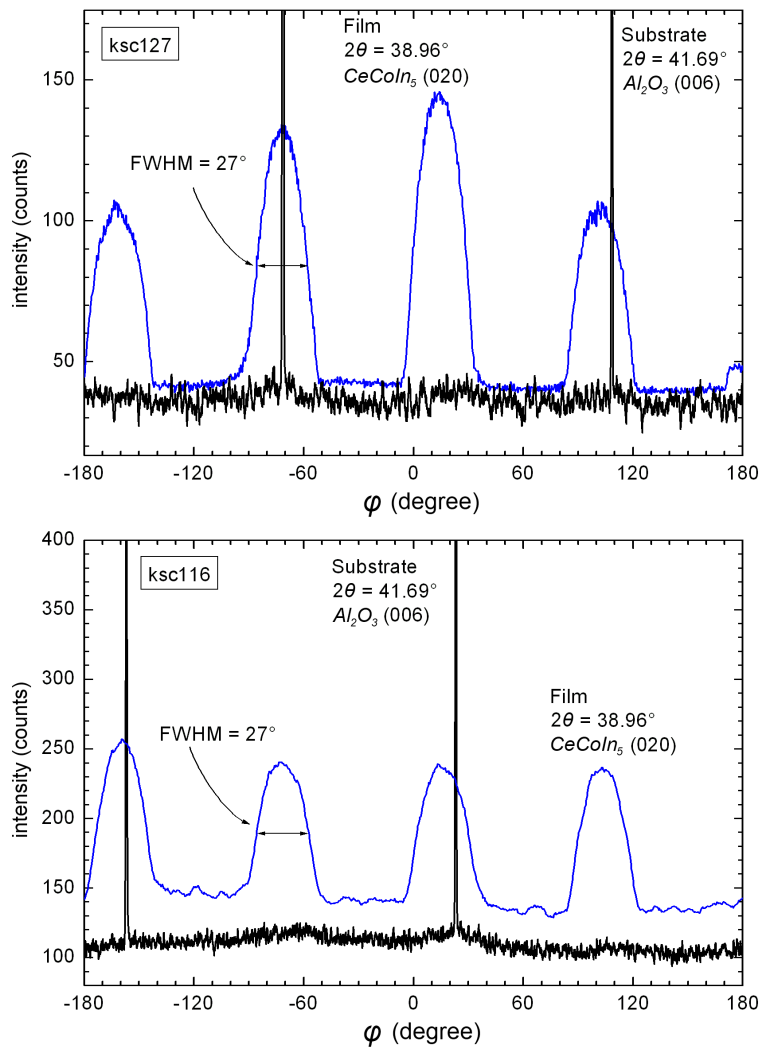


FIGURE 3.9: X-ray φ -scans on two $CeCoIn_5$ films with improved in-plane preferential orientation. The $CeCoIn_5$ (020) Bragg peaks were used for identification and are shown by blue lines. The Al_2O_3 (006) peaks of the substrate, with which the $CeCoIn_5$ crystallites are moderately aligned in terms of crystallographic orientation, are shown by black lines.

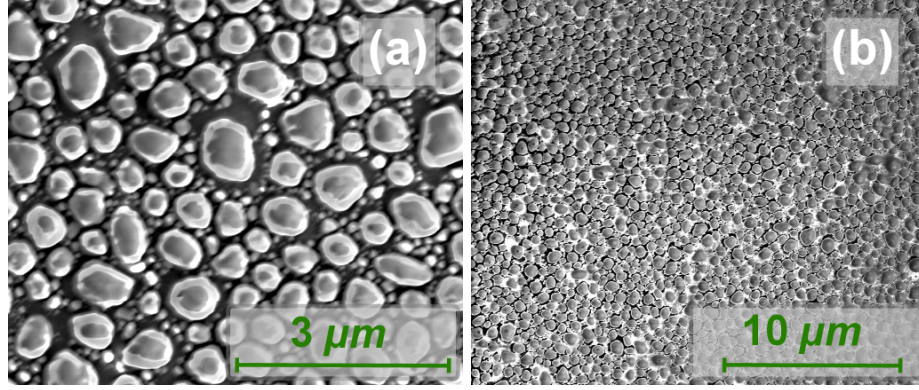


FIGURE 3.10: (a) Zoomed in and (b) zoomed out SEM micrographs of the surface morphology of a region of a $CeCoIn_5$ film where Indium segregation was found to be strong, EDXS $Ce:Co:In = 0:1:2.7$

ments are well reproducible from film to film, although the phase purity of the films may vary¹¹. For example, according to the EDXS analysis, the ratios $Ce:Co:In$ for the 60 *min* (ksc116) and 120 *min* (ksc127) samples shown in Fig. 3.9 are 1:1.7:3.8 and 1:2.6:3.2 respectively. It is not unusual for these $CeCoIn_5$ films to demonstrate local In segregation, as illustrated in Fig. 3.10. According to the EDXS analysis performed on the area shown in Fig. 3.10(a), the $Ce:Co:In$ ratio in that region of the film is 0:1:2.7 and the droplets should therefore represent an enriched In phase.

One may have noticed that the intensity of the substrate reflections in the lowest x-ray pattern in Fig. 3.8 is much reduced in comparison to the other two datasets. This was achieved using a modified sample alignment procedure. The standard sample alignment described in Sec. 2.4.1 leads to such an orientation of the sample surface that the substrate miscut angle α_{mc} , which is measured between the substrate out-of-plane crystallographic (hkl) vector \mathbf{n}_c^s and the normal to the substrate optical surface \mathbf{n}_o^s , lies in a vertical plane (see also Fig. 2.12). Thus, the angles of incident and diffracted x-ray beams, measured both with respect to vector \mathbf{n}_c^s , are equal, and the scattering vector \mathbf{Q} exactly crosses the integer-valued points in the substrate's reciprocal space. Without this alignment, the orientations of the two substrate vectors \mathbf{n}_c^s and \mathbf{n}_o^s and the goniometer axis vector \mathbf{n}^g are arbitrary, as it is shown in Fig. 3.11. In this case, the scattering vector \mathbf{Q} does not necessarily exactly cross the integer-valued points of the substrate reciprocal space, which reduces the intensity of its Bragg reflections. If one performs only optical alignment with a laser beam, vector \mathbf{n}_o^s will be aligned along vector \mathbf{n}^g with accuracy δ , such that $\alpha_{mc} = \alpha + \delta$ and $\delta \ll \alpha_{mc}$. With this alignment, the larger the projection of angle α (follow the dashed lines in the figure) on the plane of x-ray beams the farther the scattering vector \mathbf{Q} moves away from the integer-valued substrate reciprocal points, thus decreasing the intensity of its Bragg reflections. The

¹¹The variations are larger than the accuracy of the EDXS analysis.

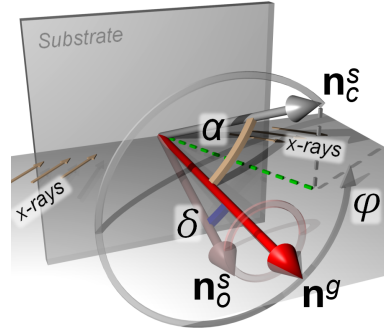


FIGURE 3.11: Precession of vector \mathbf{n}_c^s , which is associated with a certain substrate crystallographic direction (hkl), around the goniometer axis vector \mathbf{n}^g . Vector \mathbf{n}_o^s corresponds to the substrate optical surface normal, which can be aligned along \mathbf{n}_g with accuracy δ . The substrate miscut angle corresponds to $\alpha_{mc} = \angle(\mathbf{n}_o^s, \mathbf{n}_c^s) = \alpha + \delta$. The grey dashed line is a projection of \mathbf{n}_c^s on the plane of x-ray incident and diffracted beams.

Bragg reflection intensity as a function of the projection of angle α or, equivalently, as a function of angle φ will be used in the following section for polar angle orientation analysis of the $CeCoIn_5$ microcrystals on the substrate surface. For a simple $\theta/2\theta$ scan, angle φ can be adjusted such that the intensity of the substrate Bragg reflections is minimal. Since the substrate reflections are naturally very narrow, even small values of the projection of angle α reduce dramatically the intensity of these reflections, as one observes in the lowest diffractogram in Fig. 3.8. We also used the modified alignment procedure to obtain line shapes of $CeCoIn_5$ Bragg reflections, free of large distortions introduced otherwise by large tails of the substrate reflections, which are required for the LPA study (see Sec. 2.4.2 and Sec. 3.3.3)

3.3.2 Polar angle orientation of microcrystals

Let us consider a monocrystalline substrate schematically shown in Fig. 3.12(a). It is characterized by the normal to the optical surface (the semitransparent plane) \mathbf{n}_o^s , by the crystallographic vector \mathbf{n}_c^s , and by the miscut angle α_{mc} , which was defined in the previous section. If now a thin polycrystalline film is considered on such a substrate, three growth regimes can be distinguished. In the following discussion of the growth regimes we characterize the orientation of the film's microcrystals on the substrate by the polar angle $\Phi = \angle(\mathbf{n}^f, \mathbf{n}_c^s)$, where \mathbf{n}^f is the out-of-plane microcrystal's crystallographic vector, and the azimuthal angle Θ , which describes the planar rotation of a microcrystal and is defined between some selected crystallographic directions of the substrate and of the microcrystal.

In the first growth regime, adatoms form a close-packed film repeating the substrate atomic steps so that $\Phi = 0$ (Fig. 3.12(b)). In the second regime, the microcrystals are

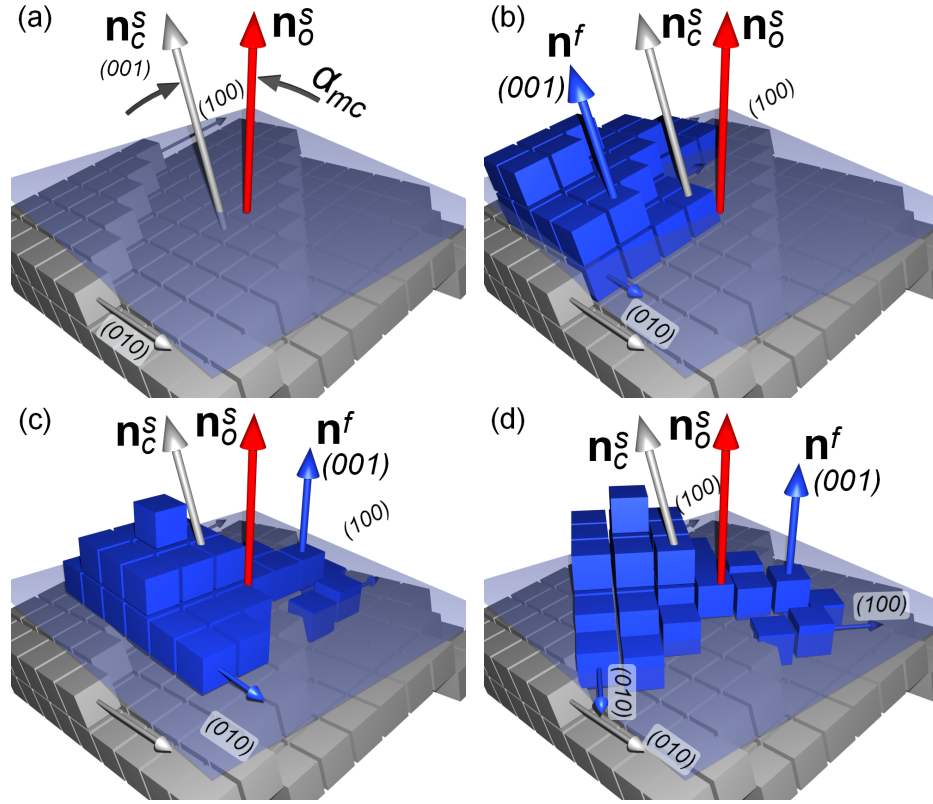


FIGURE 3.12: (a) Cartoon of monocrystalline substrate miscut. (b) The initial stage of film growth in the presence of strong interaction between the film and the substrate. (c) Thin film crystallite that is weakly interacting with the substrate. (d) Thin film crystallite with the weakest interaction with the substrate. In all the sub-figures the semi-transparent plane represents the substrate optical plane with its normal vector \mathbf{n}_o^s shown by the red arrow. The periodically arranged grey boxes represent the substrate crystallographic planes with their orientations shown by the grey arrows. The blue boxes mimic a film crystallite formed by adatoms at the first stages of the film growth. The blue arrows show the crystallographic orientations of the crystallite. Vectors \mathbf{n}_c^s and \mathbf{n}^f represent the out-of-plane crystallographic vectors of the substrate and the crystallite, respectively. See also text for explanations.

oriented such that $\mathbf{n}^f \parallel \mathbf{n}_o^s$ and the planar orientation of the microcrystals Θ is constant (Fig. 3.12(c)). In the third growth regime, neither azimuthal angle Θ nor polar angle Φ are constant, i.e., the microcrystals are arbitrarily oriented. Clearly, the intralayer coupling within the film dominates over the film-substrate coupling in the third regime, while the situation is the opposite in the first regime. In the second regime, these two characteristic couplings are comparable. Analyzing the GID data in the previous section, we suggested that the $CeCoIn_5$ film microcrystals tend to have common azimuthal orientation, which speaks for either the first or the second regime in Fig. 3.12 being realized. In the following, we present our analysis of the polar orientation of the $CeCoIn_5$ thin film microcrystals grown using the modified MBE system.

For this type of x-ray analysis, the $CeCoIn_5$ thin film samples were aligned on the goniometer using the modified alignment procedure described in the previous section.

After this alignment, angle δ did not exceed 0.0477° , using the notation in Fig. 3.11. A set of ω -scans, each at different angle φ within the range $\Delta\varphi = (-\pi; \pi)$, was taken at the substrate (110) Bragg reflection. A set of similar ω -scans was taken also for the $CeCoIn_5$ (004) Bragg reflection without re-aligning the sample. The obtained datasets for the substrate and for the film are presented as colour maps in Fig. 3.13(a) and Fig. 3.13(b) respectively, where lighter colours code larger intensities. Due to geometrical considerations, the coordinates of the maximal intensity in both maps should follow a sine wave with arbitrary phase and amplitude over one period. These coordinates were fitted numerically by a sine function. For this fitting, we first identified the coordinates of the maximal intensity for each value of φ in both datasets. This was done by numerically fitting the intensity profiles of each ω -scan by a weighed mixture of Gaussian and Lorentzian functions using self-written software. The intensity maxima resulting from all such fits are shown by crosses in Fig. 3.13(c) while the sine fits are shown by solid lines.

As expected, both the film and the substrate data points in Fig. 3.13(c) are well described by one period of a sine function. According to the fits, the phases of both waves are essentially identical: i.e., $\varphi = 137.6^\circ$ for the substrate and $\varphi = 136.5^\circ$ for the film. The fitted amplitudes of the waves are 0.364° and 0.096° for the substrate and for the film, respectively. The mean value of the fitted sine wave $\omega^{sub}=18.894^\circ$ for the substrate matches the theoretically predicted value for Al_2O_3 (110) Bragg reflection with as little deviation as 100 *ppm*, which is within the calibration accuracy of the diffractometer. The mean value of the wave $\omega^{film}=24.094^\circ$ for the film differs from the theoretically expected value for the $CeCoIn_5$ (004) reflection¹² by about 480 *ppm*, which is larger than the diffractometer calibration error. Such difference, if intrinsic to the film, may indicate a crystal structure relaxation in the $CeCoIn_5$ film caused, for example, by a lattice misfit between the substrate and the film crystal structures.

The observed common phase of the fitted intensity maxima in the polar scan maps of the substrate and of the film speaks for planar alignment of the $CeCoIn_5$ thin film microcrystals along preferred substrate crystallographic directions or, using our notation, for a preferred angle Θ among the $CeCoIn_5$ microcrystals. This interpretation is also consistent with the results of the GID analysis discussed in the previous section. The amplitude of the sine wave fitted to the substrate data, which is a measure of the substrate miscut angle, corresponds well to the miscut angle specified by the manufacturer (see Sec. 2.2.2) for this substrate. One has to note that the value of this angle is about 10 times larger than the accuracy of our experiment. The sine wave amplitude for the film is, according to the fit, about four times smaller than that for the substrate but still two times larger than the measurement accuracy. Such a difference between the

¹²See Appendix D for comparison.

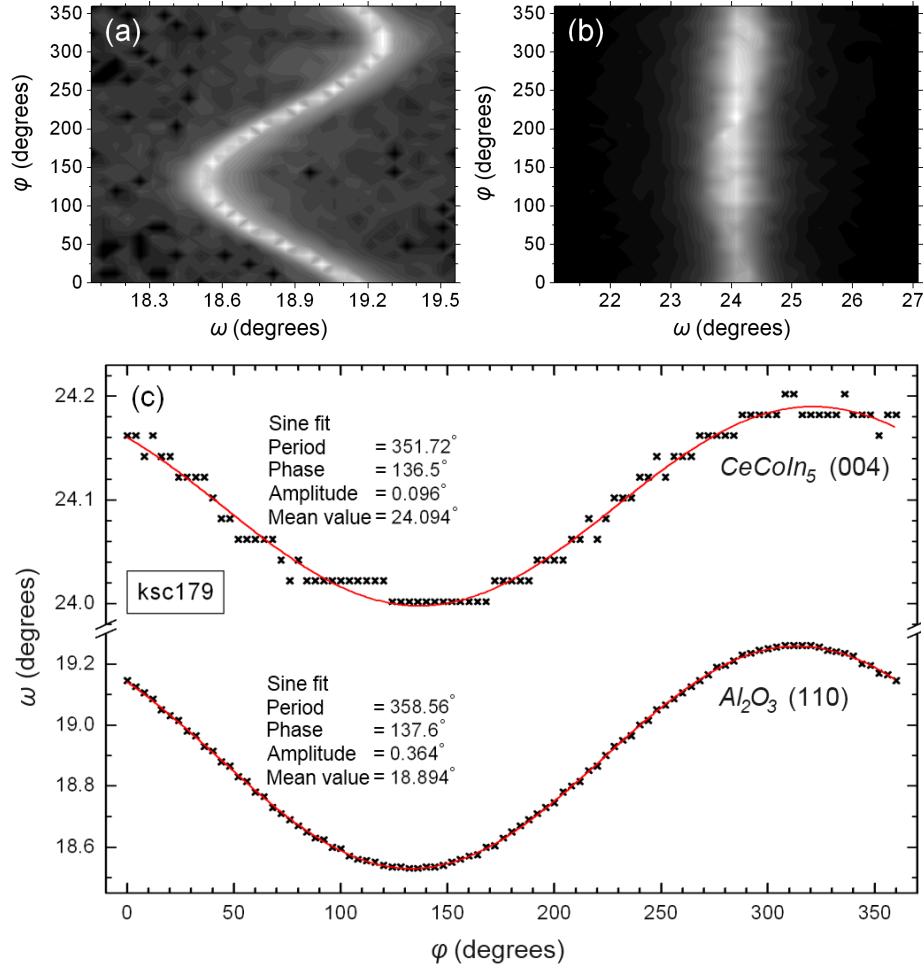


FIGURE 3.13: X-ray polar scan maps of (a) the Al_2O_3 (110) Bragg peak and (b) the $CeCoIn_5$ (004) Bragg peak. The black crosses in (c) represent the fitted positions of the maximum intensity from (a) and (b). The red solid lines are sine fits to the intensity maxima. Note the different ω scales for the film and substrate plots.

two fitted sine amplitudes suggests that the $CeCoIn_5$ thin film microcrystals grown on α - Al_2O_3 substrates tend to be oriented such that $\Phi \lesssim \alpha_{mc}$, i.e., the second regime in Fig. 3.12 is realized.

3.3.3 Microstrain study with LPA

The measured electronic transport properties of the $CeIn_3$ films and of the $CeIn_3$ thin film microcrystal (Sec. 3.2.2 and Sec. 3.2.3) suggest large concentrations of structural defects in the $CeIn_3$ films, which is also the case in the $CeCoIn_5$ thin films (Soroka *et al.* 2007, Hänisch *et al.* 2010, Foyevtsov *et al.* 2010). It is known that the superconducting state in some heavy-fermion compounds is dramatically suppressed by chemical substitutions, like in UBe_{13} or in $CeCu_2Si_2$ (see (Stewart 2001)), which can be viewed

as a controlled introduction of structural defects. In contrast, the $CeCoIn_5$ superconducting state is much less strongly suppressed by such substitutions and survives up to much larger concentrations of foreign ions in the crystal structure (Petrovic, Bud'ko *et al.* 2002). Thus, an estimation of the relative concentration of microstructural defects in our $CeCoIn_5$ thin films can be helpful not only for thin film growth studies but also for electronic transport studies.

In the following, we present a study on microstrains in the $CeCoIn_5$ thin films using the LPA method described in Sec. 2.4.2. For this analysis, we used the $CeCoIn_5$ $\{00l\}$ family Bragg reflections up to the 6-th order. The line shape of each reflection was measured individually without re-aligning the sample and using diffractometer settings that ensured sufficiently high signal-to-noise ratio. The modified alignment procedure described in Sec. 3.3.1 was used to obtain line shapes of the $CeCoIn_5$ Bragg reflections free of distortions caused by the substrate Bragg reflections. Numerical fitting of the Pearson VII model function was performed using self-made software developed during this work. Prior to the fitting, the background intensity of every reflection was approximated by a straight line. Every $CeCoIn_5$ $(00l)$ reflection was fitted by the sum of four model functions, corresponding to the four CuK^α characteristic lines. The root mean square difference between the experimental data and the simulated values was minimized during the numerical fitting. As a result, every Bragg reflection was characterized by four sets of parameters, each including the integral breadth $\beta_{2\theta}$, the mean position θ_0 , the intensity I_0 , and the line shape parameter m (see p. 96).

The parameters obtained via numerical fitting of the $CeCoIn_5$ Bragg reflections were used to build Williamson-Hall plots, which were then used for microstrain analysis of the $CeCoIn_5$ thin films. Two such plots are shown in Fig. 3.14, where the insets show optical microscope images of the surface morphology of the corresponding samples. The solid lines in the plots are linear fits to the data points. The average dimensions of the coherently scattering crystal volume K_S/D and the microstrain K_D/ε_{rms} were obtained from the line equations as discussed in Sec. 2.4.2. For a separate analysis of K_S and K_D , specific crystal shapes and microstrain models have to be assumed, which was not done here. Nevertheless, some qualitative conclusions can be made based on simple assumptions.

Both samples in Fig. 3.14 demonstrate similar surface morphologies. According to the derived size parameters K_S/D (shown in Fig. 3.14), the effective average size of the $CeCoIn_5$ microcrystals¹³ is 88 nm and 93 nm for (a) and (b), respectively, which are typical results for all analyzed $CeCoIn_5$ films. It is clear that only the smallest $CeCoIn_5$

¹³A simple cubic shape was assumed here for which $K_S \simeq 1$. The obtained values for the crystal sizes are rough estimates since the microcrystals can have various shapes each having its own value of K_S .

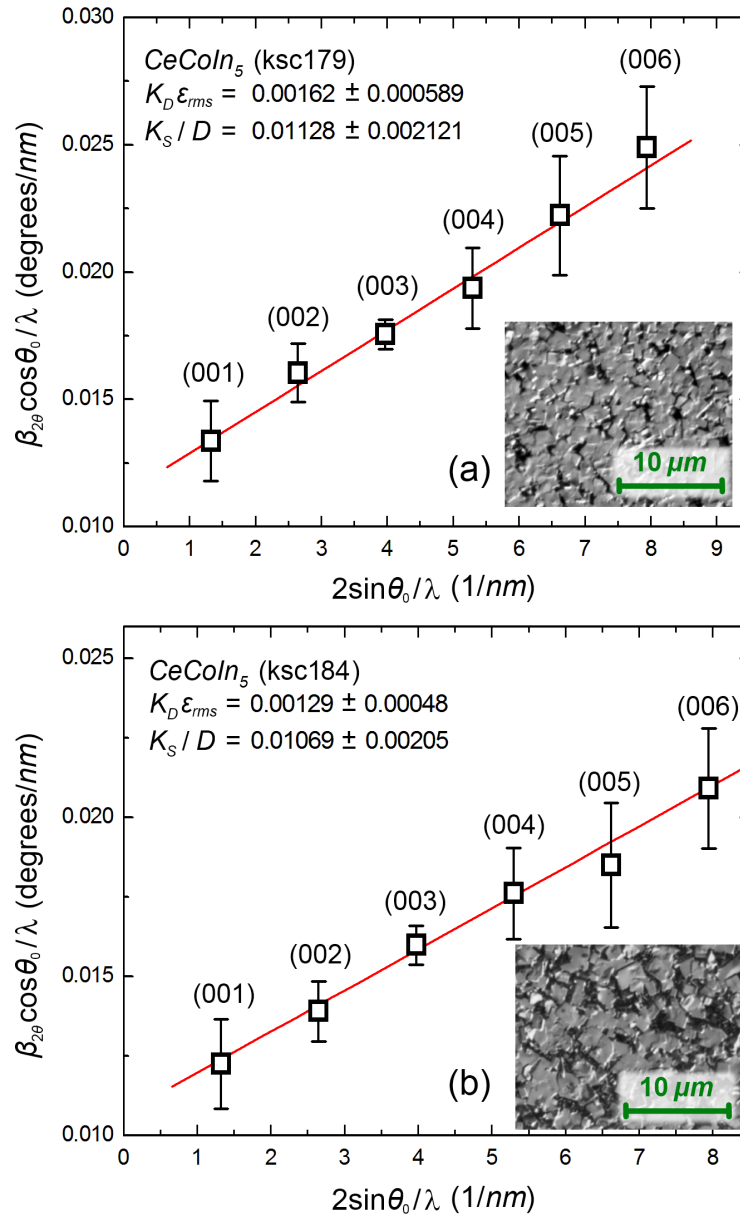


FIGURE 3.14: Williamson-Hall plots for two $CeCoIn_5$ thin films measured for the $\{00l\}$ family of crystallographic planes. The open boxes represent the fitted model parameters for the indicated Bragg reflection profiles (see text for details) and the red lines are linear fits to the obtained data. The insets demonstrate optical photographs of the respective film surface morphologies.

growth domains contribute to these values, while the micron-sized $CeCoIn_5$ domains visible on the optical photographs introduce a negligibly small broadening of Bragg reflections. This suggests that the $CeCoIn_5$ thin film microcrystals have strongly varying sizes ranging from sub-hundred nanometers to a few micrometers for a 300 nm thick film. Then, one can also speculate that at the first stages of the $CeCoIn_5$ thin film growth a large number of $CeCoIn_5$ growth centers are nucleated. At a certain film thickness a percolating thin $CeCoIn_5$ layer is formed modifying the growth conditions for the following layers, which is similar to the Stranski-Krastanov growth regime discussed in

Sec. 1.3.2. Under these new conditions many of the tiny $CeCoIn_5$ growth domains may slow down their growth in favor of larger growth domains and get eventually embedded into the growing percolating film.

Whereas the size-induced broadening can be attributed only to a fraction of the coherently scattering $CeCoIn_5$ crystal volume, the strain-induced broadening is associated with the total $CeCoIn_5$ coherently scattering volume seen by x-rays. It has been mentioned that x-rays are attenuated while traveling through the film so that under certain conditions the diffracted intensity delivered from deeper lying lattice planes may be substantially reduced. In the case of a $\theta/2\theta$ scan, the attenuation strength also depends on the Bragg angle. However, we should stress that the intensity of the substrate Bragg reflections in this study was only weakly reduced in the presence of the $CeCoIn_5$ thin film. Thus, the observed broadening of the $CeCoIn_5$ Bragg reflections should correspond to the whole film thickness of about 300 nm within the complete range of the probed Bragg angles.

According to the numerical fits shown in Fig. 3.14, the strain parameters¹⁴ $K_D \epsilon_{rms}$ for the $CeCoIn_5$ films are¹⁵ 0.00162 and 0.00129 for (a) and (b), respectively, representing typical values for all analyzed $CeCoIn_5$ films. If uniaxial strain is assumed, these values correspond to 0.15% expansion along the $CeCoIn_5$ c -axis. Such small values, however, should have a negligible effect on the electronic transport properties of $CeCoIn_5$ (Oeschler, Gegenwart *et al.* 2003, Johnson, Zieve *et al.* 2011). Nevertheless, the small values of the RRR observed in our $CeCoIn_5$ thin films and microcrystals¹⁶ speak for a rather poor crystal quality of the $CeCoIn_5$ thin films.

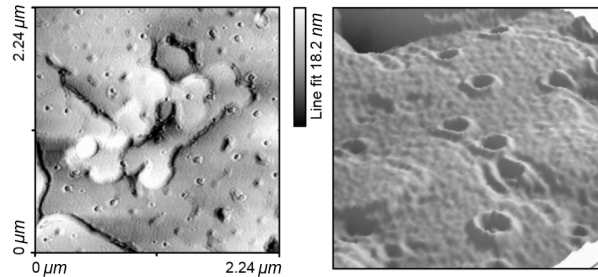


FIGURE 3.15: AFM profiles of typical defects in a $CeCoIn_5$ thin film. The left panel demonstrates a top view projection while the right panel demonstrates a zoomed in part of the same area in a tilted-view projection. The diameter of the defects is approximately 60 nm.

¹⁴The strain ϵ_{rms} was defined earlier as $\Delta d/d$. Generally, the value of ϵ_{rms} obtained from a Williamson-Hall plot is sensitive to the structural defects whose Burger vectors have non-zero components in the direction of the probed reciprocal vector \mathbf{Q} .

¹⁵Here and below, we omit the units of $K_D \epsilon_{rms}$ and K_S/D which are degrees and degrees/nm, respectively.

¹⁶The $CeCoIn_5$ microcrystal transport measurements will be discussed in one of the following sections.

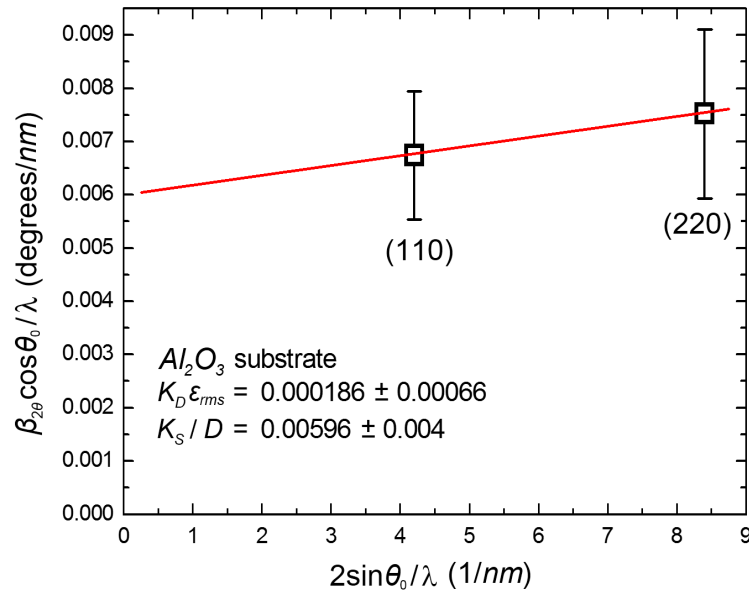


FIGURE 3.16: Williamson-Hall plot for the $\{110\}$ family of $\alpha = Al_2O_3$ Bragg reflections. The open boxes represent the fitted model parameters for the indicated Bragg reflection profiles (see text for details) and the red lines are linear fits to the obtained data from a typical sapphire substrate.

The typical surface morphology of the $CeCoIn_5$ thin films, as seen by AFM microscopy, is shown in Fig. 3.15. The surface of these films consists of overlapping plateaux of different height covered by evenly distributed round-shaped defects of about 60 nm diameter each. These defects may correspond to the threading dislocation type of defects similar to, e.g., those observed in $SiGe$ epitaxial layers (see pp. 486-487 in (Freund & Suresh 2003)) where such dislocations penetrated through a 1.5 μm thick film. Since the scattering vector \mathbf{Q} for the $\theta/2\theta$ scanning regime used for the LPA lies mainly perpendicularly to the Burger vector of such threading dislocations, the latter should produce weak broadening effects. Nevertheless, the strain fields created by the threading dislocations may still be large, which can explain the systematically observed low RRR values and small reduction of the superconducting transition temperature T_c in the $CeCoIn_5$ thin films (Hänisch *et al.* 2010) and their microcrystals (Foyevtsov *et al.* 2010, Foyevtsov, Porrati *et al.* 2011).

We applied LPA to the (110) and (220) Bragg reflections of the Al_2O_3 substrate in order to estimate the broadening introduced by diffractometer settings. Since the used Al_2O_3 substrates are essentially perfect monocrystals characterized by zero strain and size broadening parameters, we expect no broadening for these two reflections. A Williamson-Hall plot for the substrate is shown in Fig. 3.16. According to the numerical fit, the substrate size broadening parameter $K_S/D = 0.006$ is about two times smaller than that found for the $CeCoIn_5$ film and should be associated with the instrumental

settings. The substrate strain parameter $K_{D\varepsilon_{rms}} = 0.000186$, which is determined with large uncertainty, is much smaller than that of the $CeCoIn_5$ film.

Let us summarize the main results of this study. LPA can be applied to characterize microstructural defects in the $CeCoIn_5$ thin films, providing results consistent with the previous $CeIn_3$ and $CeCoIn_5$ growth studies. The obtained values of the average microcrystal dimensions for the $CeCoIn_5$ thin films add to our qualitative understanding of the growth dynamics of the $CeCoIn_5$ thin films at the initial stages of growth, which may help to further improve the $CeCoIn_5$ films quality.

3.4 $CeCoIn_5$ microcrystal studies

In this section we discuss electronic transport properties measured on individual $CeCoIn_5$ thin film microcrystals. After presenting first simple transport measurements on the $CeCoIn_5$ microcrystals we discuss the preparation and measured transport properties of cross-type planar tunnel junctions between a $W-C$ nano-composite, deposited by FIBID, and a pre-patterned $Al-Al_2O_3$ thin film. Then, planar tunneling structures created on $CeCoIn_5$ thin film microcrystals with $SiO-C$ composite tunneling barriers and $W-C$ counter electrodes will be presented. Finally we focus on our investigations of $CeCoIn_5$ microcrystals using the DC Josephson effect.

3.4.1 Transport properties of a single $CeCoIn_5$ microcrystal

To pre-pattern a $CeIn_3$ thin film for transport measurements on an individual microcrystal we used the two stencil mask technique. This preparation method, however, has disadvantages, such as long preparation time, the influence of the second stencil mask on the growth process, and a limited number of structures that can be prepared on a single substrate. For the $CeCoIn_5$ thin films we used an improved method. In this method, we make use of the metallic conductivity of the $CeCoIn_5$ thin films to prepare large contact pads. Part of a $CeCoIn_5$ thin film was mechanically removed¹⁷ such as to divide the film into four electrically disconnected regions. Selection of an appropriate microcrystal and its electrical microcontacting were performed similarly to how it was done for the $CeIn_3$ microcrystal. The electrical resistance of the patterned $CeCoIn_5$ microcrystal was measured by the four-terminal method with a constant current of $10 \mu A$ while cooling down the sample¹⁸. The measured temperature dependence of resistance $R(T)$ for

¹⁷The investigated $CeCoIn_5$ thin films demonstrate poor sticking to the substrate surface and can be easily mechanically removed.

¹⁸This current corresponds to current density of about $1.3 \times 10^7 A/m^2$, which is about 70 times smaller than the superconducting critical current at zero magnetic field reported for bulk $CeCoIn_5$ (Watanabe, Kasahara *et al.* 2004).

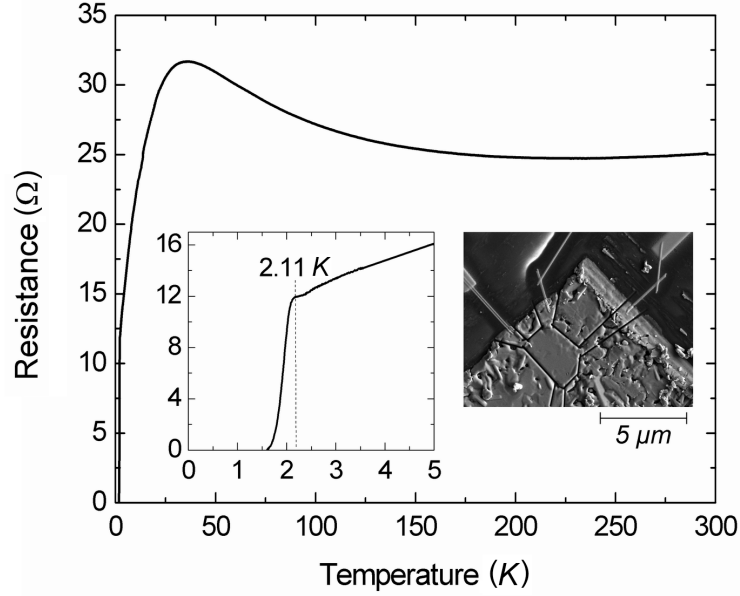


FIGURE 3.17: Four-terminal resistance of a $CeCoIn_5$ microcrystal as a function of temperature. The left inset shows the SC transition. The right inset shows an SEM micrograph of the patterned microcrystal.

this microcrystal as well as an SEM micrograph of the patterned structure are shown in Fig. 3.17. As in the $CeIn_3$ case, the qualitative behaviour of the measured $R(T)$ curve is very similar to that reported for bulk $CeCoIn_5$ crystals. The position of the minimum at about 200 K is close to that found for bulk crystals at about 190 K. The temperature at which coherent scattering of charge carriers starts to develop is observed at about 35 K, which is lower than the corresponding temperature for bulk crystals where it is observed at around 50 K. The electrical resistivity at 2.5 K deduced from Van der Paw measurements was found to be $3.4 \times 10^{-7} \Omega m$ (Foyevtsov *et al.* 2010), corresponding to $RRR = R_{300K}/2.5K = 2.2$. This value is lower compared to a typical value of $6.0 \times 10^{-7} \Omega m$ measured across a whole $5 \times 5 mm$ $CeCoIn_5$ film, suggesting better purity of the microcrystal in comparison to the $CeCoIn_5$ thin film. However, the resistivity value is still one order of magnitude larger than that of a typical bulk crystal, $3.0 \times 10^{-8} \Omega m$ (Petrovic *et al.* 2001), which can be explained by large concentrations of structural defects in the $CeCoIn_5$ thin film microcrystals. Poorer quality of the microcrystal is also suggested by a reduced value of the superconducting transition temperature which in this study was found at $T_c = 2.1 K$.

As a conclusion, we may say that the electronic transport properties of $CeCoIn_5$ thin film microcrystals demonstrate a behaviour typical to bulk $CeCoIn_5$ crystals. However, the value of RRR obtained for the microcrystal is appreciably reduced compared to that of $CeCoIn_5$ bulk crystals, suggesting an inferior crystal structure quality.

3.4.2 Planar tunneling in $Al-Al_2O_3-W-IBID$

The ability to measure the electrical resistivity of an individual $CeCoIn_5$ thin film microcrystal motivates an investigation of its electronic properties using planar tunneling spectroscopy. For microcrystal patterning, insulating tunneling barrier formation and metallic counter electrode deposition, several SEM-based techniques can be combined. As a counter electrode, $W-C$ composites deposited by FIBID¹⁹ can be used. In order to justify the usage of metallic $W-IBID$ nanostructures as tunneling counter electrodes, we characterized them by investigating tunneling spectra of $Al - Al_2O_3-W-IBID$ planar tunneling diodes.

For preparation of such tunneling diodes, an Al thin film was deposited on a $10 \times 10 \text{ mm}$ $Si-SiO$ substrate using RF sputtering²⁰. When an Al film is exposed to air, an oxide layer is formed on its surface within a few hundred picoseconds with an approximate thickness of 1-10 nm (Gulbransen & Wysong 1947, Campbell, Kalia *et al.* 1999). Depending on the quality of the oxide layer, this thickness may be sufficient for providing a large quasiparticle tunneling amplitude through the barrier compared to other transport channels. The surface morphology of the as-sputtered Al film, as seen by AFM, as well as its average S_a and root mean square S_q roughnesses²¹ are shown in Fig. 3.18. The

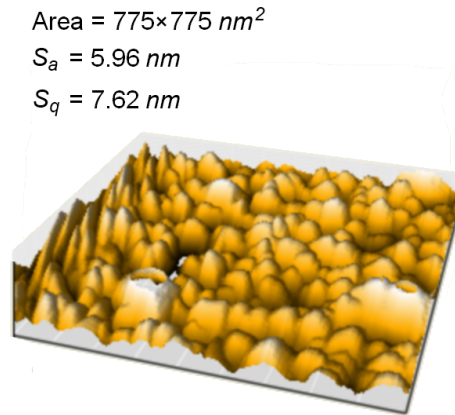


FIGURE 3.18: Surface morphology of an as-sputtered aluminium thin film as seen by AFM.

Al film was pre-patterned using photolithography²² and etched with H_2SO_4 acid solution. The pre-patterned sample was mounted on a standard PCB holder and electrically

¹⁹These $W-C$ nano-composites grown via FIBID will be referred to as $W-IBID$.

²⁰See Appendix E for growth details.

²¹The average roughness is $S_a = \frac{1}{MN} \sum_{k=0}^{M-1} \sum_{l=0}^{N-1} |z(x_k, y_l)|$ and the root mean square roughness is

$$S_q = \sqrt{\frac{1}{MN} \sum_{k=0}^{M-1} \sum_{l=0}^{N-1} (z(x_k, y_l))^2},$$

where M, N are the numbers of scanned points in x and y directions, x and y are their relative spatial coordinates, and $z(x, y)$ is their relative height.

²²The photo-mask is shown in Fig. 3.22.

connected to the holder's outer terminals via $30\ \mu\text{m}$ thick $Al-Si$ wires using an ultrasonic bonding method. Then it was transferred into the SEM chamber for preparation of the W -IBID counter electrodes. Six cross-type structures were micropatterned as shown in Fig. 3.19. The W -IBID counter electrodes were deposited using $5\ \text{kV}$, $10\ \text{kV}$,

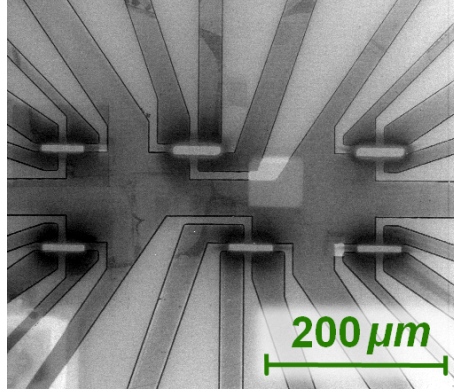


FIGURE 3.19: SEM micrograph of the six $Al - Al_2O_3 - W$ -IBID planar tunnel diodes after patterning.

and $15\ \text{kV}$ accelerating voltages²³ of the focused ion beam, each applied to prepare two planar tunnel diodes.

The electronic transport characteristics of the tunnel diodes were measured in a ^3He cryostat using a lock-in setup (see Sec. 2.5.1). The two-terminal temperature-dependent resistance of the $Al - W\text{-IBID} - Al$ path of one of the $5\ \text{kV}$ structures was measured²⁴ while cooling down the sample. The measured resistance (Fig. 3.20) demonstrates a weak temperature dependence down to the SC transition of the W -IBID at $4.9\ \text{K}$ (Spoddig, Schindler *et al.* 2007). The step at $1.5\ \text{K}$ is associated with the SC transition in Al . The barrier resistances of the tunneling diodes were measured below $10\ \text{K}$ using the four-terminal method: $A^{5\text{kV}} = 60\ \Omega$, $B^{5\text{kV}} = 11.4\ \Omega$, $A^{10\text{kV}} = 0.158\ \Omega$, $B^{10\text{kV}} = 0.07\ \Omega$, and $A^{15\text{kV}}$ and $B^{15\text{kV}}$ had less than $0.01\ \Omega$. The variation of the tunneling resistances among the structures is caused by both the etching effect of the FIB and the Ga doping of the oxide layer which modifies its electrical properties during the preparation procedure. Among the samples prepared with identical beam parameters, the samples marked A were prepared first and the samples marked B last. Thus, the oxide barriers of samples B had been exposed to a larger radiation dose which systematically reduced their resistances in comparison to samples A in spite of the unchanged beam settings.

The energy range with important spectroscopic information is given by the energy scale of the superconducting gap and for these tunneling diodes should be within about $1\ \text{meV}$.

²³Each accelerating voltage was used with an individual value of the focused ion beam current, namely $1\ \text{nA}$, $0.41\ \text{nA}$, and $0.58\ \text{nA}$, respectively. A pitch size of $20\ \text{nm}$ was used in all three cases. The composition of the W -IBID electrodes according to the EDXS analysis was determined as W : 55-59 At. %, C : 20-24 At. %, O : 6 At. %, and Ga : 13-14 At. %.

²⁴Hereafter the structures will be referred to as $A^{5\text{kV}}$, $B^{5\text{kV}}$, $A^{10\text{kV}}$, $B^{10\text{kV}}$, $A^{15\text{kV}}$, $B^{15\text{kV}}$.

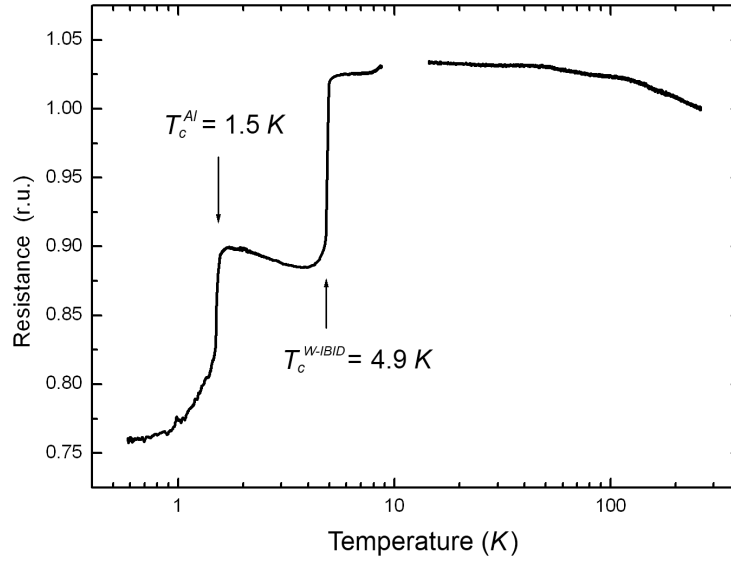


FIGURE 3.20: Typical temperature-dependent resistance curve of an $Al - Al_2O_3 - W$ -IBID planar tunnel diode. The transition at 4.9 K corresponds to the SC transition in the W -IBID composite and the transition at 1.5 K corresponds to the SC transition in the Al electrode.

Data were taken with voltages up to 4 meV for both directions of current flow. The tunneling spectra for structures A^{5kV} and B^{5kV} measured at several temperatures are shown in Fig. 3.21. The spectra (a) and (c) correspond to the $S-I-N$ regime, when Al is a normal metal, while the spectra (b) and (d) correspond to the $S-I-S'$ regime, when Al is superconducting.

Two $S-I-N$ spectra for structure A^{5kV} are shown in Fig. 3.21(a) for the temperatures 2 K and 3.7 K. The spectra demonstrate a double-peak structure which becomes completely smoothed out above 4.9 K. As one might have noticed, these tunneling spectra cannot be explained in terms of an ideal $S-I-N$ structure. They, however, can be described well within the framework of the Blonder-Tinkham-Klapwijk (BTK) model (Blonder, Tinkham *et al.* 1982). This model considers both a quasiparticle tunneling transport channel through the interface (the $S-I-N$ regime) and an Andreev reflection channel (Andreev 1964) at the $S-N$ interface. It can be used to describe a crossover between the two regimes. The red solid curve in (a) is a BTK numerical fit to the spectrum obtained at 2 K. The fit is good for energies below 2 meV but deviates from the background at around 2.5 meV , which may be caused by non-equilibrium effects within the barrier. The BTK model uses a dimensionless barrier strength parameter Z , which is zero for a pure $N-S$ interface and larger than unity for a good²⁵ $S-I-N$ interface. A Z value of approximately 0.63 was found for structure A^{5kV} by fitting its 2 K spectrum. This value

²⁵By a good $S-I-N$ interface we mean here such an interface that does not demonstrate Andreev reflection and the quasiparticle current through the barrier is carried only via quantum mechanical tunneling. See also Sec. 1.5.2.

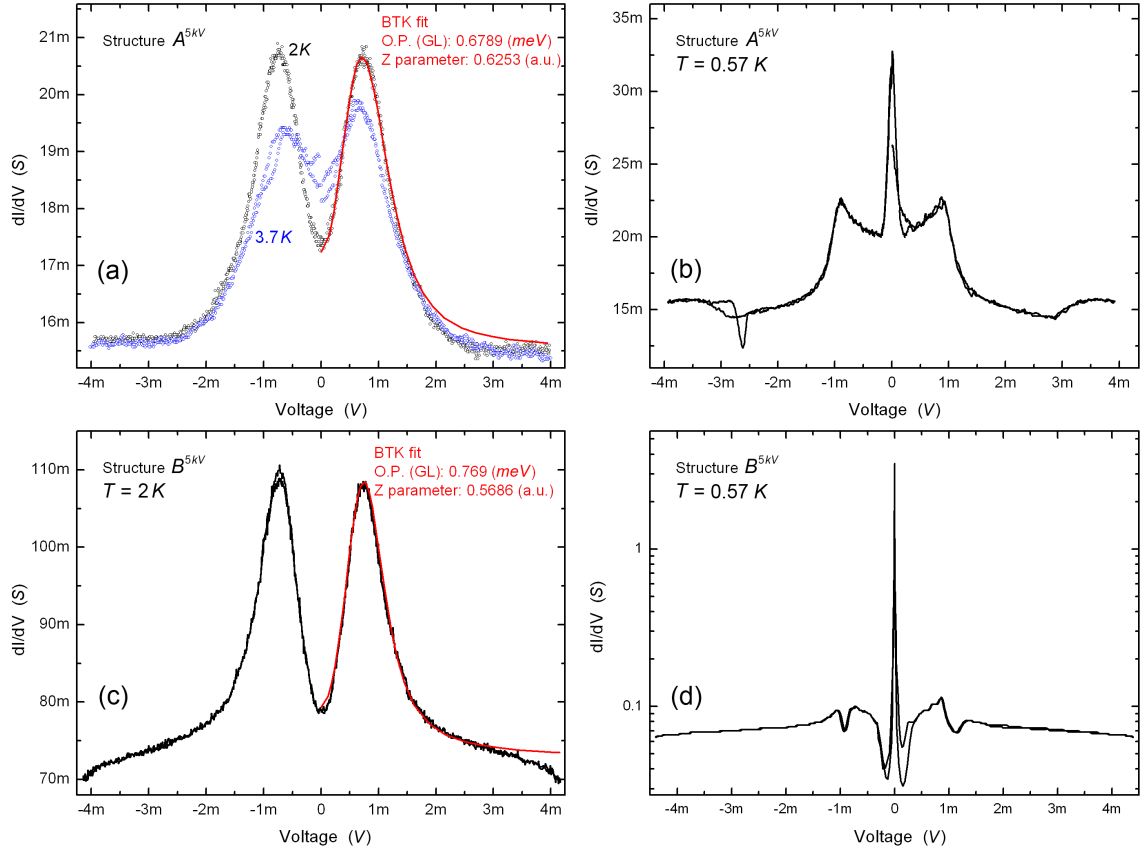


FIGURE 3.21: Differential conductance curves as a function of voltage measured for $Al-Al_2O_3-W-IBID$ planar tunnel diodes. (a) and (b) correspond to structure A^{5kV} and (c) and (d) to structure B^{5kV} (see text). The characteristics measured at temperatures below T_c^{Al} demonstrate a pronounced peak due to a Josephson transport channel (right panels). At temperatures above T_c^{Al} a quasiparticle tunneling channel is established.

The red solid curves are fits according to the BTK model.

is rather small and suggests the presence of both Andreev reflection and quasiparticle tunneling channels. The size of the SC gap obtained from this fit is $0.68 meV$, which agrees well with the temperature-dependent value obtained from the BCS theory for the measured value of $T_c^{W-IBID} = 4.9 K$.

If structure A^{5kV} is cooled below $T_c^{Al} = 1.5 K$, a strong Josephson current starts to flow between the two superconductors indicating a rather weak tunneling barrier, which supports the results of the numerical fit (Fig. 3.21(b)). However, the double-peak structure characteristic for quasiparticle tunneling is still observed around $1 mV$, which corresponds approximately to the sum of the two superconducting gaps $\Delta^{Al} + \Delta^{W-IBID}$. The tunnel spectrum for structure B^{5kV} measured in the $S-I-N$ regime is shown in Fig. 3.21(c). This spectrum was also fitted with the BTK model using the parameters given in the figure. The barrier resistance for this structure is lower than that for structure A^{5kV} and we expect an increased weight of the Andreev reflection in the $S-I-N$

regime. Indeed, according to the BTK fit the value of Z is reduced. At biases above 3 mV the best fitted curve starts to deviate strongly, which might correspond to self-heating effects since the heat dissipation in structure B^{5kV} at this bias is increased by approximately a factor of 5 compared to structure A^{5kV} . The tunneling spectrum of structure B^{5kV} measured in the $S-I-S'$ regime is shown in Fig. 3.21(d). The central sharp peak again corresponds to a Josephson current, which is now much stronger and the satellites at around 1 mV are further suppressed compared to structure A^{5kV} . The Josephson current enhancement also suggests that the insulating barrier of the interface between Al and W -IBID is much weaker in structure B^{5kV} than in structure A^{5kV} , as it was expected.

The most important result here is that, with a proper insulating tunneling barrier, W -IBID nano-deposits can be used as counter electrodes in planar tunneling structures for obtaining reliable spectroscopic information. Using the BTK model we confirmed our qualitative expectations that a large radiation dose received by the insulating tunneling barrier during the deposition of the W -IBID counter electrode can substantially modify the barrier quality, strengthening the Andreev reflection and the Josephson transport channels between two metallic electrodes.

3.4.3 Planar tunneling on $CeCoIn_5$ microcrystals

In previous sections we presented our motivation to perform a tunneling spectroscopy study on individual $CeCoIn_5$ thin film microcrystals. To prepare such tunneling structures, we used a $10 \times 10\text{ mm}$ $CeCoIn_5$ thin film whose surface morphology consisted of densely packed but well resolved microcrystals. The film was pre-patterned with UV photolithography similarly to how it was done on the Al film in the previous section. We used the photo-mask shown in Fig. 3.22 to the left and the ion beam etching technique to remove parts of the film. The procedure can be summarized as follows:

- The $CeCoIn_5$ thin film is covered with photoresist (AR-U 4040 positive resist)
- The resist film thickness is homogenized using a spin coater and baking the sample on a hot plate for 2 minutes at $95\text{ }^\circ\text{C}$
- The sample covered with the photoresist is exposed to UV light through a photo-mask
- The exposed resist is developed using an AR-300-35 developer
- The sample is etched using an ion beam

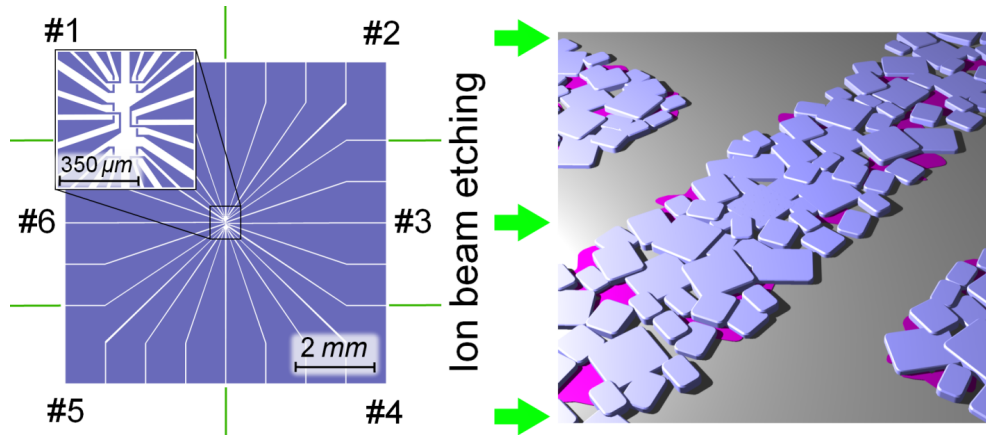


FIGURE 3.22: Left panel: photo-mask used for positive photolithography. The mask defines six cross-type structure templates to be patterned in the center and 24 outer contact pads for bonding Al wires. Right panel: central area of one of the six etched cross-type structures. The width of the stripes is $10 \mu m$.

- The remaining resist is removed from the sample by acetone cleaning in an ultrasonic bath

As a result, up to six structures can be prepared on such a sample, the central part of one such structure being schematically shown in Fig. 3.22 to the right. Here, the $CeCoIn_5$ microcrystals are shown in light blue, the segregation phases in pink, and the insulating substrate surface in grey. The same part of the film is also shown schematically in the main part of Fig. 3.23, which illustrates the microstructuring steps performed using SEM marked in chronological order by capital letters from A to F . These microstructuring steps can be summarized as follows:

- A : An approximately 10 nm thick $SiO-C$ tunneling barrier is deposited by means of FEBID; the corresponding SEM micrograph is (a)
- B : A thick (approximately 100 nm) donut-shaped insulating $SiO-C$ layer is deposited using FEBID; the corresponding SEM micrograph is (b)
- C : A thin W -IBID counter electrode is deposited by means of FIBID
- D : A part of the $CeCoIn_5$ central electrode is removed by FIB milling down to the insulating substrate; the corresponding SEM micrograph is (c)
- E : The edges of the patterned $CeCoIn_5$ microcrystal milled out in step C are covered by thick $SiO-C$ curbs for additional electrical insulation; the corresponding SEM micrograph is (d)
- F : A W -IBID top electrode is deposited by means of FIBID in order to connect the counter electrode to the outer leads; the corresponding SEM micrograph is (e)

The sequence described above is the result of a compromise between limiting the preparation time and improving the final quality of the structures. The exact realization of the preparation steps may slightly differ from sample to sample.

As was discussed in (Perentes & Hoffmann 2007), *SiO-C* composites with electrical insulating properties can be deposited by means of either a CVD method or FEBID using several precursor gases, which can modify the electronic properties of the composites. A number of microcrystal-based *CeCoIn₅* planar tunneling diodes were first prepared using a home-made gas injection system in our SEM operated with tetramethylsilane (*Si(SiH₃)₄*) as precursor gas²⁶. Most of the data presented in this section were obtained on these diodes. For some of the structures prepared later we used neopentasilane as precursor. These structures will be discussed at the end of this section. The room temperature four-terminal resistances of the tunneling barriers prepared with either precursor gas did not degrade after having exposed the structures to air.

The donut-shaped insulating deposit (step *B* and Fig. 3.23(b)) and the insulating curbs (step *E* and Fig. 3.23(d)) are intended to guide the electrical current flow only through the inner area defined in step *A*. In this case, the direction of the current flow is normal to the *CeCoIn₅* microcrystal surface, which presumably corresponds to the *c*-axis crystallographic direction. The metallic counter electrode is prepared (step *C*) by means of FIBID using tungsten hexacarbonyl (*W(CO)₆*) as precursor gas. According to our study on the *Al-Al₂O₃-W*-IBID tunneling diodes, the FIB may strongly modify the tunneling barrier. Due to this, the counter electrode was deposited in two steps. First, a thin layer was deposited at a reasonably low accelerating voltage (5 *keV*), making a compromise between the ion beam defocussing and the etching/doping effect. Second, a thick layer was deposited using 10 *keV* accelerating voltage on top of the first layer using FIBID.

The top electrode (step *F* and Fig. 3.23(e)) is electrically connected only to the counter electrode and to the outer contact pads (outside the figure). To achieve this, a channel down to the insulating substrate was etched on both sides of the patterned *CeCoIn₅* microcrystal (step *D* and Fig. 3.23(c)). Since the *CeCoIn₅* volume removed in this step is relatively large, one should consider the effect of re-deposition, which means that the etched material is partially deposited in the vicinity of the microstructure and partially leaves the surface into the SEM vacuum chamber. The re-deposited material can create unwanted paths for electrical current flow, which was monitored *in-situ* by sending a small current along different path combinations of the patterned structure. When found, the spurious conduction paths were eliminated by FIB milling.

²⁶For specific preparation parameters see Appendix E.

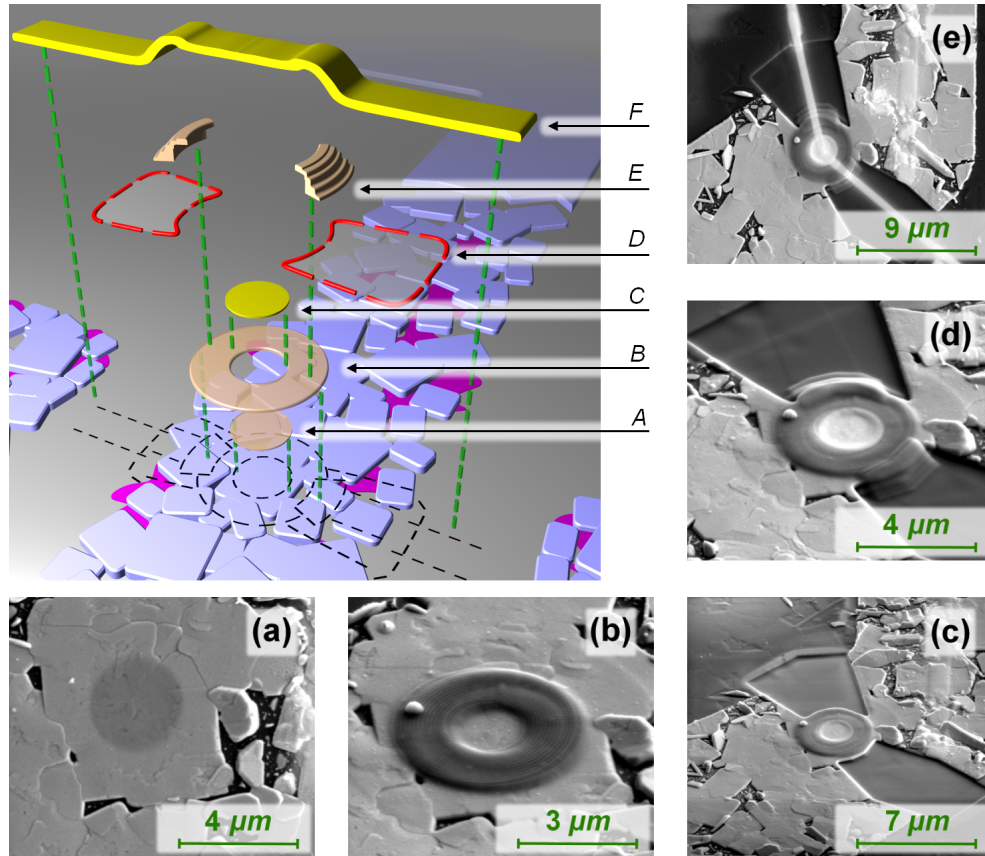


FIGURE 3.23: Preparation of a planar tunneling diode on a $CeCoIn_5$ microcrystallite with FIBID/FEBID/FIBM techniques (main panel) and several SEM micrographs of the intermediate steps taken with a focused electron beam. Here, *A* and (a) is a thin $SiO-C$ composite layer deposited by means of FEBID, *B* and (b) is a thick $SiO-C$ insulating layer, *C* is a thin $W-C$ counter-electrode deposited by means of FIBID, *D* and (c) represent the areas of the $CeCoIn_5$ crystallite milled down to the insulating substrate with FIBM for isolation purposes, *E* and (d) are the $SiO-C$ insulators deposited on the edges of the uncovered areas produced with the previous milling procedure, and *F* and (e) is a $W-IBID$ thick top-electrode that completes the electrical connections of the structure.

Several structures were prepared on a single pre-patterned $CeCoIn_5$ film following the described sequence of preparation steps with different tunneling barrier deposition times in order to optimize the value of the tunneling resistance. Then, the sample was transferred into a 3He cryostat for low-temperature measurements. A typical four-terminal temperature-dependent resistance curve of the tunneling barrier is shown in Fig. 3.24. For a tunneling oxide barrier one expects to observe a small decrease of the tunneling resistance with decreasing temperature²⁷ (Gundlach & Wilkinson 1970). However, the measured resistance is reminiscent of the $CeCoIn_5$ bulk resistance, which implies that the voltage drop in the $CeCoIn_5$ layer below the insulating barrier is comparable to the voltage drop across the barrier itself. This points towards large transparency

²⁷In the simplest case, this can be shown by considering the temperature dependence of the dielectric constant ϵ of insulator defined by the Clausius-Mossotti relation (Ashcroft & Mermin 1976) which is almost linear in T^2 .

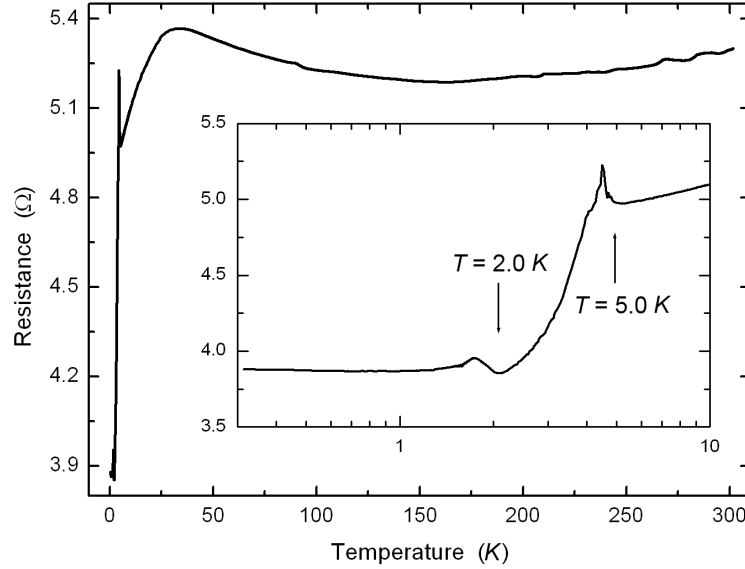


FIGURE 3.24: Four-terminal tunneling resistance as a function of temperature measured on a patterned $CeCoIn_5$ crystallite. The inset shows low-temperature data with arrows indicating the approximate temperatures of the SC transitions in W -IBID at $T = 5.0$ K and in $CeCoIn_5$ at $T = 2.0$ K. The tunneling barrier was prepared by means of FEBID using tetramethylsilane as precursor gas.

of the insulating barrier. The RRR value obtained using the characteristic shown in Fig. 3.24 is less than that obtained in simple transport measurements on a $CeCoIn_5$ microcrystal in Sec. 3.4.1. This can be explained by the contribution of the weakly temperature-dependent barrier resistivity.

The inset in Fig. 3.24 demonstrates the low-temperature part of the measured tunneling barrier resistance. The two features at around 5 K and 2 K are associated with the SC transitions in the W -IBID counter electrode and in the $CeCoIn_5$ layer, respectively. The resistance drop between these temperatures suggests a contribution of the W -IBID counter electrode to the measured resistance. The observed large contributions from the resistances of both metallic electrodes are possible only when the tunneling barrier is highly transparent.

Dynamic conductance characteristics of the planar tunneling structure (Fig. 3.25) were measured using the lock-in setup described in Sec. 2.5.1. These characteristics have the same differential conductance level of about 0.2 S at 800 μ V and the plots in Fig. 3.25 were shifted vertically for clarity. Here, the bottom curve, measured at 4.9 K, is expected to demonstrate an N - I - S type behaviour since $T_c^{W-IBID} \approx 5$ K. Indeed, one finds small non-linearities around 180 μ V which can be attributed to a developing SC gap in the W -IBID counter electrode. In the next curve above, measured at 4.55 K, the SC gap of the W -IBID counter electrode attains approximately half of its maximal size, in accordance with the BCS theory. This SC gap value corresponds to the smoothed features at

about $365 \mu V$. The smoothed nature of these features is in agreement with thermal broadening effects, in contrast to the large sharp peaks at a slightly smaller voltage. The sharpness of these peaks indicates their non-spectroscopic nature. These peaks may result from resonant tunneling via bound states within the barrier (Chang, Esaki *et al.* 1974, Esaki 1974, Wolf 1985), which can also cause the conductance enhancement around zero bias observed at temperatures above $2 K$. The possibility of multiple Andreev reflections within the barrier may also be considered, see, e.g., (Dieleman, Bukkems *et al.* 1997, Kleinsasser, Miller *et al.* 1994) and references therein.

As temperature is lowered further, the sharp features observed at $4.55 K$ get suppressed and disappear already at $4.1 K$. At this temperature the non-linearities attributed to the SC gap of *W*-IBID shift to higher bias voltages first and become barely visible below $4.1 K$. A very broad central maximum appears below $4.55 K$. This maximum grows with decreasing temperature, developing slowly a second superimposed peak at zero bias observable down to $2 K$, which corresponds to the SC transition temperature of *CeCoIn₅*. Below $2 K$ the spectra develop a series of sharp features. At the lowest measured temperature, the conductance at small bias voltages becomes substantially enhanced with respect to its high bias tails. The analysis of the spectra measured below T_c of *CeCoIn₅* is complicated by our presumably insufficient control over the quality of the insulating barrier and poor reproducibility of these features from structure to structure. Qualitatively, the conductance enhancement at small biases below $2 K$ can be at least partially due to a Josephson transport channel, which is favored in highly transparent barriers. For the resonant tunneling, proposed above as a possible cause of the sharp features, to be established, the presence of localized or bound states within the barrier is required. This seems to be plausible in our case since the barrier was exposed to a focused beam of accelerated *Ga* ions and thus doped. Although the doping dose received by the barrier during the carefully optimized patterning procedure is small, the measured tunneling spectra may be extremely sensitive to even small concentrations of the resonant levels (Duke & Alferieff 1967, Clark & Young 1968, Plummer & Young 1970). Additionally, one should not neglect the influence of the *CeCoIn₅* quasiparticle DOS, as suggested by the qualitatively different characters of the spectra above and below T_c of *CeCoIn₅*.

Clearly, in order to obtain easier analyzable tunneling spectra, one has to improve the quality of the tunneling barriers. Several microstructures were prepared with a gradually increasing nominal thickness of the insulating barrier using tetramethylsilane (*Si(SiH₃)₄*) as precursor gas which improved neither the analyzability of the tunneling spectra nor the reproducibility of the low-temperature tunneling patterns even for structures with smaller barrier transparency.

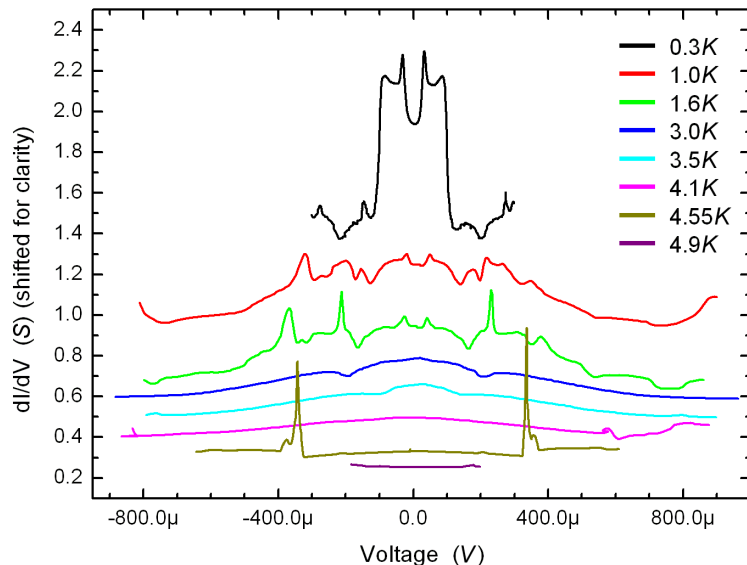


FIGURE 3.25: Set of differential conductance curves as a function of voltage for selected temperatures measured on a planar tunneling structure prepared on a $CeCoIn_5$ microcrystallite with W -IBID counter electrodes.

Several samples were also prepared using neopentasilane ($H_{12}Si_5$) as precursor gas for depositing $SiO-O$ insulating tunneling barriers²⁸. With this precursor, the transparency of the tunneling barriers at the room temperature was considerably reduced. The corresponding resistances of these barriers were in the range 270-570 Ω compared to 0.5-10 Ω for the structures obtained using $Si(SiH_3)_4$ precursor gas²⁹.

The four-terminal temperature-dependent resistance of the new barriers shown in Fig. 3.26 turned out to be qualitatively different. It increases by two orders of magnitude from room temperature down to 300 mK . This, unfortunately, makes a reliable detection of any spectroscopic response rather unlikely. Although the Johnson-Nyquist noise at 300 mK is one order of magnitude smaller than the voltage at which spectroscopic features are expected, the spectra measured on the new structures are essentially noise. The absence of spectroscopic response from the new structures can be explained by a negligibly small overlap within the barrier between the wavefunctions ψ and ϕ (using notation of Sec. 1.5.2) of the two electrodes. The residual conductance of these structures is probably due to the availability of local states within the barrier. Such states do not provide an energy continuum to the charge carriers and the latter are injected into a metal electrode around a single energy, if elastic processes are considered. As a result, the tunneling spectra cannot provide information about the electron density of states for the metal electrode. Additionally, noise that is much larger than the Johnson-Nyquist

²⁸This precursor gas was recently used to obtain Si layers of an epitaxial quality by means of CVD (Chung, Yao *et al.* 2008).

²⁹The area of the tunneling barriers was not varied.

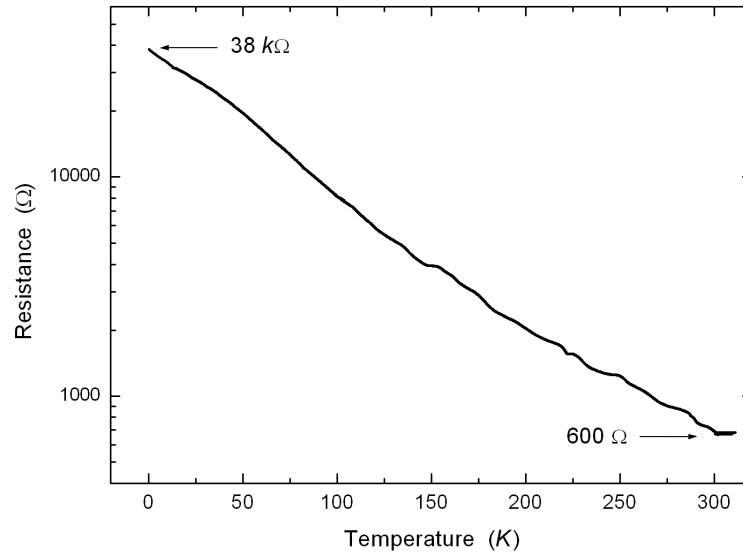


FIGURE 3.26: Four-terminal tunneling resistance measured as a function of temperature on a patterned $CeCoIn_5$ crystallite. The tunnel barrier was prepared via FEBID using neopentasilane as precursor gas.

noise may be generated within the W -IBID electrodes, which is also discussed on p. 160.

Summarizing this section, we can state the following. Planar tunneling structures with large barrier transparencies prepared on microcrystals of $CeCoIn_5$ thin films demonstrated spectroscopic features in their low-temperature dynamic resistance characteristics. We observed a rich variety of non-linearities that were poorly reproducible from structure to structure. We were not able to analytically single out the $CeCoIn_5$ spectroscopic information in these spectra. Structures with smaller barrier transparencies were also prepared using neopentasilane as precursor gas. However, the peculiar electronic properties of the insulating barriers deposited with this precursor gas did not allow us to prepare high-quality insulating tunneling barriers.

3.4.4 Quantum interferometers on $CeCoIn_5$ microcrystals

Variable width microconstrictions

As discussed, working on planar tunneling structures prepared on $CeCoIn_5$ microcrystals, we met several difficulties associated with the peculiar properties of the $SiO-C$ insulating barriers. It may well be, however, that these difficulties can be surmounted by either improving the preparation procedure or by using another tunneling barrier material. On the other hand, as we have seen, the surface of the $CeCoIn_5$ thin films contains many defects, which might affect the $CeCoIn_5$ electronic properties close to

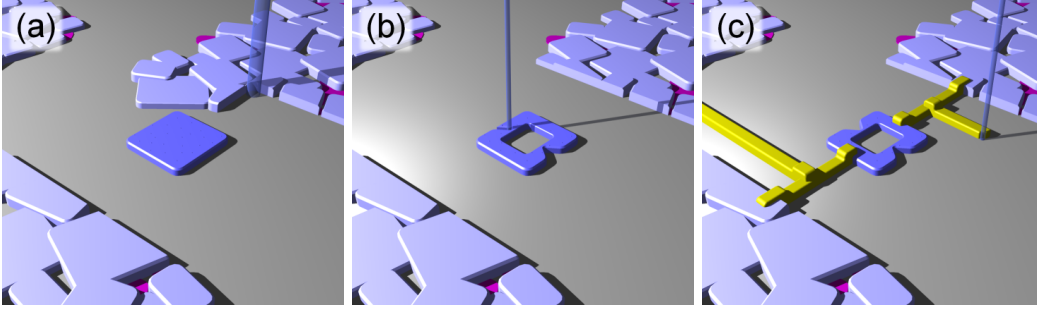


FIGURE 3.27: Sketch of the interferometer preparation steps. (a) A crystallite located in the central stripe of the cross-structure is electrically isolated via etching out the neighboring crystallites with FIBM down to the insulating substrate. (b) The selected crystallite is shaped into a closed loop via FIBM. Afterwards, microbridges are formed with the FIBM by reducing the cross-sectional areas within two opposite arms of the interferometer. (c) The interferometer is electrically connected with $W-C$ nanowires deposited using the FIBID technique.

the surface and, correspondingly, the planar tunneling spectra. In this section, we will present a different approach which does not require preparation of interfaces between dissimilar materials. As we mentioned earlier, the $CeCoIn_5$ SC state can be probed by the Josephson effects. To do that, we prepared a SQUID on a microcrystal of a $CeCoIn_5$ thin film using UV photolithography, FIB milling, and FIBID techniques in a way similar to how the planar tunneling diodes were prepared.

A $CeCoIn_5$ thin film pre-patterned with UV photolithography was mounted on a standard PCB holder (see Fig. 3.5) and connected with $30\ \mu m$ thick $Al-Si$ wires to the PCB pins by means of ultrasonic bonding. Then, the sample was transferred into the SEM chamber for micropatterning. A suitable $CeCoIn_5$ microcrystal was selected within one of the central electrodes. The selected microcrystal was etched out from the conductive medium by FIB milling (Fig. 3.27(a)). A central opening and microbridges of desired shapes and dimensions were next etched from the microcrystal (Fig. 3.27(b)). Finally, W -IBID nanowires for electrical contacting were deposited by means of FIBID (Fig. 3.27(c)). SEM micrographs of the prepared loop are shown in Fig. 3.28. Once the preparation had been finished and the four-probe resistance had been verified *in-situ*, the sample was immediately transferred into the 3He cryostat for low-temperature transport measurements. $V-I$ characteristics of this SQUID were measured with a nanovoltmeter and a programmable current source³⁰. It is known that current flowing through SC microbridges of different shapes or of different widths, as in our structure, can experience Josephson coupling (Likharev 1979). Therefore, the prepared loop is expected to demonstrate a SQUID-like behaviour, i.e., that of two Josephson junctions connected in parallel.

³⁰As a current source we used a programmable voltage source with a current compliance limit of $80\ \mu A$ connected to the SQUID current terminals via a serial resistor of $700\ \Omega$.

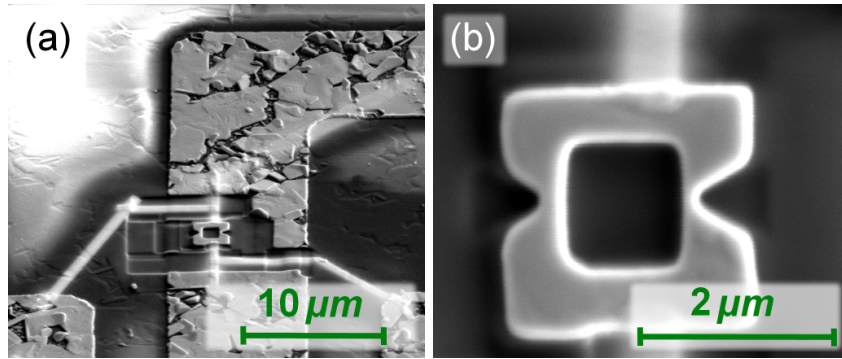


FIGURE 3.28: (a) SEM micrograph of an as-prepared interferometer. (b) Zoomed in SEM micrograph of the same interferometer. The microconstrictions are of variable width geometry. Electrical current is sent through the contact leads which appear vertically in the figure.

Let us discuss the low-temperature V - I characteristics of this structure. Fig. 3.29 demonstrates a set of V - I characteristics for temperatures 1.7-5.2 K . At temperatures below 2.0 K , when the $CeCoIn_5$ microcrystal is superconducting, one expects to observe the DC Josephson effect. Indeed, at these temperatures and at a fixed low bias (see the left top inset) the current through the loop increases as the temperature is lowered pointing to an increase of the Josephson transport channel through the microbridges. At 1.7 K the characteristics become noticeably non-linear up to approximately $4 \mu A$, which probably corresponds to the Josephson critical current I_c^J . The characteristics demonstrate a finite resistance even below 2 K (T_c of $CeCoIn_5$) which is a signature of possible dissipative transport channels through the microbridges, e.g., quasiparticle transport, SC vortex flow *etc.* At 300 mK the V - I characteristics become step-like (see Fig. 3.31) indicating that only the Josephson transport channel up to $I_c^J = 15 \mu A$ remains active. These qualitative changes of the V - I characteristics, however, are rapid, poorly reproducible and can be observed at any temperature in the range of approximately 0.3-1 K . At temperatures above T_c of $CeCoIn_5$ and low biases the V - I characteristics are essentially straight lines with varying slopes due to a steep temperature dependence of the electrical resistivity of $CeCoIn_5$. For higher biases and temperatures below 4.2 K the characteristics demonstrate two additional kinks at around 20-50 μA , which are zoomed in the right bottom inset in Fig. 3.29.

As discussed, the $CeCoIn_5$ interferometer is connected to outer contacts via W -IBID leads (see Fig. 3.27) which are superconducting below approximately 5 K . The voltage leads³¹ are located such (see Fig. 3.28(a)) that the measured voltage drop is a sum of the voltage drops on the W -IBID current leads and on the loop. The voltage drop on the current leads will not be sensed as long as they are superconducting. However, if the SC current through the W -IBID leads exceeds a certain critical value, the leads can

³¹By voltage leads we mean sensing leads of a four-terminal measuring scheme.

become normal. When this happens, a step-like increase of the measured resistance at the critical value of electrical current should be observed. The normal state resistance of the W -IBID leads can be estimated using their known dimensions and typical resistivity values of W -IBID composites ($\rho = 2\text{--}7 \mu\Omega\text{m}$ at 5 K from (Sadki, Ooi *et al.* 2004) and earlier experiments in our group). One thus obtains that the resistance is approximately 55Ω for each measurable part of the W -IBID leads when $\rho = 2 \mu\Omega\text{m}$ is used. This value is very close to the resistance increments observed on the measured characteristics in Fig. 3.29. The currents at which the steps are observed are slightly different, which can be due to a small difference between the critical currents of the two W -IBID current leads. The value of the SC critical current density for these W -IBID wires obtained in our experiment, approximately $1.0 \times 10^9 \text{ A/m}^2$, compares well with that reported in literature, approximately $1.5 \times 10^9 \text{ A/m}^2$ (Sadki *et al.* 2004).

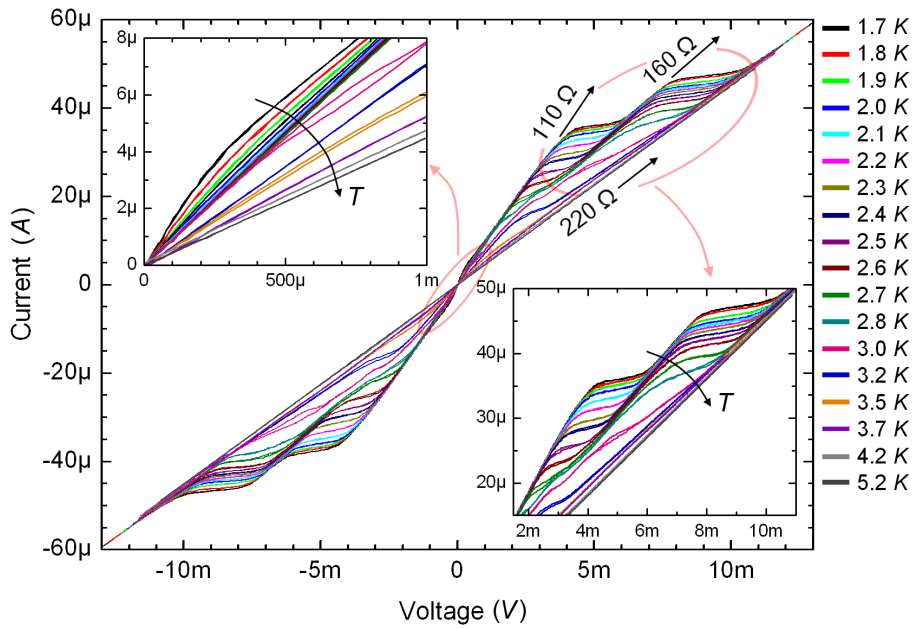


FIGURE 3.29: Set of V - I characteristics for selected temperatures of an interferometer with variable width microconstrictions prepared on a $CeCoIn_5$ microcrystal. The curves are measured in a voltage-driven mode. The left top inset demonstrates a detailed view of the temperature development of the Josephson current. The right bottom inset demonstrates a detailed view of the temperature development of the two step structure, which is due to the suppression of superconductivity in the W - C leads by a high current density.

The critical currents at which the two resistance steps appear are plotted as a function of temperature in Fig. 3.30. The solid lines are fitted temperature dependences of the SC critical current from the Ginzburg-Landau theory, which are given by $I_c^J(T) \sim (1 - T/T_c)^{3/2}$ with the SC critical temperatures 3.8 K and 4.3 K for curves A and B respectively. The Ginzburg-Landau theory is valid only for temperatures close to T_c ,

which explains the deviation of the theoretical curves from the experimental data at lower temperatures observed in Fig. 3.30.

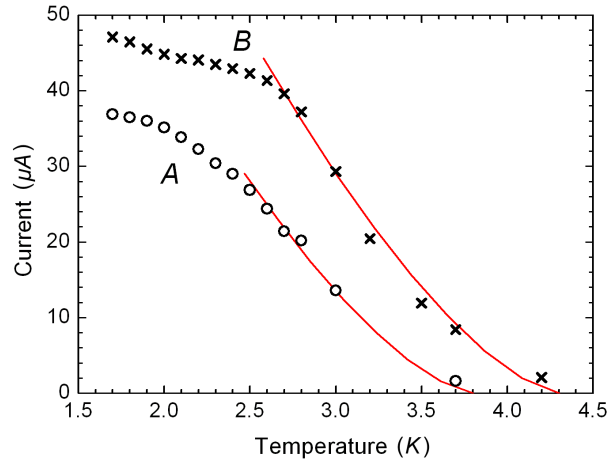


FIGURE 3.30: Values of the critical current for the two sets (A and B) of resistance steps in Fig. 3.29 as a function of temperature with crosses and open circles. The red solid curves are calculated from the Ginzburg-Landau theory (see text).

From our earlier analysis of the curves in Fig. 3.29 for low biases followed that a small Josephson current is present at low enough temperatures. Thus, for two Josephson junctions connected in parallel one expects to observe a modulation of the Josephson critical current I_c^J or, equivalently, a modulation of the measured voltage by varying the external magnetic field. A set of V - I characteristics measured at 300 mK in an external magnetic field, which varied from $-5 mT$ to $5 mT$ with a step width of $0.2 mT$, is shown in Fig. 3.31. This particular choice of the magnetic field range and step width was made considering the value of one flux quantum through the SQUID area, which is reached in a field of $0.25 mT$ ³². As is clear from the data shown in Fig. 3.31, the modulations of the Josephson critical current are non-systematic. Additionally, one observes non-systematic occurrences of hysteresis in either direction of the magnetic field. According to the resistively and capacitively coupled junction (RCSJ) model commonly used for the analysis of Josephson junctions, a hysteresis in V - I curves is expected for Josephson junctions with large capacitances (Tinkham 2004), which is not the case for our microbridges. Thus, the observed hysteresis is most likely caused by trapped magnetic flux and by the vortex dynamics within the SQUID arms.

Let us summarize the most important results of this study. The DC Josephson effect can be observed on a properly microstructured $CeCoIn_5$ thin film microcrystal. However, Josephson critical current modulations with external magnetic field could not be detected. As possible reasons we suggested the complex dynamics of the superconducting vortices and the associated trapped flux which can smear out the effects of externally

³²This value is still large compared to the magnetic field of the Earth, which is about $50 \mu T$.

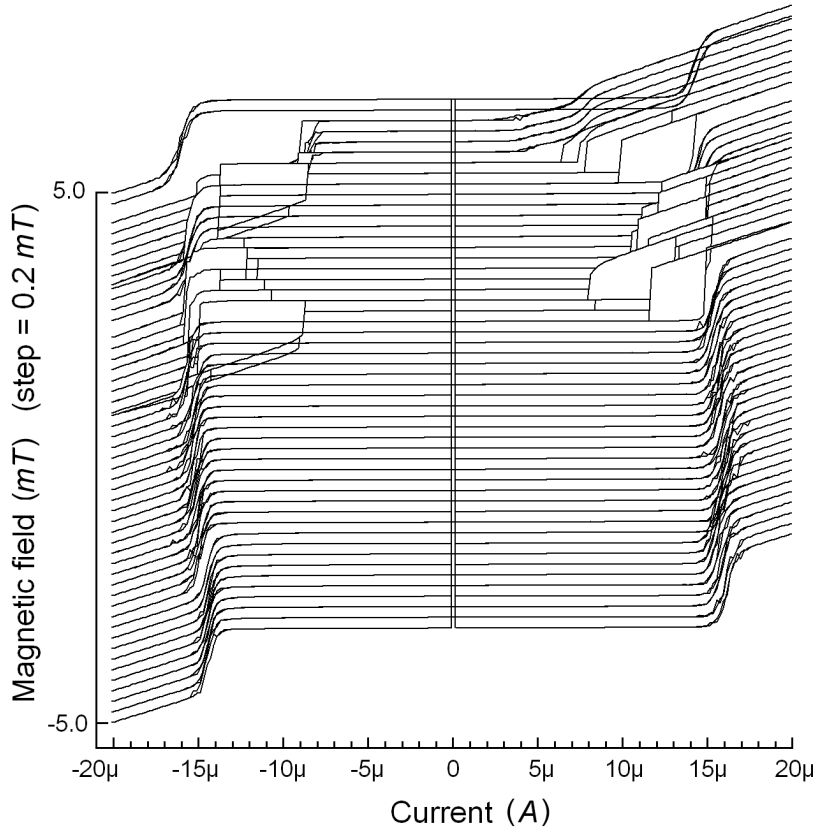


FIGURE 3.31: Modulation of the Josephson critical current by a magnetic field measured on a $CeCoIn_5$ interferometer with variable width microconstrictions at 300 mK . The magnetic field was varied from -5 to 5 mT with a step width of 0.2 mT .

applied magnetic fields. Additionally, one should be aware of the large current densities involved in measurements of the SC microbridges, which have to be properly accounted for during the preparation of the current leads.

Variable width and thickness microconstrictions

In the next step, we investigated a SQUID prepared with variable thickness microbridges on an individual $CeCoIn_5$ thin film microcrystal. A $CeCoIn_5$ thin film was pre-patterned as shown in Fig. 3.22. The microstructuring was done using FIBID and focused ion beam etching, similarly to the previous study. A selected $CeCoIn_5$ microcrystal was etched out from overlapping $CeCoIn_5$ microcrystals within the central electrode (Fig. 3.32(a)) using the FIB milling technique. In contrast to the previous SQUID, the current (marked by red arrows) and voltage (marked by green arrows) leads were etched out from the $CeCoIn_5$ film in the vicinity of the SQUID loop, so that no other materials were required here. FIB milling was applied to etch out the central hole and the microbridges in the $CeCoIn_5$ microcrystal (Fig. 3.32(b)). The voltage leads were prolonged with W -IBID nanowires to complete the electrical connections

(Fig. 3.32(c)), while for current paths only the $CeCoIn_5$ film was used. An SEM mi-

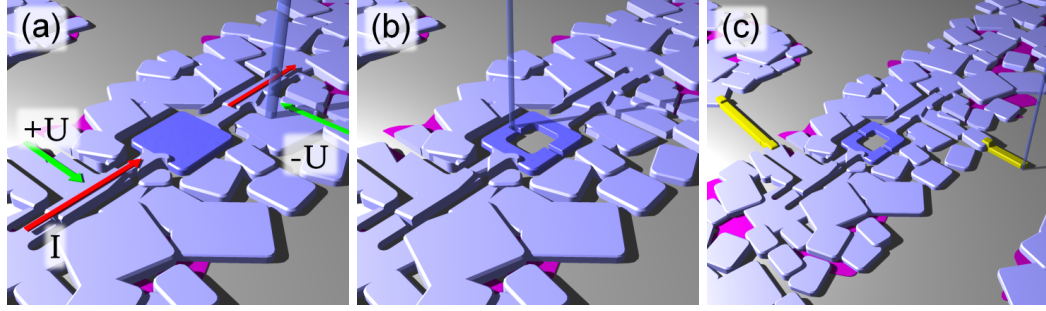


FIGURE 3.32: Sketch of the interferometer preparation steps. (a) A crystallite located in the central stripe of the cross-type template etched before is selected for micropatterning. The current and voltage leads are etched out from the neighboring crystallites by means of FIBM. The current flow is shown by red arrows, while the voltage probes are highlighted by green arrows. (b) The loop is shaped via etching with FIBM. Variable thickness microconstrictions are created on the interferometer arms via milling with FIBM. (c) Outer electrical $W-C$ leads are deposited by means of FIBID.

crograph of the prepared SQUID is shown in the left panel of Fig. 3.33. The inset demonstrates a zoomed in part of one of the SQUID arms with a microconstriction. The dimensions of the loop and of the bridges are given in the caption to this figure. The thickness of the film, as measured by means of AFM, is approximately 300 nm . The

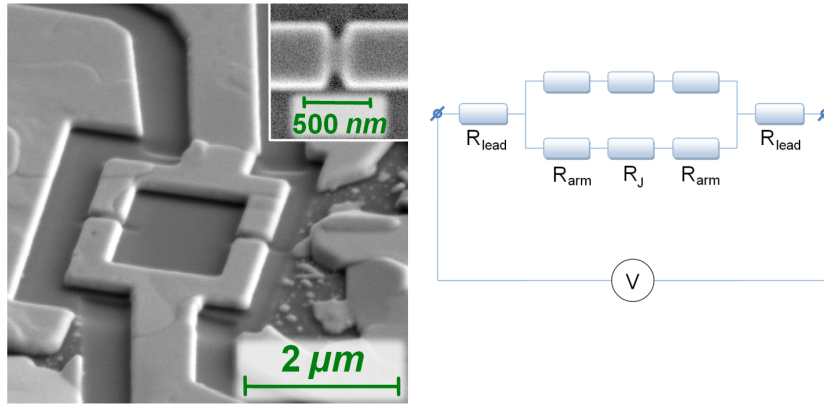


FIGURE 3.33: Left panel: SEM micrograph of the as-prepared SQUID on a $CeCoIn_5$ microcrystal. The inset shows a detailed view of one of the SQUID microbridges. The length of the microbridges, measured along the current flow, is approximately 90 nm . Their width, measured perpendicularly to the current flow, is approximately 225 nm . Right panel: equivalent electrical scheme of the SQUID. Here, R_{lead} are the $CeCoIn_5$ leads, which lie outside the loop and in between the voltage probe leads. R_J are the microbridges and R_{arm} are the SQUID arms.

variable thickness microbridges of this SQUID are much more constricted as compared to the variable width microbridges of the previous SQUID, which implies a weaker coupling between the two SC semicircles of the SQUID. The four-terminal resistivity of the SQUID appears in Fig. 3.34. The RRR ($R_{300K}/R_{2.5K}$) was found to be 2.9, which is slightly larger than the RRR measured on a $CeCoIn_5$ microcrystal before (see Sec. 3.4.1)

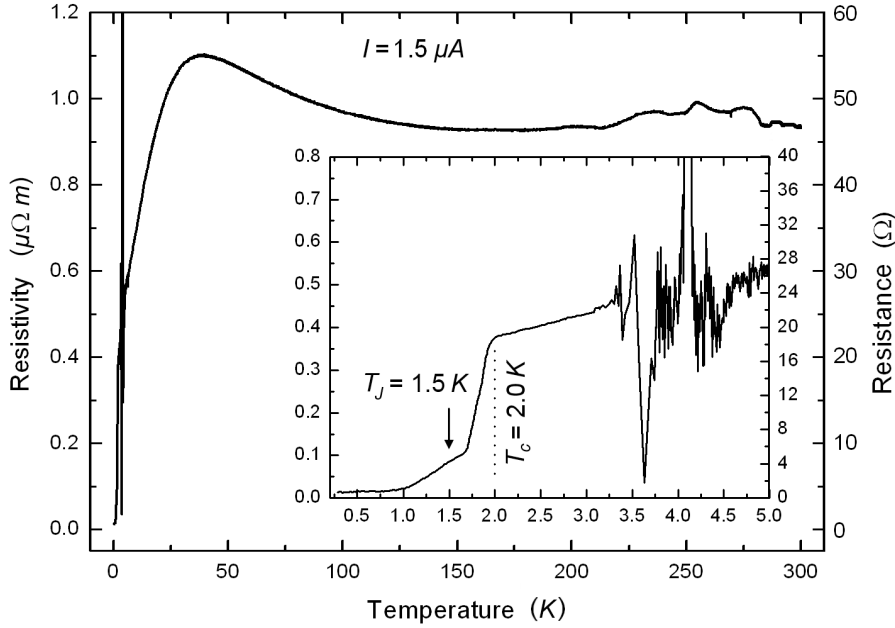


FIGURE 3.34: Temperature-dependent resistivity of the $CeCoIn_5$ SQUID measured during cooling down. The inset shows a low-temperature region of the resistivity where the noise is associated with the SC transition in the W -IBID leads. The SC transition of $CeCoIn_5$ is found at $T_c = 2\text{ K}$, and the second kink at 1.5 K is associated with the Josephson coupling temperature T_J .

but still smaller than the RRR of bulk crystals. The resistivity above T_c is also larger than that reported in Sec. 3.4.1 and in (Foyevtsov *et al.* 2010). The small RRR and the large resistivity above T_c measured on the SQUID support the suggested poor structural quality of the $CeCoIn_5$ thin film crystallites (see Sec. 3.3.3). The noisy variations of the resistivity at around 250 K are not due to intrinsic properties of the microcrystal, but rather due to a variation of the contact resistance resulting from an instable cooling rate at these temperatures. The inset shows the zoomed in low-temperature part of the resistivity curve. The noise at around $4.0\text{--}4.5\text{ K}$ is most likely related to the SC transition in the W -IBID nanowires. This is in fact quite surprising because these wires are a part of the voltage leads only and therefore conduct a negligible current. It might be, however, that large voltage noise is generated in W -IBID nanowires at temperatures close to the SC transition temperature of W -IBID, as was also reported for other granular materials (Aponte, Bellorín *et al.* 1993, Kiss & Svedlinh 1993). The SC transition of $CeCoIn_5$ is found at 2.0 K , which is a typical value for both the $CeCoIn_5$ microcrystals and the $CeCoIn_5$ thin films discussed earlier. An additional smooth transition is also found at around 1.5 K (see inset in Fig. 3.34), which is associated with the Josephson coupling temperature T_J . The fact that the Josephson coupling is established at $T_J < T_c = 2.0\text{ K}$ is probably due to a reduction of T_c in the bridges caused by the FIB milling during the micropatterning. One may notice that even at the lowest temperatures and at a current density in the microbridges as small as 22 A/m^2 , the resistance is saturated to

a finite value $R_{0,SC}^{loop} \approx 0.07 \Omega$. This can be explained by considering thermally activated processes, which might substantially modify the V - I relation of a Josephson junction. Particularly, it was shown by Ambegaokar and Halperin (Ambegaokar & Halperin 1969) that the resistance of such a Josephson junction is finite below I_c^J . In terms of the RCSJ model, this Josephson junction may be viewed as overdamped, i.e., with small capacitance, which is naturally expected for microconstrictions (Likharev 1979).

The theoretical analysis of bridges whose dimensions are large compared to the Ginzburg-Landau coherence length ξ is difficult. For large ratios³³ W/ξ and L/ξ the bridge leaves the regime of the “ideal” Josephson behaviour and enters the Abrikosov vortex motion regime, as was pointed out by Likharev (Likharev 1979). As a result, essential characteristics of the bridge are modified, such as the shape of the SQUID voltage modulations or the dependence $I_c^J(T)$ (Likharev 1979, Golubov, Kupriyanov *et al.* 2004). Given the dimensions of our bridges and $\xi_{CeCoIn_5} \approx 5 \text{ nm}$ (DeBeer-Schmitt, Dewhurst *et al.* 2006), one finds that both ratios $W/\xi \approx 18$ and $L/\xi \approx 50$ are large.

A set of dynamic resistance curves as a function of current measured using the lock-in setup described earlier are shown for selected temperatures in Fig. 3.35. The curves measured above T_c show an anomalous background resistance, visible up to 10 K, out of which the SC state evolves. Signatures of superconductivity appear on top of the background anomaly at about 2.0 K and become more pronounced as the temperature decreases. At temperatures below T_J the curves develop additional features, which are marked by arrows on the lowest curve. We attribute these features to the periodic motion of Abrikosov vortices. Before discussing these features in detail, let us demonstrate that well-resolved SQUID oscillations can be measured on this microstructure. The inset of Fig. 3.36 shows typical measured SQUID voltage modulations as a function of an externally applied magnetic field. The oscillations are well reproducible and of a sine-like shape without asymmetries. The period of the oscillations corresponds to one flux quantum $\Phi_0 = h/2e$ over the average area³⁴ of the SQUID loop with excellent agreement. Occasionally, the phase of the oscillations is randomly shifted. Since the SQUID oscillations are a measure of the SC phase difference between the two SC banks modulated by an external magnetic field, these phase slips may be attributed to randomly trapped flux. The main part of Fig. 3.36 shows a long period modulation with the superimposed SQUID oscillations, which appear as a band due to the scale. The former modulations are associated to the Josephson modulations of the two individual bridges, which will be supported by additional data below. These long period modulations are also affected by random phase slips. Their perturbed periodicity might be caused by

³³Here, W is the width and L is the length of a microbridge.

³⁴We define the average area of the SQUID loop as the area of a contour which can be drawn through the middle points of the SQUID arms.

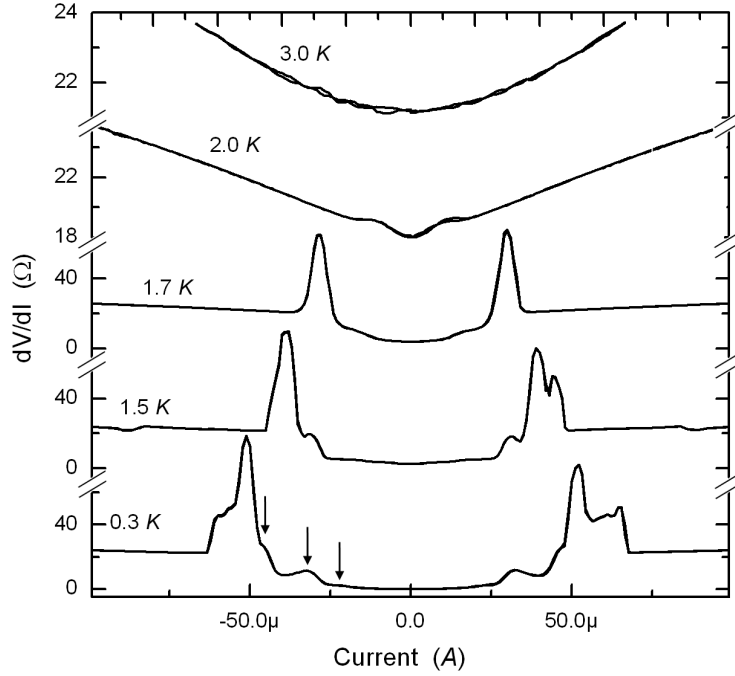


FIGURE 3.35: Dynamic resistance characteristics of the SQUID measured at several temperatures. The features in the lowest curve marked by arrows are ascribed to the periodic motion of SC Abrikosov vortices (see text for details). The dynamic resistance at 0.3 K and small current biases is non-zero.

interference effects between the two microbridges since they are coupled through the SC wave function in the arms. A rough estimate of the period of these oscillations gives $\Delta B \approx 10 \text{ mT}$ and, according to³⁵ $s = \Phi_0/\Delta B$, implies that the effective dimensions of each bridge extend into each SC bank by about 200 nm, which compares favorably with the London penetration depth λ_L for $CeCoIn_5$ (DeBeer-Schmitt *et al.* 2006).

A single Josephson interface is often characterized by measuring the oscillatory $I_c^J(B)$ relation. In principle, parallel arrangement of two Josephson interfaces, when they are identical, should give the same periodicity of $I_c^J(B)$ as in the case of a single interface. If some asymmetry is present, a small beating effect is to be expected. Since the observed SQUID modulations confirmed the Josephson coupling within both microbridges, we attempted to measure the $I_c^J(B)$ relation in the same way as it was done for the previous microcrystal-based SQUID. In contrast to the previous case, one can clearly see in Fig. 3.37 the modulations of the SQUID critical current $I_c^J(B)$ with a period of approximately 0.5 mT, which is consistent with the observed periodicity of the SQUID voltage modulations. The critical current modulations, however, demonstrated poor reproducibility and were occasionally disturbed by stochastic jumps, which can be associated with trapped flux. This behaviour might be due to several reasons. First,

³⁵Here s is the area of one microbridge.

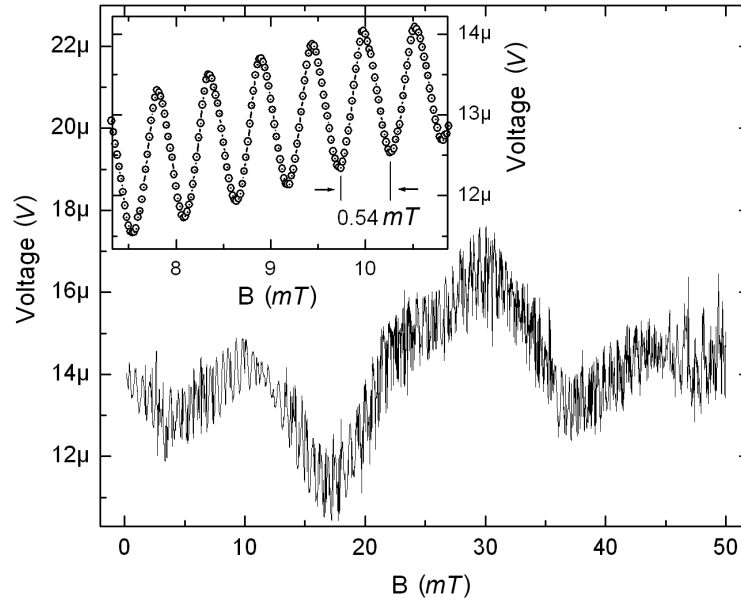


FIGURE 3.36: Measured SQUID voltage oscillations as a function of an external magnetic field on a large scale. The inset shows the SQUID oscillations on a smaller scale. Note that on the large scale the SQUID oscillations appear as a band of values on top of a slow modulation.

interference effects, as was suggested above, may disturb the $I_c^J(B)$ dependence. Second and most important, the complex dynamics of Abrikosov vortices, discussed below, may have a substantial influence in the performed measurements. The second scenario is highly plausible, since the position of I_c^J on every V - I characteristic has a complex magnetic history, which introduces additional, barely controllable variations of the critical current from curve to curve. This is in contrast to the SQUID voltage modulation measurements, which are performed at a fixed current bias in a slowly varying magnetic field. As will be shown below, the current bias has substantial influence on the vortex dynamics within the microbridges.

Let us now go back to the features marked by arrows in Fig. 3.35. The strong manifestation of the Josephson effect observed on this SQUID enables us to analyze the peculiarities of the transport characteristics at low temperatures in the framework of models developed for the Josephson effect in microbridges (Aslamazov & Larkin 1975, Kulik & Omelyanchuk 1975, Kulik & Omelyanchuk 1977, Ishii 1970). The Aslamazov-Larkin (AL) theory (Aslamazov & Larkin 1975) may be used for the analysis of the V - I characteristics of microbridges of a geometry similar to ours when vortex dynamics has to be accounted for, i.e., when $W \gg \xi$ and $L > \xi$. In the framework of this model, the electrical current density across the bridge is non-uniform (see Fig. 3.38(a)) and is described as $j(x) = I/\pi d\sqrt{a^2 - x^2}$, where I is the total current through the bridge, d is the bridge thickness, a is equal to $W/2$, and x is the coordinate along the width of the

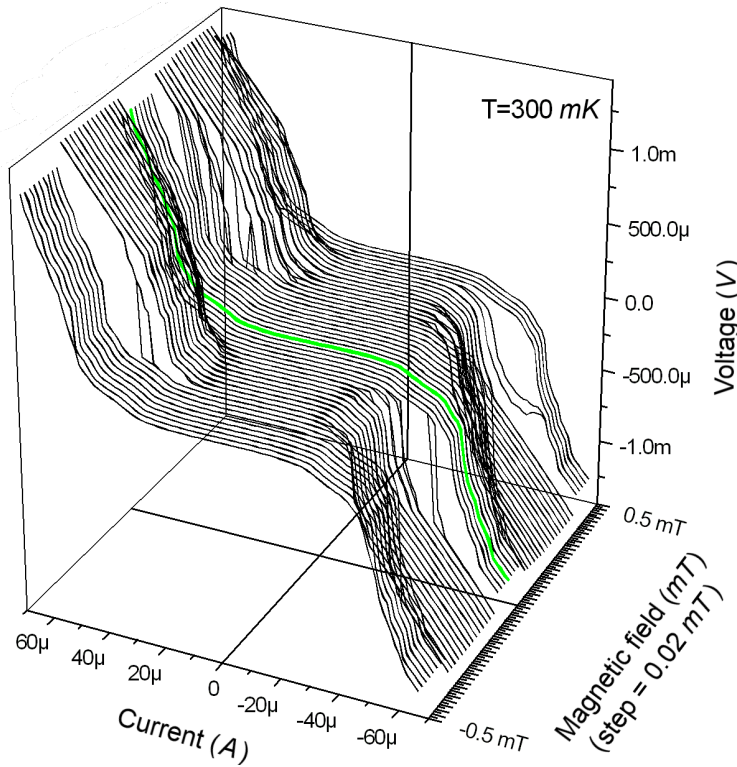


FIGURE 3.37: Set of V - I characteristics of the $CeCoIn_5$ thin film microcrystal-based SQUID demonstrating a modulation of the Josephson critical current in an applied magnetic field.

bridge with $x = 0$ at the bridge center. It may be shown that two vortices of opposite vorticity are most likely to enter the bridge from opposite edges due to the locally highest current density there. As is shown in the AL model, the total force acting on the n -th vortex is $F_n = -F_L + F_s \pm F_{vv}$ (see Fig. 3.38(b)). Here, F_L is the Lorentz force due to the interaction with the current I , F_s is the interaction with the edge, and F_{vv} is the vortex-vortex interaction term. At low currents a vortex remains pinned to the edge due to F_s as long as the counteracting Lorentz force is $F_L \leq F_s$. Neglecting the F_{vv} term, when the number of vortices in the bridge is small, one may derive the current at which $F_L = F_s$ as $I_{AL} \approx I_0 \sqrt{a/2\xi}$, where $I_0 = c^2 \hbar d / 8e \lambda_L^2$. At this and larger currents, vortex pairs start a periodic viscous motion towards the bridge center with successive annihilation and creation of a new vortex pair at the edges. As I and F_L increase, more than one vortex pair may be present simultaneously within the bridge giving a discontinuity on the V - I characteristic. However, due to the associated increase of F_{vv} , any succeeding current span will differ from the previous one. The equation of motion of the n -th vortex is given by $\dot{x}_n = F_n / \eta$, where η is the viscosity coefficient. Finally, solving this equation one finds the period of moving vortices, which is equal to the period T in the Josephson frequency relation $\hbar \omega = 2\pi \hbar / T = 2e \bar{V}$, where \bar{V} is the averaged measured voltage. Hence, the electrical current I is related to \bar{V} . According to the AL model, discontinuities on the V - I characteristics are periodic in voltage. One

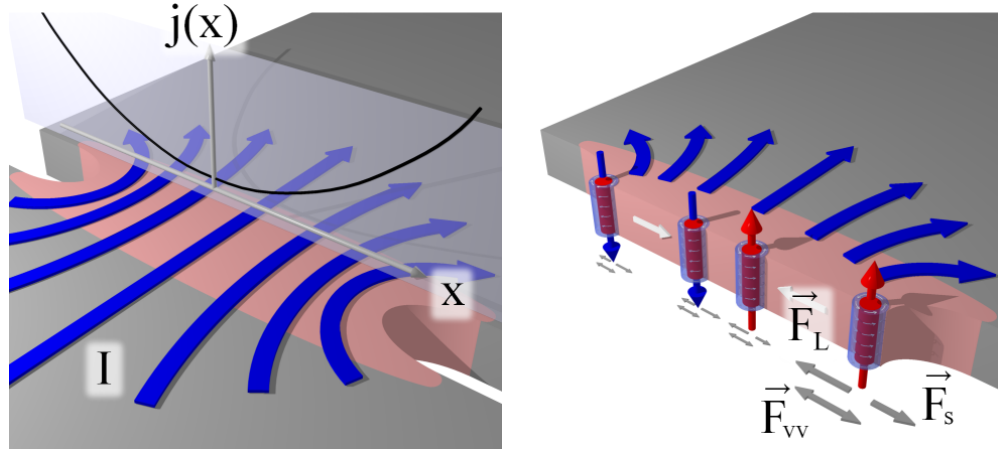


FIGURE 3.38: Effects of penetration of Abrikosov vortices into a microconstriction according to the Aslamazov-Larkin model. The left panel demonstrates the theoretical current density distribution function $j(x)$ within the bridge which has the largest values at the edges of the constriction. The right panel demonstrates a cross-section of the microconstriction with vortices of opposite vorticity penetrating inside. These vortices enter the bridge from opposite edges, move towards the bridge center and get annihilated there. \vec{F}_L , \vec{F}_s , and \vec{F}_{vv} are the Lorentz force, the force associated with the edge interaction energy, and the vortex-vortex interaction force which act on every vortex within the bridge.

may show that this periodicity is given by (SI units)

$$V_0 = \frac{1}{2\sqrt{2}} \frac{4\pi}{\mu_0} \frac{d\hbar^3}{a\sqrt{\xi a}\lambda_{eff}^2} \frac{1}{e^3\eta} \quad (3.1)$$

where λ_{eff} is the effective penetration depth, which is taken here as λ_L since $\lambda_L \approx d$ and the correction is small. The smoothed peaks marked by arrows in Fig. 3.35 are attributed each to a new number of vortex pairs moving simultaneously in the bridge. They appear, as expected, just above I_c^J . Three corresponding peaks are well resolved, which in our case implies that the strong repulsion between neighboring vortices of equal vorticities limits considerably their number. This is very probable because the average inter-vortex distance $a/3$ is comparable with the vortex radius. Also, large values of $\lambda_L \approx 235 \text{ nm}$ (Özcan, Broun *et al.* 2003) for *CeCoIn₅* do increase the inter-vortex repulsive coupling.

As it is clear from Fig. 3.35, the marked peaks are not equidistant with current, which follows from the AL model calculations, but they are, within good accuracy, equidistant with voltage with a period of about $125 \mu V$, which is demonstrated in Fig. 3.43(a). This period corresponds to V_0 , as predicted by the AL model calculations. One can obtain the viscosity coefficient η from (3.1). Using $\lambda_L = 235 \text{ nm}$, $d = 150 \text{ nm}$, and $\xi = 10 \text{ nm}$ (DeBeer-Schmitt *et al.* 2006), one finds $\eta \approx 5.0 \times 10^{-15} \text{ (AVs}^2\text{m}^{-2}\text{)}$. This result agrees well with the viscosity coefficient calculated within the Bardeen-Stephen

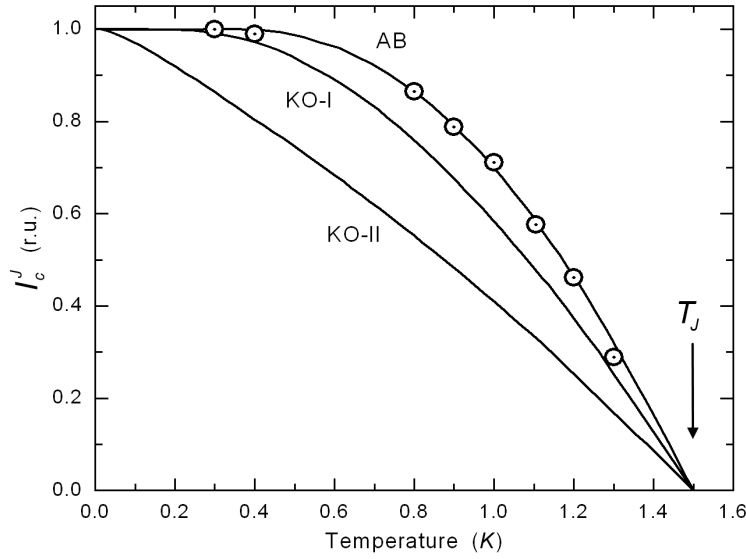


FIGURE 3.39: Normalized Josephson critical current of the two SQUID microbridges measured in parallel as a function of temperature (open circles). The solid lines AB, KO-I, and KO-II are theoretically calculated curves with the Ambegaokar-Baratoff, Kulik-Omelyanchuk-I, and Kulik-Omelyanchuk-II models, respectively. T_J denotes the Josephson coupling temperature.

theory (Bardeen & Stephen 1965) $\eta \approx 2.6 \times 10^{-15}$ (AVs^2m^{-2}), where $\xi = 10$ nm and the normal state resistivity $\rho_n = 4.0 \times 10^{-7}$ Ωm were used.

The temperature dependence of the normalized Josephson critical current I_c^J for the two bridges is shown in Fig. 3.39. The open circles represent measured data and the solid lines are theoretical curves calculated with several models using the measured Josephson coupling temperature T_J and fitted normal state resistance R_n . The AB model (Ambegaokar & Baratoff 1963) describes the experimental data quite well, although $R_n = 68$ Ω has to be used instead of the measured value of 42 Ω . This is not unexpected. Indeed, on the one hand, the AB fit tends to overestimate the value of I_c^J for $L > \xi$, since R_n grows linearly with L but the Ginzburg-Landau order parameter in the middle of the bridge falls off exponentially. On the other hand, the AB model is derived for tunnel junctions, that is for $L \ll \xi$, and with no scattering within the barrier. In contrast, models derived for microconstrictions, such as those by Kulik and Omelyanchuk in the dirty and clean limits (Kulik & Omelyanchuk 1975, Kulik & Omelyanchuk 1977) or Ishii's model (Ishii 1970) for long bridges, do not fit the data. Additionally, the shape of the voltage modulations is not asymmetric, as one would expect within these models. The models by Kulik and Omelyanchuk and by Ishii, however, do not take into account the possible influence of Andreev bound states (Gumann, Dahm *et al.* 2007), which may introduce phase-coherent reflections at two effective interfaces of every bridge and may be a reason for their poor description of the experimental data.

We can conclude that the *CeCoIn₅* thin film microcrystal SQUID based on variable thickness microbridges, contrary to the variable width microbridge geometry, demonstrated a well-characterized SQUID behaviour. The measured SQUID voltage modulations were found to be in excellent agreement with theoretical predictions. The fine structure of the transport characteristics is very likely to be a consequence of the complex dynamics of Abrikosov vortices within the bridges. The vortex dynamics may also explain the occasional non-systematic variations of I_c^J in an external magnetic field. The temperature dependence of I_c^J demonstrated unexpectedly good agreement with the Ambegaokar-Baratoff model.

Josephson effects on a single microconstriction

The previous study of a tunneling structure with two microconstrictions posed the following questions. Are the observed long period voltage modulations a characteristic of individual Josephson microbridges modified by interference effects between them? Is the non-linear dynamic resistance observed above T_c of *CeCoIn₅* an intrinsic behaviour of *CeCoIn₅* or not?

The first question can be answered if one of the microbridges is excluded from the SQUID loop. Such a single microbridge structure was obtained in this study by permanently suppressing the Josephson coupling in one of the microbridges of the SQUID discussed in the previous section via increasing the current density through the SQUID. As a result, due to a small asymmetry between the cross-sections of the two SQUID microbridge arms, the Josephson coupling through the weaker bridge was permanently suppressed. The temperature-dependent resistivity $\rho(T)$ of the microbridge was measured in the range 0.3-300 *K* during cooling down. In the heavy fermion state of *CeCoIn₅* $\rho(T)$ demonstrates its typical behaviour with a residual resistance ratio of $RRR_{300K/2.5K} \approx 1.73$. This value is lower than that obtained for the SQUID structure, which we attribute to the rather intrusive transformation of the SQUID into the single bridge structure that involved high current densities. The low-temperature part of $\rho(T)$ for the microbridge is shown in Fig. 3.40. The superconducting transition of *CeCoIn₅* was found at $T_c \approx 2$ *K*, as in the previous studies (Soroka *et al.* 2007, Zaitsev *et al.* 2009, Hänisch *et al.* 2010). The additional transition at about 1.5 *K* is associated with the Josephson coupling temperature T_J , as in the SQUID structure before.

The resistivity of the single microbridge structure at 2.5 *K* is approximately 0.47 $\mu\Omega m$, which is deduced considering a single branch in the equivalent electrical scheme of the initial SQUID and its geometry (see also right part in Fig. 3.33). This value is by about

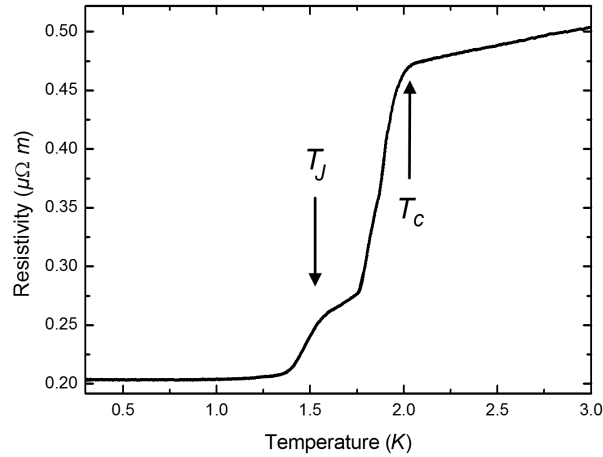


FIGURE 3.40: Low-temperature part of the temperature dependence of resistivity $\rho(T)$ measured on a single microbridge structure during cooling down with a constant current of $0.5 \mu A$. The arrows denote the superconducting transition temperature T_c of $CeCoIn_5$ and the Josephson coupling temperature T_J .

9% larger than that for the SQUID structure, which is consistent with qualitative expectations. Moreover, when this increase of resistivity is assigned solely to the constriction area, the weakest part of the structure, its resistivity must increase by about 300%, if no asymmetry between the initial SQUID bridges is assumed. Another remarkable feature is the relatively large residual resistivity $\rho_0 = 0.2 \mu\Omega m$ of the microbridge below T_J . While a much smaller value of ρ_0 of the SQUID was previously associated with the Ambegaokar and Halperin mechanism (Ambegaokar & Halperin 1969), here this mechanism cannot be justified. In this case, the large value of ρ_0 can be related to an increased weight of dissipative transport channels within the microbridge. It should be stressed that, in spite of the reduced RRR and suggested substantial increase of the resistivity within the microbridge, no noticeable change of T_J with regard to our previous analysis is observed. We may speculate that the T_J value is strongly influenced by the anomalously large electronic mean free path in $CeCoIn_5$ at low temperatures (Kasahara *et al.* 2005, Movshovich, Jaime *et al.* 2001, Ikeda, Shishido *et al.* 2001), which still could be large when compared to the microbridge length.

The Josephson effects in a single weak link are usually recognized by Shapiro steps in the V - I characteristics under microwave radiation, by the modulation of the Josephson critical current I_c^J , or, similarly, by voltage modulations ΔV in a variable external magnetic field B applied perpendicularly to the junction/microbridge plane. The periodicity of these $\Delta V(B)$ modulations is given by $\Delta B = \Phi_0/s$, where Φ_0 is the flux quantum and s is the effective area of the weak link exposed to the field. For microbridges demonstrating a Josephson effect the effective area is given as $s = [W(2\lambda + L)]$, where W and L are the microbridge width and length, and λ is the Josephson penetration depth (Rosenthal, Beasley *et al.* 1991). The effective area s is small for microbridges when compared to

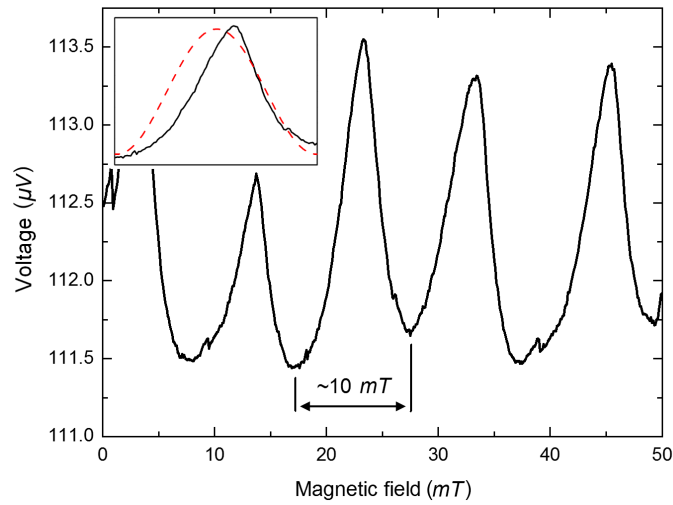


FIGURE 3.41: Typical weak link voltage modulations by an external magnetic field measured at $T = 0.3 K$ with constant current $I = 8 \mu A > I_c^J$. The inset shows a comparison between the shapes of the measured modulations (solid line) and of the theoretically expected sinusoidal modulations for an ideal Josephson tunnel junction (dashed line).

the SQUID and, hence, ΔV has a larger period ΔB . In the main part of Fig. 3.41 we present the measured $\Delta V(B)$ modulations for the single $CeCoIn_5$ microbridge, which we ascribe to Josephson voltage modulations.

The harmonicity of the $\Delta V(B)$ modulations is much improved for the single microbridge supporting our assumption of interference effects in the SQUID structure. The period of the modulations is $10 mT$, which is in good agreement with the estimated microbridge effective area if $\lambda = 235 nm$ is used (Özcan *et al.* 2003). In contrast to the previous study, no small period superimposed SQUID voltage modulations were detected, which also confirms the single microbridge geometry. Another feature is the pronounced asymmetry of the $\Delta V(B)$ modulations shown in the inset of Fig. 3.41, which could not be observed before for the SQUID. Such deviations from the ideal Josephson effect in microbridges were reported before for various types of weak links (Golubov *et al.* 2004, Likharev 1979). In these works, it was also shown that the ratio between the electron mean free path l , the Ginzburg-Landau superconducting coherence length ξ , and the microbridge dimensions L, W defines different transport regimes and that in some of these regimes the voltage modulations can be asymmetric. According to the predictions, when those regimes are established within a microbridge, another essential characteristic, the temperature dependence of the Josephson critical current $I_c^J(T)$, must also deviate from its ideal behaviour in tunneling junctions. However, one should mention that the specific properties of $CeCoIn_5$, such as very large l and small ξ (DeBeer-Schmitt *et al.* 2006), combined with the microbridge dimensions L, W do not

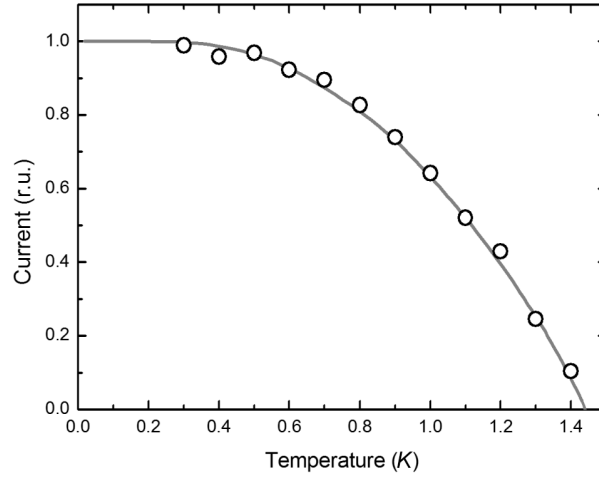


FIGURE 3.42: Josephson critical current measured as a function of temperature (circles) and an Ambegaokar-Baratoff fit (solid line) with $R_n^{fit} = 71 \Omega$ and $T_c = 1.45 K$.

allow for a strict classification of our microbridge in terms of the regimes mentioned above.

The measured temperature dependence of the Josephson critical current $I_c^J(T)$ is shown in Fig. 3.42 by open circles. The solid line is an Ambegaokar-Baratoff fit to the measured data. The function $I_c^J(T)$ measured on the $CeCoIn_5$ SQUID also followed the AB model (Fig. 3.39). In both cases, the expected behaviour of $I_c^J(T)$ derived for microbridges (Kulik & Omelyanchuk 1975, Kulik & Omelyanchuk 1977, Ishii 1970) is not observed. In contrast, the AB model is derived in the tunneling limit with small barrier transparency and without coordinate dependencies of the SC parameters within the barrier. This suggests that the requirement $l \gg L$ is fulfilled in this case. In the AB fit of $I_c^J(T)$ for the SQUID the values of the local T_c and T_J were not discriminated. For the single microbridge we find a local $T_c = 1.45 K$ according to the best AB fit, which is lower than $T_J = 1.55 K$ derived from the $\rho(T)$ curve. On the one hand, a reduced value of the local T_c with respect to the SQUID results should not be surprising due to the properties of the microbridge being modified during the preparation. On the other hand, the emerging difference between the values of T_J and the local T_c for the single microbridge suggests different processes associated with each of the two temperatures. The value of the normal state resistance R_n^{fit} in the AB fit is found to be almost identical in the SQUID and in the single microbridge.

Previously, we suggested that the periodic vortex motion regime might be realized for the SQUID's microbridges. The $dI/dV(V)$ curves measured in the current-driven mode for both the SQUID and the single microbridge are shown in Fig. 3.43(a). The same data are also shown as $dV/dI(IR_n)$ in Fig. 3.43(b). It should be noted that $I_c^J R_n$ is invariant for Josephson junctions and reflects only essential material properties (see p. 200 in

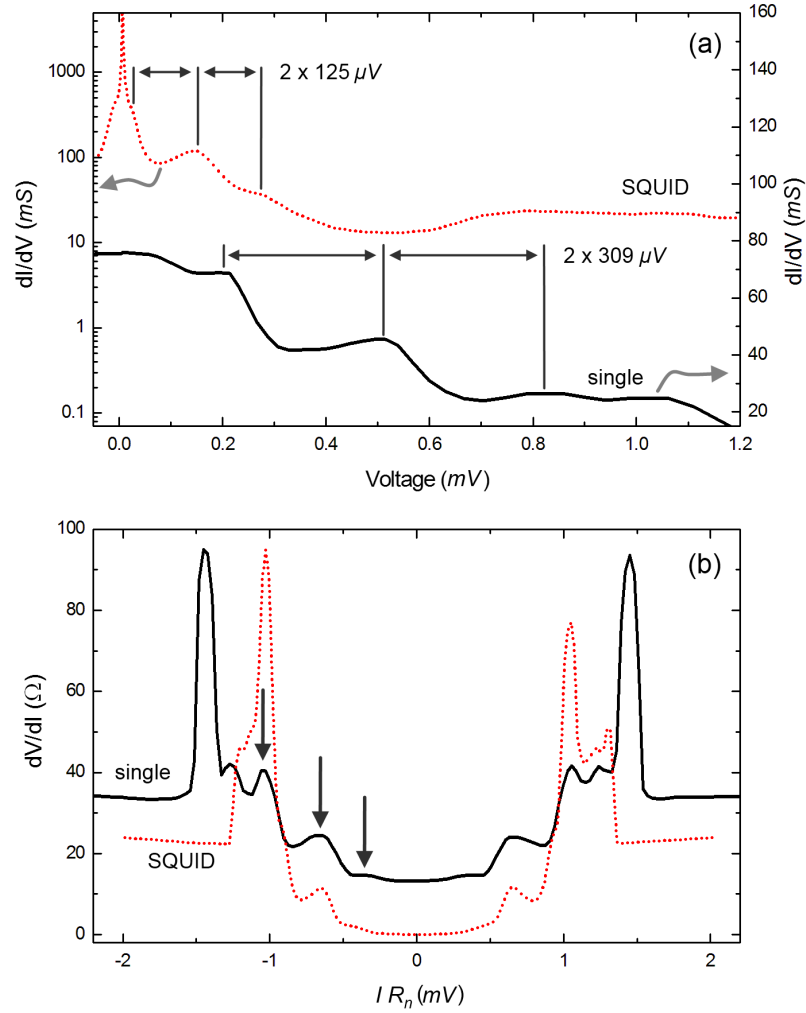


FIGURE 3.43: Typical dynamic resistance/conductance characteristics of the single $CeCoIn_5$ microbridge (solid lines) and the SQUID (dotted lines) measured at $T = 0.3 K$ with no external magnetic field. The data are shown in (a) $dI/dV(V)$ representation and (b) $dV/dI(IR_n)$ representation, where R_n is the normal state resistance.

(Tinkham 2004)), hence it is convenient to compare different microbridges in coordinates $dV/dI(IR_n)$. In Fig. 3.43(a) the curve measured for the SQUID demonstrates a sharp Josephson conductance peak around zero voltage bias. When $I > I_c^J$, a voltage drop along the SQUID's microbridges develops and the first shallow knee appears just above I_c^J , which is linked to the entrance of the first Abrikosov vortex pair into the bridge. Three similar features are observed on both the $dI/dV(V)$ and $dV/dI(IR_n)$ curves for the SQUID microbridges, which are associated with three pairs of vortices moving simultaneously within each of the microbridges. As it was mentioned, according to the AL model these features in the dynamic resistance should be periodic with voltage, but not with current or IR_n , reflecting the non-linear vortex-vortex interaction. The presented curves for the SQUID follow these AL model predictions, which supports the vortex origin of the conductance features.

The conductance and resistance curves for the single microbridge demonstrate the same qualitative behaviour as for the SQUID, which suggests an unchanged mechanism of periodic vortex motion within the single microbridge. In contrast to the SQUID data, the single microbridge curve $dI/dV(V)$ in Fig. 3.43(a) demonstrates an only weakly enhanced conductance around zero voltage, which is in both cases the effect of the Josephson current. Currents $I < I_c^J$, however, are accompanied by a voltage drop, which suggests the presence of dissipative transport channels within the bridge. Up to three periodic features are still recognized for the single bridge on the respective plot in Fig. 3.43(a) at 0.2 mV , 0.51 mV , and 0.82 mV corresponding each to the entrance of a new vortex pair into the bridge. These features are also marked by arrows in Fig. 3.43(b). Their slightly non-periodic occurrence in the $dV/dI(IR_n)$ plot and periodic occurrence in the corresponding $dI/dV(V)$ plot are evident, which is consistent with the AL model. The first two features at small IR_n values for the single bridge coincide with those measured for the SQUID. This suggests a similar vortex dynamics in the single bridge and in the SQUID at moderate vortex densities. The third feature is shifted towards larger values of IR_n for the single microbridge when compared with the SQUID. This may be explained by an increased local magnetic penetration depth λ enhancing the vortex-vortex repulsion at larger vortex densities. The increase of λ may not be surprising since it is inversely proportional to the density of SC electrons, which may well be reduced due to the mentioned additional dissipation transport channels. At even larger values of IR_n the SC current density within the bridge reaches its critical value for $CeCoIn_5$ (Watanabe *et al.* 2004), above which the dynamic resistance characteristics become essentially flat, which is expected for microbridges.

Summary and outlook

In this work, we studied the growth of $CeIn_3$ and $CeCoIn_5$ thin films as well as the electronic transport properties of these films and of their microcrystals. The films were grown by the molecular beam epitaxy method, using Knudsen effusions cells and electron beam assisted evaporation to produce fluxes of the constituent elements. The transport properties were investigated on several types of structures performing several types of measurements:

- Temperature-dependent resistivity measurements on
 - Thin films, $CeIn_3$ thin film microcrystals, $CeCoIn_5$ patterned and not patterned thin film microcrystals
- Dynamic conductance/resistance measurements on
 - $CeCoIn_5$ patterned thin film microcrystals

In the $CeIn_3$ and $CeCoIn_5$ growth studies, we observed strongly discontinuous surface morphologies of the thin films for these compounds, in accordance with earlier reports. We also found poor reproducibility of the thin film surface morphology from growth to growth, which was explained by the high sensitivity of the growth dynamics at the early stages of growth and the de-wetting properties of In . This conclusion was confirmed in the simultaneous growth study where we observed a logical variation of the $CeIn_3$ film surface morphology within one growth process and less systematic variations between several growth processes.

In the $CeCoIn_5$ growth studies, we observed an improved quality of thin films as compared to literature reports and our own previous results. This improvement was ascribed to a modified thin film growth procedure, in particular, to a change of the Co flux production method from the Knudsen evaporation to the electron beam assisted evaporation. The improved quality of the films was systematically observed using x-ray characterization techniques, such as the grazing incidence diffraction method and the analysis of

the polar orientation of the $CeCoIn_5$ thin film crystallites. Using x-ray techniques and AFM, we found indications of a large concentration of, possibly, threading dislocations in the $CeCoIn_5$ thin films, which is consistent with the electronic transport studies on these films. Based on our structural analysis, we proposed a qualitative description of the $CeCoIn_5$ thin film growth mechanism at the initial stages of growth.

In simple electronic transport measurements conducted on thin films of $CeIn_3$, we systematically observed the presence of an In impurity phase. In contrast, no In impurity phase was found during transport measurements on either $CeIn_3$ or $CeCoIn_5$ thin film microcrystals, which qualitatively supports our proposal for the $CeIn_3$ and $CeCoIn_5$ thin film growth mechanism.

The electronic properties of $CeCoIn_5$ microcrystals were investigated using the planar tunneling and the DC Josephson effect in SC microbridges. For this purpose, $CeCoIn_5$ microcrystals were patterned using focused ion beam milling, focused ion beam induced deposition, and focused electron beam induced deposition techniques. Tunneling spectra of the planar tunneling diodes featured pronounced non-linearities at temperatures below the SC transition temperature of $CeCoIn_5$. However, due to our limited control over the tunneling barrier quality, this behaviour was poorly reproducible which prevented us from singling out spectroscopic information about the $CeCoIn_5$ SC state from the tunneling spectra.

Electronic transport measurements on $CeCoIn_5$ SC microbridges provided valuable information. First, we observed the expected response from a $CeCoIn_5$ microcrystal-based SQUID. We also identified signatures of the complex dynamics of SC vortices in the superconducting bridges in both, SQUID and single microbridge, geometries. Second, we found that the temperature dependence of the Josephson critical current of the $CeCoIn_5$ microbridges of both geometries was very similar to that of a Josephson tunnel junction, which was not expected. We ascribed this peculiar behaviour of the Josephson critical current in our microbridges to a unique combination of the electronic properties of $CeCoIn_5$, such as a small SC coherence length and a large quasiparticle mean free path, which limits the applicability of standard models developed for SC microbridges. Generally, no non-linearities are expected in the dynamic conductance characteristics of a $CeCoIn_5$ microbridge in the normal metallic state. Nevertheless, we observed a non-linear dynamic response from our bridges up to 10 K, which is far in the $CeCoIn_5$ metallic heavy-fermion state. This heavy-fermion metallic state response is also strongly modified in the presence of a magnetic field, field-induced features surviving down to 300 mK. So far, we have not been able to provide a unified view on the observed normal state peculiarities and therefore further research is desired.

As an outlook, we would like to utilize our microbridge-based approach for further investigations of not only the SC state but also of the low-temperature heavy-fermion metallic state in $CeCoIn_5$. We envisage two possible research directions, focused mainly on the low-temperature heavy-fermion metallic state of $CeCoIn_5$ but also giving access to the SC properties. First, we believe that one could distinguish the intrinsic low-temperature $CeCoIn_5$ heavy-fermion metallic properties from those characteristic for microbridges by investigating transport properties of a set of microbridges with variable width. Second, as we shortly discussed in Chapter 1, due to the anomalously large quasiparticle mean free path in $CeCoIn_5$, the observation of quasiparticle interference effects, such as the Aharonov-Bohm or Aronov-Altshuler-Spivak effects, on microcrystal-based interferometers seems to be possible. These interference effects give direct access to important electronic relaxation times which are at the heart of the poorly understood low-temperature heavy-fermion state.

Appendices

A Tunneling measurement calculations

An example of calculations required for dynamic resistance lock-in measurements.

Structure: A^{5kV}

Barrier resistance:

$$R^b = 60 \Omega$$

Desired range of DC voltage drop on the structure:

$$\Delta V_{DC} = (0; 4) \text{ mV}$$

Programmed DC range:

$$V_{DC} = (0; 10) \text{ V}$$

$$V_{DC}^{max} = 10 \text{ V}$$

Then, appropriate DC current range:

$$\Delta I_{DC} = (0; 67) \mu\text{A} \leftarrow (\Delta V_{DC}^{max} / R^b, \text{ or } 4 \text{ mV} / 60 \Omega)$$

Then, serial resistor for DC branch:

Programmed AC voltage:

$$V_{AC}^{rms} = 0.1 \text{ V}$$

$$\underline{R_{DC} = 150 \text{ k}\Omega} \leftarrow (V_{DC}^{max} / \Delta I_{DC}^{max}, \text{ or } 10 \text{ V} / 67 \mu\text{A})$$

Desired AC voltage drop amplitude on the structure:

$$\Delta V_{AC}^{sample} \approx 1/10 \times \Delta^{BCS} = 45 \mu\text{V}$$

Then, AC current amplitude through the structure:

$$\Delta I_{AC}^{sample} = 0.75 \mu\text{A} \leftarrow (\Delta V_{AC}^{sample} / R^b, \text{ or } 45 \mu\text{V} / 60 \Omega)$$

Then, serial resistor for AC branch:

$$\underline{R_{AC} = 130 \text{ k}\Omega} \leftarrow (V_{AC}^{rms} / \Delta I_{AC}^{sample}, \text{ or } 0.1 \text{ V} / 0.75 \mu\text{A})$$

The structure A^{5kV} has a tunneling barrier resistance of $R^b = 60 \Omega$ measured at saturation. The density of single electron levels will be measured within the energy/voltage range ΔV_{DC} around the Fermi energy. The corresponding DC current range ΔI_{DC} required for producing a voltage drop of the order of ΔV_{DC} is calculated next. The programmed DC voltage range V_{DC} of the voltage source is fixed at 0-10 V where the maximum voltage is V_{DC}^{max} . The current limiting serial resistor for obtaining ΔI_{DC} at V_{DC}^{max} is R_{DC} .

In the case of tunneling from/to a superconductor, the desired AC voltage drop amplitude across the tunneling diode ΔV_{AC}^{sample} should be selected such as to produce a small excitation when compared to the expected superconducting energy gap Δ_{BCS} and is 10% of Δ_{BCS} in our example. The AC voltage amplitude ΔV_{AC}^{rms} of the AC voltage source is fixed at 0.1 V. The desired value of ΔV_{AC}^{sample} requires an AC current through the sample ΔI_{AC}^{sample} and, using the tunneling resistance R^b and Ohm's law, we obtain the value of the AC current limiting resistor R_{AC} .

Eventually, the sample is driven by a DC and an AC current sources formed by the corresponding voltage sources and the current limiting resistors such that $R_{DC} \sim R_{AC} \gg R^b$. Thus, programming the AC and the DC voltages on the appropriate sources we obtain voltage controllable current sources.

B Vapour pressure charts for ${}^4\text{He}$ and ${}^3\text{He}$

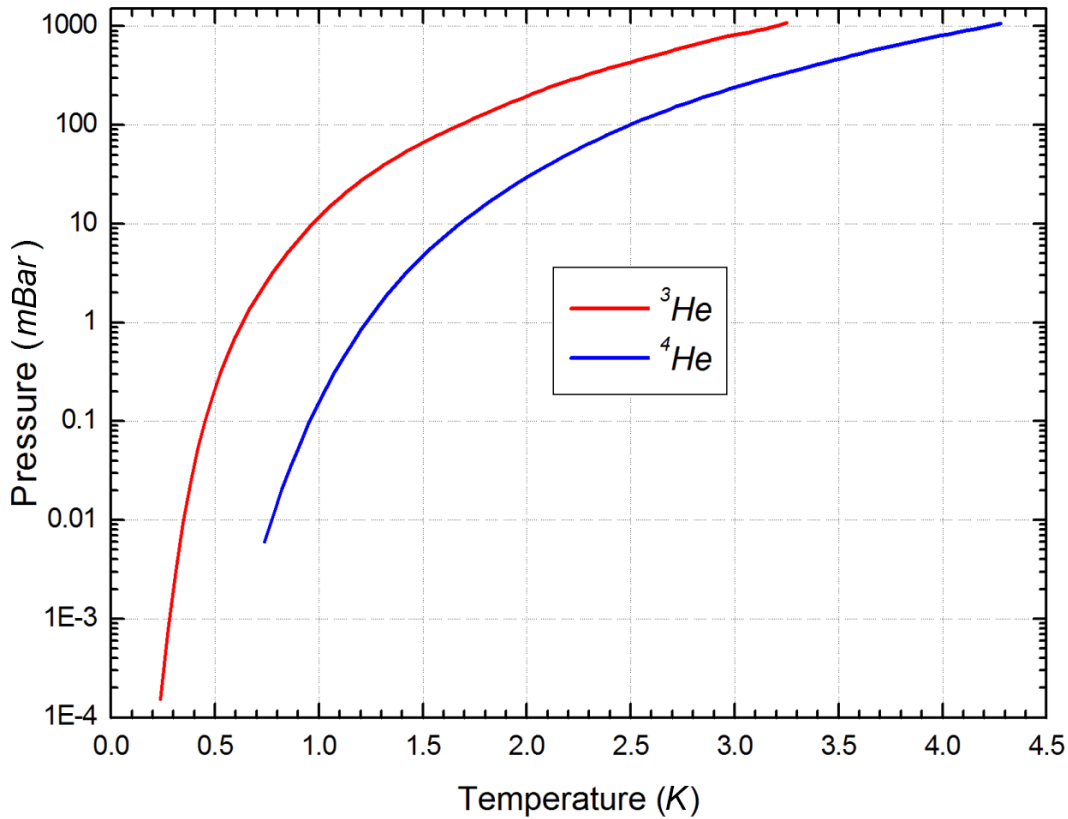


FIGURE B.1: Vapour pressure charts for ${}^4\text{He}$ and ${}^3\text{He}$

C Random walk

According to Einstein's theory of diffusion, the probability of finding a classical particle in time t from the beginning of its random motion and at distance r from its starting point is

$$p(r, t) = \frac{1}{\sqrt{4\pi Dt}} e^{-\frac{r^2}{4Dt}} \quad (\text{C.1})$$

where D is the diffusion constant. If we detect an electron in C (see Fig. 1.24) and let it diffuse, then after times t_1 and $3t_1$ the probabilities to find the electron at distance r are as shown in Fig. C.1 by solid black and red curves, respectively. The chances to

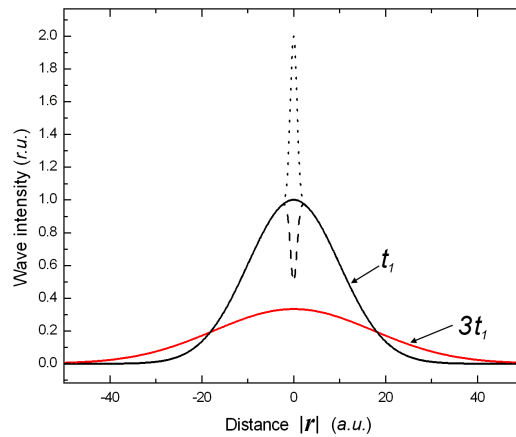


FIGURE C.1: Comparison between the diffusion of a classical and a quantum-mechanical particles.

return to C (placing $r = 0$ in (2)) are then given by

$$p(0, t) = \frac{1}{\sqrt{4\pi Dt}} \quad (\text{C.2})$$

If, however, the second term in (1.68) is also considered, then this probability is doubled, which is shown by the dotted line in Fig. C.1. The dashed line corresponds to the weak antilocalization effect discussed in Sec. 1.6.2.

D Crystallographic data

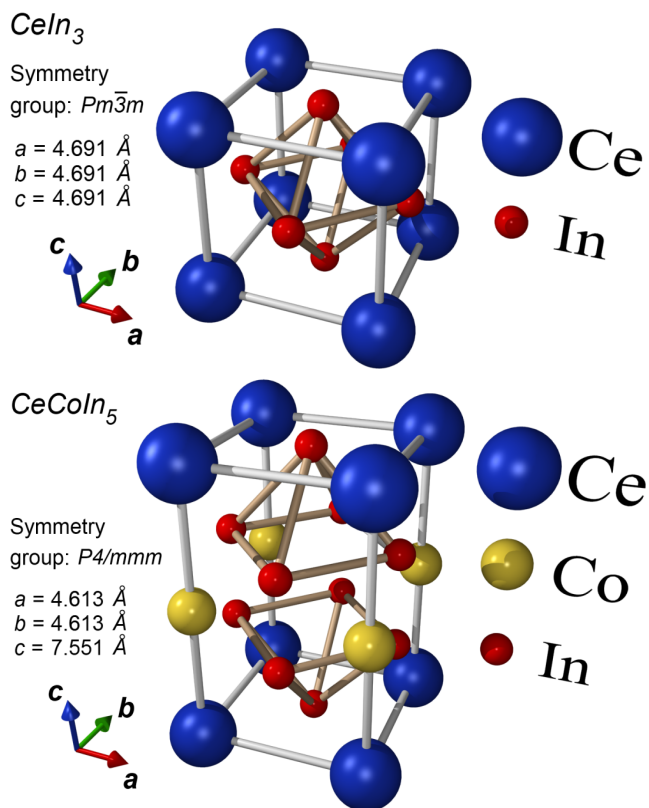


FIGURE D.1: $CeIn_3$ and $CeCoIn_5$ crystal structures.

The tables below contain the theoretically calculated coordinates of the Bragg reflection maxima in x-ray powder diffraction of $CeCoIn_5$, $CeIn_3$, and Al_2O_3 using the $Cu-K^{\alpha_1}$ characteristic line. Here, m stands for multiplicity, d for inter-planar spacing, and $|F|^2$ for the squared structure factor. The intensity of Bragg reflections has been normalized to 5.

<i>CeCoIn₅</i>						<i>CeIn₃</i>					
2θ (degree)	(hkl)	d (Å)	Relative intensity	$ F(hkl) ^2$	m	2θ (degree)	(hkl)	d (Å)	Relative intensity	$ F(hkl) ^2$	m
11.710	001	7.551	0.00851	12200	2	18.903	001	4.691	0.70035	2.69E8	6
19.225	010	4.613	0.34824	3.87E7	4	26.857	011	3.317	0.59800	2.12E8	12
22.568	011	3.937	2.38080	8.8E8	8	33.049	111	2.708	5.00000	8.12E10	8
23.544	002	3.776	0.13380	5.31E7	2	38.347	002	2.345	2.49030	6.87E10	6
27.318	110	3.262	0.15000	3.12E7	4	43.085	012	2.098	0.32910	1.26E8	24
29.812	111	2.994	4.87220	1.19E10	8	47.436	112	1.915	0.24668	1.09E8	24
30.572	012	2.922	0.22507	2.84E7	8	55.351	022	1.658	1.66460	4.02E10	12
35.640	003	2.517	1.74590	5.31E10	2	59.028	003	1.564	0.06225	7.52E7	12
36.368	112	2.468	5.00000	2.98E10	8	62.569	013	1.483	0.10343	6.72E7	24
39.019	020	2.307	3.75610	9.16E10	4	65.999	113	1.414	1.92250	2.93E10	24
40.806	013	2.210	0.49401	4.84E8	8	69.340	222	1.354	0.55140	2.67E10	8
40.876	021	2.206	0.00213	9040	8	72.609	023	1.301	0.06514	4.96E7	24
43.848	120	2.063	0.08336	1.9E7	8	75.821	123	1.254	0.11483	4.53E7	48
45.480	113	1.993	0.35509	4.07E8	8	82.120	004	1.173	0.25946	1.91E10	6
45.544	121	1.990	0.71295	4.12E8	16						
46.077	022	1.968	0.08572	2.51E7	8						
48.164	004	1.888	0.03962	1.05E8	2						
50.363	122	1.810	0.11035	1.56E7	16						
52.321	014	1.747	0.04912	1.47E7	8						
53.869	023	1.701	2.07900	3.01E10	8						
56.257	114	1.634	1.14490	1.11E10	8						
56.366	220	1.631	1.24180	5.28E10	4						
57.733	123	1.596	0.33903	2.74E8	16						
60.125	030	1.538	0.01599	1.17E7	4						
61.491	031	1.507	0.13834	2.42E8	8						
61.925	222	1.497	0.03396	1.5E7	8						
63.644	024	1.461	0.06611	6.43E7	8						
63.746	130	1.459	0.02669	1.06E7	8						
64.917	015	1.435	0.11619	2.17E8	8						
65.068	131	1.432	1.00740	4.11E9	16						
65.489	032	1.424	0.02457	1.01E7	8						
67.159	124	1.393	0.04552	9.6E6	16						
68.398	115	1.370	0.52948	5.61E9	8						
68.496	223	1.369	0.98917	1.97E10	8						
68.955	132	1.361	1.44490	1.08E10	16						
71.892	033	1.312	0.08431	1.74E8	8						
74.035	230	1.279	0.01710	8E6	8						
75.129	025	1.264	0.00132	50100	8						
75.224	133	1.262	0.14600	1.55E8	16						
75.271	231	1.261	0.14695	1.57E8	16						
75.477	006	1.259	0.25174	2.98E10	2						
77.239	224	1.234	0.03699	4.36E7	8						
78.412	125	1.219	0.13077	1.43E8	16						
78.756	016	1.214	0.01448	7.11E6	8						
78.942	232	1.212	0.02878	7.08E6	16						
80.496	034	1.192	0.01370	6.82E6	8						
81.997	116	1.174	0.01220	5.71E6	8						
83.722	134	1.154	0.71175	5.14E9	16						
83.814	040	1.153	0.38782	2.45E10	4						
84.966	233	1.141	0.10638	1.19E8	16						

<i>Al₂O₃</i>					
2θ (degree)	(hkl)	d (Å)	Relative intensity	$ F(hkl) ^2$	m
20.488	003	4.331	2.13030	2.11E7	2
25.568	012	3.481	3.07160	6.91E6	8
37.762	110	2.380	0.74518	8.73E6	4
41.020	015	2.199	0.00972	536	8
41.670	006	2.166	0.36784	1.32E7	2
43.339	113	2.086	5.00000	1.81E8	8
44.462	021	2.036	0.02051	3430	8
52.534	024	1.741	2.48180	1.07E8	8
57.483	116	1.602	3.10510	2.52E8	8
61.106	122	1.515	0.13782	163000	16
61.290	018	1.511	0.38561	5.18E6	8
64.487	009	1.444	0.03750	980000	2
67.891	027	1.379	0.00363	717	8
68.181	030	1.374	1.91290	8.08E8	4
70.391	125	1.336	0.12707	254000	16
72.036	033	1.310	0.08018	443000	8
77.216	119	1.234	0.48586	2.1E7	8
80.664	220	1.190	0.11628	5.53E6	4
83.185	036	1.160	0.00694	5370	8
84.320	223	1.148	0.29648	1.02E7	8

E Equipment settings

The following tables contain important settings of the equipment used in this work. In the second column of every table, programmed settings are commented as “(set)”, settings which can be only monitored are marked as “(read)”, settings which cannot be altered are highlighted as “(default)”, and parameters calculated using the equipment settings are marked as “(obtained)”.

FEBID and FIBID parameters

Deposition of *SiO-C* by means of FEBID using the FEI Nova NanoLab 600 scanning electron microscope a home-made capillary system

Parameter	Value
Chamber pressure during growth using either tetramethylsilane ($Si(CH_3)_4$) or neopentasilane (Si_5H_{12}) precursor gases	$1.2-1.4 \times 10^{-5}$ mbar (read)
Electron accelerating voltage	5 kV (set)
Beam current (thin layers)	1.6 nA (set)
Beam current (thick layers)	6.3 nA (set)
Dwell time	10 μ s (set)
Pitch	20 nm (set)
Deposition time (a disc of 2.5 μ m diameter and \approx 6 nm thick)	\approx 4 min (read) for either precursor gas
Deposition time (a \approx 40 nm thick donut-shaped structure of 4 μ m outer and 2 μ m inner diameters)	\approx 12 min (read) for either precursor gas
Ratio between the programmed and the actual structure thicknesses (either beam current)	
Si_5H_{12}	\approx 100 (obtained)
$Si(CH_3)_4$	\approx 16 (obtained)

Deposition of *W-C* metallic structures by means of FIBID using the FEI Nova NanoLab 600 scanning electron microscope with a commercial gas injection system and $W(CO)_6$ precursor gas

Beam ions type	<i>Ga</i> (default)
Ion accelerating voltage	10 kV; 30 kV (set)
Ion beam current	0.12 nA; 10 pA (set)
Deposited thickness	150-250 nm; 400 nm (set)

***CeIn₃* and *CeCoIn₅* growth**

Metal MBE chamber and related equipment	
Parameter	Value
<i>Ce</i> high-temperature Knudsen effusion cell	$T = 1610\text{-}1650\text{ }^\circ\text{C}$ (set)
Power supply	25 V, 14 A (read)
<i>Co</i> high-temperature Knudsen effusion cell	$T = 1560\text{-}1600\text{ }^\circ\text{C}$ (set)
<i>In</i> Knudsen effusion cell	$T = 810\text{-}850\text{ }^\circ\text{C}$ (set)
Power supply	10 V, 4 A (read)
Nominal substrate temperature T_s^a	$T = 500\text{-}600\text{ }^\circ\text{C}$ (set)
Growth duration	10-100 min typically 60 min (set)
Chamber base pressure	$< 5 \times 10^{-9}$ mbar (read)
Chamber pressure during growth	7×10^{-9} – 3×10^{-8} mbar (read)
Electron beam assisted evaporation of <i>Co</i> using the FerroTec EV1-8 electron beam evaporator and the flux rate monitor Inficon XTC/2 deposition controller	
Flux rate	0.2 Å/s (set)
Flux rate sensing element	Gold coated quartz crystal (default)
Quartz crystal oscillating frequency	6 MHz (default)
Electron beam accelerating voltage	6.8 kV (set)
Electron beam current	21 mA (read)
Maintained flux rate	0.1-0.7 Å/s typically 0.2 Å/s (set)
Rate calibration factor $\text{Flux}_{\text{quartz}}/\text{Flux}_{\text{substrate}}$ using the <i>CeCoIn₅</i> film thickness of 300 nm, the growth time 60 min, and the added thickness on the quartz monitor of 73 nm	≈ 6.4 (obtained)
Reflection high-energy electron diffraction (RHEED)	
Electron accelerating voltage	15 kV (set)
Filament current	< 1.5 A (set)

Al RF-sputtering

Parameter	Value
Chamber pressure during growth	0.06 <i>mbar</i> (read)
Ar gas pressure reducing valve	1 <i>bar</i> (set)
Turbomolecular pump spinning rate	50 % of its maximum (set)
Sputtering duration	100 <i>min</i> (set)
Obtained film thickness	22 <i>nm</i> (measured with AFM)
RF-generator Hüttinger PFG 600 RF	
Power	50-100 <i>W</i> typically 50 <i>W</i> (set)
Reflected power	0 <i>W</i> (read)
DC bias	260 <i>VDC</i> (set) 211-240 <i>V</i> (read)
Load capacitor (CL parameter)	60 (set) 61-64 (read)
Tune capacitor (CT parameter)	750 (set) 750-803 (read)
Alicat scientific 16 series Mass and Volumetric precision gas flow controller	
Gas type	Ar with purity 99.999% (5N gas cylinder) (set)
Gas temperature	26.16 °C (read)
Gas Pressure	1.64 <i>psi</i> (read)
Mass flow rate	12.5 <i>sccm</i> (set)
Volume flow rate	113 <i>ccm</i> (read)

Here, *sccm* stands for standard cubic centimeters per minute and *ccm* for cubic centimeters per minute. *ccm* corresponds to the measured value of volumetric flow rate under given conditions. *sccm* corresponds to the corrected value of the volumetric flow rate so that the true mass flow m is obtained using the relation $m = V \times \rho$, where ρ is the gas density under normal conditions (i.e., temperature 25 °C and pressure 1 *bar*) and V is the mass flow meter reading.

Al DC plasma oxidation

Parameter	Value
Anode-Cathode DC voltage	470 <i>VDC</i> (set)
Anode-Cathode DC current	≈ 10 <i>mA</i> (set)
Process duration	≈ 3 <i>min</i> (set)
Alicat scientific 16 series Mass and Volumetric precision gas flow controller	
Gas type	<i>O</i> (set)
Gas temperature	24.8 $^{\circ}\text{C}$ (read)
Gas Pressure	4.15 <i>psi</i> (read)
Mass flow rate	15.0 <i>sccm</i> (set)
Volume flow rate	53 <i>ccm</i> (read)

FIB milling

FIB milling settings required for milling a 300 *nm* thick *CeCoIn₅* or *CeIn₃* thin film down to the substrate using the FEI Nova NanoLab 600 scanning electron microscope

Parameter	Value
Beam ions type	<i>Ga</i> (default)
Milling thickness	100 <i>nm</i> (set using parameters for <i>Si</i>) resulted in > 300 <i>nm</i> of <i>CeCoIn₅</i>
Ion accelerating voltage	30 <i>kV</i> (set)
Ion beam current	50 <i>pA</i> (set)
The rest of the settings were selected the same as the device's pre-programmed settings for milling <i>Si</i>	

Cr growth

Cr growth using the electron beam evaporator “Preiffer Classic 500”

Parameter	Value
Electron beam accelerating voltage	10 kV (set)
Electron beam current	≈ 6 mA (read)
Chamber pressure during growth	$< 1.3 \times 10^{-5}$ mbar (read)
Deposition time	typically 15 min (read)
Nominal programmed thickness	20 nm (set)
Growth rate sensing element	Gold coated quartz crystal (default)

F $CeCoIn_5$ normal state properties

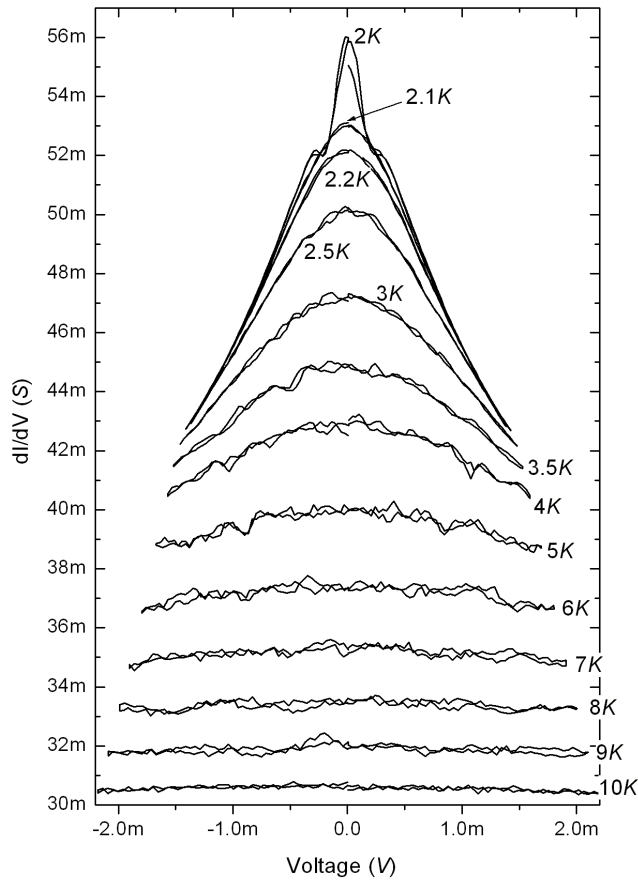


FIGURE F.1: Dynamic conductance curves measured at several temperatures on the $CeCoIn_5$ thin film microcrystal-based interferometer described in Sec. 3.4.4. The curves have not been shifted. The sharp peak at 2 K superimposed on top of the broad maximum around zero bias corresponds to an increase of conductance due to the SC transition in $CeCoIn_5$.

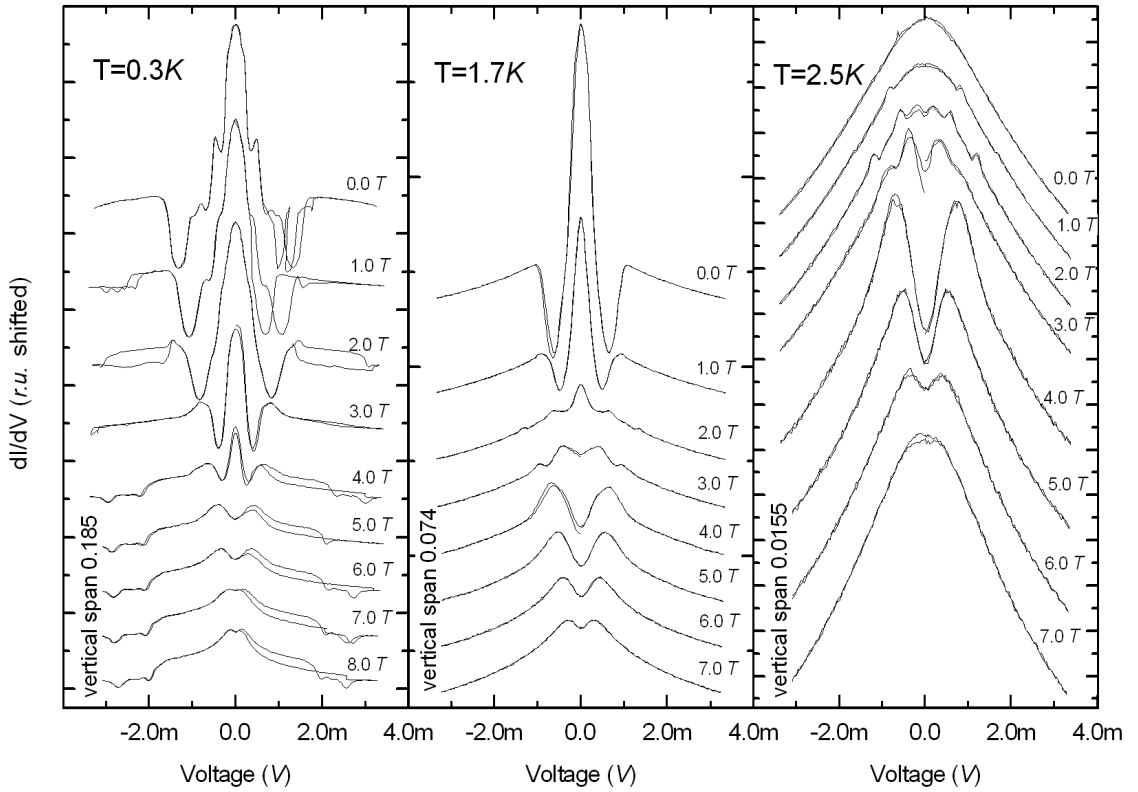


FIGURE F.2: Selected dynamic conductance curves measured at several temperatures with varying external magnetic field on the $CeCoIn_5$ thin film microcrystal-based interferometer described in Sec. 3.4.4. The curves were shifted vertically for clarity. The characteristics measured in the $CeCoIn_5$ normal state at 2.5 K feature a broad maximum around zero bias which demonstrates splitting in the magnetic field range of approximately 2-6.5 T. Additional satellite peaks at 2.5 K appear at about 0.25 T and shift towards zero bias in larger fields eventually evolving into the line shape of the split broad maximum at about 4 T. Both, the splitting of the broad maximum and the satellite peaks, are also observed in the $CeCoIn_5$ SC regime. The curves measured in the $CeCoIn_5$ SC regime demonstrate a central peak at zero field assigned to the Josephson current. This peak disappears in larger magnetic fields as the SC state in $CeCoIn_5$ gets suppressed. The characteristics measured on a single microbridge structure described in Sec. 3.4.4 are qualitatively not changed.

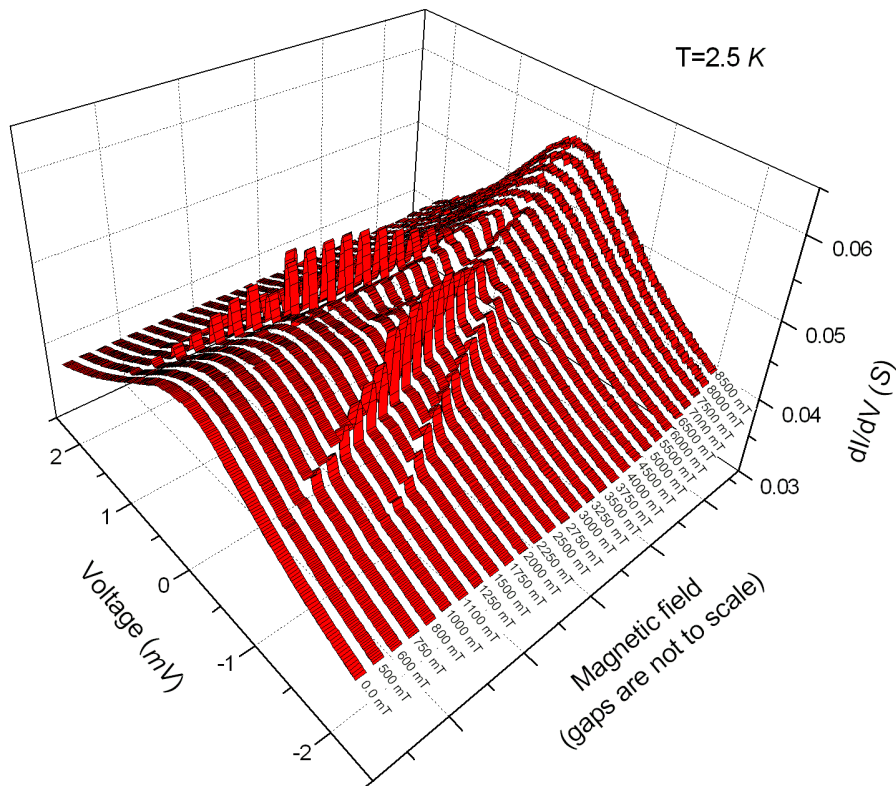


FIGURE F.3: Perspective representation of the dynamic conductance curves measured at 2.5 K with varying external magnetic field on the $CeCoIn_5$ thin film microcrystal-based interferometer described in Sec. 3.4.4. Sharp satellite peaks appear at about 250 mT and shift linearly with increasing field towards zero bias disappearing at about 4.0 T.

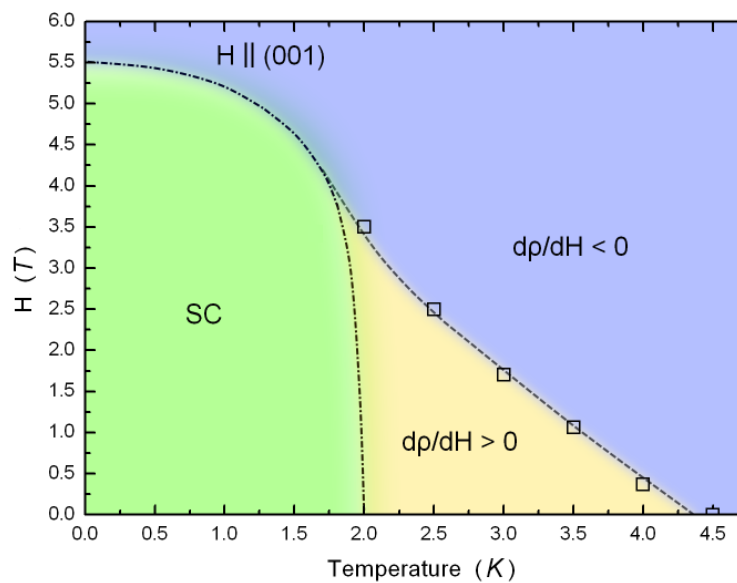


FIGURE F.4: H - T phase diagram based on the magnetoresistance measurements performed on both the SQUID and the single microbridge structures patterned on a $CeCoIn_5$ thin film microcrystal and described in Sec. 3.4.4. For comparison with results on $CeCoIn_5$ bulk crystals see, e.g., (Paglione *et al.* 2003).

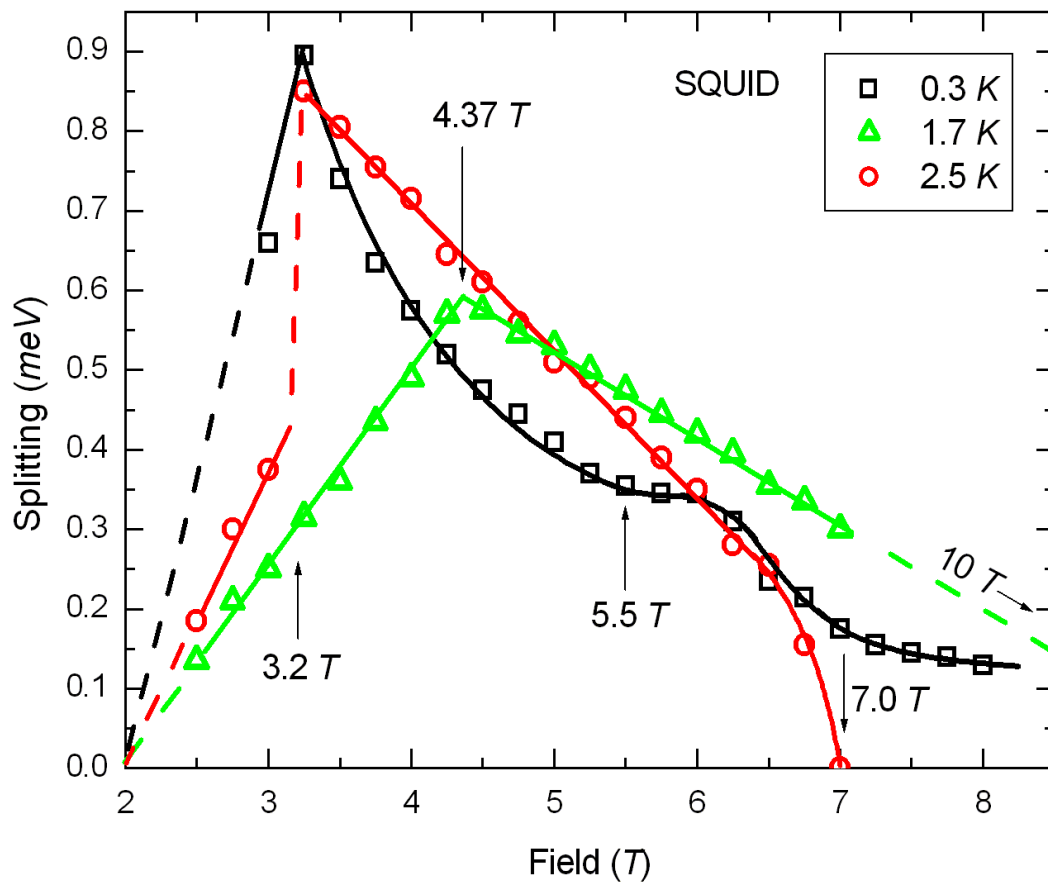


FIGURE F.5: (marks) Measured splitting of the broad maximum around zero bias in external magnetic field. The data points are based on the complete data sets shown partially in Fig. F.2. The solid and dashed lines are guides to the eye. For the curves measured at 1.7 K the splitting linearly increases with increasing magnetic field up to about 4.37 T and decreases linearly at higher fields with a linearly extrapolated value of magnetic field corresponding to zero splitting of about 10 T. For the curves measured at 0.3 K the splitting increases till about 3.2 T and decreases at larger magnetic fields. For the curve measured at 2.5 K the splitting reaches its maximum at about 3.2 T and tends to zero at about 7 T. 5.5 T denotes the second critical magnetic field for $CeCoIn_5$ along the c crystallographic direction.

Bibliography

- Abraham F., Rudge W., Auerbach D., & Koch S., Molecular-dynamics simulations of the incommensurate phase of krypton on graphite using more than 100 000 atoms, *Phys. Rev. Lett.* **52** (6), 445–448 (1984).
- Abrikosov A., Fundamentals of the theory of metals, North-Holland (1988).
- Alexander L., The Synthesis of X-ray Spectrometer Line Profiles with Application to Crystallite Size Measurements, *J. Appl. Phys.* **25** (2), 155–161 (1954).
- Altshuler B. & Aronov A., Electron-Electron Interaction in Disordered Conductors, Amsterdam: Elsevier Scientific Publishing (1985).
- Ambegaokar V. & Baratoff A., Tunneling Between Superconductors, *Phys. Rev. Lett.* **10** (11), 486–489 (1963).
- Ambegaokar V. & Halperin B.I., Voltage Due to Thermal Noise in the dc Josephson Effect, *Phys. Rev. Lett.* **22** (25), 1364–1366 (1969).
- Anderson P., Localized Magnetic States in Metals, *Phys. Rev.* **124** (1), 41 (1961).
- Anderson P.W. & Dayem A.H., Radio-Frequency Effects in Superconducting Thin Film Bridges, *Phys. Rev. Lett.* **13**, 195–197 (1964).
- Andreev A.F., *Sov. Phys. JETP* **19**, 1228 (1964).
- Andres K., Graebner J., & Ott H., $4f$ -Virtual-Bound-State Formation in $CeAl_3$ at Low Temperatures, *Phys. Rev. Lett.* **35** (26), 1779–1782 (1975).
- Andreussi F. & Gurtin M.E., On the wrinkling of a free surface, *J. Appl. Phys.* **48** (9), 3798–3799 (1977).
- Aponte J.M., Bellorín A., Oentrich R., van der Kuur J., Gutiérrez G., & Octavio M., Resistance noise in high- T_c and low- T_c granular superconducting films, *Phys. Rev. B* **47** (14), 8964–8967 (1993).
- Ashcroft N.W. & Mermin D.N., Solid State Physics, Thomson Learning, Toronto, 1 edition (1976).
- Aslamazov L.G. & Larkin A.I., Josephson effect in wide superconducting bridges, *Sov. Phys. JETP* **41**, 381 (1975).
- Avron J., Balfour L., Kuper C., Landau J., Lipson S., & Schulman L., Roughening

- Transition in the ^4He Solid-Superfluid Interface, *Phys. Rev. Lett.* **45** (10), 814–817 (1980).
- Balberg I. & Binenbaum N., Scher and Zallen criterion: Applicability to composite systems, *Phys. Rev. B* **35** (16), 8749–8752 (1987).
- Bardeen J., Tunneling Into Superconductors, *Phys. Rev. Lett.* **9**, 147–149 (1962).
- Bardeen J., Cooper L., & Schrieffer J., Theory of superconductivity, *Phys. Rev.* **108** (5), 1175 (1957).
- Bardeen J. & Stephen M.J., Theory of the Motion of Vortices in Superconductors, *Phys. Rev.* **140** (4A), A1197–A1207 (1965).
- Bauer E., Phänomenologische Theorie der Kristallabscheidung an Oberflächen, *Z. Kristallogr.* **110** (1-6), 372–394 (1958).
- Belen’kii B.I., Computation of the bandwidth of a digital-voltmeter comparison device, *Measurement Techniques* **11**, 203–206 (1968).
- Bergmann G., Weak localization in thin films: a time-of-flight experiment with conduction electrons, *Phys. Rep.* **107** (1), 1 – 58 (1984).
- Bergmann G., Magnetic Screening of Fe Impurities in Mg, *Phys. Rev. Lett.* **57**, 1460–1463 (1986).
- Bianchi A., Movshovich R., Oeschler N., Gegenwart P., Steglich F., Thompson J.D., Pagliuso P.G., & Sarrao J.L., First-Order Superconducting Phase Transition in CeCoIn_5 , *Phys. Rev. Lett.* **89**, 137002 (2002).
- Birkholz M., Fewster P., & Genzel C., Thin film analysis by X-ray scattering, Wiley-VCH (2006).
- Blonder G.E., Tinkham M., & Klapwijk T.M., Transition from metallic to tunneling regimes in superconducting microconstrictions: Excess current, charge imbalance, and supercurrent conversion, *Phys. Rev. B* **25** (7), 4515–4532 (1982).
- Bragg W. & Bragg W., The reflection of X-rays by crystals, *Proceedings of the Royal Society of London. Series A* **88** (605), 428 (1913).
- Callen H., Thermodynamics and an Introduction to Thermostatistics, 2nd Edition, volume 1, Wiley-VCH (1985).
- Campbell T., Kalia R.K., Nakano A., Vashishta P., Ogata S., & Rodgers S., Dynamics of Oxidation of Aluminum Nanoclusters using Variable Charge Molecular-Dynamics Simulations on Parallel Computers, *Phys. Rev. Lett.* **82** (24), 4866–4869 (1999).
- Chang L.L., Esaki L., & Tsu R., Resonant tunneling in semiconductor double barriers, *Appl. Phys. Lett.* **24** (12), 593–595 (1974).
- Chao K.A., Band narrowing and metal-insulator transition in Gutzwiller’s variational scheme, *Solid State Commun.* **14** (7), 525–528 (1974).
- Cheary R. & Coelho A., A fundamental parameters approach to X-ray line-profile fitting, *J. Appl. Crystallogr.* **25** (2), 109–121 (1992).

-
- Chen J.R. & Liu Y.C., Thermal outgassing from stainless steel vacuum chambers, *Chin. J. Phys.* **24** (1), 29–36 (1986).
- Chung K.H., Yao N., Benziger J., Sturm J.C., Singh K.K., Carlson D., & Kuppurao S., Ultrahigh growth rate of epitaxial silicon by chemical vapor deposition at low temperature with neopentasilane, *Appl. Phys. Lett.* **92** (11), 113506 (2008).
- Clark H.E. & Young R.D., Field emission through single strontium atoms adsorbed on a tungsten surface, *Surf. Sci.* **12** (2), 385 – 389 (1968).
- Clausius R., Ueber die Art der Bewegung, welche wir Wärme nennen, *Ann. Phys.* **100**, 353–379 (1857).
- Coleman P., Theories of non-Fermi liquid behavior in heavy fermions, *Physica B: Condensed Matter* **259-261**, 353 – 358 (1999).
- Continentino M., Wilson and Kadowaki-Woods ratios in heavy fermions, *The European Physical Journal B - Condensed Matter and Complex Systems* **13**, 31–35 (2000).
- Continentino M.A., Universal behavior in heavy fermions, *Phys. Rev. B* **47** (17), 11587–11590 (1993).
- Cornelius A.L., Gangopadhyay A.K., Schilling J.S., & Assmus W., Hydrostatic high-pressure studies on the ferromagnetic Kondo-lattice compounds *CePdSb* and *CeAg* to 16 GPa, *Phys. Rev. B* **55** (21), 14109–14112 (1997).
- Dahmen U., Orientation relationships in precipitation systems, *Acta Metallurgica* **30** (1), 63–73 (1982).
- Datta S., Quantum phenomena, Modular series on solid state devices, Addison-Wesley (1989).
- de Broglie L., Waves and quanta, *Nature* **112** (2815), 540–540 (1923).
- De Haas W. & De Boer J., The electrical resistance of platinum at low temperatures, *Physica* **1** (7-12), 609–616 (1934).
- De Haas W., De Boer J., & Van Den Berg G., The electrical resistance of gold, copper and lead at low temperatures, *Physica* **1** (7-12), 1115–1124 (1934).
- Deaver B.S. & Fairbank W.M., Experimental Evidence for Quantized Flux in Superconducting Cylinders, *Phys. Rev. Lett.* **7**, 43–46 (1961).
- DeBeer-Schmitt L., Dewhurst C.D., Hoogenboom B.W., Petrovic C., & Eskildsen M.R., Field Dependent Coherence Length in the Superclean, High- κ Superconductor *CeCoIn₅*, *Phys. Rev. Lett.* **97** (12), 127001 (2006).
- Demsar J., Sarrao J.L., & Taylor A.J., Dynamics of photoexcited quasiparticles in heavy electron compounds, *J. Phys. Condens. Matter* **18** (16), R281 (2006).
- Dieleman P., Bukkems H.G., Klapwijk T.M., Schicke M., & Gundlach K.H., Observation of Andreev Reflection Enhanced Shot Noise, *Phys. Rev. Lett.* **79** (18), 3486–3489 (1997).
- Dieny B., Speriosu V.S., Parkin S.S.P., Gurney B.A., Wilhoit D.R., & Mauri D., Giant magnetoresistive in soft ferromagnetic multilayers, *Phys. Rev. B* **43**, 1297–1300

- (1991).
- Dobrosavljević V., Kirkpatrick T., & Kotliar B., Kondo effect in disordered systems, *Phys. Rev. Lett.* **69** (7), 1113–1116 (1992).
- Doll R. & Näbauer M., Experimental Proof of Magnetic Flux Quantization in a Superconducting Ring, *Phys. Rev. Lett.* **7**, 51–52 (1961).
- Doniach S., The Kondo lattice and weak antiferromagnetism, *Physica B + C* **91**, 231–234 (1977).
- Duke C.B. & Alferieff M.E., Field Emission through Atoms Adsorbed on a Metal Surface, *The Journal of Chemical Physics* **46** (3), 923–937 (1967).
- Dushman S., Scientific foundations of vacuum technique, 1962 (various printings), Wiley (1962).
- Elenbaas R., Schinkel C., & van Deudekom C., Heat capacity and electrical resistivity of $(Ce, La)In_3$ and $Ce(In, Sn)_3$, *J. Magn. Magn. Mater.* **15-18** (Part 2), 979 – 981 (1980).
- Esaki L., New Phenomenon in Narrow Germanium $p - n$ Junctions, *Phys. Rev.* **109**, 603–604 (1958).
- Esaki L., Long journey into tunneling, *Rev. Mod. Phys.* **46** (2), 237–244 (1974).
- Fazekas P., Lecture notes on electron correlation and magnetism, Series in modern condensed matter physics, World Scientific (1999).
- Feynman R., Leighton R., & Sands M., The Feynman Lectures on Physics: Quantum mechanics, The Feynman Lectures on Physics, Addison-Wesley Pub. Co. (1965).
- Ford P.J., Babic E., & Mydosh J.A., Electrical resistivity of concentrated AuCr alloys, *J. Phys. F* **3** (4), L75 (1973).
- Fowler R. & Nordheim L., Electron emission in intense electric fields, *Proceedings of the Royal Society of London. Series A* **119** (781), 173–181 (1928).
- Foyevtsov O., Porrati F., & Huth M., Josephson effect in $CeCoIn_5$ microbridges as seen via quantum interferometry, *Phys. Rev. B* **84**, 045103 (2011).
- Foyevtsov O., Reith H., & Huth M., Transport measurements on microcrystals of oriented $CeIn_3$ and $CeCoIn_5$ thin films, *Thin Solid Films* **518** (23), 7064 – 7069 (2010).
- Frenken J. & Veen J., Observation of surface melting, *Phys. Rev. Lett.* **54** (2), 134–137 (1985).
- Freund L. & Suresh S., Thin film materials: stress, defect formation, and surface evolution, Cambridge University Press (2003).
- Friedrich W., Knipping P., & Laue M., Interference Phenomena with Rontgen Rays, *Acad. Wiss. Munich* **42**, 303 (1912).
- Gamow G., Quantum theory of atomic nucleus, *Zeits. Phys.* **51**, 204 (1928).
- Gantmakher V., Electrons and disorder in solids, International series of monographs on physics, Clarendon Press (2005).

-
- Giaever I., Energy gap in superconductors measured by electron tunneling, *Phys. Rev. Lett.* **5** (4), 147–148 (1960).
- Gibbs J., Collected Works, volume 1, Yale University Press (1948).
- Golubov A.A., Kupriyanov M.Y., & Il'ichev E., The current-phase relation in Josephson junctions, *Rev. Mod. Phys.* **76** (2), 411–469 (2004).
- Grimes C. & Adams G., Evidence for a liquid-to-crystal phase transition in a classical, two-dimensional sheet of electrons, *Phys. Rev. Lett.* **42** (12), 795–798 (1979).
- Grosche F.M., Walker I.R., Julian S.R., Mathur N.D., Freye D.M., Steiner M.J., & Lonzarich G.G., Superconductivity on the threshold of magnetism in $CePd - 2Si_2$ and $CeIn_3$, *Journal of Physics: Condensed Matter* **13** (12), 2845 (2001).
- Gulbransen E.A. & Wysong W.S., Thin Oxide Films on Aluminum, *The Journal of Physical and Colloid Chemistry* **51** (5), 1087–1103 (1947).
- Gumann A., Dahm T., & Schopohl N., Microscopic theory of superconductor-constriction-superconductor Josephson junctions in a magnetic field, *Phys. Rev. B* **76** (6), 064529 (2007).
- Gundlach K.H. & Wilkinson A., Experimental evidence for the temperature dependence of the barrier height in $Al-Al_2O_3$ -metal tunneling junctions, *Phys. Status Solidi A* **2** (2), 295–298 (1970).
- Haesendonck C.V., Vranken J., & Bruynseraede Y., Resonant Kondo Scattering of Weakly Localized Electrons, *Phys. Rev. Lett.* **58**, 1968–1971 (1987).
- Hahn T., International Tables for Crystallography, number . 1 in International tables for crystallography, International Union of Crystallography (2006).
- Hamilton C.A., Josephson voltage standards, *Rev. Sci. Instrum.* **71** (10), 3611–3623 (2000).
- Hänisch J., Ronning F., Movshovich R., & Matias V., Pulsed laser deposition of $CeCoIn_5$ thin films, *Physica C: Superconductivity* **470** (Supplement 1), S568 – S569 (2010).
- Herring C., Some Theorems on the Free Energies of Crystal Surfaces, *Phys. Rev.* **82** (1), 87–93 (1951).
- Hikami S., Larkin A.I., & Nagaoka Y., Spin-Orbit Interaction and Magnetoresistance in the Two Dimensional Random System, *Prog. Theor. Phys.* **63** (2), 707–710 (1980).
- Hill T., An introduction to statistical thermodynamics, Addison-Wesley series in chemistry, Dover Publications (1960).
- Hoffman D., Singh B., & Thomas J., Handbook of vacuum science and technology, Academic Press (1998).
- Hölzer G., Fritsch M., Deutsch M., Härtwig J., & Förster E., $K\alpha_- \{1, 2\}$ and $K\beta_- \{1, 3\}$ x-ray emission lines of the 3d transition metals, *Phys. Rev. A* **56** (6), 4554 (1997).
- Honig R. & Kramer D., Vapor pressure data for the solid and liquid elements, RCA Laboratories, David Sarnoff Research Center (1969).

- Hori H., Teranishi T., Nakae Y., Seino Y., Miyake M., & Yamada S., Anomalous magnetic polarization effect of Pd and Au nano-particles, *Phys. Lett. A* **263** (4-6), 406–410 (1999).
- Ikeda S., Shishido H., Nakashima M., Settai R., Haga Y., Harima H., Aoki Y., Namiki T., Sato H., & Ōnuki Y., Unconventional Superconductivity in $CeCoIn_5$ Studied by the Specific Heat and Magnetization Measurements, *J. Phys. Soc. Jpn.* **70** (8), 2248–2251 (2001).
- Ishii C., Josephson Currents through Junctions with Normal Metal Barriers, *Prog. Theor. Phys.* **44** (6), 1525–1547 (1970).
- Izaki M., Shishido H., Kato T., Shibauchi T., Matsuda Y., & Terashima T., Superconducting thin films of heavy-fermion compound $CeCoIn_5$ prepared by molecular beam epitaxy, *Appl. Phys. Lett.* **91** (12), 122507 (2007).
- Jacko A., Fjærestad J., & Powell B., A unified explanation of the Kadowaki–Woods ratio in strongly correlated metals, *Nature Physics* **5** (6), 422–425 (2009).
- Jaklevic R.C., Lambe J., Silver A.H., & Mercereau J.E., Quantum Interference Effects in Josephson Tunneling, *Phys. Rev. Lett.* **12**, 159–160 (1964).
- Johnson S.D., Zieve R.J., & Cooley J.C., Nonlinear effect of uniaxial pressure on superconductivity in $CeCoIn_5$, *Phys. Rev. B* **83**, 144510 (2011).
- Josephson B., Possible new effects in superconductive tunnelling, *Phys. Lett.* **1**, 251–253 (1962).
- Josephson B., Coupled superconductors, *Rev. Mod. Phys.* **36** (1964).
- Kadowaki K. & Woods S., Universal relationship of the resistivity and specific heat in heavy-fermion compounds, *Solid State Commun.* **58** (8), 507–509 (1986).
- Kasahara Y., Nakajima Y., Izawa K., Matsuda Y., Behnia K., Shishido H., Settai R., & Onuki Y., Anomalous quasiparticle transport in the superconducting state of $CeCoIn_5$, *Phys. Rev. B* **72**, 214515 (2005).
- Kasuya T., A theory of metallic ferro- and antiferromagnetism on Zener’s model, *Prog. Theor. Phys.* **16** (1), 45–57 (1956).
- Keene B., Review of data for the surface tension of pure metals, *International Materials Reviews* **38** (4), 157–192 (1993).
- Kirkpatrick P., The Polarization Factor in X-ray Reflection, *Phys. Rev.* **29**, 632–636 (1927).
- Kiss L.B. & Svedlindh P., New noise exponents in random conductor-superconductor and conductor-insulator mixtures, *Phys. Rev. Lett.* **71** (17), 2817–2820 (1993).
- Kitaoka Y., Ishida K., Kawasaki Y., Trovarelli O., Geibel C., & Steglich F., Coexistence of superconductivity and antiferromagnetism in the heavy-fermion superconductor $CeCu_2(Se_{1-x}Ge_x)_2$ probed by means of Cu nuclear quadrupole resonance - a test case for the SO(5) theory, *Journal of Physics: Condensed Matter* **13** (4), L79 (2001).

- Kitaoka Y., Kishimoto Y., Asayama K., Kohara T., Takeda K., Vijayaraghavan R., Malik S., Dhar S., & Rambabu D., Magnetic behavior of $RERh_3B_2$ ($RE = La, Ce, Nd$ and Gd), *J. Magn. Magn. Mater.* **52** (1-4), 449–451 (1985).
- Kittel C., Introduction to solid state physics, Wiley (2005).
- Kittel C. & Fong C., Quantum theory of solids, Wiley (1987).
- Kleinsasser A.W., Miller R.E., Mallison W.H., & Arnold G.B., Observation of multiple Andreev reflections in superconducting tunnel junctions, *Phys. Rev. Lett.* **72** (11), 1738–1741 (1994).
- Kondo J., Resistance minimum in dilute magnetic alloys, *Prog. Theor. Phys.* **32** (1), 37–49 (1964).
- Kondo J., Resistance minimum and heavy fermions, *Proceedings of the Japan Academy, Series B* **82**, 328–338 (2006).
- Kosterlitz J. & Thouless D., Ordering, metastability and phase transitions in two-dimensional systems, *J. Phys. C* **6**, 1181 (1973).
- Kulik I.O. & Omelyanchuk A.N., *Sov. Phys. JETP* **21**, 96 (1975).
- Kulik I.O. & Omelyanchuk A.N., *Fiz. Nizk. Temp.* **3**, 945 (1977).
- Lafferty J.M., Foundations of vacuum science and technology, Wiley-Interscience publication, Wiley (1998).
- Lagendijk A., Van Tiggelen B., & Wiersma D., Fifty years of Anderson localization, *Phys. Today* **62** (8), 24–29 (2009).
- Landau L.D. & Lifshitz E.M., Theory of Elasticity, Pergamon, Oxford (1970).
- Landau L.D. & Ter-Haar D., Collected papers of L.D. Landau, Oxford: Pergamon, Oxford (1965).
- Lawson A.W. & Tang T.Y., Concerning the High Pressure Allotropic Modification of Cerium, *Phys. Rev.* **76** (2), 301–302 (1949).
- Li C.Y., Wu C.M., Karna S.K., Wang C.W., Hsu D., Wang C.J., & Li W.H., Intrinsic magnetic moments of gold nanoparticles, *Phys. Rev. B* **83**, 174446 (2011).
- Likharev K.K., Superconducting weak links, *Rev. Mod. Phys.* **51** (1), 101–159 (1979).
- Lindelof P.E., Superconducting microbridges exhibiting Josephson properties, *Rep. Prog. Phys.* **44** (9), 949 (1981).
- Mahan G., Many Body Physics, Plenum, New York (1981).
- Malinowski A., Hundley M.F., Capan C., Ronning F., Movshovich R., Moreno N.O., Sarrao J.L., & Thompson J.D., c -axis magnetotransport in $CeCoIn_5$, *Phys. Rev. B* **72**, 184506 (2005).
- Marks L., Heine V., & Smith D., Direct observation of elastic and plastic deformations at Au (111) surfaces, *Phys. Rev. Lett.* **52** (8), 656–658 (1984).
- Maslen E., Fox A., & O’Keefe M., X-ray scattering, *International Tables for Crystallography C*, 554 (2006).
- Mathur N., Grosche F., Julian S., Walker I., Freye D., Haselwimmer R., & Lonzarich

- G., Magnetically mediated superconductivity in heavy fermion compounds, *Nature* **394** (6688), 39–43 (1998).
- Meissner H. & Zdanis R., Paramagnetic Effect in Superconductors. VI. Resistance Transitions in Indium Wires, *Phys. Rev.* **109** (3), 681–685 (1958).
- Misra P., Heavy-fermion systems, volume 2, Elsevier Science (2008).
- Movshovich R., Jaime M., Thompson J., Petrovic C., Fisk Z., Pagliuso P., & Sarrao J., Unconventional Superconductivity in $CeIrIn_5$ and $CeCoIn_5$: Specific Heat and Thermal Conductivity Studies, *Phys. Rev. Lett.* **86** (22), 5152–5155 (2001).
- Nakatsuji S., Pines D., & Fisk Z., Two Fluid Description of the Kondo Lattice, *Phys. Rev. Lett.* **92**, 016401 (2004).
- Narlikar A., Frontiers in superconducting materials, Springer (2005).
- Nemes G., New asymptotic expansion for the Gamma function, *Archiv der Mathematik* **95**, 161–169 (2010).
- Nozières P. & Blandin A., Kondo effect in real metals, *J. Phys. (Paris)* **41** (3), 193–211 (1980).
- Oeschler N., Gegenwart P., Lang M., Movshovich R., Sarrao J. L., Thompson J. D., & Steglich F., Uniaxial Pressure Effects on $CeIrIn_5$ and $CeCoIn_5$ Studied by Low-Temperature Thermal Expansion, *Phys. Rev. Lett.* **91**, 076402 (2003).
- Ohno T., Kishimoto Y., Yamada Y., Michihiro Y., & Kanashiro T., UB Nuclear Spin-Lattice Relaxation in Itinerant Weak Antiferromagnetic $SmRh_3B_2$, *J. Phys. Soc. Jpn.* **58** (1), 50–53 (1989).
- Oppenheimer J.R., On the Quantum Theory of the Capture of Electrons, *Phys. Rev.* **31**, 349–356 (1928).
- Ott H.R., Rudigier H., Fisk Z., & Smith J.L., UBe_{13} : An Unconventional Actinide Superconductor, *Phys. Rev. Lett.* **50**, 1595–1598 (1983).
- Özcan S., Broun D.M., Morgan B., Haselwimmer R.K.W., Sarrao J.L., Kamal S., Bidinosti C.P., Turner P.J., Raudsepp M., & Waldram J.R., London penetration depth measurements of the heavy-fermion superconductor $CeCoIn_5$ near a magnetic quantum critical point, *Europhys. Lett.* **62** (3), 412 (2003).
- Paglione J., Tanatar M.A., Hawthorn D.G., Boaknin E., Hill R.W., Ronning F., Sutherland M., Taillefer L., Petrovic C., & Canfield P.C., Field-Induced Quantum Critical Point in $CeCoIn_5$, *Phys. Rev. Lett.* **91**, 246405 (2003).
- Pecharsky V. & Zavalij P., Fundamentals of powder diffraction and structural characterization of materials, volume 69, Springer Verlag (2009).
- Perentes A. & Hoffmann P., Focused Electron Beam Induced Deposition of Si -Based Materials From SiO_xC_y to Stoichiometric SiO_2 : Chemical Compositions, Chemical-Etch Rates, and Deep Ultraviolet Optical Transmissions, *Chemical Vapor Deposition* **13** (4), 176–184 (2007).

- Petrovic C., Bud'ko S.L., Kogan V.G., & Canfield P.C., Effects of La substitution on the superconducting state of $CeCoIn_5$, *Phys. Rev. B* **66**, 054534 (2002).
- Petrovic C., Pagliuso P.G., Hundley M.F., Movshovich R., Sarrao J.L., Thompson J.D., Fisk Z., & Monthoux P., Heavy-fermion superconductivity in $CeCoIn_5$ at 2.3 K, *Journal of Physics: Condensed Matter* **13** (17), L337 (2001).
- Pines D. & Nozières P., The theory of quantum liquids, WA Benjamin (1966).
- Plummer E.W. & Young R.D., Field-Emission Studies of Electronic Energy Levels of Adsorbed Atoms, *Phys. Rev. B* **1** (5), 2088–2109 (1970).
- Ramirez R., Rahman A., & Schuller I.K., Epitaxy and superlattice growth, *Phys. Rev. B* **30** (10), 6208–6210 (1984).
- Rasul J.W., Weak-localization effects in heavy-fermion systems, *Phys. Rev. B* **44**, 11802–11805 (1991).
- Reich S., Leitus G., & Feldman Y., Observation of magnetism in Au thin films, *Appl. Phys. Lett.* **88** (22), 222502–222502 (2006).
- Rez D., Rez P., & Grant I., Dirac-Fock calculations of X-ray scattering factors and contributions to the mean inner potential for electron scattering, *Acta Crystallogr. Sec. A* **50** (4), 481–497 (1994).
- Rice M.J., Electron-Electron Scattering in Transition Metals, *Phys. Rev. Lett.* **20**, 1439–1441 (1968).
- Rosenthal P.A., Beasley M.R., Char K., Colclough M.S., & Zaharchuk G., Flux focusing effects in planar thin-film grain-boundary Josephson junctions, *Appl. Phys. Lett.* **59** (26), 3482–3484 (1991).
- Sachdev S., Quantum phase transitions, Cambridge University Press (2001).
- Sadki E.S., Ooi S., & Hirata K., Focused-ion-beam-induced deposition of superconducting nanowires, *Appl. Phys. Lett.* **85** (25), 6206–6208 (2004).
- Sarachik M.P., Corenzwit E., & Longinotti L.D., Resistivity of $Mo-Nb$ and $Mo-Re$ Alloys Containing 1% Fe , *Phys. Rev.* **135** (4A), A1041–A1045 (1964).
- Sarpeshkar R., Delbruck T., & Mead C., White noise in MOS transistors and resistors, *Circuits and Devices Magazine, IEEE* **9** (6), 23–29 (1993).
- Sato N., Sakon T., Imamura K., Inada Y., Aono H., & Komatsubara T., Superconductivity and magnetism in a single crystal of UPd_2Al_3 , *Physica B: Condensed Matter* **186188** (0), 195 – 200 (1993).
- Scardi P. & Leoni M., Line profile analysis: pattern modelling versus profile fitting, *J. Appl. Crystallogr.* **39** (1), 24–31 (2006).
- Scherrer P., *Gttinger Nachrichten Gesell* **2**, 98 (1918a).
- Scherrer P., Bestimmung der Grösse und der inneren Struktur von Kolloidteilchen mittels Röntgenstrahlen, *Nachr. Ges. Wiss. Göttingen* **2**, 98–100 (1918b).
- Schopfer F., Bäuerle C., Rabaud W., & Saminadayar L., Anomalous Temperature Dependence of the Dephasing Time in Mesoscopic Kondo Wires, *Phys. Rev. Lett.* **90**,

- 056801 (2003).
- Schrieffer J.R. & Wolff P.A., Relation between the Anderson and Kondo Hamiltonians, *Phys. Rev.* **149** (2), 491–492 (1966).
- Seaman C.L., Maple M.B., Lee B.W., Ghamaty S., Torikachvili M.S., Kang J.S., Liu L.Z., Allen J.W., & Cox D.L., Evidence for non-Fermi liquid behavior in the Kondo alloy $Y_{1-x}U_xPd_3$, *Phys. Rev. Lett.* **67** (20), 2882–2885 (1991).
- Settai R., Kubo T., Shiromoto T., Honda D., Shishido H., Sugiyama K., Haga Y., Matsuda T.D., Betsuyaku K., Harima H., Kobayashi T.C., & Ōnuki Y., Change of the Fermi Surface across the Critical Pressure in $CeIn_3$: The de Haas–van Alphen Study under Pressure, *J. Phys. Soc. Jpn.* **74** (11), 3016–3026 (2005).
- Settai R., Shishido H., Ikeda S., Nakashima M., Aoki D., Haga Y., Harima H., & nuki Y., Scattering rate of quasiparticles both in the normal and superconducting mixed states in $CeCoIn_5$ studied by the dHvA effect, *Physica B: Condensed Matter* **312-313** (0), 123–125 (2002).
- Shapiro S., Josephson currents in superconducting tunneling: The effect of microwaves and other observations, *Phys. Rev. Lett.* **11** (2), 80–82 (1963).
- Shiba H., Properties of Strongly Correlated Fermi Liquid in Valence Fluctuation System—a Variational Monte-Carlo Study, *J. Phys. Soc. Jpn.* **55** (8), 2765–2776 (1986).
- Shih A. & Parsegian V., Van der Waals forces between heavy alkali atoms and gold surfaces: Comparison of measured and predicted values, *Phys. Rev. A* **12** (3), 835 (1975).
- Shishido H., Shibauchi T., Yasu K., Kato T., Kontani H., Terashima T., & Matsuda Y., Tuning the Dimensionality of the Heavy Fermion Compound $CeIn_3$, *Science* **327** (5968), 980–983 (2010).
- Smith C. & Gomer R., Structure and properties of solid surfaces, University of Chicago Press and US National Research Council (1953).
- Snyder R., Fiala J., & Bunge H., Defect and microstructure analysis by diffraction, International Union of Crystallography monographs on crystallography, Oxford University Press (1999).
- Sondheimer E.H., The Theory of the Transport Phenomena in Metals, *Proceedings of the Royal Society of London. Series A. Mathematical and Physical Sciences* **203** (1072), 75–98 (1950).
- Sørensen E.S. & Affleck I., Scaling theory of the Kondo screening cloud, *Phys. Rev. B* **53** (14), 9153–9167 (1996).
- Soroka O.K., Blendin G., & Huth M., Growth of $CeCoIn_5$ thin films on *a* and *r*- Al_2O_3 substrates, *Journal of Physics: Condensed Matter* **19** (5), 056006 (2007).
- Spoddig D., Schindler K., Rdiger P., Barzola-Quiquia J., Fritsch K., Mulders H., & Esquinazi P., Transport properties and growth parameters of PdC and WC

- nanowires prepared in a dual-beam microscope, *Nanotechnology* **18** (49), 495202 (2007).
- Steglich F., Aarts J., Bredl C., Lieke W., Meschede D., Franz W., & Schäfer H., Superconductivity in the Presence of Strong Pauli Paramagnetism: $CeCu_2Si_2$, *Phys. Rev. Lett.* **43** (25), 1892–1896 (1979).
- Stewart G.R., Non-Fermi-liquid behavior in d - and f -electron metals, *Rev. Mod. Phys.* **73** (4), 797–855 (2001).
- Stoop L. & der Merwe J.V., Misfit accommodation in epitaxial monolayers on (111) f.c.c. and (110) b.c.c. substrates II: Analytical approach to monolayers in the Nishiyama-Wassermann orientation, *Thin Solid Films* **91** (3), 257–276 (1982).
- Sumiyama A., Oda Y., Nagano H., Shibutani Y., & Komatsubara T., Coherent Kondo State in a Dense Kondo Substance: $Ce_xLa_{1-x}Cu_6$, *J. Phys. Soc. Jpn.* **55** (4), 1294–1304 (1986).
- Sweet J., Roth E., & Moss M., Thermal conductivity of Inconel 718 and 304 stainless steel, *International Journal of Thermophysics* **8**, 593–606 (1987).
- Tchokonté M.B.T., Tshabalala K.G., de Villiers du Plessis P., & Kaczorowski D., Magnetic substitution in $CeIn_3$, *J. Phys. Chem. Solids* **71** (3), 181–186 (2010).
- Thompson A., Vaughan D., for X-ray optics C., & advanced light source, X-ray data booklet, Lawrence Berkeley National Laboratory, University of California Berkeley, CA: Berkeley, California USA (2001).
- Thouless D.J., Electrons in disordered systems and the theory of localization, *Phys. Rep.* **13** (3), 93–142 (1974).
- Tinkham M., Introduction to Superconductivity: Second Edition (Dover Books on Physics) (Vol i), Dover Publications, 2 edition (2004).
- Tsunetsugu H., Sigrist M., & Ueda K., The ground-state phase diagram of the one-dimensional Kondo lattice model, *Rev. Mod. Phys.* **69** (3), 809–864 (1997).
- Van Der Pauw L.J., A method of measuring the resistivity and Hall coefficient on lamellae of arbitrary shape, *Philips Technical Review* **20** (8), 220–224 (1958).
- Varma C.M., Nussinov Z., & van Saarloos W., Singular or Non-Fermi Liquids, *AIP Conf. Proc.* **629** (1), 189–192 (2002).
- Venables J., Introduction to surface and thin film processes, Cambridge University Press (2000).
- Verman B. & Kim B., Analytical Comparison of Parallel Beam and Bragg-Brentano Diffractometer Performances, in *Materials Science Forum*, volume 443, Trans Tech Publ. (2004), 167–170.
- Vossen J. & Kern W., Thin film processes II, Thin Film Processes, Academic Press (1991).
- Waldram J., The Josephson effects in weakly coupled superconductors, *Rep. Prog. Phys.* **39**, 751 (1976).

- Walker I.R., Grosche F.M., Freye D.M., & Lonzarich G.G., The normal and superconducting states of $CeIn_3$ near the border of antiferromagnetic order, *Physica C: Superconductivity* **282-287** (Part 1), 303–306 (1997).
- Watanabe T., Kasahara Y., Izawa K., Sakakibara T., Matsuda Y., van der Beek C.J., Hanaguri T., Shishido H., Settai R., & Onuki Y., High-field state of the flux-line lattice in the unconventional superconductor $CeCoIn_5$, *Phys. Rev. B* **70**, 020506 (2004).
- Williamson G. & Hall W., X-ray line broadening from filed aluminium and wolfram, *Acta Metallurgica* **1** (1), 22–31 (1953).
- Wilson K.G., The renormalization group: Critical phenomena and the Kondo problem, *Rev. Mod. Phys.* **47**, 773–840 (1975).
- Wolf E., Principles of electron tunneling spectroscopy, International series of monographs on physics, Oxford University Press (1985).
- Wolf P.E. & Maret G., Weak Localization and Coherent Backscattering of Photons in Disordered Media, *Phys. Rev. Lett.* **55**, 2696–2699 (1985).
- Yamada K., Cambridge University Press (2004).
- Yosida K., Magnetic properties of $Cu - Mn$ alloys, *Phys. Rev.* **106** (5), 893 (1957).
- Zaitsev A., Beck A., Schneider R., Fromknecht R., Fuchs D., Geerk J., & v. Löhneysen H., Deposition of superconducting $CeCoIn_5$ thin films by co-sputtering and evaporation, *Physica C: Superconductivity* **469** (1), 52–54 (2009).
- Zangwill A., Physics at surfaces, Cambridge Univ Press (1988).
- Zener C., Interaction between the d -Shells in the Transition Metals. II. Ferromagnetic Compounds of Manganese with Perovskite Structure, *Phys. Rev.* **82** (3), 403–405 (1951).

Acknowledgements

I am thankful to all the people who made this work possible and as complete as it appears and whom I would like to acknowledge here. First of all, I am grateful to my adviser Prof. Dr. Michael Huth, who courteously granted me a possibility to conduct research in his work group. With his inexhaustible ideas and continuous motivation, I gained substantial knowledge in the field of strongly correlated systems that helped me to focus on the most relevant aspects of this exciting work which I liked a lot.

I want to gratefully mention Dr. Oleksiy Soroka who supported me during the first and, probably, the most important period of my work. I would like to thank all the members of our group for their support and friendly attitude. Separately, I want to acknowledge Dr. Fabrizio Porrati who kindly spent many hours performing and optimizing all the micropatterning procedures presented in this work. I would like to thank Christina Grimm for the routine quantification analysis on $CeCoIn_5$ and $CeIn_3$ thin films that she did using EDXS, which eventually became an important part of the thin film growth studies.

The $Al - Al_2O_3 - W$ -IBID planar tunneling diodes were prepared and characterized in collaboration with Dirk Klingenberger and Albrecht Köhler. However, I present only a part of those studies which were substantially extended by Dirk Klingenberger and Dr. Fabrizio Porrati. A part of the measurements on $CeCoIn_5$ microcrystal-based interferometers were done in collaboration with Paul Weirich.

The planar tunneling diodes on $CeCoIn_5$ thin film microcrystals could not be realized without the help of Dr. Martin Jourdan from the Johannes Gutenberg University in Mainz who kindly granted us an access to the ion beam etching facility.

I would like to express a gratitude to my wife Kateryna for many fruitful discussions and for her continuous support. Without her critical and professional view this manuscript would appear much less strict and accurate.

Eventually, I would like to acknowledge the Deutsche Forschungsgemeinschaft (DFG) for financial support of this project under grant no. HU 752/3-3.

Curriculum Vitae

Oleksandr Foyevtsov

Birth: December 23-rd, 1982 in Kryvyj Rig

Citizenship: Ukrainian

Marital status: married



Education:

02/2007– PhD student [funded from the German Research Foundation (DFG)] in the present group of Prof. Dr. Michael Huth, Physical Institute, Johann Wolfgang Goethe-Universität, Frankfurt am Main. Doctoral thesis title: *“Electron-tunneling studies on CeCoIn₅ heavy-fermion thin films and microstructures”*.

07/2004– Graduate student at Lviv National Polytechnic University (Lviv, Ukraine),
12/2005 Institute of Telecommunications, Radioelectronics and Electronic Engineering (formerly Department of Electrophysics and Semiconductor Electronics). The degree of Master of Science received; Master thesis: *“The influence of thermochemical treatment on properties of epitaxially grown Ca²⁺-doped iron-garnet thin films”* under supervision of Prof. Dr. Sergii Ubizskii.

09/2000– Undergraduate student at Lviv National Polytechnic University (Lviv,
06/2004 Ukraine), Department of Electrophysics and Semiconductor Electronics; Bachelor degree received.

Teaching experience:

Eight semesters as an Advanced Physics lab instructor at the Frankfurt University (in English).

Publications:

- [1] Foyevtsov O., Porrati F., and Huth M., Josephson effect in CeCoIn₅ microbridges as seen via quantum interferometry, *Phys. Rev. B* **84**, 045103 (2011).
- [2] Foyevtsov O., Reith H., and Huth M., Transport measurements on microcrystals of oriented CeIn₃ and CeCoIn₅ thin films, *Thin Solid Films* **518**, 7064-7069 (2010).
- [3] Foyevtsov O. B., Huth M., Morphological variability of CeIn₃ thin films grown by molecular beam epitaxy, *J. Phys.: Conf. Ser.* **150**, 052057 (2009).